The velocity-field characteristic of indium phosphide.

by

Roland Leonard Tebbenham

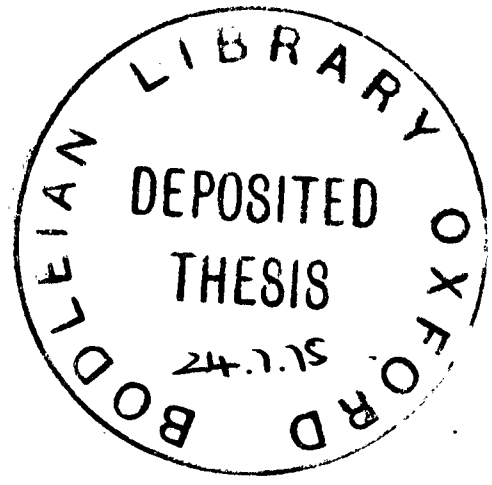

Thesis submitted for the degree of Doctor of Philosophy at the University of Oxford.

Hilary 1975.

ACKNOWLEDGEMENTS

I wish to thank Dr. D. Walsh and Dr. L. Solymar of the Department of Engineering Science of the University of Oxford for their help, ideas and guidance during their supervision of this work. Many other members of the Department rendered considerable assistance Dr. D.A. Spence and Dr. B. Minakovic with helpful suggestions, Mr. G.N. Roger and Mr. R. Smurthwaite with the availability of their facilities and the members of the Physical Electronics Group with whom I worked, particularly Mr. D. Hamilton.

Thanks are due to the Science Research Council and the General Electric Company (Hirst Research Centre) for funds to enable me to pursue the work, Lincoln College for accommodation and services and The Plessey Company Limited (Allen Clark Research Centre) for the supply of material and many valuable suggestions; and for the latter particularly Dr. G. Gibbons.

Thanks are due to Mrs. H. Barbour for typing the work, and to my wife for helping with the proof reading.

ABSTRACT

The introductory chapter commences with a brief perspective, continues with a description of the compound III-V semiconductors and concludes with a survey of solid-state microwave devices including current commercial and state-of-the-art results.

The properties of indium phosphide are outlined in Chapter two commencing with the preparation and physical properties, continuing with a description of the band-structure and related electrical properties and including a survey of scattering processes. Inter-valley transfer is discussed leading to the three-level transfer system and the concept of negative-differential mobility. The consequential operation of devices is considered and the chapter concludes with an outline of the Boltzmann transport equation and the solutions thereof by various means and a summary of non-linear effects in the carrier transport theory.

Chapter three describes measurement methods of the velocity-field characteristic, and in particular the working equations and analysis of the experiment to measure microwave-conductivity. Perturbing mechanisms of doping inhomogeneity and energy relaxation are considered and other work on these reviewed. Numerical approximation techniques in the experimental analysis are compared and developed, leading to a complete analysis of experimental data and criteria to handle space-charge suppression. Calculations of the effects of transient heating of samples are produced, together with the effects of temperature induced carrier-concentration variation which in the experiments was small. The chapter concludes with a description of the experimental apparatus, its calibration and predicts a microwave measurement accuracy of 5%.

The results of a computer simulation of the experiment and analysis of theoretical data and derived results are presented in Chapter four, where the various computer programmes are described. It is demonstrated that the velocity-field characteristic may be accurately recovered from data derived from it via the experimental method, assumptions therein being justified numerically. This Chapter concludes with a presentation of the interaction by microwave signals with inductively mounted semiconducting obstacles in rectangular waveguide. Some numerical calculations are described and presented.

Chapter five describes the calibration of the experimental system using gallium arsenide samples. The sample preparation, mounting and biassing methods are described. Results from these experiments yielded salient values of threshold field, E_T = 4.9 kV cm^{-1} peak velocity, V_p = 2.1 10^7 cms^{-1}, peak-to-valley ratio, r = 2.3. These data are in reasonable agreement with results published elsewhere.

The sixth chapter describes the experimental detail relating to the indium phosphide samples, discusses measurement of sample uniformity and work at liquid nitrogen temperatures. The experimental results are presented and variations with epilayer thickness, carrier density, conductivity and temperature are described, this together with possible space-charge growth reduction in thinner layers produces figures 50% above the average in the velocity field characteristic derived from 5μ layers, rather than 10-20μ layers. Carrier density increase from 7.2×10^{14} cm^{-3} to 2.4×10^{15} cm^{-3} led to threshold field decrease from 10.7 kV cm^{-1} to 9.5 kV cm^{-1} and peak velocity decrease from 2.6×10^7 cms^{-1} to 2.3×10^7 cms^{-1}, the negative differential mobility being unaffected within the experimental standard deviation. The results at 100°K indicated a lower threshold field of 9.1 kV cm^{-1} and a higher peak velocity of 4.4×10^7 cms^{-1}.

Assumptions are then reviewed and comparison with other published data made. Space-charge effects and relaxation effects are suggested to produce the largest errors, also the results depend strongly on material quality. No correction for relaxation effects is made since it would be comparable to the overall experimental error, which was of the order of $\pm$ 15%. Comparison with other published data is good, especially bearing in mind the experimental differences, particularly in the material used.

The peak-to-valley ratio was calculated to be in the range $2.15 \leqslant r \leqslant 3.2$ at $300^{\circ}K$. These results are used to make a calculation of the efficiency of a notional LSA device. A sinusoidal mode efficiency of 7.0% is predicted for operation at $300^{\circ}K$, squarewave efficiencies being some four times this figure. No estimate of frequency dependence is made.

Chapter seven forms the work's conclusion presenting the results formally, briefly discussing perturbing effects and errors and considering the device efficiency calculations. The chapter concludes with comments on further investigation into the semiconductor and devices made using it. Work on material, fundamental experiments and device operation and characterisation being associated to bring better understanding of the features of the material and its application.

INDEX OF CONTENTS

LIST OF PRINCIPAL SYMBOLS USED IN THE TEXT

a_o	lattice constant
a_1	interatomic spacing
a,b,	rectangular waveguide dimensions
c_o	velocity of light in vacuo
c_p	specific heat
c_{jj}	secondary elastic constant
C_o	primary elastic constant
C	capacitance
d	characteristic diameter
D	diffusion constant
E	electric field
E_t	threshold field
f	frequency
g	thermal generation rate
h,ħ,	Plank's constant/reduced value
h_n	harmonic component
i	current
j	$\sqrt{-1}$ (operator)
J	current density
k	Boltzmann's constant
k_d	thermal diffusivity
k_t	thermal conductivity
l	characteristic length
l_f	mean free path
m_o	electronic mass
m*	effective mass
m	mass
M_r	reduced atomic mass

n	refractive index
n_e	electron carrier density
n_h	hole carrier density
N_O	atomic density
N_A	acceptor density
N_D	donor density
N_N	neutral impurity density
N_C	conduction band density of states
N_V	valence band density of states
$p(x)$	probability function
q_o	electronic charge
q^*	effective charge
r	peak-to-valley ratio
R	resistance
s	voltage standing wave ratio
s_{ij}	scattering parameter
t	time
T	temperature
T_D	Debye temperature
u_s	sonic velocity
v	velocity
v_p	peak velocity
v_v	valley velocity
V_a	unit cell volume
V	volume
V	voltage (e.m.f.)
W	power
W_a	power absorbed
xyz	Cartesian co-ordinates

X	reactance
Z	impedance
Z_o	characteristic impedance
α	linear expansion coefficient
β	isothermal compressibility
γ	propagation constant
$\gamma = \alpha + j\beta$	attenuation and phase constants
Γ	voltage reflection coefficient
Γ_w	power reflection coefficient
γ_w	power transmission coefficient
δ	skin depth
ϵ	permittivity
ϵ_o	free space permittivity
ϵ_r	relative permittivity
$\hat{\epsilon}_r$	complex relative permittivity
$\mathcal{E}$	energy
$\Delta\mathcal{E}_{ij}$	energy difference
$\mathcal{E}_g$	energy gap
ϕ, θ	angles
λ	wavelength
λ_c	cut-off wavelength
λ_g	guide wavelength
λ_o	free-space wavelength
η	efficiency
μ	mobility
μ_o	low-field mobility
μ_o	permeability of free space
ρ	resistivity
ρ_s	space charge density
ρ_d	mass density
σ	conductivity

τ_{ij}	characteristic time
τ_e	energy relaxation time
τ_m	momentum relaxation time
τ_f	mean free time
τ_d	dielectric relaxation time
Ξ_{ij}	deformation potential
ω	angular frequency

Chapter one.

Introduction.

1.1. HISTORICAL PERSPECTIVE

The study of semiconducting materials and their properties was begun early in the nineteenth century. Sample purity was a particular problem associated with these early investigations and this continues to be a major technological barrier in the study and analysis of hitherto uninvestigated materials. During the first decades of this century much work was done to characterise the differences between metals and semiconductors, some of the most salient steps being associated with the appreciation of crystal structure as a result of improved manufacturing techniques. The effects of damage, defects and doping with impurities began to be studied and described.

Work on the transistor led to an appreciation of scattering processes and relaxation time effects, the inclusion of quantum-mechanical theory leading to refinements to the band-theory description of semiconductors. Prior to the transistor, materials finding application as semiconductor junction rectifies were studied in detail principally selenium and the oxides of copper and lead. Interest in transistors led to work on the elemental semiconductors germanium and silicon. Silicon technology has been refined and extended to include high-field and high-frequency device operation. Interest has been diversified in the last decade to include a number of compound semiconductors, notably those formed from groups III and V of the periodic table of the elements. One of these, indium phosphide, is the subject of study in this work.

1.2. THE GROUPS III-V COMPOUND SEMICONDUCTORS

In groups IIIa and Va of the periodic table of the elements are located the transition metals, not of direct interest in this context. In the -b subgroups however we find the elements surrounding the familiar group IVb elemental semiconductors germanium and silicon (ref. Fig. 1A). The compounds of these surrounding elements are of considerable interest as semiconductor materials. Those most usually encountered are the phosphides, arsenides and antimonides of aluminium, gallium and indium, together with a number of ternary compounds, notably gallium indium arsenide, gallium indium phosphide and gallium arsenide phosphide.

Some of the properties of these materials are shown at table 1B (1) there compared with those of the group IVb elements. There are clear gradations in the data on melting points, energy gaps, similarities in interatomic spacing and large variations in carrier effective masses, mobilities and temperature dependence of the carrier properties. These reflect the interplay between the different mechanisms controlling carrier transport within the family of compounds.

Silicon and germanium find many applications as devices, especially the former due to its superior thermal properties. Gallium arsenide and indium phosphide in particular offer higher carrier mobilities and higher saturation velocities, which have encouraged their exploitation for certain applications. Negative differential mobility is peculiar to these III-V compounds in usable states, hence further applications. Gallium arsenide is used in Gunn diodes, Impatt diodes, field-effect transistors, amplifiers, infra-red emitters and detectors, (being especially valuable for optic-fibre communication since the wavelengths of radiation are most convenient for fibre transmission) varactor diodes and tunnel diodes. Other compounds, due to less developed

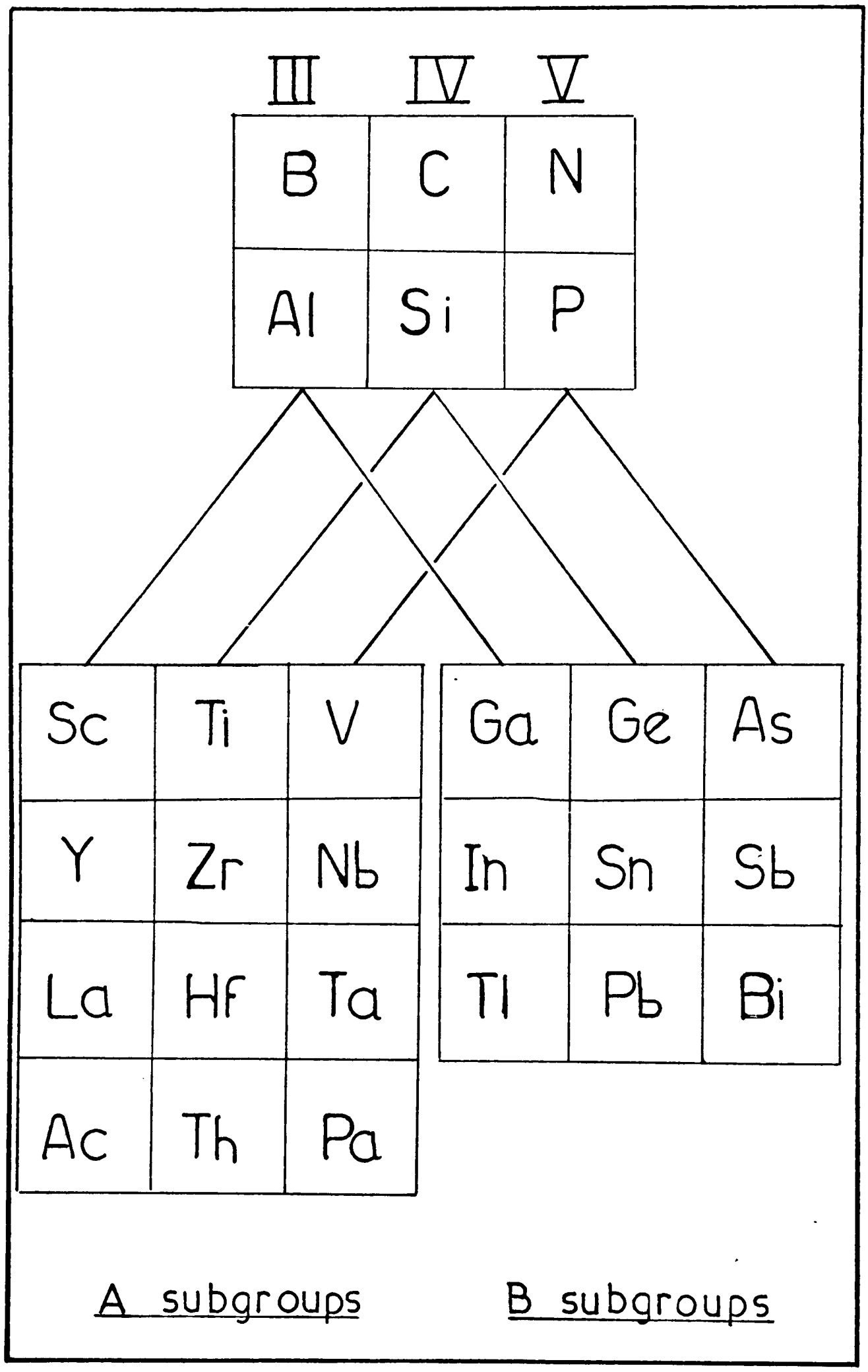

FIG. 1A

The periodic table of the elements - groups III, IV and V.

FIG. IB

Material properties

group IV elements and III.V compounds.

	a_o	a_1	n	m.pt	$\epsilon_g(0)$	$\epsilon_g(300)$	μ_e	μ_h	$\mu \alpha T^{-n}$ n_e	n_h	m^*_e.	m^*_h.
C		3.57	2.4	4300	5.4	5.2	1400	500				
Si	2.35	5.43	3.4	1420	1.15	1.11	1900	425	2.5	2.7	0.19	0.16
Ge	2.44	5.62	4.0	936	0.75	0.67	3450	3400	1.6	2.3	0.082	0.04
α-Sn	2.80	6.46		232	0.08						1.0	0.5
AlP	2.36	5.41	3.4	1770		3.0						
AlAs	2.44	5.65		1970		2.16						
AlSb	2.63	6.14	3.2	1050	1.75	1.63	200	420		1.8	0.3	0.4
GaP	2.36	5.44	2.9	1350	2.40	2.24	110	75	1.5	1.5		
GaAs	2.44	5.63	3.2	1240	1.58	1.39	8500	400	1.0	2.1	0.072	0.5
GaSb	2.63	6.09	3.7	705	0.80	0.67	4000	1400	2.0	0.9	0.049	0.5
InP	2.54	5.87	3.3	1070	1.42	1.26	4600	150	2.0	2.4	0.073	0.4
InAs	2.62	6.06	3.4	940	0.43	0.33	33000	460	1.2	2.3	0.02	0.41
InSb	2.80	6.48	3.1	525	0.22	0.16	78000	750	1.6	2.1	0.013	0.06
	Å	Å	-	°C	eV	eV.	$cm^2 v^{-1} s^{-1}$		-	-	-	-

technology have, as yet, found somewhat fewer applications.

Indium phosphide is used for transfered electron oscillator and amplifier devices and also as an experimental field effect transistor material, gallium antimonide finds application in tunnel diodes and backward diodes as does indium antimonide; gallium arsenide phosphide is used for high-power rectifying devices, although in general the ternary compounds have smaller thermal conductivities than the binaries and hence their usefulness in high-power environments may be limited. Electroluminescent devices are made from gallium phosphide and two of the ternaries; gallium arsenide phosphide and gallium indium phosphide. There are other promising compounds, notably gallium nitride with its large band gap of 3.5 eV giving basic electro-luminescent output in the blue of the visible spectrum, but also being dopable for other visible wavelength emissions of various colours. State-of-the-art results are continuously being improved and these will be discussed briefly with respect to the microwave devices.

1.3. SOLID STATE MICROWAVE DEVICES

The feasibility of exploitation of bulk properties of materials led workers to examine the III-V compounds, especially after Gunn (32) had observed the effect (in 1964) now named after him. Gallium arsenide was first appreciated in technological depth although attention has now turned to the other materials in the search for improved efficiency, higher frequency operation and possible high-power applications.

The microwave industry is an extensive user of solid-state devices, since small, lightweight, rugged devices operated from light, compact, low voltage d-c power supplies are attractive in many applications.

Devices are required to produce, amplify, mix, limit, modulate, detect and switch signals. These devices are incorporated into modules used in assembly of systems for radar, communication, electronic warfare, control and instrumentation. State-of-the-art results are necessarily better than commercially available performance data, some of the latter are summarised for reference (2).

Silicon power transistors in the S and C bands offer 10W, 2 GHz and 5W, 5 GHz, silicon Impatts 5W, 12 GHz (9%) whilst 1W CW 50 GHz has been measured in the laboratory. Double drift silicon Impatts have been measured at 11W 16 GHz (11%), 4W, 36 GHz (4%) and 120 mW, 140 GHz, all CW figures. Gallium arsenide Impatts are more promising up to 40 GHz as a result of superior material properties. Gallium arsenide field-effect transistors are offering 8 dB gain with 3 dB noise figure in the X band whilst gallium arsenide field-effect transistor amplifiers are offered with 15 dB gain, 6 dB noise figure in the S band and 10 dB gain, 10 dB noise figure in the J band.

Gallium arsenide Gunn devices currently (1974) available offer 1W (CW) and 30W (1% pulsed) in the X band, 300 mW (CW) and 10W (1% pulsed) in the J band and 200 mW (CW) in the Q band. Recent experimental results (3) indicate 150 mW, 54 GHz and 30 mW, 70 GHz.

Indium phosphide transfered-electron oscillators are reported to have given 0.45W, 19.5 GHz (3%) and 1W, 18 GHz (10%) pulsed, but with poor switch-on characteristics. Field-effect transistors in this material are reported to be capable of higher maximum operating frequencies compared to gallium arsenide by some 30%, but with 14% worse noise figures. Indium phosphide reflection amplifiers are now being examined in the X and J bands and offer good noise performance with noise figures of less than 10 dB; gains of up to 30 dB are practicable over narrow bandwidths. Material growth and doping

parameters need to be accurately defined to obtain such results, indeed considerable effort is expended examining the manufacturing techniques.

There are many applications where solid-state devices offer advantages over vacuum tubes, but for particular environments and applications the valve is superior, shown by the considerable market for travelling-wave-tubes, klystrons, backward-wave oscillators, magnetrons and high-power, high-frequency triodes. In fact one of the main targets of semiconductor material and device research is to produce higher powers more efficiently than the valves.

The aim of this work was to increase the available data on the carrier-property of indium phosphide in the velocity-field characteristic, and its measurement, since at the commencement of the work (1970) little experimental data was available, theoretical predictions only being reported and device performance little more than conjectured.

Chapter two.

Properties of indium phosphide.

2.1. PREPARATION AND PHYSICAL PROPERTIES

Indium phosphide exhibits a vapour pressure of approximately twenty six atmospheres (4) at its melting point (1062°C). This enables the compound to be prepared by slow cooling of the two component solution providing a phosphorus atmosphere is maintained at around five atmospheres; this is necessary since the liquid composition at equilibrium with solid is only 35-40% phosphorus. Zone refining is possible under these conditions. Single crystals are somewhat difficult to prepare by the Czochralski method of 'pulling' a seed due to the excess of indium in the liquid phase. The melt may be encapsulated in a vitreous, non-reactive material such as boric oxide, perhaps with an inert gas at high pressure. The horizontal Bridgemann-Stockbarger method is more widely used, where a sealed crucible is passed slowly through a zone of uniform temperature gradient spanning the melting point; it is possible to obtain growth in particular planes by seeding, and to produce dislocation free material using subslow cooling rates (5).

The compound is self-stoichiometric and crystallises, (in common with many other III-Vs) in a zincblende (sphalerite) structure. This is composed of two interpenetrating sublattices, each face-centred cubic, being separated by the vector $[1,1,1]\ a_o/4$. This structure has no inversion centre and as a consequence opposite directions are not necessarily equivalent. This is particularly manifest in $\{111\}$ and $\{\bar{1}\bar{1}\bar{1}\}$ planes. If there is a III atom at (000), then on $\{111\}$ the III atoms are held by one bond, and the V atoms by three, the reverse being true on $\{\bar{1}\bar{1}\bar{1}\}$. Considerable variations in reactivity are noted here, particularly when etching, also electrically - for example in the formation of Schottky barriers (6).

The tetrahedral radii of the elements are 1.10Å for phosphorus and 1.44 Å for indium giving an interatomic separation of 2.54Å.

Views along principal crystal directions are shown at Fig. 2B, together with the crystal surface meshes, verified by electron diffraction studies.

The principal planes are composed as follows:

$\{1,0,0,\}$ - alternate layers of III and V

$\{1,1,1\}$ - alternate layers of III and V

$\{1,1,0\}$ - equal numbers of III and V

The crystal cleaves most easily along $\{110\}$ in contrast with other tetrahedral arrangements as in diamond, which cleave along $\{111\}$. This difference is due to the partial ionicity of the crystal, since $\{111\}$ is alternately composed of III and V atoms and the electrostatic attraction inhibits cleavage. Indeed the degree of $\{111\}$ cleavage relates to the ionicity, and indium phosphide is the most ionic of the group III-V compound semiconductors.

Some other physical properties are listed in Fig. 2A.

The compound may be doped either p- or n-type, the latter being of greater use for devices owing to the larger electron mobility. P-type dopants are commonly cadmium and zinc from group II. N-type dopants may be from either group IV, germanium or tin, or group VI - selenium, tellurium and chromium. The doping may be performed by diffusion into prepared crystals or directly during epitaxial growth. Ion implantation as yet finds little application due to extensive crystal damage. The growth of semi-insulating material can be accomplished by doping with both p- and n-type dopants and relying on compensation to produce the balance of carriers of very low density. Conductivities down to $10^{-8}\ \Omega.cm^{-1}$ are attainable by this method.

Diffusion data (18) indicates sub-lattice self diffusion of both indium and phosphorus, their activation energies being 3.85 eV and 5.65 eV respectively. Should all sites be equivalent for diffusion

atomic weights:	In	-	114.82
	P	-	30.98
molecular weights	InP	-	145.8
	M_R	-	24.4
melting point		-	1070 °C
lattice constant	a_o	-	5.8686Å
density	ρ_d	-	$4.787\ 10^{3}\ Kg.m^{-3}$
thermal expansion	α	-	$4.5\ 10^{-6}\ °K^{-1}$
thermal conductivity	k_t	-	$1.19\ 10^{-6}\ KCal\ m^{-1}.°K^{-1}$
specific heat 300 °K	c_p	-	$5.30\ KCal\ Kgmole^{-1}.°K^{-1}$
77 °K	c_p	-	$2.80\ KCal\ Kgmole^{-1}.°K^{-1}$
thermal diffusivity	k_d	-	$3.0\ 10^{-3}\ m^2$
§ isothermal compressibility	β	-	$1.48\ 10^{-12}\ m^2\ N^{-1}$
§ sonic velocity	u_s	-	$4.5\ 10^{3}\ m\ s^{-1}$
elastic constants	C_o	-	$5.53\ 10^{11}\ N.m^{-2}$
	§ C_{11}	-	$1.80 \times C_o$
	§ C_{22}	-	$0.91 \times C_o$
	§ C_{44}	-	$0.87 \times C_o$

§ approximate values.

FIG. 2A

Indium phosphide - physical properties.

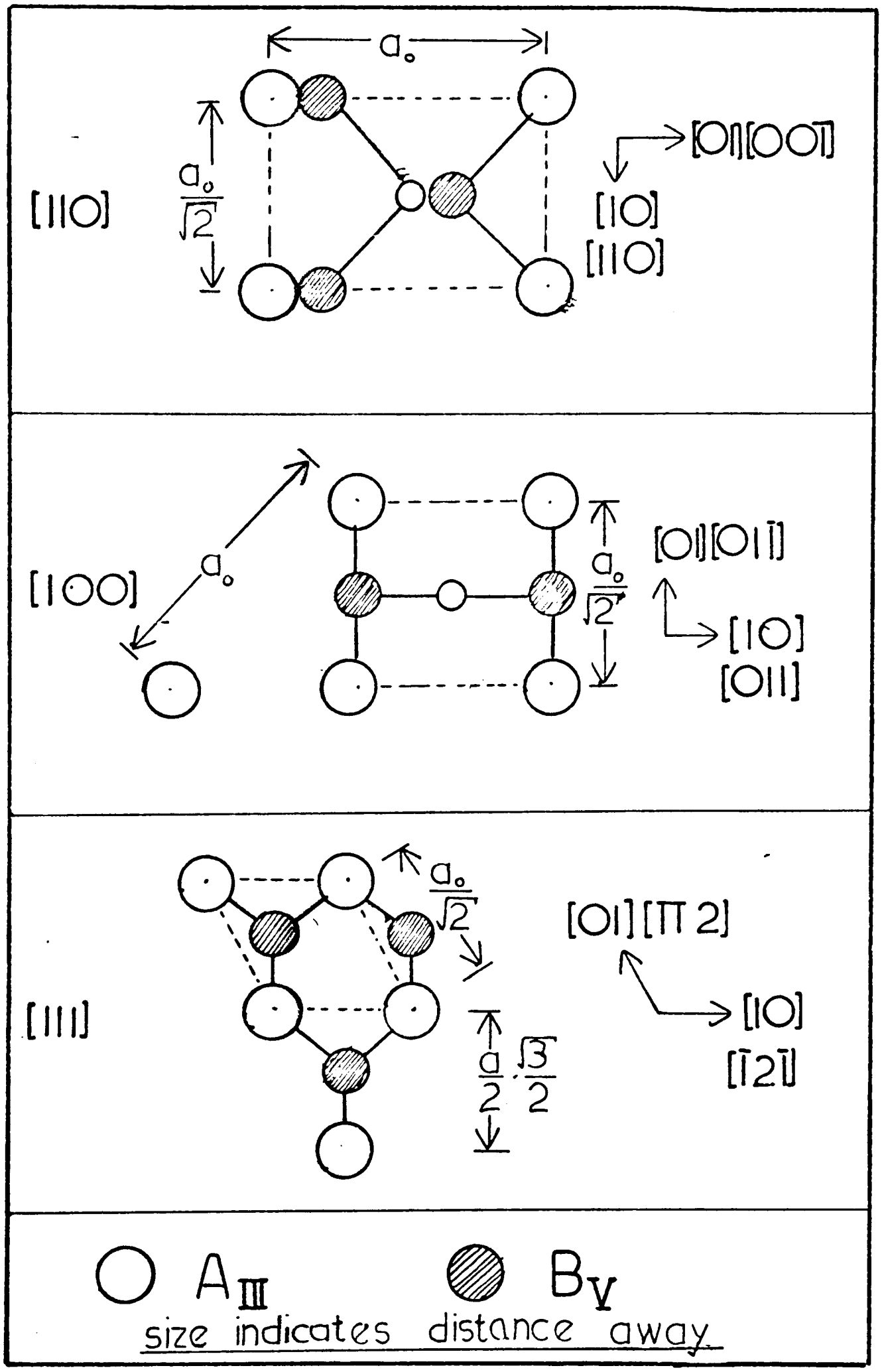

FIG. 2B

Sphalerite structure –

views along principal directions.

the phosphorus activation energy would be smaller due to its smaller atomic radius. Other dopants have smaller activation energies indicating diffusion via lattice interstices, for example cadmium 0.30 eV, gold 0.48 eV.

Contacts may be applied by two major techniques, alloying and evaporating. The latter finds greater use due to better control. Gold contacts are evaporated where Schottky barriers are required, silver-tin alloys where ohmic contacts are needed, sometimes on n^+ layers to minimise contact resistance. Alloying of tin and silver-tin alloys is simple, but fine control of position and contact dimensions is difficult. However good ohmic contacts can be very easily produced and this method was used in this work; it is described in chapters five and six, where applicable to particular material samples.

2.2. ELECTRICAL PROPERTIES

2.2.1. Band Structure

The Brillouin zone is shown at Figure 2C (9), this is the standard Sphalerite form. The symmetry points are also shown there; being eight L points, six X points and one Γ point the significance of which is important in assessment of the band structure and electronic properties.

The band structure is shown at Fig. 2D in the form reported by James et al (10). Many workers (11) have studied the features by various methods. The features are a central Γ valley, of direct band-gap position and a number of satellite valleys of X & L types. The exact positions of these in the zone have not yet been discovered precisely, hence the effective number of each is not known exactly, If they were all at the zone edge then there would effectively be four L valleys and three X valleys.

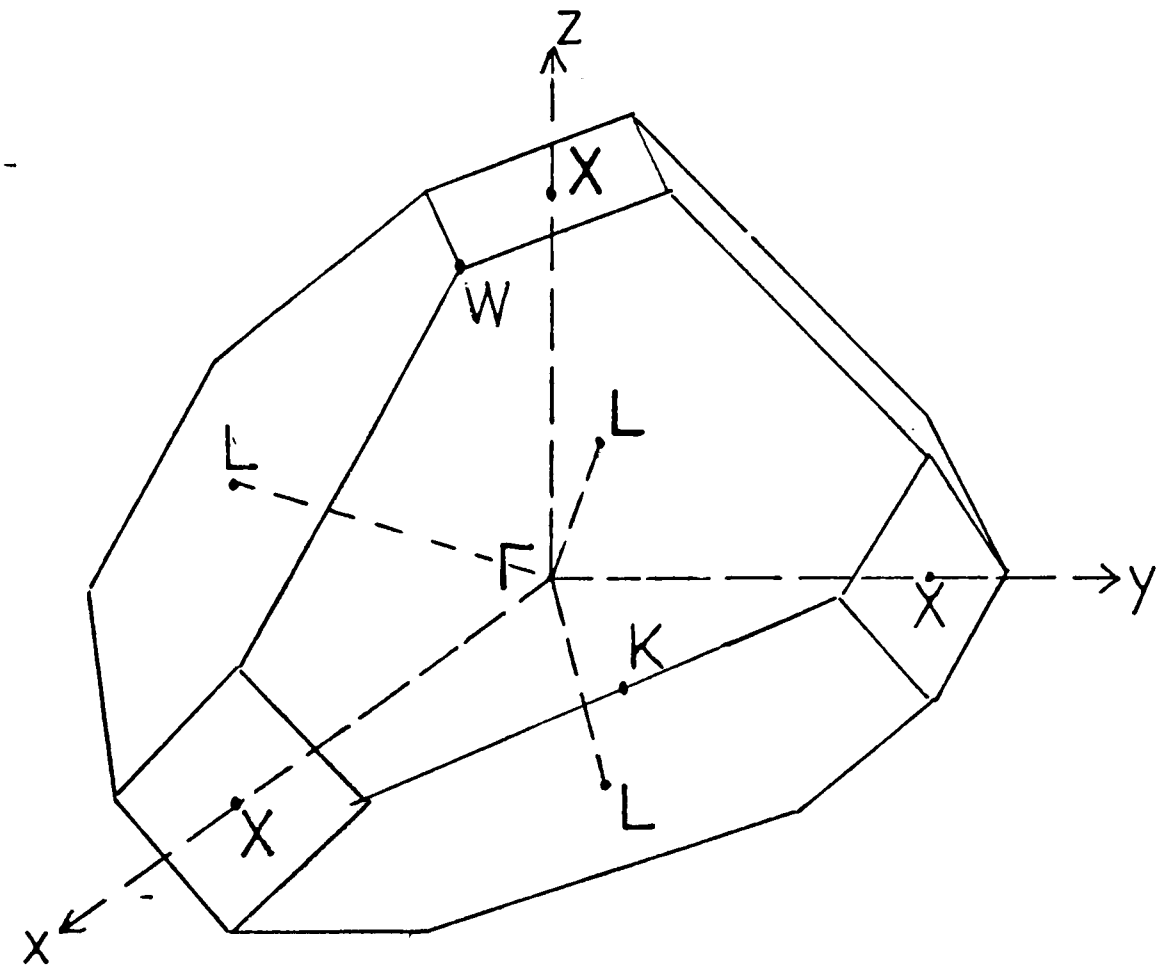

symettry points: Γ (0,0,0)

X $(0,0,2\pi/a_0)$

L $(\pi/a_0,\pi/a_0,\pi/a_0)$

K $(3\pi/2a_0,3\pi/2a_0,0)$

W $(\pi/a_0,0,2\pi/a_0)$

$a_0 = 5{\cdot}58$ Å

FIG. 2C

Indium phosphide – Brillouin zone (9).

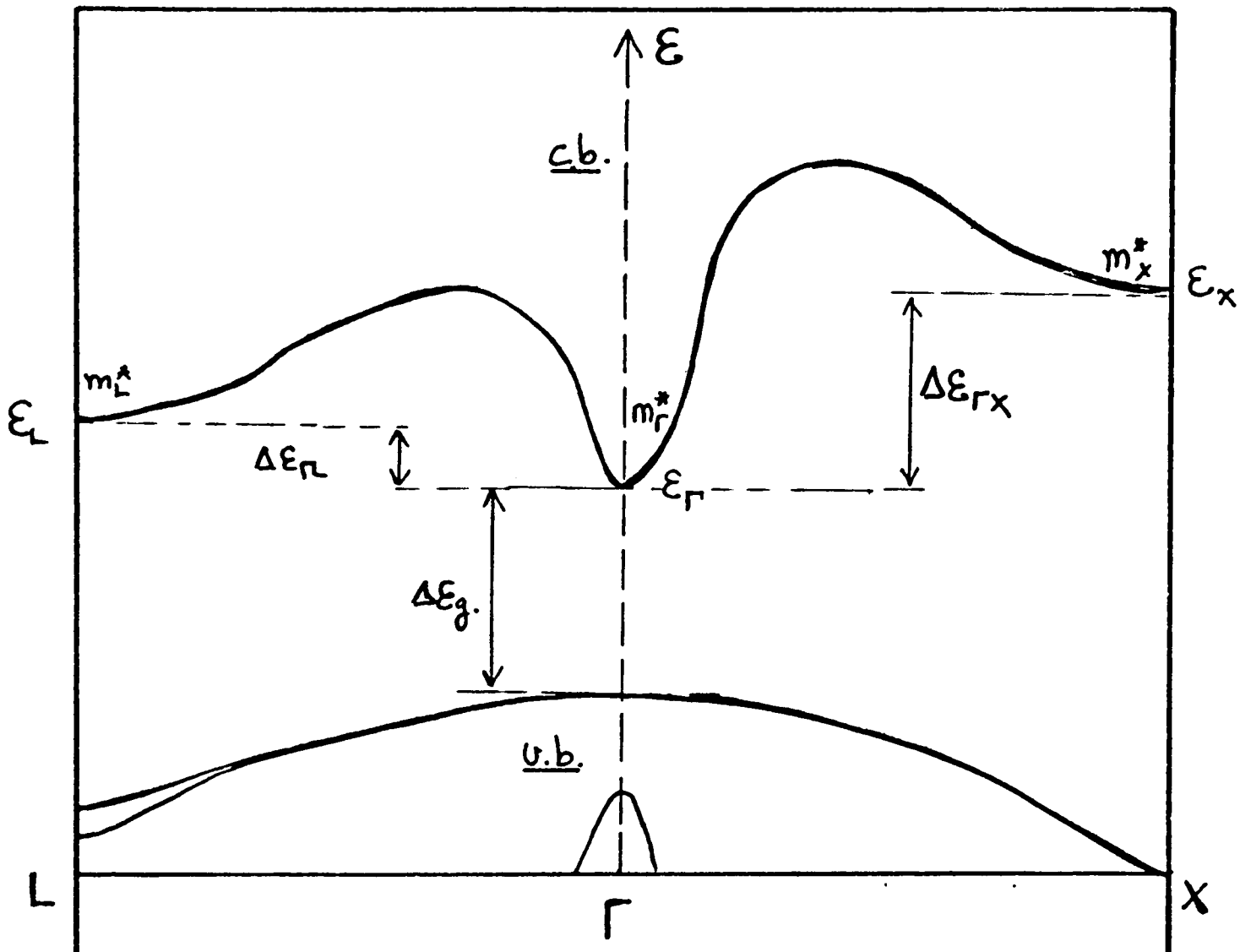

$\varepsilon_g(0) = 1{\cdot}42\ eV$, $\varepsilon_g(300) = 1{\cdot}26 eV$, $\partial\varepsilon_g/\partial T = -4.6\ 10^{-4}$

$\varepsilon_L = 1{\cdot}87 eV$ $\Delta\varepsilon_{\Gamma L} = 0{\cdot}61 eV$, $\varepsilon_X = 2{\cdot}16 eV$, $\Delta\varepsilon_X = 0{\cdot}81 eV$

$m^*_{e\Gamma} = 0{\cdot}078\, m_o$, $m^*_{eL} = 0{\cdot}4\, m_o$, $m^*_{eX} = 0{\cdot}4\, m_o$

$m^*_{h\Gamma} = 0{\cdot}4\, m_o$

$\mu_{e\Gamma} = 4{,}600\ cm^2 v^{-1} s^{-1}$, $\mu_{h\Gamma} = 150\ cm^2 v^{-1} s^{-1}$

$\varepsilon_r(0) = 12{\cdot}53$, $\varepsilon_r(\infty) = 9{\cdot}61$

$\varepsilon_{Ic} = 3{\cdot}16\ eV.cm^{-1}$

FIG. 2D

Indium phosphide – band structure (10) and electrical properties.

The energy gap and its temperature dependence are also included in Fig. 2D, as are the valley energy separations and effective masses. In general these are the values to be used in the calculations presented later, although recently (1973) some controversy has arisen over the exact effective mass values in the higher valleys.

The carrier mobilities specified in Fig. 2D are the observed experimental values, the band edge deformation potential is an approximate figure derived from other data.

2.2.2. Crystal Ionicity

Indium phosphide is the most ionic of the III-V compound semiconductor group, this was mentioned in connection with cleavage planes. This ionicity may be described using the concept of effective charge. Consider an ionic III-V, the III ion has a charge +3 since all its valence electrons will be with the V ion, which will have a charge -3. Were the position to be entirely covalent (homopolar) then the III charge would be -1 and the V charge +1 since each electron would spend $\frac{1}{2}$ of its time with each of the atoms. Any intermediate state is a combination of both, and if an effective charge is assigned according to Szigeti (12) then the times spent by an electron with each atom are (13)

$$t_A = b^2/1 + b^2, \qquad t_B = {}^1/1 + b^2 \tag{2.1}$$

where $$b = \sqrt{\frac{3 - q_s^{*2}}{5 + q_s^{*2}}}$$

q_s^* being the Szigeti effective charge from the expression

$$\left[q_s^*\right]^2 = \frac{\epsilon_r(0) - \epsilon_r(\infty)}{\{\epsilon_r(\infty) + 2\}^2} \cdot \frac{9 M_r \omega_{to}^2}{4\pi . N_o} \tag{2.2}$$

which for indium phosphide gives

$$q_s^* = 0.68q_o$$

and

$$t_A = 0.27, \quad t_B = 0.73$$

There is another definition of effective charge by Callan, this is related to the Szigeti definition by the optical dielectric constant such that:

$$q_c^* = q_s^* \left\{ \frac{\epsilon_r(\infty)+2}{3\epsilon_r(\infty)} \right\} \tag{2.3}$$

this is used in the calculation of optic phonon scattering in section 2.3.5. and for indium phosphide is

$$q_c^* = 0.27q_o$$

The ionicity results in different dielectric constants at zero and optical frequencies, the difference being proportional to the ionicity; also the optic phonon frequencies are different for longitudinal and transverse directions, these are related by the LST relation (Lyddane, Sachs and Teller)

$$\frac{\omega_{LO}}{\omega_{TO}} = \left\{ \frac{\epsilon_r(o)}{\epsilon_r(\infty)} \right\}^{1/2} \tag{2.4}$$

This agrees with the observed ratio of 1.13 in indium phosphide.

2.3. CARRIER MOBILITY

2.3.1. Theory

The concept of mobility of carriers is an expression of their mean free time between collisions, together with the effect of their thermal velocity and effective mass, the relations may be written:

$$\mu = \frac{q_o}{m^*} \cdot \tau_f \qquad (2.5)$$

and

$$l_f = \tau_f \cdot v_{th}$$

This drift mobility μ_D must be distinguished from the Hall mobility, which is the figure for mobility derived from the Hall effect experiment. The difference comes from the difference in averaging processes in the definitions of each quantity viz:

$$\frac{\mu_H}{\mu_D} = \frac{(\text{weighted average of } \tau^2)}{(\text{weighted average of } \tau)^2} \qquad (2.6)$$

in general

$$\frac{\mu_H}{\mu_D} > 1$$

and in particular for spherical energy surfaces and τ a constant, independent of other quantities:

$$\frac{\mu_H}{\mu_D} = \frac{3\pi}{8} = 1.18.$$

The thermal velocity is the average velocity of the carriers considered over their distribution function. It is distinguished from the drift velocity, which is that due to the effect of fields, and generally directionally related to the fields; the thermal velocity being random. In conditions of moderate doping the thermal energy distribution obeys Maxwell-Boltzmann statistics such that:

$$\frac{dn}{n} = 4\pi\left\{\frac{m}{2\pi kT}\right\}^{3/2} v^2 \exp\left\{\frac{-mv^2}{2kT}\right\} dv. \qquad (2.7)$$

where n is the total population and T, the lattice temperature.

Writing $\langle n \rangle$ for the average value of the variable n we have:

$$\langle u \rangle = \int_{-\infty}^{+\infty} u \cdot dn/n.$$

putting u = v, the velocity, we have

$$\langle v \rangle = v_{th} = \int_{-\infty}^{+\infty} 4\pi\left\{\frac{m}{2\pi kT}\right\} v^3 \cdot \exp\left\{\frac{-mv^2}{2kT}\right\} \cdot dv. \qquad (2.8)$$

Using the integral relation

$$\int_{-\infty}^{+\infty} x^n \cdot x^2 \exp\{-a^2x^2\} \cdot dx = \frac{1}{a^n} \cdot \frac{\left(\frac{n+1}{2}\right)!}{\left(\frac{1}{2}\right)!}$$

we find that

$$v_{th} = \left\{\frac{8kT}{\pi m}\right\}^{1/2} \qquad (2.9)$$

Using data values for the Γ valley in indium phosphide we find that the thermal velocity is

$$v_{\Gamma th} = 3.64.10^7 \text{ cm.s.}^{-1} \qquad 300^\circ K$$

$$v_{\Gamma th} = 1.84.10^7 \text{ cm.s.}^{-1} \qquad 77^\circ K$$

From the Brillouin zone dimensions (Fig. 20)

$$k_m = 2.4\ 10^{-10}\ m^{-1}$$

we may calculate the velocity for a free electron at the edge as:

$$v = \hbar k/m^*_e \ , \quad m^*_e = 1$$

hence: $v = 4.10^8 \text{ cms}^{-1}$.

Comparing the value of the thermal velocity we see that the electrons only occupy a fraction of the Brillouin zone by dint of their thermal energy.

The observed electronic mobility at low fields (i.e. in the Γ valley) is 4600 $cm^2/v.s.$, this leads, from (2.5) to $(m_\Gamma^* = 0.078 m_0)$.

$$\tau_f = 2.04\ 10^{-13}\ S \quad \text{and} \quad \ell_f = 7.8\ 10^{-6}\ cm\ (300^0K)$$

In the equilibrium conditions with no external fields applied then the carriers absorb and emit phonons equally such that the number of phonons with wave vector $\underline{q}$ is, according to Bose-Einstein statistics, given by:

$$N_{\underline{q}} = \exp\left\{\frac{\hbar\omega_q}{kT}\right\} - 1 \qquad (2.10)$$

When an electric field $\underline{E}$ is applied energy is supplied to the carriers at a rate $\mu.q.E^2$, manifested by Joule heating; this increases the carrier energy and also the phonon emission rate. For small fields the perturbation may often be analysed as a small drift term f_1 in the Maxwell Boltzmann distribution function f_0 such that:

$$f = f_0(\varepsilon, T) + f_1 \qquad f_1 << f_0$$

At higher fields the effects are more complex and the individual scattering mechanisms must be considered in depth and their effects on mobility assessed in order to examine the behaviour of carriers in high fields. A brief survey of scattering mechanisms will now be presented.

2.3.2. Crystal Damage

If the perfectly periodic crystal structure of the lattice is disturbed by damage of any kind, the carriers will be influenced by the aperiodicity near the damage site, they may be scattered by this.

Little effect is noted except at very low temperatures or high dislocation densities (14), greater than 10^{14} m^{-2}. Slow grown crystals from fairly pure liquids have dislocation densities typically (15) of 10^{8} to 10^{10} m^{-2} or even less in extremely pure systems. This density will be increased to a value producing appreciable scattering by 10% plastic strain(16). Consequently we may ignore this in indium phosphide at the temperatures of interest as long as measures are taken to minimise damage in processing and handling (17).

2.3.3. Impurity Scattering

These also affect the periodicity of the crystal lattice and may be either neutral or ionised. Erginsoy (18) calculates the effect of neutral impurities on the carrier mobility as limiting it such that:

$$\mu \leq 1.58.10^{33}.\ m^{*}/\epsilon_r N_n \qquad cm^2.v^{-1}.s^{-1} \qquad (2.11)$$

which for indium phosphide will give (Γ valley)

$$\mu \leq 10^{32}/N_n \qquad cm^2.v^{-1}.s^{-1}.$$

This will have little effect save at very high doping densities of neutral impurities - a situation unlikely to exist in material of interest.

Ionised impurities have a greater effect since they are charged. Conwell and Weisskopf (19) describe the limiting mobility as

$$\mu_I = \sqrt{\frac{2}{\pi}} \cdot \frac{2^7 \pi \epsilon^2 (kT)^{3/2}}{q^3 . m^{*3/2} N_I . \ell_n(x)} .$$

$$x = \left\{1 + \left(\frac{28\sqrt{\pi}\,\epsilon\, kT}{q^2 N_I^{1/3}}\right)^2\right\} \qquad (2.12)$$

for an impurity density of 10^{15} cm^{-3} we find that the limiting mobility values in each valley are:

	Γ	L	X	
77°K	$1.9\ 10^5$	$8.4\ 10^4$	$8.4\ 10^4$	
300°K	$1.48\ 10^6$	$6.5\ 10^5$	$6.5\ 10^5$	$cm^2.v^{-1}.s^{-1}$

The mobility depends on the temperature to the $+^3/2$, also there is an effect from the logarithmic term. Ionised impurities may actually conduct at low temperatures and Blood et al (20) experimentally assess this transition to impurity conduction to take place at $+5^c K$.

2.3.4. Carrier-Carrier Scattering

Should carriers collide with one another then thisscattering effect will reduce their mobility. This effect will only be significant under two circumstances, either a very large population or a large mobility difference in a population consisting of significant numbers of both types of carrier. The former is unlikely in material of interest since this is a degenerate condition. The latter could be effective since the observed mobilities at low fields are

$$\mu_e = 4600\ cm^2/vs \qquad \mu_h = 150\ cm^2/vs$$

and effective masses

$$m_e^* = 0.078\ m_o \qquad m_h^* = 0.40\ m_o$$

However there would have to be a significant hole population for the electronic mobility to be reduced and this is unlikely in material of interest except in a near intrinsic region at high temperatures. In the saturated region where:

$$n_e \simeq N_d$$

the hole population will be

$$n_h = n_i^2/n_e \quad \text{and} \quad n_h \ll n_e$$

So the effect may be discounted in the range of interest.

2.3.5. Scattering by Lattice Vibrations

In a periodic crystal lattice the atoms may vibrate about their mean positions; these vibrations may interact with the carriers and scatter them. For a slightly ionic, diatomic lattice the modes of vibration are shown at Fig. 2E, together with the critical frequencies at symmetry points after measurements of Alfrey et al (21). Both longitudinal and transverse, acoustic and optic modes may interact.

The acoustic modes have been described by Shockley et al (22), who ascribe a mobility limit:

$$\mu \leq \frac{2 q_o \pi \hbar^4 C_{11}}{m^* \mathcal{E}_{ic}^2 kT} \qquad (2.13)$$

Substituting values for indium phosphide we find:

	Γ	L	X	
77°K	$2.5\ 10^6$	$9.75\ 10^6$	$9.75\ 10^6$	$cm^2/v.s.$
300°K	$9.5\ 10^4$	$3.2\ 10^4$	$3.2\ 10^4$	

The temperature variation being $-3/2$ overall.

The optic modes are more difficult to describe analytically, since a relaxation time or critical lifetime is indefinable for polar modes with $T \leqslant T_D$, where T_D is the Debye temperature:

$$T_D = \frac{\hbar \omega_{LO}}{k} \qquad (2.14)$$

For carriers with temperature less than T_D the mobility decreases as temperature increases, then increases as T approaches T_D, where little change in mobility is observed. For temperatures greater than T_D mobility increases.

Howarth et al (23) and Ehrenreich (24,25) describe the mobility for temperatures much greater than the Debye temperature as

$$\mu \leqslant \frac{1.7 \times 10^{30} T^{1/2} M_R V_A \omega_{LO}}{2\pi . q_{rc}^{*2} m^{*3/2}} \cdot F\left(\frac{T_D}{T}\right) \cdot \exp\left\{\frac{T_D}{T} - 1\right\} \cdot \qquad (2.15)$$

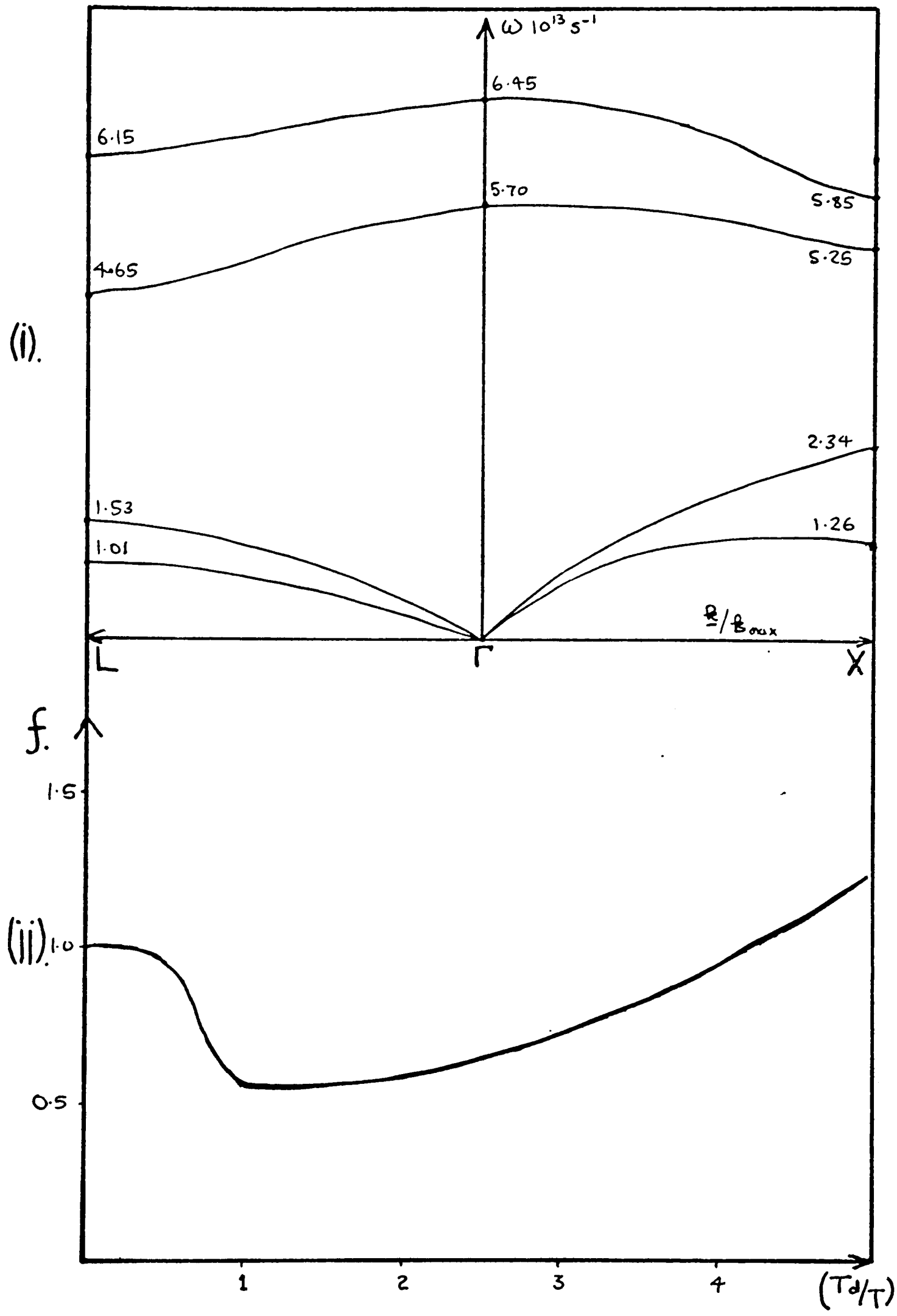

FIG. 2E

(i). lattice vibration dispersion diagram (21).

(ii). the function $f(T_d/T)$ (24).

the Function F is shown at Figure 2E. For indium phosphide this gives a result for temperatures greater than 480°K of $\mu \leqslant 1.5\ 10^4$ $cm^2\ v^{-1}\ s^{-1}$. Hilsum (26) calculated the room temperature mobility of r valley electrons limited by polar-optical scattering as 6800 $cm^2\ v^{-1}\ s^{-1}$, using these room temperature values the mobilities of electrons in the other valleys would be approximately

	Γ	L	X	
77°K	$6.3\ 10^5$	$3.7\ 10^4$	$2.6\ 10^4$	$cm^2\ v^{-1}\ s^{-1}$
300°K	$6.8\ 10^3$	$5.5\ 10^2$	$5.1\ 10^2$	

Now we are able to compare these limits and estimate the important mechanisms of scattering in each valley.

2.3.6. Summary of Scattering Processes

The three salient processes described above are ionised impurity, acoustic and polar optic scattering. The calculations indicate that in the Γ valley at room temperature polar optic phonons have the most effect on scattering, but at 77°K both acoustic and impurity scattering mechanisms influence the mobility. In the upper (L and X) valleys polar-optic scattering dominates at all but the lowest temperatures.

These rough calculations are borne out by the work of Blood et al (20) who find increasing mobility from room temperature to a maximum value at 70°K, below this temperature a decrease is observed due to the effects of acoustic and impurity scattering. Calculations of the mobilities for each valley give results as follows:

	Γ	L	X	
77°K	37,700	14,000	12,000	$cm^2\ v^{-1}\ s^{-1}$
300°K	6,800	550	500	

The observed electronic drift mobility in the Γ valley is $4{,}600\ cm^2\ v^{-1}\ s^{-1}$ and the temperature variation in the range 100^oK to 400^oK of the order of $T^{-2.0}$. This different value of mobility indicates something of the insufficiency of the calculations presented but these take no account of band non-parabolicity and effective-mass anisotropy, which are discussed in section 2.6.3. Ehrenreich (28) made improvements to his calculations (24,25) to include non-parabolic bands and screening effects and he obtained an upper limit of mobility of $4700\ cm^2\ v^{-1}\ s^{-1}$, close to the observed value.

Hilsum (29) calculates a simple expression for mobility and carrier concentration in the semiconductors commonly employed in devices, (Si, Ge, GaAs, GaSb and InP) which he states to be:

$$\mu = \mu_L \left(1 + \sqrt{N_b/10^{17}}\right) \qquad (2.16)$$

which can be useful in estimation of the device operational parameters, rather than following the lengthy calculations of individual scattering processes. There is broad, not precise, agreement with the material supplied for this work. The expression (2.16) bears comparison to the work of Blood et al (20) who state the onset of metallic conduction to be associated with a doping density of the order of $3.10^{16}\ cm^{-3}$.

Carriers may be scattered within a valley or between valleys (either equivalent or non-equivalent valleys). Considering the former, since the electron remains in the valley the momentum change must be small, of the order of:

$$\Delta P = m^* V_{th}$$

the interacting phonon must be of comparable momentum:

$$\hbar k_p \simeq m^* V_{th}$$

For low-frequency (dispersionless) acoustic phonon:

$$\omega_p = C_s k_p$$

Comparison of the energy exchange, phonon:carrier is:

$$\frac{\hbar\omega_p}{kT_e} = \frac{\hbar c_s \upsilon_p}{kT_e} = \frac{C_s m^* \upsilon_{th}}{\frac{1}{3} m^* \upsilon_{th}^2} = \frac{3c_s}{\upsilon_{th}}$$

now for indium phosphide $V_{th} \simeq 3.10^7$ cms^{-1} and the sonic velocity $C_s \simeq 5.10^5$ cms^{-1}, hence the energy exchange is of the order of 10% of the carrier energy. The momentum change may be larger.

For inter valley scattering the wave vector $\underline{k}$ is changed over a substantial part of the Brillouin zone, corresponding to the valley separation in $\underline{k}$ space. Thus the energy interchange may be considerable almost the entire carrier energy for the most energetic optic phonons.

2.4. INTERVALLEY TRANSFER

2.4.1. Theory

Since there are a number of valleys within the band structure, carriers may populate any of them according to the energy, temperature etc. The distribution function will express these populations and average values of variables calculated from it will be affected by the relative numbers of carriers in each valley and the properties of those particular valley states. Consequently any mechanism controlling population arrangement or transitions will be most important in the assessing of the properties of the carriers as a function of field, energy, temperature etc.

The transfer of carriers may take place between identical or non-identical valleys. These mechanisms are termed equivalent and non-equivalent intervalley scattering respectively. The valleys can

be considered to be coupled to each other, the constant of coupling controlling the transition rate viz:

$$n_{ij} \propto \Xi_{ij}^2$$

using the most usual argument. The transfer mechanism may be assigned a relaxation time such that (30)

$$\frac{1}{\tau_{ij}} = \sum_j \frac{\Xi_{ij}^2 m_j^{*3/2}}{\sqrt{2}\pi\hbar^3 \omega_{ij} N_{cj}} \left\{ N_{\underline{q}} \left(\mathcal{E}_{oi} - \mathcal{E}_{oj} + \hbar\omega_{ij}\right) + \left(N_{\underline{q}} + 1\right)\left(\mathcal{E}_{oi} - \mathcal{E}_{oj} - \hbar\omega_{ij}\right) \right\} \quad (2.17)$$

where $\mathcal{E}_{oj}$, N_{cj} and w_{ij} are the energy, density of states and transition frequency of the jth valley. $N_{\underline{q}}$ is the number of phonons according to equation (2.10). Calculations of these transition rates and relaxation times must be included with mobility calculations in order to obtain the behaviour as a function of field in the velocity-field characteristic.

Considering a set of two valleys, the lower a high-mobility, small effective-mass environment and the upper a low-mobility, large effective-mass environment. Let the separations be such that thermal interference is negligible at the temperatures of interest and the vast majority of carriers populate the lower valley at low fields. As the field is raised the carrier energy increases and some of the population may now be energetic enough to transfer from lower to upper valley. This process could continue until the majority of the carriers were populating the upper valley; the transfer rate and regime of electric field values being dependent on the coupling constant between the valleys and the availability of states for occupation in them. Whilst the transfer was taking place there would be a regime of negative differential mobility as illustrated in Fig. 2F.

The density of states is proportional to the number of valleys and the effective masses therein. For gallium arsenide the data gives

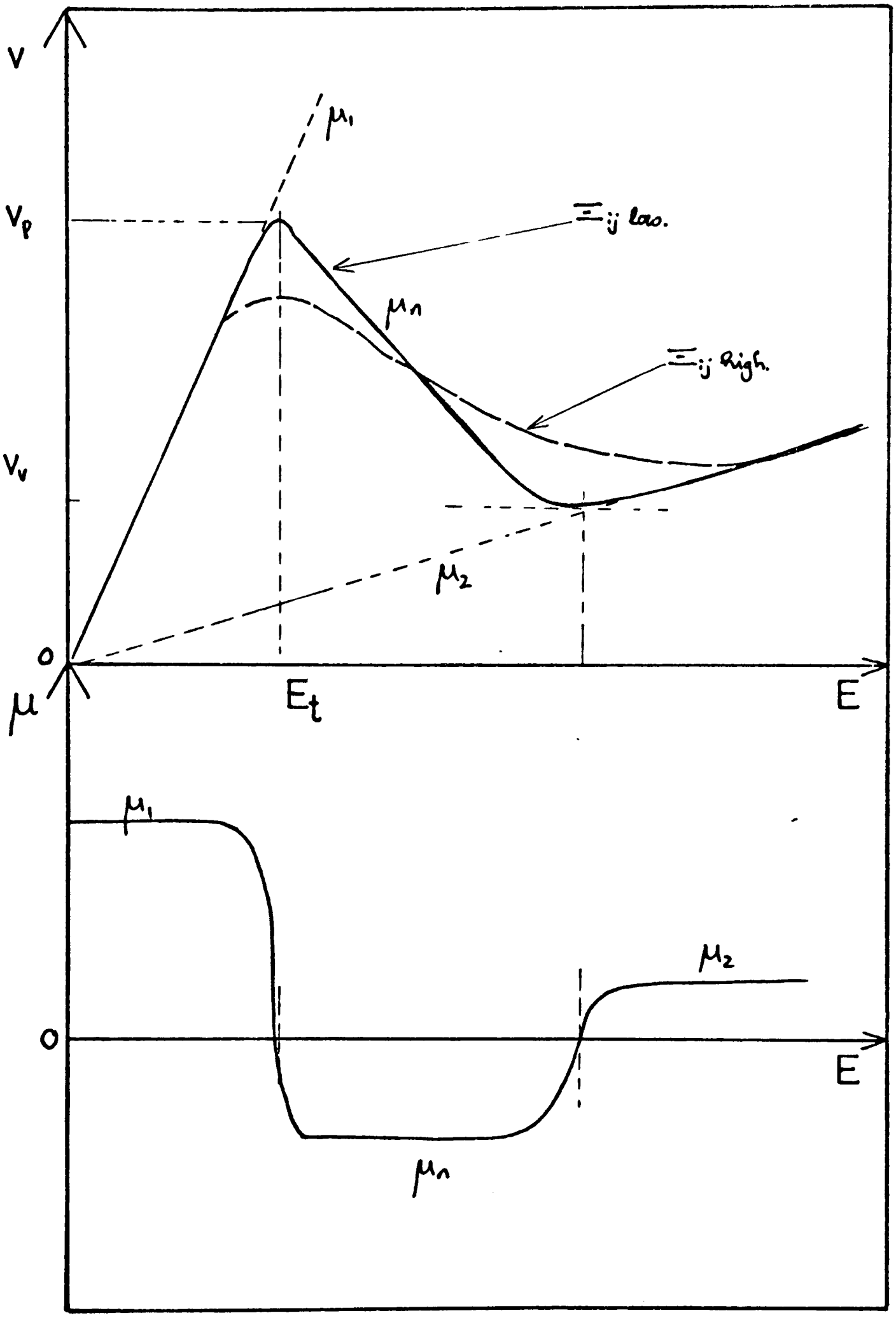

FIG. 2F

Negative differential mobility -

(i) velocity. (ii) mobility.

Valley type	Number	Eff mass	density of states
j	n_j	m_j^*	$n_j (m_j^*)^{3/2}$
Γ	1	0.078	0.0218
X	3	1.25	4.2

Density of states ratio Γ :X is 1:193. For indium phosphide using the data for isotropic valleys (recently challenged by Janes (58))

j	n_j	m_j^*	$n_j(m_j^*)^{3/2}$
Γ	1	0.078	0.0218
L	4	0,4	1.012
X	3	0.4	0.759

giving density of states ratio Γ:L:X = 1:47:35.

This ratio controls the fraction of the population having the ability to transfer and from the above figures demonstrates the lack of constraint of upper states available in both these compounds.

The negative mobility would not be observed if the lattice temperature was too high or the valley energy difference too small since in either case there would be comparable probabilities of occupation of both valleys; hence the 'effective' mobility would not show the negative region. If the energy gap was very small then the negative mobility would also be small since only a small energy increase would be necessary to transfer carriers, alternatively if the gap was much wider it would be more difficult for carriers to overcome this barrier, but increased densities of states would enhance the probability of upper valley capture-hence little negative mobility.

Should be coupling constant be very large then all the carriers would transfer as soon as they had sufficient energy to populate the upper valley. Transfer would occur over a large regime of electric field values than for smaller coupling constant values. The negative mobility would then be smaller. For the smaller values of coupling constant the transfer would take place over a narrower band of electric

field values but this advantage might be outweighed by the higher velocities in the lower minimum leading in the limit to avalanche prior to transfer even if the higher minima were nearer in energy than the valence band.

It may be possible to discover a system in which these various requirements are realised, then we would have a useful material as far as the exhibition of negative mobility was concerned. One such arrangement is the 'three level system' propounded by Hilsum et al (31).

2.4.2. The Three-Level System

This was suggested by Hilsum et al (31) who postulated an arrangement of three valleys as follows: the lowest exhibiting a small effective mass, the intermediate a larger effective mass and loose coupling to the lowest level and the highest exhibiting large effective mass and tight coupling to both the lowest and intermediate levels. Thus the transfer between lowest and intermediate valleys would be completed over a small field range giving high negative-differential-mobility and the peak velocity and tendency to avalanche would be minimised by the uppermost level being tightly coupled to the other two.

There are a number of other factors influenced by the coupling constant between the lowest and intermediate levels, if this is small the transfer is slow and therefore relaxation effects may limit the frequency performance of the material, but a smaller coupling constant entails an increased diffusion constant, so inhibiting the formation of domains and therefore the possibility of using the more efficient limited space charge accumulation mode (LSA) may be viable.

There are a number of III-V semiconducting compounds in which the band structure exhibits three different valleys. These are as follows:

	m^*_Γ	m^*_L	m^*_X	$\mathcal{E}_g$	$\Delta\mathcal{E}_{\Gamma L}$	$\Delta\mathcal{E}_{\Gamma X}$
GaSb	0.047	0.25	0.40	0.72	0.08	0.33
InAs	0.022	0.25	0.40	0.35	1.25	1.35
InP	0.062	0.25	0.40	1.34	0.60	0.80
InSb	0.014	0.25	0.40	0.175	0.60	0.80

(note these were Hilsum's (31) figures - some have since been more accurately measured).

The correct energy dispositions are found in gallium antimonide, indium arsenide and indium antimonide, but in these three cases the valley energy separations are small, so that thermal interference restricts any usefulness of negative-differential mobility. Only in indium phosphide are the valleys separated by more than several kT at room temperature. The relation $\Delta\mathcal{E}_{\Gamma X} < \mathcal{E}_g$ is also found, this inhibits avalanche breakdown. The only other compounds of possible application, bearing these limiting factors in mind, are certain compositions of the ternary systems indium gallium antimonide and indium arsenide phosphide, especially the latter, which was suggested by Fawcett et al (133) in their discussion of optimum semiconductors for microwave devices from a high drift-velocity criterion.

2.5. NEGATIVE DIFFERENTIAL MOBILITY

2.5.1. Consequences of negative differential mobility

This negative mobility property gives rise to the effect observed and reported by Gunn (32) and named after him. This concerns the formation of dipole domains of charge in samples of the material biassed above the threshold field for exhibition of negative mobility. This domain formation process is illustrated in Fig. 2G. Various

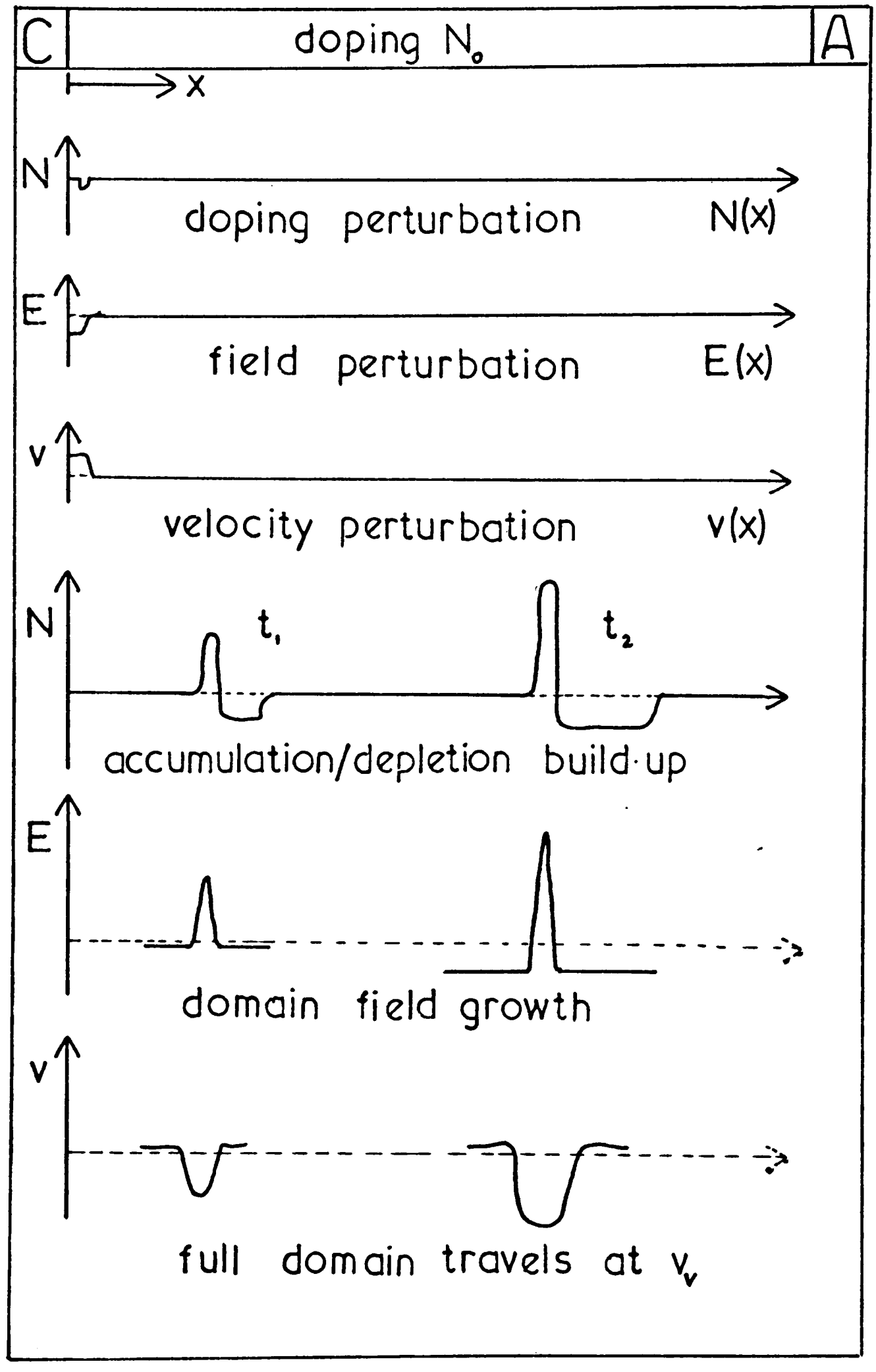

FIG. 2G

Domain formation.

theories (33,34,35,36) have been advanced to describe domain nucleation including effects of local doping fluctuations, space-charge perturbations and cathode contact properties.

These domains have been observed (37,38,39) and studied in indium phosphide and velocity-field characteristics calculated from these observations. This domain property has been exploited for direct dc to rf conversion in microwave oscillators and also as amplifying elements (40,41). Considerable efforts have been expended on the study of oscillators, some of the early reports (42), observing pulsed efficiencies of up to 7% in the X band. These results were extended and improved by many workers to include work in the Q band (43), improvements in heat-sinking and construction enabling useful CW powers to be generated, (44) and work on contacts (45) producing particularly high efficiency devices 21% at 11 GHz and 18% at 15 GHz (46).

The characteristics of bulk indium phosphide oscillators have been examined by Paxman et al (47) who estimated the threshold field for oscillation to be in the range 7-10 kV cm^{-1}, and from the transit velocity suggested operation based on an accumulation mode or quenched domain modes. Other workers (48,49) have analysed the efficiencies and limitations of the devices and Carroll (50) in his assessment of materials suitable for exploitation as transfered-electron devices cites other important criteria. He suggests the ratio of high-field to low-field mobility should be as small as possible to maintain high efficiency, indeed for the highest possible efficiency the high-field mobility should be zero (saturated) rather than even slightly positive. The power handling capacity is also dependent strongly upon the thermal conductivity, this to a certain extent determines the device construction arrangements.

2.5.2. Device Operation

A device in which a domain propagates exhibits a current waveform as shown in Fig. 2H, the different phases of domain life being clearly visible there. The criteria governing the build up of a dipole domain in a bulk sample are those of sufficient available charge, a long enough sample for growth to occur within the transit-time; and of course a negative dielectric relaxation time. These factors may be written in the relations

$$\frac{1}{v\tau_D} > 1$$

for growth to be large, and

$$n_o L > \frac{\epsilon v}{q|\mu_D|}$$

such that τ_D, the dielectric relaxation time is given by:

$$\tau_D = \frac{\epsilon}{q n_o |\mu_D|} \qquad (2.18)$$

This limiting value for $n_o L$ is similar for both gallium arsenide and indium phosphide and is $n_o L \simeq 10^{12}$ cm^{-2}. The cases of this product being less than, or greater than the limiting value are both worthy of consideration for device operation as follows:

$n_o L < 10^{12}$ cm.$^{-2}$ - no domains may form, but space-charge waves may propagate, hence this regime may be used for stable linear amplifiers. Connected to a resonant circuit the accumulation mode will operate.

If $n_o L > 10^{12}$ cm^{-2} - domains may form, Gunn oscillations operate if connected to a constant voltage source. Connection to a resonant circuit, multiple domains may propagate or domain quenching may operate if $fL > 10^7$ cms.$^{-1}$ or complete domain inhibition is possible in the LSA mode where $fL > 2.10^7$ cms.$^{-1}$ and $2.10^4 < n_o/f < 2\ 10^5$ cms^{-3} s.

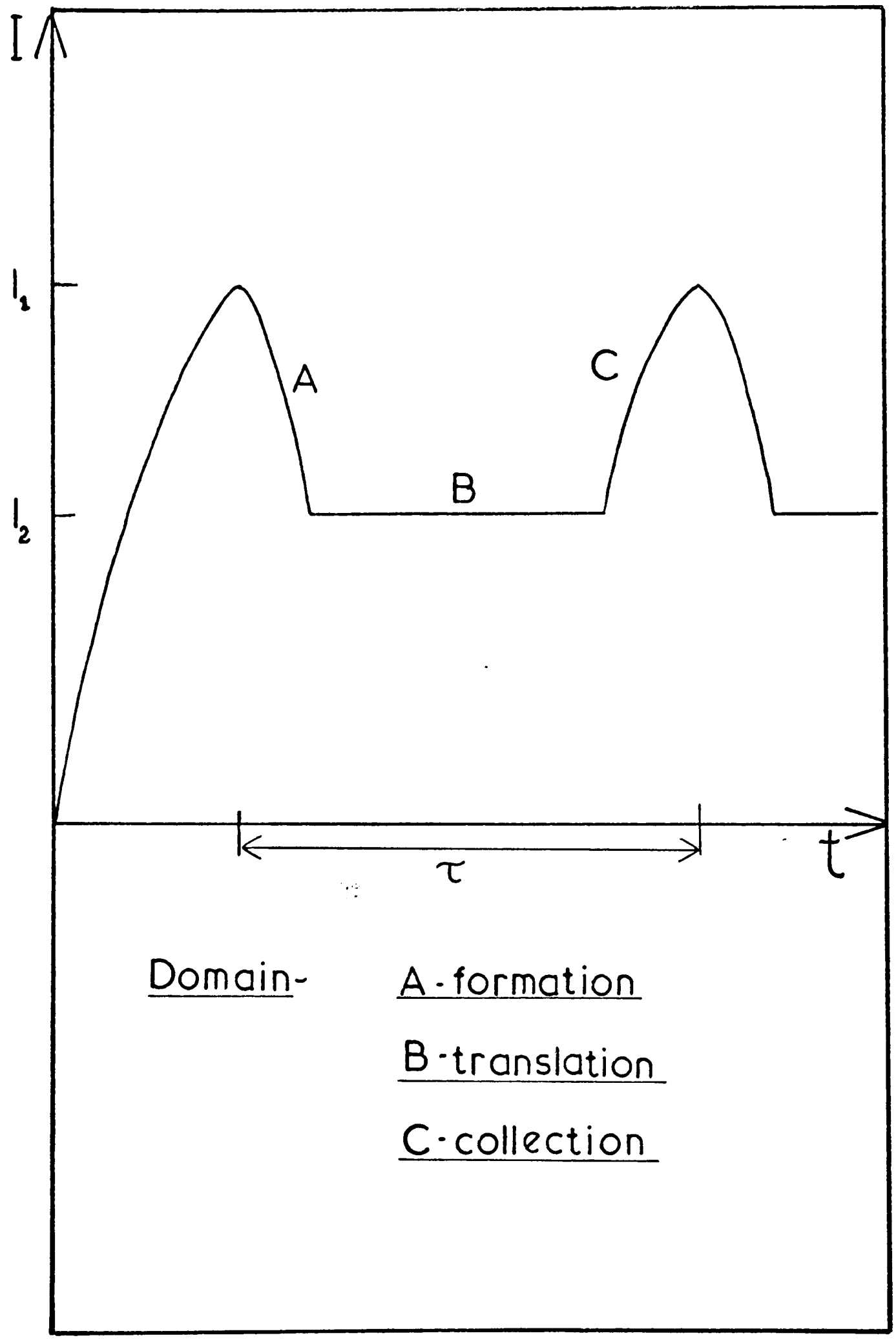

FIG. 2H

Transit-time device current waveform.

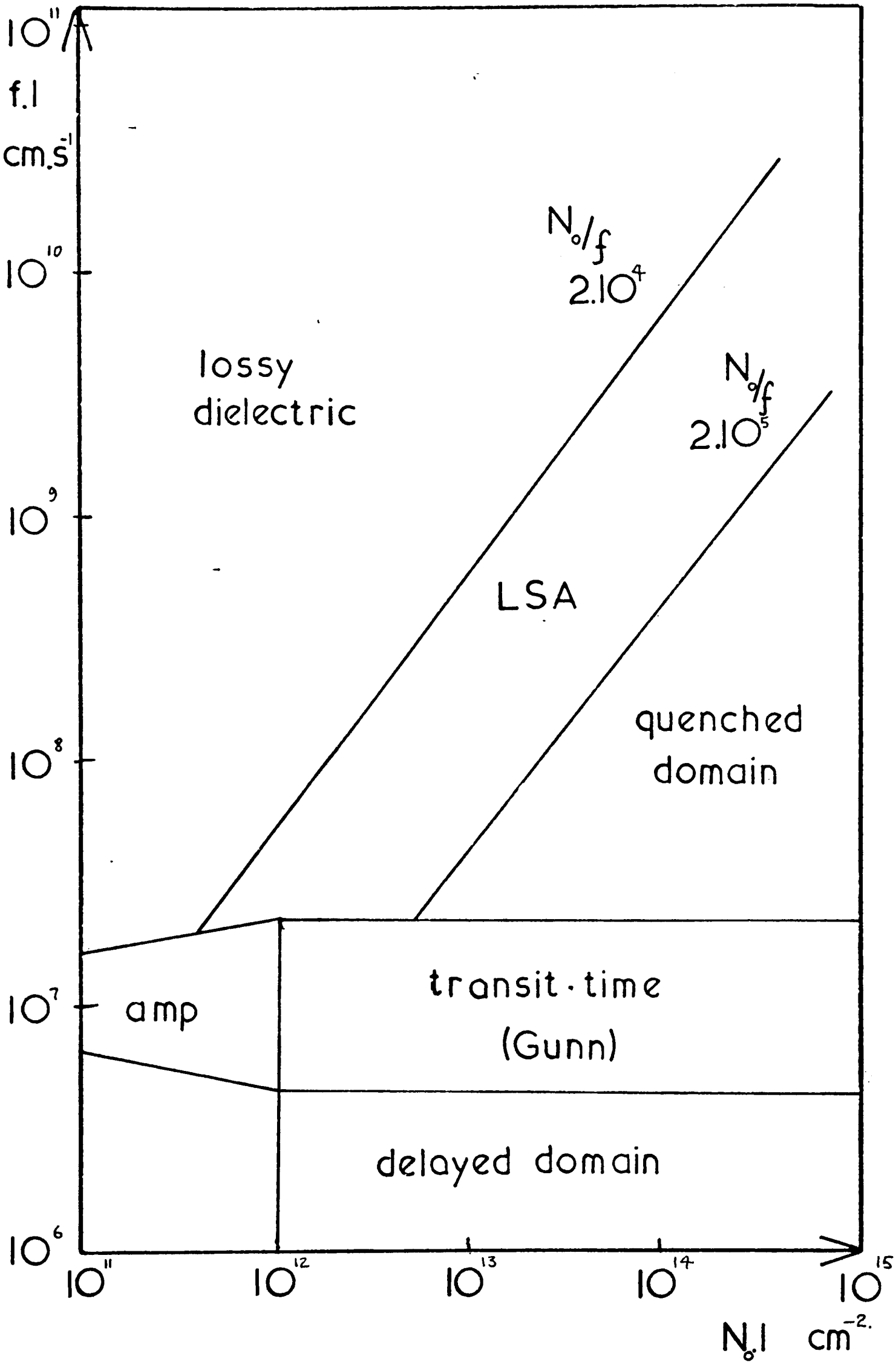

FIG. 2J

N.D.M. devices – mode chart.

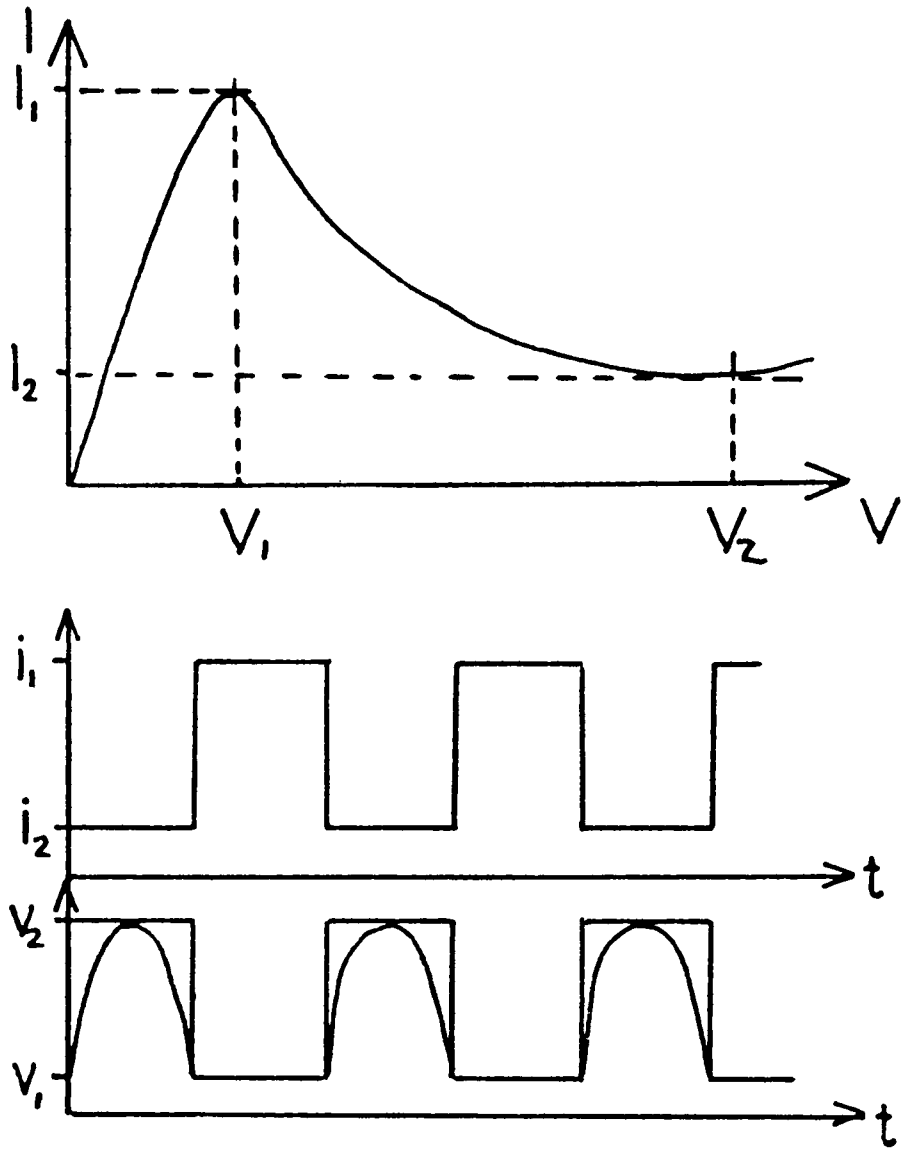

– square and half-sine outputs

efficiencies.

V_2/V_1 =	∞		10		2	
	sq	$\frac{1}{\pi}$s	sq	$\frac{1}{\pi}$s	sq	$\frac{1}{\pi}$s
r = 2	27%	33	22	25	7.7	9
2.5	35	43	29	32	10	12
3	41	50	33	37	12	14
4	49	60	40	45	14	16

FIG. 2K

Transfered electron devices

square and half-sine wave output efficiencies.

These modes of operation are shown schematically on the mode chart in Fig. 2J.

The efficiency of transfered-electron-devices is governed strongly by the peak-to-valley ratio (r). Following the simple approach (52) using the definition of square-wave and half-sinusoid efficiencies we may calculate these efficiencies for various voltage ratios and peak-to-valley ratios. Fig. 2K summarises these results and it may be seen that considerable gains in efficiency may be derived by using materials with higher peak-to-valley ratios. The three-level system should have a higher ratio r than a corresponding two-level system since the third level prevents carriers achieving high energies and therefore limits the transfer range of fields. This higher value of r was one reason for the interest in indium phosphide. During device manufacture various parameters are controllable, the quality and uniformity of material, the doping density, device active length and the shape and quality of contacts. Methods of mounting and packaging the active device control heat dissipation and surface protection from corrosion and thence surface-state formation.

2.6. VELOCITY-FIELD CHARACTERISTIC

2.6.1. Boltzmann's Transport Equation

This is an equation which describes the behaviour of the electronic distribution function $F_k(\underset{\sim}{r})$ in $\underset{\sim}{k}$ space, describing the changes which may occur in its value at a point $\underset{\sim}{r}$ in space. These changes are due to diffusion of carriers, effects of applied fields and scattering of carriers by any of the processes involved. These effects may be described as follows(53)

- by diffusion:

$$\dot{F}_{\underset{\sim}{k}}(\underset{\sim}{r})\Big|_d = -\underset{\sim}{v}_{\underset{\sim}{k}} \cdot \frac{\partial F_{\underset{\sim}{k}}(\underset{\sim}{r})}{\partial \underset{\sim}{r}}$$

$\underset{\sim}{v}_{\underset{\sim}{k}}$ is spatial carrier velocity and the derivative is the concentration gradient of the distribution function,

- by fields:

$$\dot{F}_{\underset{\sim}{k}}(\underset{\sim}{r})\Big|_f = \frac{-q_o}{\hbar}\left\{\underset{\sim}{E} + \frac{1}{c_o}\,\underset{\sim}{v}_{\underset{\sim}{k}} \wedge \underset{\sim}{H}\right\} \frac{\partial F_{\underset{\sim}{k}}(\underset{\sim}{r})}{\partial \underset{\sim}{r}}$$

which describes how the fields drive carriers through the states $\underset{\sim}{k}$ at $\underset{\sim}{r}$.

-by scattering:

$$\dot{F}_{\underset{\sim}{k}}(\underset{\sim}{r})\Big|_s = \sum_n \dot{F}_{\underset{\sim}{k}}(\underset{\sim}{r})\Big|_n$$

where the sum denotes the effects of all the processes of scattering n, acoustic and optic phonons, impurities etc. This term is the most difficult to write analytically since it involves integrals over all states $\underset{\sim}{k}$. Consequently the equation written in full as:

$$\dot{F}_{\underset{\sim}{k}}(\underset{\sim}{r})\Big|_d + \dot{F}_{\underset{\sim}{k}}(\underset{\sim}{r})\Big|_f + \sum_n \dot{F}_{\underset{\sim}{k}}(\underset{\sim}{r})\Big|_n = 0 \qquad (2.19)$$

is usually a non-linear integro-differential equation, even in the equilibrium case shown. Assumptions regarding the boundary conditions of the problem and equations for electric fields and currents must usually be employed. Solution of these determines the distribition function and carrier properties.

However, interpretation of the Boltzmann equation in analytic form is difficult without considerable data on the material being investigated. The transport equations are often derived via appropriate integrations. Some of the terms are collision-free and would appear in the analysis of any gas, these are straight forward in derivation from Boltzmann's equation. The collision terms by contrast are often too difficult to analyse hence a phenomenological approach in terms of relaxation times

for momentum, energy and particles may yield a suitable set of terms. Blotekjaer (54) offered a set of equations following these lines and indeed criticised other worker's assumptions following these general methods. Herbert (55) has developed an analysis from first principles to calculate the intervalley coupling constants to assist the solution of the Boltzmann equation.

2.6.2. Solutions of Boltzmanns equation

Since the direct analytic solution of the Boltzmann equation is frequently impossible, a distribution for carriers in each valley may be assumed; usually in the form of a drifted Maxwellian distribution due to the similarity of the electrons with a classical gas.

$$f_j(\underset{\sim}{k}) = a_j \exp\left(-b_j(\underset{\sim}{k}-\underset{\sim}{k}_j)^2\right).$$

$$a_j = \frac{n_j h^3}{(2\pi m_j^* k T_j)^{3/2}} \quad , \quad b_j = \frac{h^2}{2 m_j^* k T_j} \qquad (2.20)$$

T_j is the electron temperature in the j^{th} valley and

$\underset{\sim}{k}_j$ is the displacement of the valley bottom in $\underset{\sim}{k}$ space.

This assumption enables the solutions to be adjusted according to the boundary conditions. The loss rates of energy and momentum to the scattering processes are calculated and compared to the gains due to the applied fields to obtain a solution.

Heinle (56) has published results of this type of solution (including one for $InAs_{0.2}P_{0.8}$), James (10) published similar work when little upper-valley data was available. Hammar et al (57) and Hilsum et al (58) used numerical solutions based on this type of approach.

An alternative approach is to simulate the path of an election in $\underline{k}$-space which experiences alternate scattering and constant-velocity drift processes. The times spent in each state $\underline{k}$ are summed and hence the distribution obtained. This is the basis of the Monte Carlo (59) method of calculation used by Fawcett et al (60,61) Bauhahn et al (62) and Hillbrand (63,64). This avoids the assumptions made in the use of the drifted Maxwellian distribution and makes no a priori assumptions whatever. The difficulty here lies in the exact determination of the probability parameters for individual scattering processes.

A general comparison of results obtained by the aforementioned workers is shown at Fig. 2L. Also included there are the effective mass values employed in the calculations and the ΓL coupling constants and number of levels considered. Perhaps the most likely to be correct is due to Fawcett et al (60,61) since they used the most modern data and analysis methods.

The X valley was found to be very unpopulated, even at high fields (Fawcett et al (60) 6% occupation at 75 kV/cm contributing 3% to the velocity), this led many workers to favour a two-level system, contrary to the work of Hilsum who favoured that three-levels were involved significantly in the transfer mechanism. Hammar et al (57) compared the two- and three-level methods, and others (56,58,63,64) checked on the effect of ΓL coupling constant variations.

The variation of effective masses is shown at Fig. 2M after Hilsum et al (58) together with the two- or three-level calculations of Hammar (57). The coupling constant variations are perhaps the most striking. Temperature variations calculated by James et al (10) and Bauhahn et al (62) are shown in Fig. 2N, increased temperature increasing the threshold-field and decreasing the peak velocity. Various non-linear effects will now be discussed.

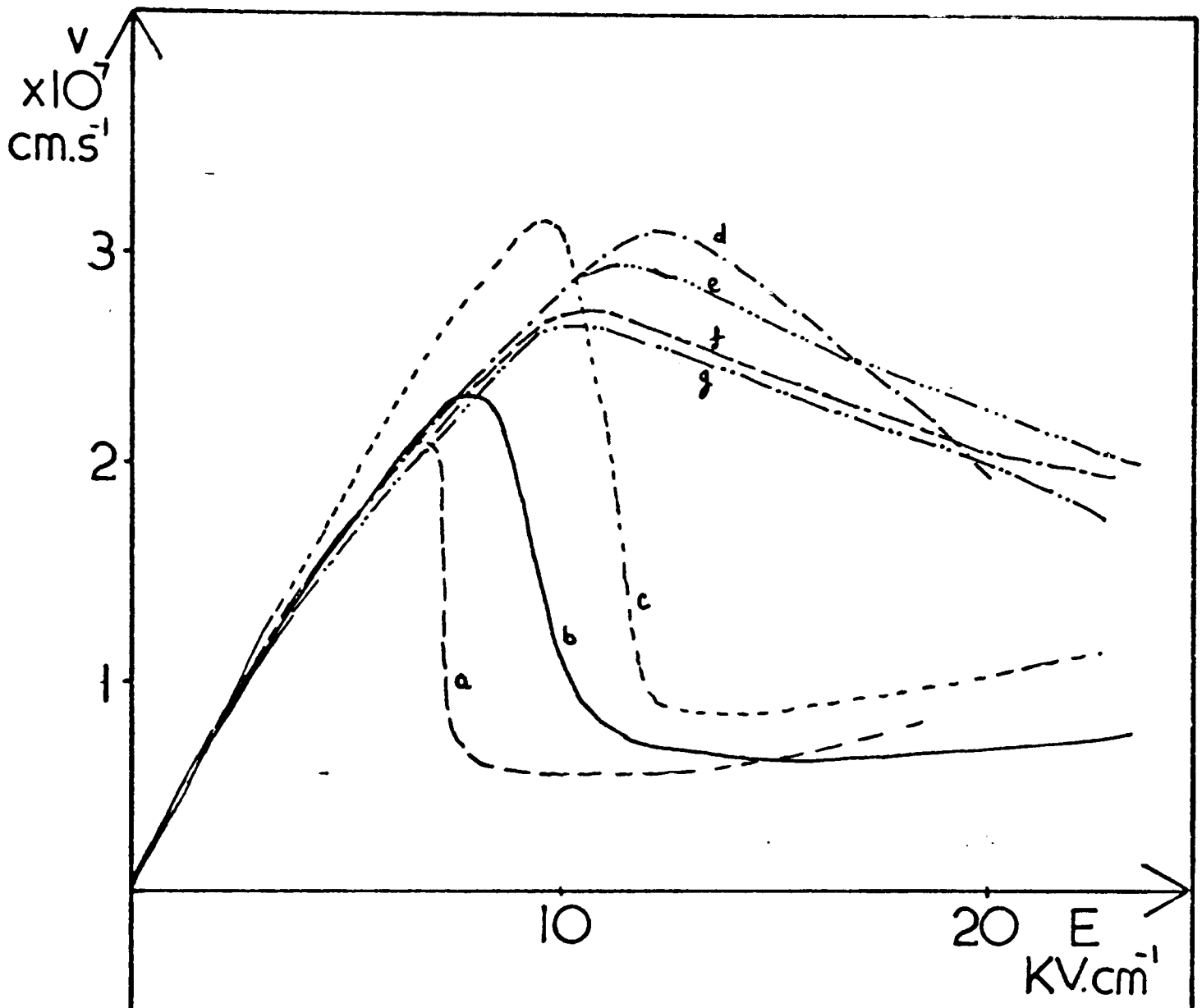

		m^*_Γ	m^*_L	m^*_X	$\Xi_{\Gamma L}$	v_ρ	E_t	n_L
a.	(58)	0.08	0.4	0.4	1.10^9	2.1	7	3
b.	(58)	0.08	0.4	0.4	3.10^8	2.3	8	3
c.	(56)	0.062	0.25	0.4	1.10^9	3.0	10	3
d.	(10)	0.06				3.0	13	2
e.	(57)	0.08	0.25	0.4	5.10^8	2.7	12	2
f.	(57)	0.08	0.25	0.4	3.10^8	2.5	11	3
g.	(60)	0.072	0.4	0.4	$2.9.10^8$	2.5	11	2

FIG. 2L

Indium phosphide – v(E) characteristic theoretical estimates at 300°K.

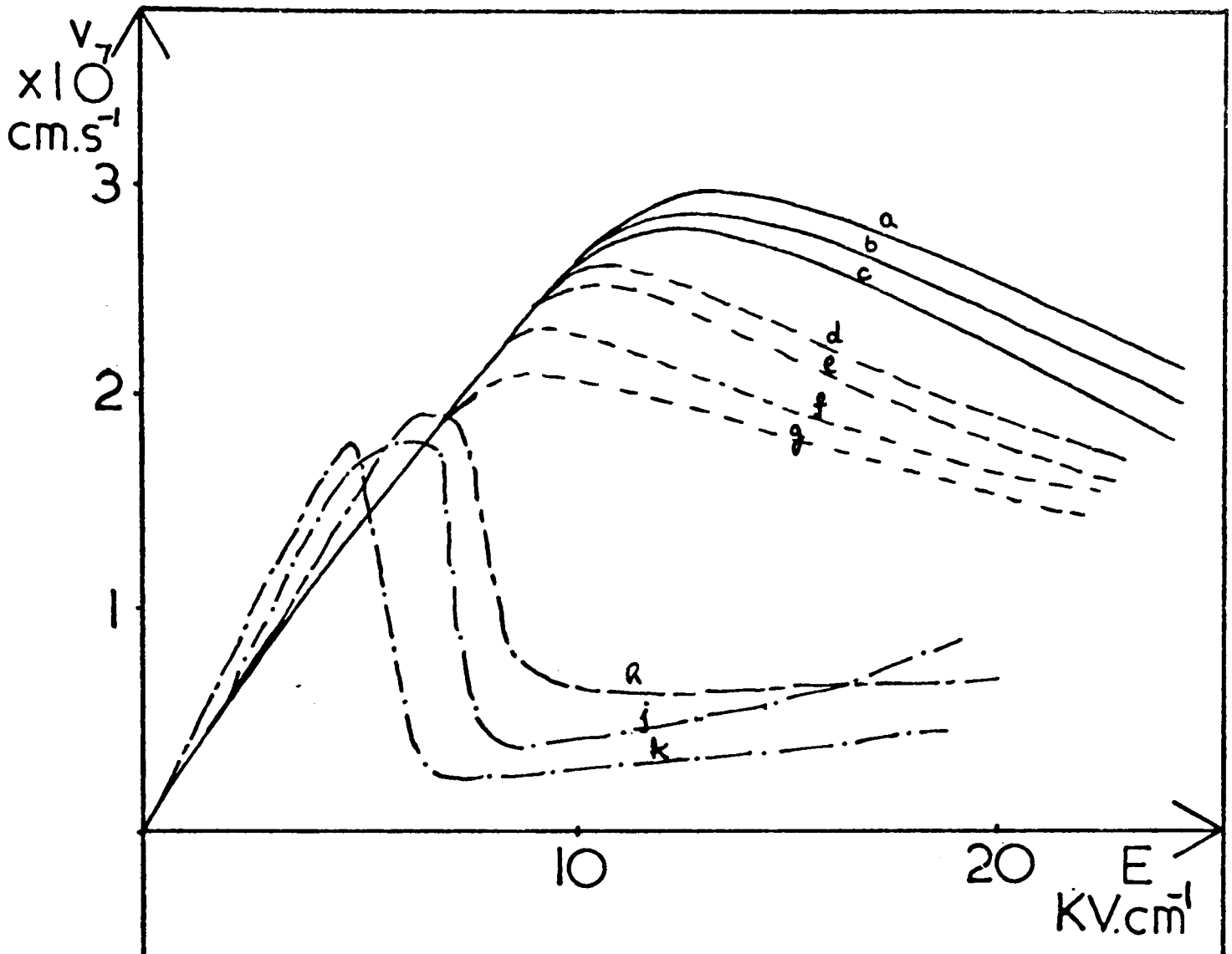

(57) $m_r^* = 0.08$, $m_L^* = 0.25$, $m_x^* = 0.4$.

$n_L = 2$ a $\Xi_{rL} = 2.10^9$

b $\Xi_{rL} = 1.10^9$

c $\Xi_{rL} = 5.10^8$

$n_L = 3$ d $\Xi_{rL} = 2.10^9$

e $\Xi_{rL} = 1.10^9$

f $\Xi_{rL} = 5.10^8$

g $\Xi_{rL} = 3.10^9$

(58) $n_L = 3$ $\Xi_{rL} = 1.10^9$

h $m_r^* = 0.08$, $m_L^* = 0.25$, $m_x^* = 0.4$

j $m_r^* = 0.062$, $m_L^* = 0.25$, $m_x^* = 0.4$

k $m_r^* = 0.062$, $m_L^* = 0.4$, $m_x^* = 0.4$

FIG. 2M

Indium phosphide - v(E) characteristic

effective mass (15) and energy level (28) variation.

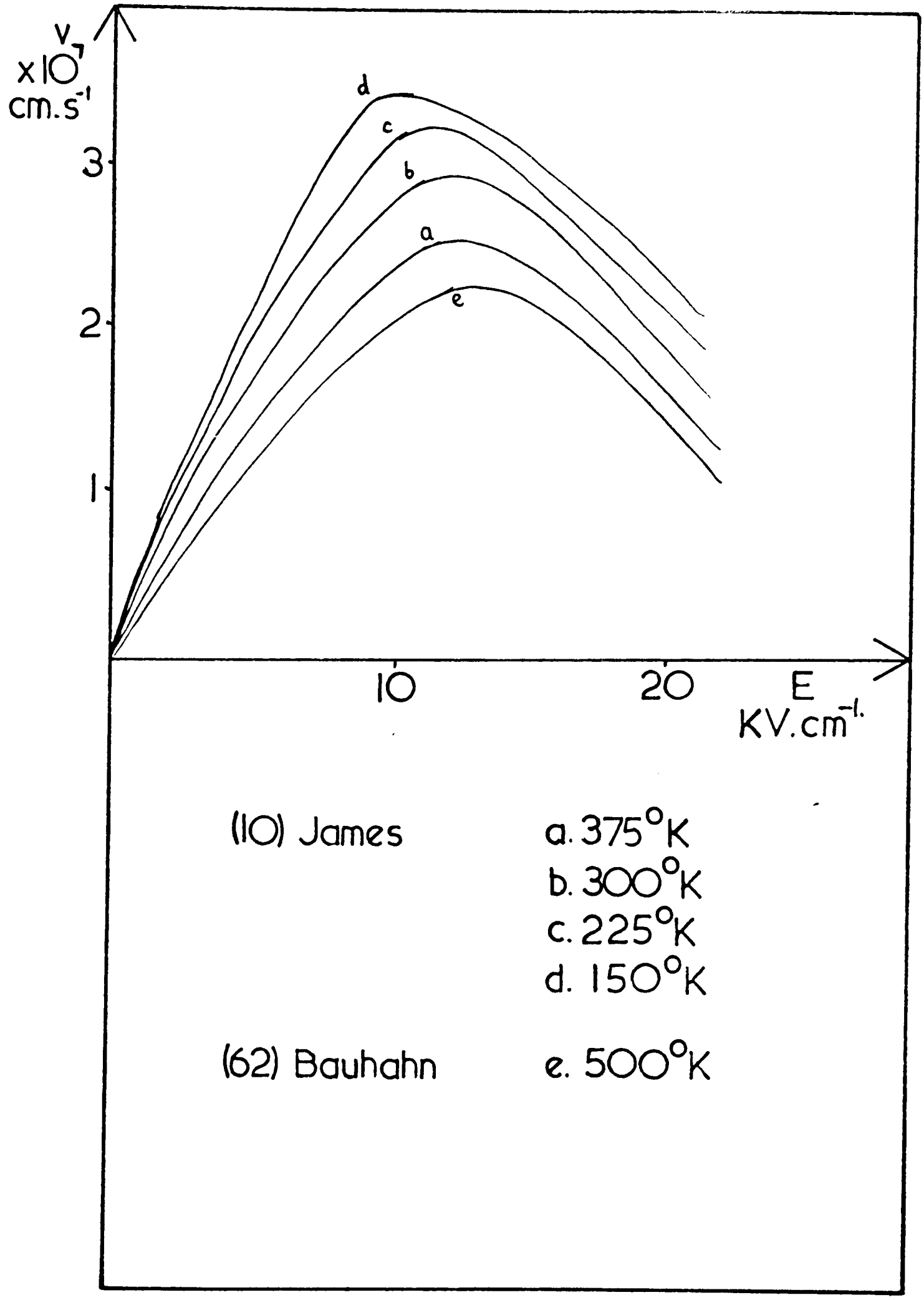

FIG. 2N

Indium phosphide – v(E) characteristic temperature variations.

2.6.3. Non-linear Effects

The four main effects to be considered are anisotropy of effective mass, non-parabolicity of the central valley, energy relaxation and diffusion effects.

Any departure from isotropic, parabolic energy surfaces within the minima in the conduction band affects the carrier properties. Departures from spherical symmetry result in anisotropic effective mass values and non-parabolicity results in a departure from the simple $\mathcal{E}(\underset{\sim}{k})$ relations previously assumed. James (65) has published work on both these effects in indium phosphide. He criticised the the accuracy of previous calculations (10,56,57,58,63) using the approximations for non parabolicity due to Kane (66) on the grounds that this approximation includes only the effects of nearby valence bands, not the entire conduction band within the first Brillouin zone; resulting in applicability to only the bottom of the central valley minimum. He presents calculations using the methods of Herman et al (67), and produces a plot of the effective masses of electrons in the ΓL and ΓX directions. These results are shown in Fig. 2P. The effective mass in the central valley is therefore anisotropic and the $m^*_{\Gamma L}$ value goes to infinity at an energy of approx. 0.46 eV. This will result in anisotropic velocity-field characteristic, with a higher threshold field than previously calculated. James also calculates the ΓL coupling constant and finds a result disagreeing with Fawcett et al (60):

$$4.1\ 10^8 \leqslant \Xi_{\Gamma L}\ \text{eV/cm} \leqslant 1.5\ 10^9$$

whereas Fawcett et al obtained a value

$$\Xi_{\Gamma L} = 2.9\ 10^8\ \text{eV/cm}$$

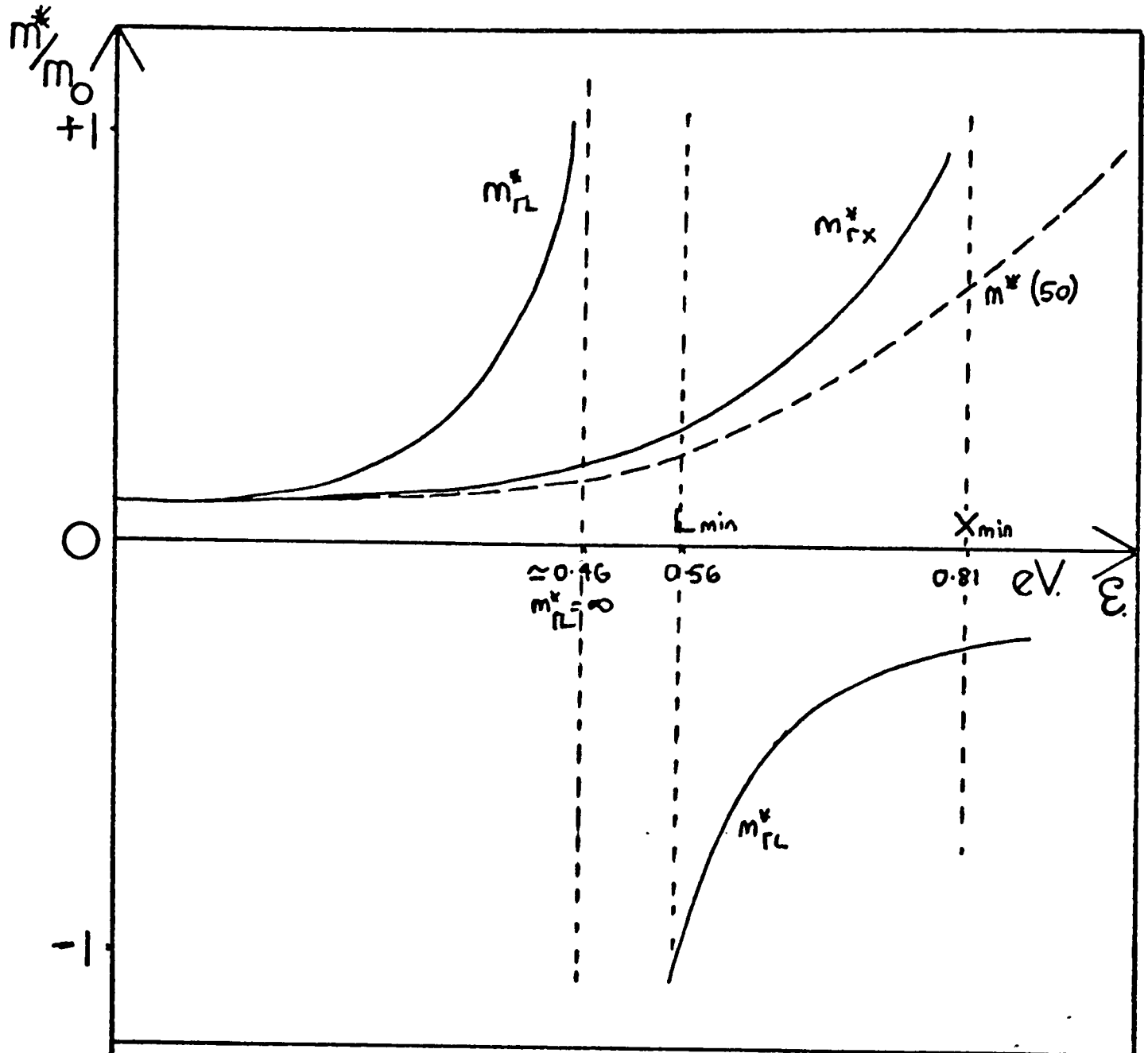

upper valley effective·mass values

$m^*_{tL} = 0.15, \quad m^*_{tX} = 0.28$

$m^*_{lL} = 0.55, \quad m^*_{lX} = 0.47$

conductivity effective mass $m^{*-1}_{ci} = \frac{1}{3}\left(m^{*-1}_{li} + 2m^{*-1}_{ti}\right)$

$m^*_{tL} = 0.19, \quad m^*_{tX} = 0.32$

density of states mass $m^*_d = \left(m^*_{li}\, m^{*2}_{ti}\right)^{1/3}$

$m^*_{dL} = 0.23, \quad m^*_{dX} = 0.33$

$n_L = 4 \qquad n_X = 3$

total density of states mass m^*_{dT}

$m^*_{dTL} = 0.90 \quad m^*_{dTX} = 0.99$

FIG. 2P

Indium phosphide – carrier effective mass

(65).

The energy relaxation time in indium phosphide has been studied by Glover (68) by experiment and also from theoretical calculation. He calculated the effects of polar optic scattering and intervalley transfer and these effects are shown at Fig. 2Q, the experimental determination is also shown there. He found a low field energy relaxation time of 1.7 pS, which increased near threshold. This value is above the simple mean free time calculated in eq. (2.17) by an order and means that energy relaxation takes much longer than the time of flight between collisions. Glover concludes that energy relaxation is faster in indium phosphide than gallium arsenide, but the behaviour near threshold is still uninvestigated.

The characteristic times τ_i may be regarded as the time taken to randomise a component i. Thus the momentum and energy relaxation times may not be less than the mean free time between collisions, but may be equal to or greater than that value. The differences are a measure of the type of collision process involved, and the sizes of the momentum and energy exchanges in the process. A complete system has both field-induced directional properties and random properties and a complete description of it requires knowledge of both momentum and energy, consequently both characteristic relaxation times are required in this description.

The individual transfer processes in the material may each be allocated characteristic times (54,69), which can be grouped into particle, momentum and energy times as follows:

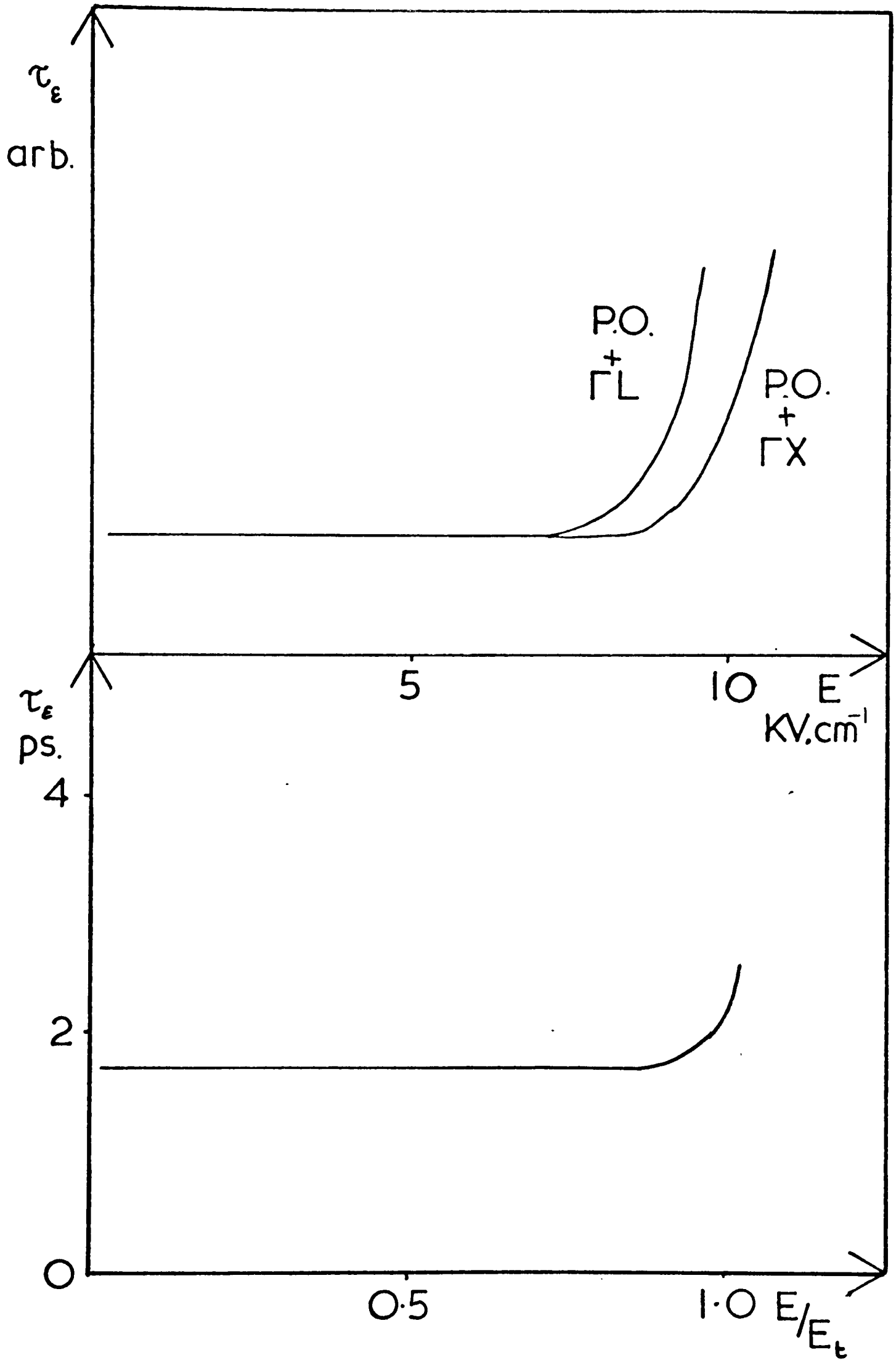

FIG. 2Q

Indium phosphide – carrier relaxation time

(i). theory (ii). experiment (68).

	central/satellite		
	τ_{n1}	CV → SV	} Particles
*	τ_{n2}	SV → CV	
	τ_{m1}	CV	} momentum
*	τ_{m2}	SV	
	$\tau_{\varepsilon 1}$	CV → SV (all)	} energy
*	$\tau_{\varepsilon 2}$	SV → CV	
		SV → SV	
	τ_{11}	CV → SV	
*	τ_{21}	all SV → CV	

*times are not functions of the drift energy since satellite valley velocity is low; others are, since central valley velocity may be high. All are functions of the electron temperature.

Diffusion of electrons affects the domain formation properties, due to the smoothing of space charge gradients. Hammar et al (70) and Bauhahn et al (62) have produced calculations of the diffusion constant as a function of field in indium phosphide. These are shown at figure 2R. Hammar et al (70) produced calculations for both two- and three-level systems, varying the ΓL coupling constant in both cases, also Bauhahn et al (62) presented calculation of a two-level system with $\Xi_{\Gamma L} = 1\ 10^9$ eV/cm at 500°K. Various points of structure are observed, especially in the three-level system with $\Xi_{\Gamma L} = 5\ 10^8$ eV/cm a moderate value. The zero field value agrees with the classical Einstein relation

$$\frac{D}{\mu} = \frac{kT}{q_0} \qquad \text{giving } D = 103 \text{ cm}^2/\text{s}$$

The field dependent value may be written

$$D(E) = \frac{k}{q_0} \sum_j \frac{n_j \mu_j T_j}{n_j} \qquad (2.21)$$

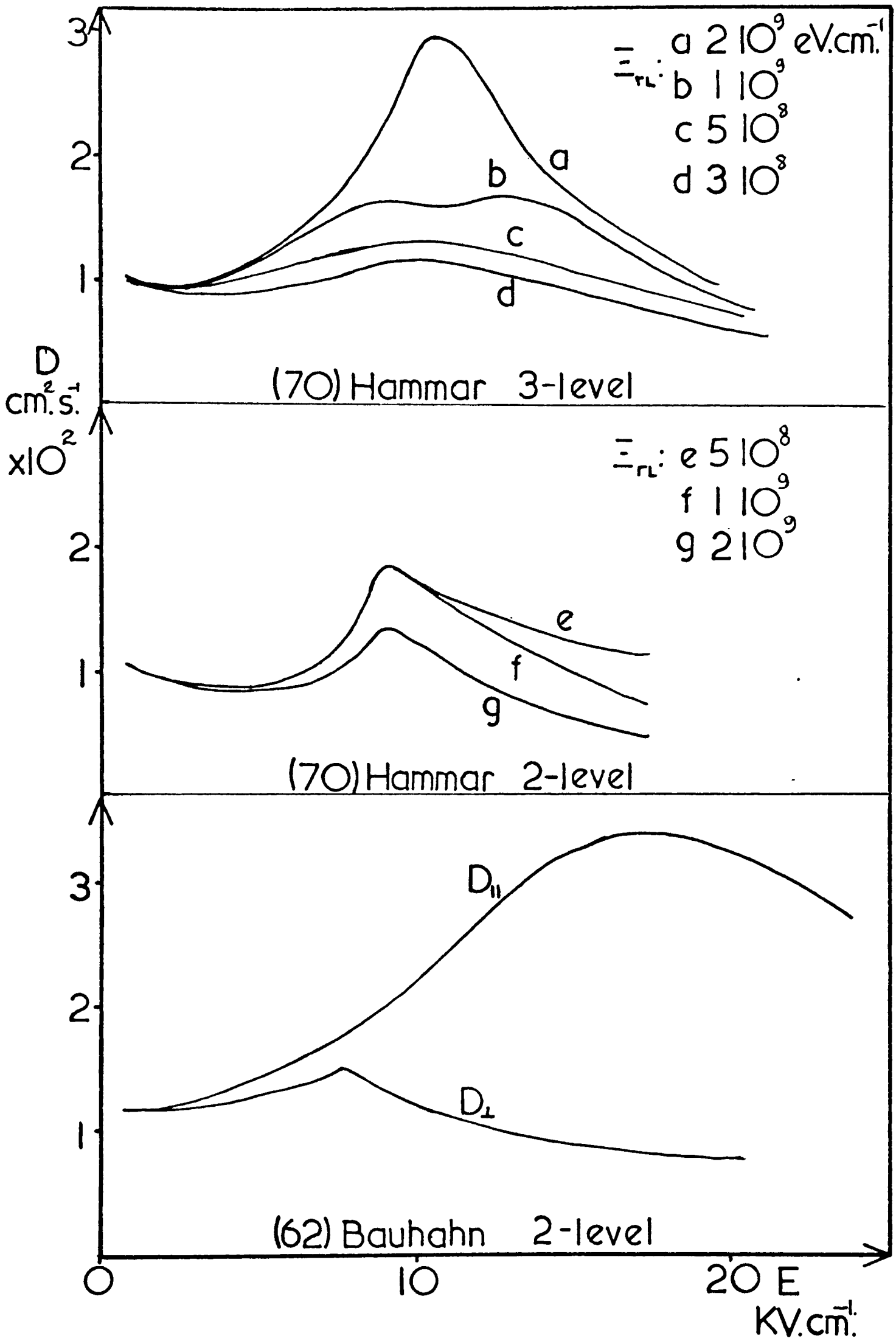

FIG. 2R

Indium phosphide - diffusion constant.

where j is the sum over the valleys. This leads to a maximum diffusion constant at $\simeq$ 12 kV/cm. The lower minimum is due to electrons emitting polar-optical phonons and falling to lower energies. Karshak et al (71) calculated a generalised relation for non-equilibrium conditions, which may be applied, but care should be taken over the inclusion of all the scattering effects correctly.

A measurement of the field-dependent diffusion constant would be an excellent method for checking the value of $\Xi_{\Gamma L}$, however at present no method exists for direct measurement.

Hauge (72) performed calculations of the effects of diffusion in a material exhibiting electron-transfer derived negative mobility. He concluded the possibility of static negative resistance and backward (anode to cathode) travelling domains and depletion layers. In GaAs he found the condition for SNR satisfied - albeit over a small field range and possibly masked by other effects. Carroll (73) comments on the relative importance of diffusion and dielectric relaxation effects that the former is more important for higher conductivities.

Chapter three.

Experimental method for the determination of the velocity-field characteristic.

3.1. MEASUREMENT METHODS

3.1.1. Transit-time and Space-charge Waves

For very high resistivity material where no space-charge effects are apparent due to the extremely low doping it is possible to observe the time-of-flight of an electron traversing a specimen under the influence of a field. Ruch et al (74) used this to study gallium arsenide by depositing a Schottky barrier on one face of a sample and injecting pulses of electrons using an electron beam. A laser could also be employed. A modification of this would be to induce space charge waves in a sample and this was done by Fay et al (75) on gallium arsenide. Boers (76) used this to study indium phosphide, the material being of resistivity $4.10^3\ \Omega$cm. Evans et al (77) have extended this basic technique to lower resistivity thin layers by modulating a beam with a microwave field (instead of switching it) to obtain better time resolution.

3.1.2. Dipole-domain Measurements

Boers (76,78) supplemented his results from space-charge waves by measurements on domains. He plotted the field distributions and using the equal area (33) rule modified from the work of Bastida et al (79) calculated the velocity-field characteristic. The material used was bulk, of resistivity 2 Ω.cm. and the pre-threshold measurements were made using d.c.

Prew (80) has also produced an experimental determination of the velocity-field characteristic from dipole-domain measurements.

He differed from Boers by using a point-contact probe rather than a capacitative probe. One advantage of the former is the measurement of static fields is possible, whereas dynamic effects only may be studied with a capacitative probe technique. Prew produces measurements of depletion ratios, where he disagrees with Boers as to their constancy, and incorporates these into the final curve, this (together with the others) is shown at Fig. 3A. Prew predicts a higher peak velocity than Boers and a lower threshold field. The results of Prew's work agree with the three-level calculation of Hilsum et al (58) and pre-threshold measurements of Kaul et al (82), Boers (83) disagrees with the use of the point-contact probe and comments that this may affect the field distribution within the translating domain, thus distorting the results. Prew (84) replied by describing the effects and precautions and answering comment on domain shapes. The two results are in disagreement, although Prew later (81) supplemented this work by measurements of domain charge and capacitance predicting an upper limit to the velocity-field characteristic still below that of Boers (83).

3.1.3. Microwave Heating Methods

There are two approaches using high-power microwave signals, the measurement of the conductance via the reflection coefficient and the modulation of the conductivity with a small d.c. current flowing.

T.Lam et al (85) used both techniques on 0.6 Ω.cm epitaxial material on semi-insulating substrates, their results are shown at Fig. 3A. Since their experimental results agreed with the predicted curve from James (10) calculation they concluded that a two-level transfer mechanism operated and that the Ξ_{rL} coupling constant was large. They also suggest the absence of relaxation effects, and support their results with measurements on gallium arsenide using the same equipment. They operated at 33 GHz and both methods produced results in agreement with

each other.

Glover (86) reports measurements at 9.5 and 35 GHz on 1.4 Ωcm. material. He used 'sandwiches' of n^+ n n^+ material (similar to those used in Gunn diode production) mounted as sections of inductive posts (87). He derives the field at the sample from the power absorbed by it, rather than from the incident power as some other workers have done. His results agree with the foregoing measurements of T.Lam et al, except that the 9.5 GHz results produce a lower peak velocity and also a lower negative differential mobility. He attributes the variation in peak velocity to relaxation effects, and the lower negative-differential mobility to field inhomogeneities due to space-charge effects. Nielsen (80) also published measurements at these frequencies on bulk material (10^{14} cm^{-3}) which are in fair agreement with Glovers work.

In general the microwave methods give threshold fields greater than those from domain measurements. Hilsum et al (89) discuss the variation in results and comment on the fortuitous agreement of the calculation made by James et al (10) using some incorrect data and the experimental measurements (78,85,86,88). They suggest that the assumed Maxwellian energy distribution underestimates the number of high-energy electrons - leading to overestimates in the threshold field. They also comment on the effect of band non-parabolicity, later corroborated by James (65). They comment that threshold fields of < 9 kV/cm can only be fitted by a three-level model, but those between 9 and 11 kV/cm may be fitted by either. They also cite the measurements of Boers (76) suggesting a peak velocity of 3.10^7 cm/s at a high threshold field value of 13 kV/cm and an extremely low valley velocity ($7\ 10^6$ cm/s) at 140 kV/cm, as being unable to be fitted to any existing model using currently measured data.

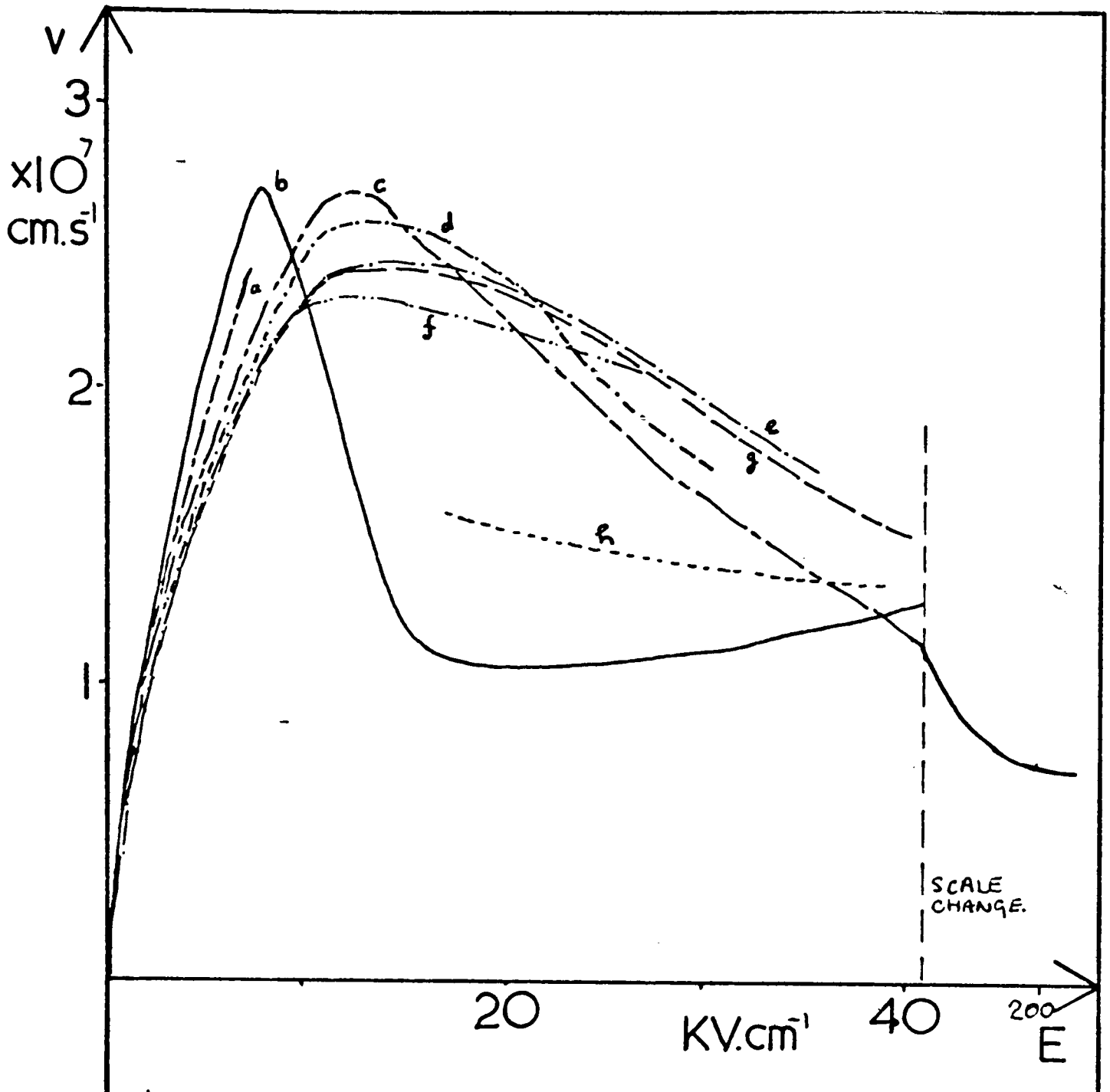

	method	material	E_t	v_p	r
a. (82)	d.c.	bulk	6.8	$2.5.10^7$	
b. (80)	domain	bulk	7.0	2.7	2.7
c. (78)	sp.ch.	bulk	13.0	3.0	4.3
d. (85)	mic 35GHz	epi/si.	12.0	2.8	
e. (86)	mic 35GHz	epi/n+	11.0	2.7	
f. (88)	mic 9.5GHz	epi/n+	10.0	2.5	
g. (87)	mic 35GHz	bulk	11.0	2.7	
h. (81)	domain	bulk	upper limit shown		

FIG. 3A

Indium phosphide - v(E) characteristic experimental determinations at 300°K.

3.1.4. Subthreshold Measurements

The foregoing (80,82,83,86) experimental measurements of the velocity-field characteristic have included subthreshold measurements, including the technique of using H shaped samples and probing the field remote from the contacts. This was also used by Majerfield et al (90) who obtain a threshold field in the range 10.5-11.5 $kV \cdot cm^{-1}$, considerably higher than measured by Kaul et al (82) as 6.8 $\pm$ 0.6 $kV.cm^{-1}$. The former authors report, however, that measurements on certain bulk samples gave apparent threshold fields in the range 7.0-7.7 $kV.cm^{-1}$, but in these the field was not uniform. The carrier velocity at the threshold field was found to be 2.5 x 10^7 $cm.s^{-1}$.

3.1.5. Selection of Experimental Method for this Work

The work reported in this thesis employed the technique of modulating the d.c. conductivity with pulses of microwave power. This method was particularly suitable for the Gunn diode type material, which was available to the laboratory. The method was technologically fairly straightforward, especially insofar as equipment was concerned. The analysis developed by Glover (87) I considered superior to alternative methods since it did not rely on calculation of the electric field in the semiconductor via the incident power and geometrical considerations, but rather via measurement of the absorbed fraction of the microwave power. The analysis will be described, followed by an evaluation of non-linear effects. Experimental analysis will then be developed and finally the experimental apparatus will be described and its capabilities considered.

It was intended to compare the results of this work with work by Hamilton on the same or similar indium phosphide slices, he examining dipole domains and following the method of Bastida et al (79) to extract the velocity-field characteristics. The microwave method

would provide the low field (above threshold) information and the dipole-domain measurements higher-field information; sub-threshold probing and the microwave method also correlating the exact threshold field value.

3.2. MICROWAVE CONDUCTIVITY EXPERIMENT

3.2.1. Assumptions

The concept of microwave conductivity is the result of the carrier properties changing due to high fields. Considering an electron in a periodic field in one dimension.

$$\frac{\partial}{\partial t}(mv) = q_0 E_0 \exp(j\omega t) - \frac{mv}{\tau_m(v)}$$

v is the drift velocity, $\tau_m(v)$ is the momentum relaxation time, in general a function of energy. We assume that the effective mass remains constant at m*, then the steady state solution will be:

$$v = \frac{\tau_m(v)\, q_0 E_0 \exp(j\omega t)}{m^* \left(1 + j\omega \tau_m(v)\right)}$$

the current density may be written

$$J = j\omega \epsilon E_0 \exp j\omega t + \sum_n n q_0 v.$$

n is the sum over the carrier concentration; using the two foregoing equations we have:

$$J = j\omega\epsilon E_o \exp(j\omega t) + \sum_n \frac{n q_o^2 \tau_m(v) E_o \exp(j\omega t)}{m^*(1 + j\omega\tau_m(v))}$$

The summation being carried out over the carrier distribution, which will be known from the solution of Boltzmann's transport equation eq. (2.19), or a Monte-Carlo calculation assuming all carrier scattering mechanisms are explicitly understood and their effects calculable.

Considering the in-phase component and writing:

$$\bar{\sigma} = J/E.$$

$$\bar{\sigma} = \frac{n q_o^2 \tau_m(v)}{m^*(1 + \omega^2 \tau_m^2(v))} \qquad (3.1)$$

this being analagous to eq. (2.5) etc.

$$\sigma = n q_o \mu, \qquad \mu = q_o \tau_f / m^*$$

If the applied field E_o is small then the distribution function is approximately equal to that with the d.c. field only, also if $\omega^2\tau_m^2(\sigma) \ll 1$ then $\bar{\sigma}$ is equal to the d.c. value. However if the E_o field is large or $\omega^2\tau_m^2(\sigma)$ is comparable to or greater than unity then $\bar{\sigma}$ is different from the d.c. value. This then is the microwave conductivity.

3.2.2. Working Equations and Analysis

Certain assumptions are necessary for the formation of the working equations for the microwave conductivity experiment, these will be described.

The r.f. frequency must be high enough so as to avoid space-charge growth effects during the r.f. cycle. Glover (87) and Braslau et al (91) state this limit to be

$$\rho \cdot f \geqslant 20\ \Omega\text{cm. GHz (87)}, \geqslant 35\ \Omega\text{cm. GHz (91)} \qquad (3.2)$$

Braslau et al also state that the limit may be decreased by a factor of 3 for homogeneous material samples. Using the criteria after Glover and substituting the operating frequency of the equipment (35 GHz) we find:

$$\sigma < 1.75\ \Omega.\text{cm}^{-1}, \quad \rho > 0.57\ \Omega\text{cm}.$$

and for material of mobility $\mu_o = 4600\ \text{cm}^2/\text{vs}$ this means a limit on the number density of electrons (assuming n-type).

$$n_e \lesssim 2.4\ 10^{15}\ \text{cm}^{-3} \qquad (3.3)$$

this will allow Gunn diode type material to be investigated as was intended.

The r.f. frequency must be low enough that energy-relaxation effects will be negligible. This may be expressed via the relaxation time expression:

$$(\omega^2 \tau_\varepsilon^2) << 1 \qquad (3.4)$$

the time τ_ε being the relaxation time for energy. In this case Glover (68) suggests that $\tau_\varepsilon \simeq 1.7$ pS, but increasing at threshold. With the operating frequency as 35 GHz this results in:

$$(\omega \tau_\varepsilon)^2 = 0.14$$

which is not very much less than one, but the effects are not very large from this analysis, approximately 16% (68), except that the behaviour near threshold is, as yet, unknown. Discussion of these effects are made in Section 3.3.2.

These last two criteria produce conflicting limits upon the choice of r.f. frequency, if low resistivity material is to be investigated.

The electric field throughout a sample is uniform, this places restrictions on the dimensions of the sample compared to the waveguide as also to doping profile inhomogeneity, which is discussed in Section 3.3.1.

Glover (87) and Marcuvitz (92) both quote less than 10% field distortion if the sample dimensions of a post are less than 15% of the waveguide width. Using WG22 for the experiments this restriction on post diameter is

$$d < 1.06 \text{ mm}$$

which is easily obeyed. Holmes et al (93) report measurements of conductivity on square posts and conclude that it is possible to equate these to circular posts of the same area, thus:

$$d_s = \frac{d_o\sqrt{\pi}}{2}$$

(d_s = side of square, d_o = diameter of circle).

Using these last two criteria we find that the maximum dimension of a square post is 0.935 mm.

The static electric field gradients are sufficiently small so as not to interfere with the local electronic concentration by space-charge effects. Using Poisson's equation for a local population excess Δn:

$$\Delta n = \frac{-\epsilon}{q_o}\cdot\frac{\partial E}{\partial x}$$

For less than 1% perturbation in the doping density, and for the smallest concentration of carriers likely to be used $\simeq 10^{14}$ cm^{-3} we find that

$$\frac{\partial E}{\partial x} < 1.1\ 10^{11} \quad V/m^2$$

which is

$$\frac{\partial E}{\partial x} < 0.11 \text{ kV/cm}/\mu \qquad (3.5)$$

In a 10μ layer this would place a restriction on the static d.c. transverse field of 11 kV/cm or an applied voltage of 11V. In the case of a layer mounted across the narrow dimension of the waveguide, the d.c. field must be less than 400 kV/cm or an applied voltage of 110 kV. These limits produce no problems since the d.c. fields must be low to avoid undue heating.

With these assumptions we may now write

$$J(t) = J(E(t))$$

where the electric field is the sum of a d.c. component, an r.f. fundamental and harmonics viz:

$$E(t) = E_1 + E_o \sin\omega t + \sum_{n=2}^{\infty} h_n E_o \sin n\omega t$$

assume that all harmonics above the first are negligible and that the first is small so that,

$$h_2 \ll 1 \qquad h_n = 0, \quad n \geqslant 3$$

we also assume that the d.c. term is much smaller than the r.f. fundamental so that:

$$E_1 \ll E_o$$

then we may write the current as a function of the form:

$$J(t) = J(E_o \sin\omega t, \ E_1, \ h_2)$$

where $E_o \sin\omega t$ is the main variable and E_1 and h_2 are perturbing variables. This enables the expansion in the form of a Taylor series:

$$J(a,b) = J(a) + \sum_{n=1}^{\infty} \frac{b^n \partial^n J(a)}{n!\, \partial a^n}$$

where $a = E_o \sin\omega t$,

$b = E_1 + h_2 E_o \sin 2\omega t$.

Assuming that the series will converge rapidly and defining the average current:

$$\bar{J}(E_o, E_1, h_2) = {}^1/_{2\pi} \int_o^{2\pi} J(E_o \sin\omega t, E_1, h_2)\, d(\omega t).$$

we may write the sum of the first six terms:

$$\bar{J}(E_o,E_1,h_2) = \frac{1}{2\pi}\int_o^{2\pi} J\, d\phi + \frac{E_1}{2\pi}\int_o^{2\pi} J'\, d\phi + \frac{h_2 E_o}{2\pi}\int_o^{2\pi} J' \sin 2\phi\, d\phi$$
$$+ \frac{E_1^2}{4\pi}\int_o^{2\pi} J''\, d\phi + \frac{h_2 E_1 E_o}{2\pi}\int_o^{2\pi} J'' \sin 2\phi\, d\phi + \frac{h_2^2 E_o^2}{4\pi}\int_o^{2\pi} J'' \sin^2 2\phi\, d\phi$$

where: $J = J(E_o \sin\phi)$

$J' = \dfrac{\partial J(E_o \sin\phi)}{\partial(E_o \sin\phi)}$

$J'' = \dfrac{\partial^2 J(E_o \sin\phi)}{\partial(E_o \sin\phi)^2}$

$\phi = \omega t$.

If we now define the average conductivity as

$$\bar{\sigma}(E_o) = \frac{\bar{J}(E_o, E_1, h_2) - J(E_o, -E_1, h_2)}{2E_1} \qquad (3.6)$$

and we apply this to the series for $\bar{J}$ above, we find that the average conductivity may be written:

$$\bar{\sigma}(E_o) = \frac{1}{2\pi}\int_o^{2\pi} J'\, d\phi + \frac{E_1}{4\pi}\int_o^{2\pi} J''\, d\phi + \frac{h_2 E_o}{2\pi}\int_o^{2\pi} J'' \sin^2 2\phi\, d\phi \qquad (3.7)$$

The definition of the conductivity as the average value of the currents for opposite polarities of d.c. field removes terms due to rectification and harmonic mixing, leaving the expression (3.7). If the last two terms are numerically insignificant we may write:

$$\bar{\sigma}(E_o) = \frac{1}{2\pi}\int_0^{2\pi} J'(E_o \sin\phi)\, d\phi$$

This assumption is checked in section 4.1.2. and Glover (87) also concludes that the two terms may be ignored. This equation may be written as

$$\bar{\sigma}(E_o) = \frac{2}{\pi}\int_0^{\pi/2} J'(E_o \sin\phi)\, d\phi. \qquad (3.8)$$

due to the symmetry of the function $J(E_o \sin\phi)$. This is a form of Schlömilch's Integral equation, whose solution (94) is analytic and unique (see Appendix 1).

$$J(E_o) = \int_o^{\pi/2} \bar{\sigma}(E_o \sin\phi).E_o \sin\phi.\, d\phi. \qquad (3.9.)$$

If the function of J(E) may be derived then the velocity-field characteristic may be related by:

$$V(E) = \frac{J(E)}{nq_o} \quad \text{or} \quad v(E) = J(E)\frac{\mu_o}{\sigma_o}$$

The data required may be analysed as follows; from measurements of absorbed power and conductivity. We have for the absorbtion of power:

$$W_a = \frac{1}{t}\int_0^t \int_V \underset{\sim}{J}(\underset{\sim}{r},t)\cdot\underset{\sim}{E}(\underset{\sim}{r},t)\; dV\, dt.$$

for a volume V, in time t, where $\underset{\sim}{r}$ is a spatial vector. Assuming uniform electric fields in our sample we may write

$$W_a(E_o) = \frac{V}{2\pi} \int_0^{2\pi} J(E_o \sin\phi).\, E_o \sin\phi .\, d\phi .$$

if the effects due to the perturbing agents h_2 and E_1 are also negligible. Differentiating this we obtain:

$$\frac{dW_a(E_o)}{dE_o} = \frac{V}{2\pi} . \int_0^{2\pi} \left(J(E_o \sin\phi).E_o \sin^2\phi + J(E_o \sin\phi).\sin\phi \right) d\phi$$

noting that $\sin^2\phi = \frac{1}{2}(1-\cos 2\phi)$ we find upon re-arrangement that:

$$\frac{dW_a(E_o)}{dE_o} = \frac{W_a(E_o)}{E_o} + \frac{V.E_o}{4\pi} \left\{ \int_0^{2\pi} J' d\phi - \int_0^{2\pi} J' \cos 2\phi \, d\phi \right\} \quad (3.10)$$

the second integral is numerically insignificant, see section 4.1.2., and Glover (87), consequently we have, using the result of eq. (3.8) for $\bar{\sigma}(E_o)$:

$$\frac{dW_a(E_o)}{dE_o} = \frac{W_a(E_o)}{E_o} + \frac{1}{2} V E_o . \bar{\sigma}(E_o). \quad (3.11)$$

with the initial, low field condition being:

$$W_a(E_o)_{E_o \to 0} = \frac{1}{2} V E_o^2 \sigma_o ,$$

the simple ohmic law. From this equation (3.11) a scheme may be devised (see Section 4.2.) to calculate $(\bar{\sigma}, E_o)$ from $(\bar{\sigma}, W_A)$ data.

3.3. PERTURBING MECHANISMS

3.3.1. Doping Inhomogeneity

This has been studied by Glover (95) during the course of his work on gallium arsenide. He specifies the doping density as a function of distance - $n_\ell(x)$. We may write:

$$J = n_\ell(x) \cdot q_o \cdot v\left(E(x,t)\right) + \epsilon \frac{\partial E(x,t)}{\partial x}$$

current continuity requires that $\frac{\partial J}{\partial x} = 0$ hence integrating this we find that

$$J(t) = \frac{q_o}{\ell} \int_0^\ell n_\ell(x) \cdot v \cdot dx + \epsilon \frac{d\bar{E}(t)}{dt}$$

where $\bar{E}$ is the applied electric field, l is the sample length. Glover performed calculations for various population functions $n_\ell(x)$ and found that an 'effective density' $\bar{n}_\ell$ could be defined:

$$\bar{n}_\ell = \frac{1}{\ell} \int_0^\ell n_\ell(x) \cdot dx.$$

and that the experimentally determined peak to valley ratio r was a function of $n_{\ell(min)}/\bar{n}_\ell$, and was degraded by wide variations in doping density. The negative-differential mobility was also degraded. Results are shown in Fig. 3B. This inhomogeneity of doping was one possible cause for the variety of results of experimental work, especially on higher resistivity material.

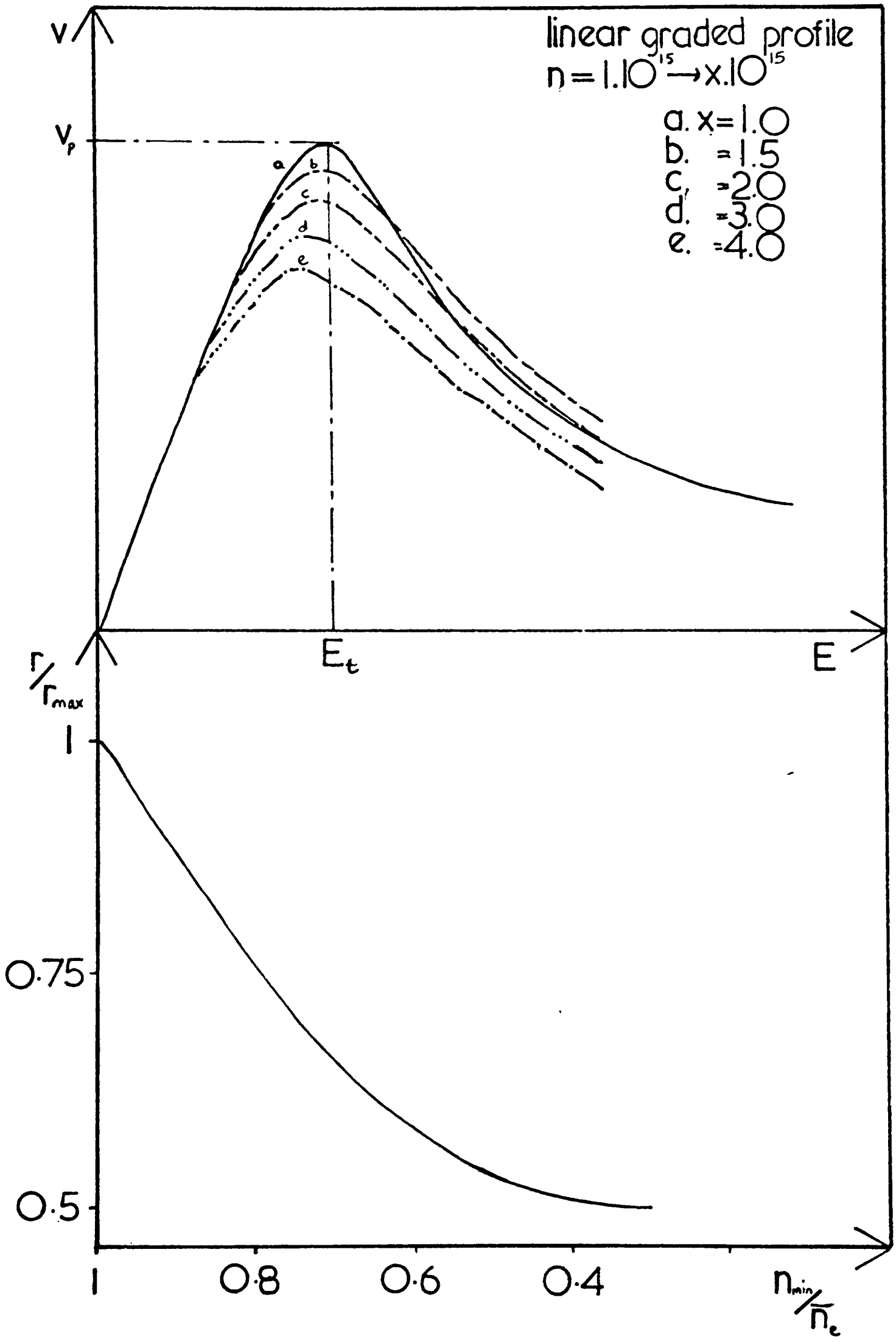

FIG. 3B

Doping profile effects :-

(i) carrier velocity (ii) peak-to-valley ratio.

3.3.2. Relaxation Effects

In the course of his work on gallium arsenide Glover (96) reported theoretical and experimental assessments of energy relaxation effects and estimated the error in velocity-field characteristics calculated from the results of microwave conductivity experiments. He considered a simplified two-valley model and concluded that the hysteresis of electron velocity due to energy relaxation overestimated the velocity as the frequency increased. Curves are shown in Fig. 3C.

The peak velocity increases with frequency, whilst the valley velocity remains substantially unchanged. Hence the apparent peak to valley ratio and negative-differential mobility appear larger than the d.c. values, the error being estimated as approximately +15% at 35 GHz.

In indium phosphide Glover (86) concludes that energy relaxation is of the same order as gallium arsenide or slightly faster $\tau_\varepsilon \simeq 1$ pS, but he does not estimate his error. In his study of relaxation times (68) he concludes $\tau_m < \tau_\varepsilon$, the former being approximately

$$\tau_m \simeq \frac{m^*_\Gamma \mu_o}{q_o}$$ at low fields, electrons in Γ valley.

This gives $\tau_m \simeq 0.20$ pS, equal to the mean free time as calculated by (2.17). The measured relaxation (68) time is $\tau_\varepsilon = 1.77$ pS, (Fig. 2Q) but effects near the threshold field are still unclear, save that relaxation effect is larger there. The error in the velocity-field characteristic is certainly 10% or greater. Should the coupling-constant be small and a three-level transfer operate, the small value of $\Xi_{\Gamma L}$ would make transfer slow and τ_ε larger than for tighter coupling.

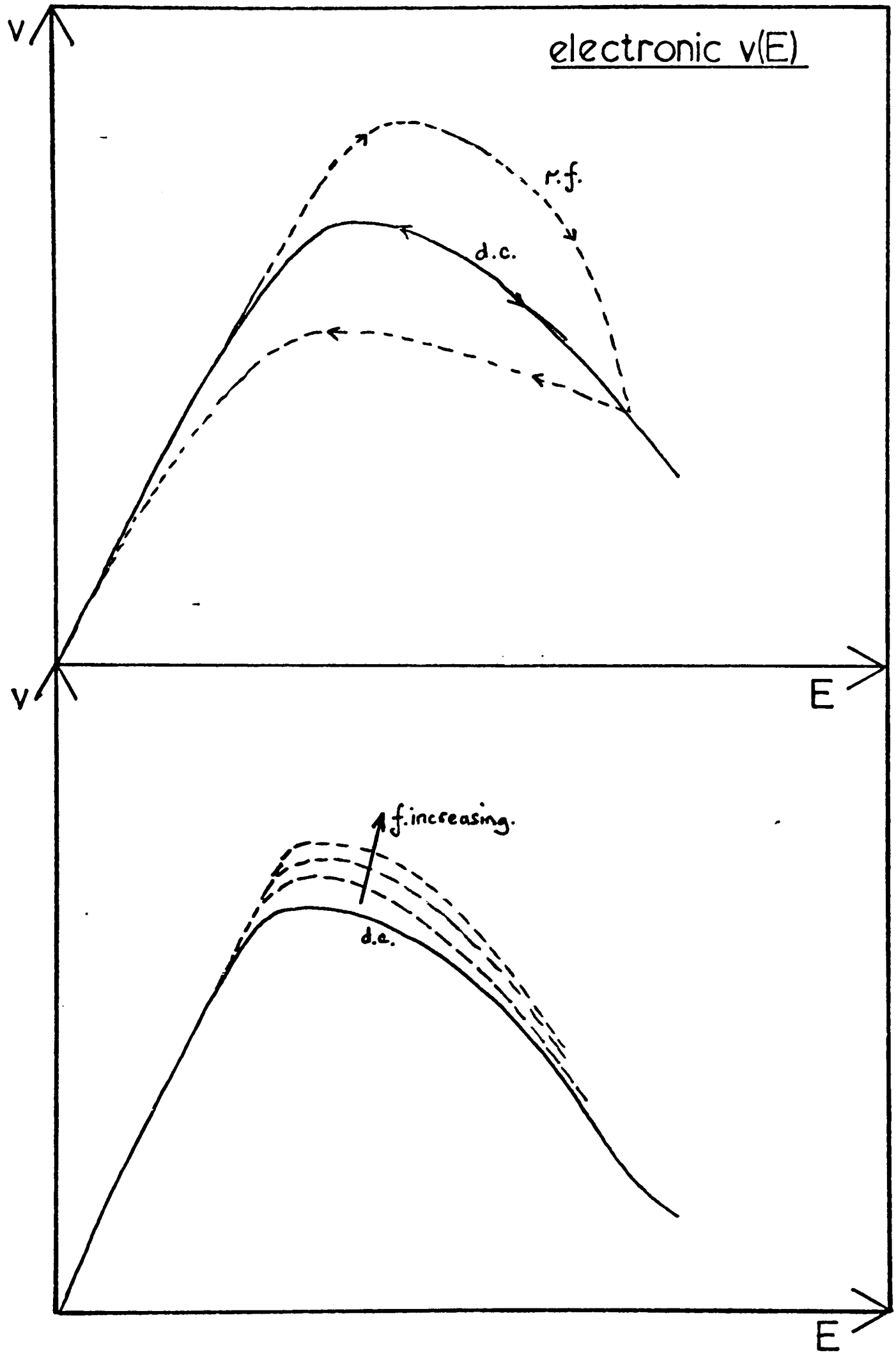

FIG. 3C

Energy relaxation effects:-

(i). electron velocity (ii). average velocity

3.3.3. Other Mechanisms

Some other data is available concerning experiments to determine semiconductor properties in waveguide using microwave techniques. Champlin et al (97) report the effects of contact and surfaces on the permittivity measured by an 'electrodeless' technique, viz. using the reflection coefficient to derive the conductivity at microwave frequencies. The method of modulating d.c. conductivity should not be affected as much save that contact should allow conduction currents to propagate freely between the samples and the waveguide walls: disturbances here would affect the fields and hence the absorbed power, rather than the conductivity.

Tree et al (98) report a failure mechanism of indium phosphide layers with tin-dot contacts exposed to pulses of high-power microwave radiation. In devices which failed in a short-circuit mode they found a metallic region a few microns wide between the contacts, where the tin concentration was enhanced and the phosphorus concentration degraded. They concluded that overheating in the vicinity of the anode had caused local vapourisation of phosphorus and then the tin contact had migrated along the indium-rich path, continuing until failure.

Bostock (99) reports measurements of the velocity-field characteristic of gallium arsenide using the high-power microwave technique, measuring the conductivity and deducing the electric field from other parameters. Their results are in agreement with other published data.

3.4. NUMERICAL APPROXIMATION TECHNIQUES

3.4.1. Pówer Series

Zucker et al (100) report that in the microwave conductivity experiment the average current during the microwave pulse is:

$$\bar{J} = \frac{E_L}{2\pi}\int_0^{2\pi} J'(E_o \sin\phi)\, d\phi. \qquad (3.12)$$

and one can fit to this data:

$$\frac{\bar{J}}{J_o} = \left(1 - \frac{\sigma_\infty}{\sigma_o}\right)\left(1 + \left(\frac{E_o}{E_c}\right)^2\right)^{-\frac{1}{2}} + \frac{\sigma_\infty}{\sigma_o}$$

E_c and σ_∞ being chosen to fit the data. This:

$$\frac{dJ(E_o)}{dE_o} = \sigma_\infty + (\sigma_o - \sigma_\infty)\left(1 + \left(\frac{E_o}{E_c}\right)^2\right)^{-1}$$

which yields:

$$J(E_o) = (\sigma_o - \sigma_\infty) E_c \tan^{-1}\left(\frac{E_o}{E_c}\right) + \sigma_\infty E_o \qquad (3.13)$$

This is fairly straightforward to fit to the data and $v(E_o)$ may be simply calculated. They note that the estimation of E_o from low values of absorbed power, (when using high resistivity material) is inaccurate and yields poor results, otherwise this is a reasonable method. This was used and compared to the polynomial approximation next described. It was a poor fit to the 'ideal' curve, but fitted to better than $\pm$ 5% to a real experimental result; although the applicability of this approximation was limited to electric fields only up to twice threshold. It fits the characteristics of Ge and Si better than InP and GaAs since any negative conductance is less marked.

Let us write a polynomial approximation for J in powers of electric field, up to the fifth order. Then:

$$J(E) = \sigma_o E\left(1 + b_1 E + b_2 E^2 + b_3 E^3 + b_4 E^4 + b_5 E^5\right). \qquad (3.14)$$

this is valid for $E \geqslant 0$. For validity when $E < 0$ then we must use a series in E^2, however this will be sufficient for our needs.

The power absorbed is, as before,

$$W_a = \frac{2V}{\pi} \int_{-\pi/2}^{+\pi/2} J(E_o \sin\phi).\, E_o \sin\phi .\, d\phi$$

substituting for J(E) in this equation, we have:

$$W_a(E_o) = \frac{2V\sigma_o E_o^2}{\pi}\left(\frac{\pi}{2} + \frac{4}{3} b_1 E_o + \frac{3\pi}{8} b_2 E_o^2 + \frac{4}{15} b_3 E_o^3 + \frac{5\pi}{16} b_4 E_o^4 + \frac{32}{35} b_5 E_o^5\right)$$

writing the average conductivity $\bar{\sigma}$ and inserting this into the general equation for absorbed power:

$$W_a(E_o) = \frac{V}{2} \bar{\sigma} . E_o^2$$

Comparing these last two expressions:

$$\bar{\sigma}(E_o) = \sigma_o\left(1 + \frac{8b_1}{3\pi} E_o + \frac{3b_2}{4} E_o^2 + \frac{8b_3}{15\pi} E_o^3 + \frac{5b_4}{8} E_o^4 + \frac{64 b_5}{35\pi} E_o^5\right) \qquad (3.15)$$

If we measure $\bar{\sigma}(E_o)$ and calculate the terms in the series in (3.15) we derive the coefficients $b_1 - b_5$ and hence we know $\sigma(E_o)$ according to eq. (3.14). Hence we may calculate v(E) from:

$$v(E_o) = \frac{\sigma(E_o) . E_o}{n_e q_o}$$

We may calculate the terms in the series from the relations

$$\overline{\sigma_j}(E_j) = \sigma_o \left(1 + \sum_k a_k E_j^k\right)$$

viz: $$\left(\sigma_j - \sigma_o\right) = (a_k)(E_j)$$

where $\left(\sigma_j - \sigma_o\right)$ and (a_k) are column vectors and

(E_j) is a square matrix of order k

Thus: $$(a_k) = \left(\overline{\sigma_j} - \sigma_o\right) . (E)^{-1}$$

3.4.2. Tschebeychev Polynomials

The last approximation for J(E) gives no control over the approximating function between the points chosen for manipulation of the data. This may result in large errors between the points and limited applicability just outside the data range. Tschebychev polynomials have superior approximating properties (see Appendix 2) and may be employed. Consider a set of Tschebychev polynomials of electric field such that:

$$\overline{\sigma}(E) = \sum_{K=o}^{n} A_k T_k(E).$$

where $T_k(E)$ is the polynomial of degree k and A_k is a multiplying coefficient such that

$$A_k = \frac{2}{\pi} \int_{-1}^{+1} \frac{f(x)\, T_k(x)}{\sqrt{1 - x^2}} \cdot dx \qquad -1 \leq x \leq +1.$$

Substituting $x = \cos\theta$ $\quad T_k(x) = \cos k\theta$,

$$a_k = \frac{2}{\pi} \int_{\pi}^{o} f(\cos\theta) . \cos k\theta . d\theta.$$

and

$$y(x) = {}^1/2a_o + a_1 T_1(x) + \ldots + {}^1/2a_n T_n(x)$$

$T_k(x)$ is derived from the recurrence relations:

$$T_k(x) = \cos(k\cos^{-1}x)$$

$$T_o(x) = 1,\ t_1(x) = x$$

$$T_{k+1}(x) = 2xT_k(x) - T_{k-1}(x)$$

Hence we may write for the average conductivity:

$$V(E_o) = \sigma_o\left(\tfrac{1}{2}a_o + a_1T_1(E_o) + \ldots\ldots + a_5T_5(E_o)\right) \qquad (3.16)$$

preserving the same order as we had used in the power series of eq. (3.14). Expansion of the polynomials yields:

$$\frac{\bar{\sigma}(E_o)}{\sigma_o} = \frac{a_o}{2} + a_1(E_o) + a_2(2E_o^2-1) + a_3(4E_o^3-3E_o)$$

$$+ a_4(8E_o^4-8E_o^2+1) + a_5(16E_o^5-20E_o^3 + 5E_o)$$

Comparison of this series with that of equation (3.15) yields the relations:

$$b_1 = {}^3/_8\cdot(a_1-3a_3-5a_5)$$

$$b_2 = {}^4/_3\cdot(2a_2-8a_4)$$

$$b_3 = {}^{15}/_{32}\cdot(4a_3-20a_5) \qquad (3.17)$$

$$b_4 = {}^8/_5\cdot(8a_4)$$

$$b_5 = {}^{35}/_{64}\cdot(20a_5)$$

also $a_o/2-a_2 + a_4 = 1$

Thus calculation of the Tschebychev coefficients a_k yielding a good approximation to the function may be extended to the power series coefficients b_k.

3.4.3. Space-Charge Suppression Criteria

Considering an isotropic, homogeneous, semiconductor with a propagating electromagnetic field, Maxwells equations are

$$\nabla \wedge \underset{\sim}{E} = -\frac{\partial B}{\partial t}$$

$$\nabla \wedge \underset{\sim}{H} = J + \frac{\partial D}{\partial t}$$

$$\nabla . \underset{\sim}{B} = 0$$

$$\nabla . \underset{\sim}{D} = \rho_s$$

in addition we have the definitions for $\underset{\sim}{D}$, $\underset{\sim}{B}$ and σ such that

$$\underset{\sim}{D} = \epsilon_o \epsilon_r \underset{\sim}{E}$$

$$\underset{\sim}{B} = \mu_o \mu_r \underset{\sim}{H}$$

$$\sigma = \frac{\partial J}{\partial E}$$

writing $\nabla \cdot (\nabla \wedge \underset{\sim}{H}) = 0$ and using $\nabla \cdot \underset{\sim}{E}$ we find:

$$\frac{\sigma}{\epsilon} \rho_s + \frac{\partial \rho_s}{\partial t} = 0$$

$$\rho_s = -\frac{\epsilon}{\sigma} \cdot \frac{\partial \rho_s}{\partial t}.$$

Integrating this gives:

$$\rho_s = \rho_s(0) \exp\left(-\frac{t}{\tau_D}\right)$$

$$\tau_D = \frac{\epsilon}{\sigma}$$

τ_D is the dielectric relaxation time, and may be of either sign according to the sign of the conductivity. Hence the perturbation $\rho_s(0)$ may decay or grow.

Writing $\Delta \underset{\sim}{E}$ for a field perturbation and using the foregoing relations for ρ_s and σ we then write

$$\frac{\partial}{\partial t}(\Delta \underset{\sim}{E}) = -\frac{1}{\epsilon} \frac{\partial J}{\partial E}(\Delta \underset{\sim}{E}) \qquad (3.18)$$

We have for J(E)

$$J(E) = \sigma_o \in \left(1 + b_1 E + \ldots\ldots + b_5 E^5\right) \qquad (3.14)$$

hence

$$\frac{dJ(E)}{dE} = \sigma_o \left(1 + \sum_{n=1}^{5} (n+1) b_n E^n\right). \qquad (3.19)$$

integrating equation (3.18) leads to

$$\Delta E_t = \Delta E_o \exp - \frac{1}{\epsilon} \int_o^t \frac{dJ(E)}{dE} \cdot dt. \qquad (3.20)$$

Substituting eq. (3.19) in this and evaluating we find the integral is (where $E = E\cos\omega t$)

$$t\left(1 + \frac{3b_2}{2}E^2 + \frac{15b_4}{8}E^4\right) + \frac{\sin\omega t}{\omega}\left(2b_1 E + 3b_3 E^3 + \frac{15b_5}{4}E^5\right) \ldots$$

$$+ \frac{\sin 2\omega t}{\omega}\left(\frac{3b_2}{4}E^2 + \frac{5b_4}{4}E^4\right) + \frac{\sin 3\omega t}{\omega}\left(\frac{b_3}{3}E^3 + \frac{5b_5}{8}E^5\right) \ldots.$$

$$+ \frac{\sin 4\omega t}{\omega}\left(\frac{5b_4}{32}E^4\right) + \frac{\sin 5\omega t}{\omega}\left(\frac{3b_5}{40}E^5\right).$$

as $t \to 0$ in the limit this becomes:

$$t\left(1 + 2b_1 E + 3b_2 E^2 + 4b_3 E^3 + 5b_4 E^4 + 6b_5 E^5\right)$$

since $\sin n\omega t \longrightarrow n\omega t$

Hence the expression for the growth of a perturbation ΔE_o (3.20) is

$$\Delta E_t = \Delta E_o \exp - \frac{\sigma_o}{\epsilon} t\left(1 + \sum_{n=1}^{5} (n+1) b_n E^n\right).$$

this may be written

$$\Delta E_t = \Delta E_o \exp - \frac{t}{\tau_o}$$

where τ_o is analogous to a dielectric relaxation time.

Where:

$$\frac{1}{\tau_o} = \frac{\sigma_o}{\epsilon}\left(1 + \sum_{n=1}^{5} (n+1) b_n E^n\right) \qquad (3.21)$$

the field perturbation will begin to grow at a rate set by τ_o , if the frequency is high enough, the field will not grow at all, this may be described by the condition $\omega\tau_o > 1$, thus:

$$\frac{\sigma}{\omega\epsilon}\left(1 + \sum_{n=1}^{5} (n+1) b_n E^n\right) < 1 \qquad (3.22)$$

this is one condition of space charge suppression, which may be simply checked during analysis of experimental data. This is an extension to the simpler form of dielectric relaxation consideration producing the rules of thumb governing the choice of resistivity and frequency specified in equation (3.2). In the linear case:

$$\frac{\sigma_o}{\omega\epsilon} < 1 \qquad b_n = 0,\ n \geq 1$$

simplifying to

$$\rho f > (2\pi \epsilon_o \epsilon_r)^{-1}$$

inserting values for ρ in Ω cm, f in GHz and the dielectric constant of indium phosphide we derive the inequality

$$\rho f > 150$$

which is an upper limit of the calculation computed graphically by Braslau et al (91).

This only specifies a condition for no growth of space-charge instabilities, should there be growth during an r.f. cycle, there must also be decay, otherwise build-up will occur over a number of cycles. Returning to eq. (3.18) we note that it yields growth or decay according to the sign of τ_D . We may write a condition such that:

$$\exp\left(-\frac{t_p}{\tau_{DP}}\right)\cdot\exp\left(-\frac{t_n}{\tau_{DN}}\right)<1 \qquad (3.23)$$

where t_p and t_n are the times spent in positive and negative mobility regimes respectively, and τ_{DP} and τ_{DN} are the dielectric relaxation times, τ_{DP} being positive and τ_{DN} negative and expressed as:

$$\tau_{DP}=\frac{\epsilon}{n_o q_o \mu_P}\ , \qquad \tau_{DN}=\frac{-\epsilon}{n_o q_o \mu_N}$$

taking the logarithm of eq. (3.23).

$$\frac{t_N}{\tau_{DN}}<\frac{t_P}{\tau_{DP}}$$

Specifying an electric field $E = E_o \sin\omega t$, and the threshold field as E_T we have:

$$E_T = E_o \sin\phi_o$$

$$t_p = 2\frac{\phi_o}{\omega}\ , \quad t_N=\frac{\pi}{\omega}-2\frac{\phi_o}{\omega}$$

hence substituting these in the inequality

$$\frac{\phi_o}{\pi/2-\phi_o}>\frac{\tau_{DP}}{\tau_{DN}}$$

We may substitute the expressions for τ_{DP}, τ_{DN}, and assuming that all parameters are equal over the entire cycle:

$$\frac{\phi_o}{\pi/2-\phi_o}>\frac{|\mu_N|}{\mu_p}$$

This would give a condition if μ_p and μ_N retained their value over the entire range of fields of interest, but since they are smooth curves, not straight lines, then the average values should be employed:

$$\frac{\phi_o}{\pi/2-\phi_o}>\frac{|\bar{\mu}_N|}{\bar{\mu}_p} \qquad (3.24)$$

These are examined numerically for GaAs and InP in Section 4.2.

3.5. TRANSIENT HEATING CALCULATIONS

3.5.1. Theory

The temperature of the bar samples of semiconductor mounted in the waveguide may rise during the pulses of power and may not cool to ambient in the period of no incident power, hence a temperature distribution may be set up. The temperature was calculated using the following method. Radiative and convective losses were assumed negligible, a fact which will only serve to overestimate the temperature, since we want to know the maximum rise, this is a reasonable neglect. The bar was considered to be connected at its ends to infinite sinks at ambient temperature. The distribution will therefore be symmetric about the bar centre. The differential equations governing heating and cooling are respectively (101)

$$\frac{\partial^2 T(x,t)}{\partial x^2} - \frac{1}{k_D}\frac{\partial T(x,t)}{\partial t} = -\frac{g_o}{k_T}$$

$$\frac{\partial^2 T(x,t)}{\partial x^2} - \frac{1}{k_D}\frac{\partial T(x,t)}{\partial t} = 0$$

where g_o is the thermal generation rate and T is the temperature increment above ambient such that:

$$g_o = \frac{P_{absorbed}}{volume}, \quad T(x,t) = T_{actual}(x,t) - T_{amb}.$$

The time of heating is t_h and that of cooling t_c, these being in general

$$t_h = 200\ nS, \qquad 500\mu S \leq t_c - t_h \leq 2\,mS$$

The solutions to the differential equations are:

$$T(x,t_h) = \frac{g_o}{2k_t}\cdot x(l-x) - \left\{\frac{4g_o l^2}{\pi^3 k_t}\sum_{n=0}^{\infty}\frac{1}{(2n+1)^3}\cdot \sin(2n+1)\frac{\pi x}{l}\cdot \exp\left\{-\frac{k_d(2n+1)^2\pi^2 t_h}{l^2}\right\}\right\}$$

and

$$T(x,t_c+t_h) = \frac{2}{\ell}\sum_{n=1}^{\infty} \sin\frac{n\pi x}{\ell}\cdot \exp\left\{-\frac{k_d n^2\pi^2 t_c}{\ell^2}\right\}\int_0^{\ell} T(x,t_h)\cdot \sin\frac{\pi x}{\ell}\, dx$$

where $T(x,t_c+t_h)$ is the temperature distribution after one complete period of heating and cooling. This temperature distribution is assumed not to affect the next heating pulse, such that the temperature at the end of this will be:

$$T(x,t_c+2t_h) = T(x,t_c+t_h) + T(x,t_h)$$

This will also slightly overestimate the temperature, but this should not be serious since indium phosphide is a poor thermal conductor.

After a number of periods equilibrium will be reached such that the temperature oscillates between two values differing by the heating increment. The final maximum centre temperature will be:

$$T(\ell/2,\infty) + T_{amb} + T(\ell/2,\ (n+1)t_h+nt_c)$$

where equilibrium is reached after n cycles.

3.5.2. Results

A programme was written to evaluate the problem, the distribution being specified by Gauss Legendre Quadrature using 24 points (see Appendix 3). The final distribution was found to be nearly parabolic and is shown in Fig. 3D.

The centre of bar temperature was plotted for various power and duty cycle values, these are shown in Fig. 3E. The time taken to reach equilibrium was found to be approximately 200 mS in each case. The maximum absorbtion of power would produce up to +250°K increase in a small sample, but in most cases the centre temperature rise was much less than this, being of the order of 30-50°K. The thermal

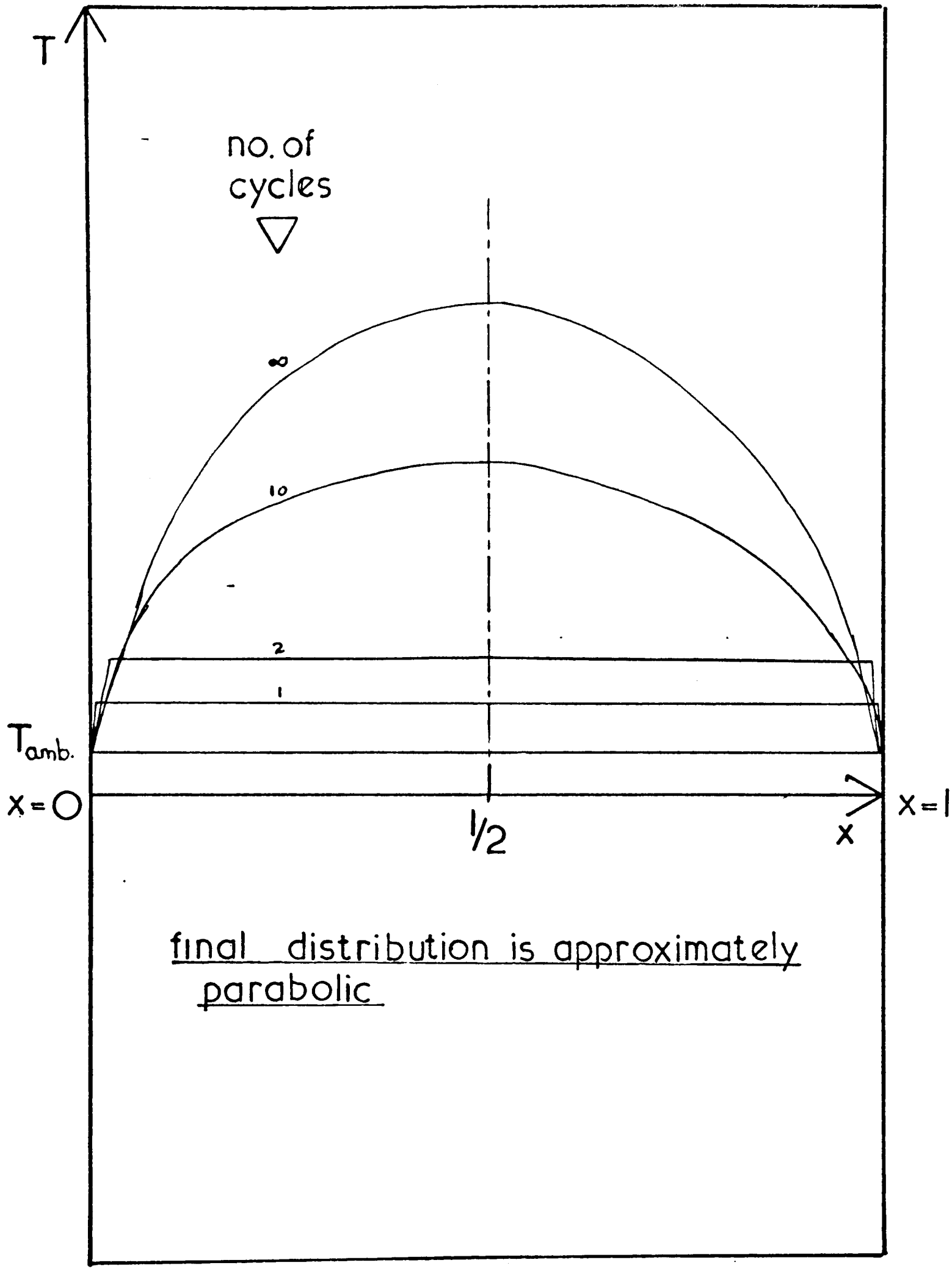

FIG. 3D

Temperature profile of semiconducter bar heated by pulsed microwaves.

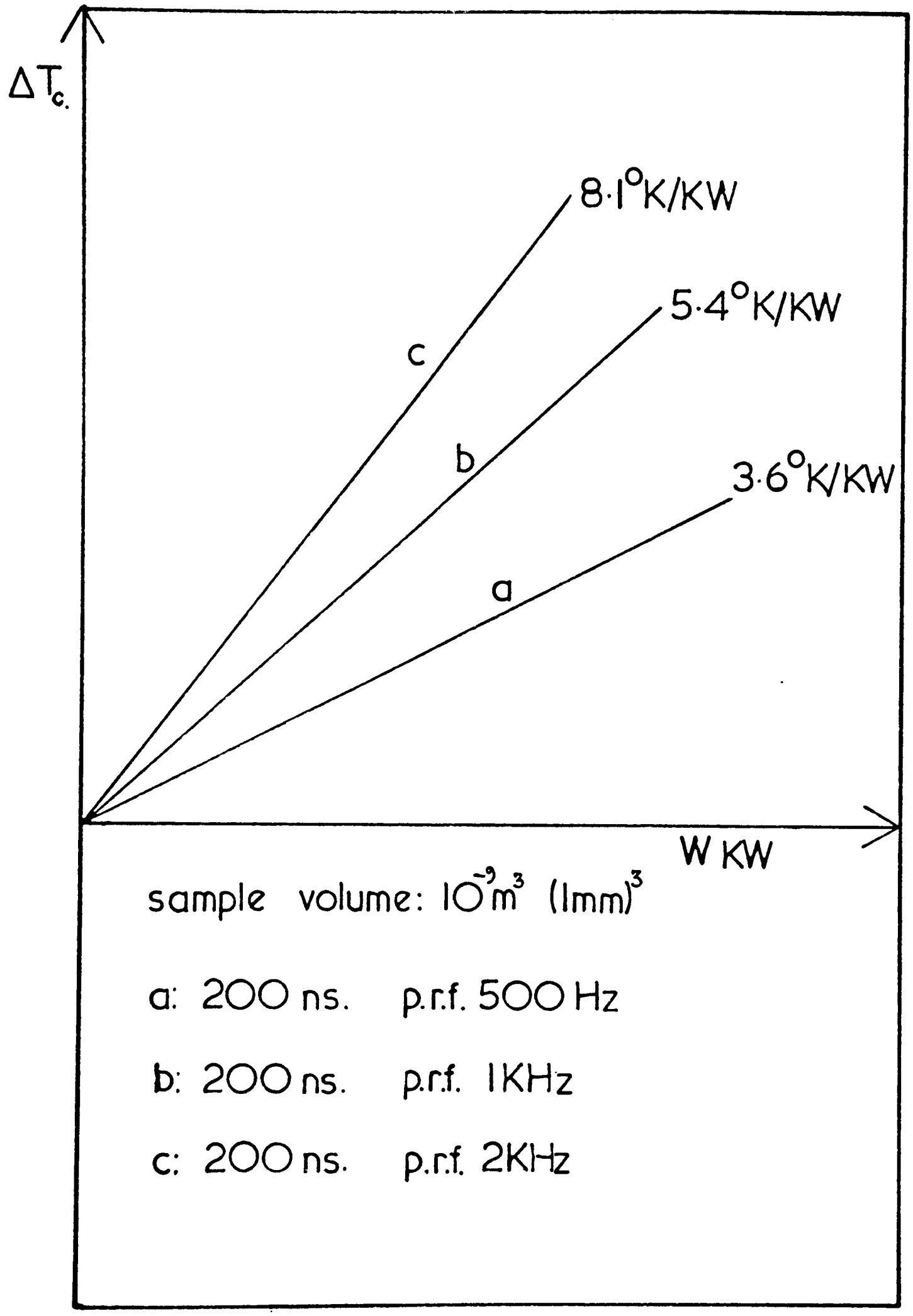

FIG. 3E

Bar-centre temperature rise vs. power and pulse duty cycle.

properties, C_p, k_T, k_D were fairly constant over this range, certainly not in error to merit a further recalculation or correction of the results.

The d.c. current should also be small to minimise heating. Using the steady state solution for CW operation:

$$T(x,\infty) = \frac{g_o}{2k_T} x(1-x)$$

For an indium phosphide bar mounted transversely in the waveguide we find that the centre temperature difference is:

$$\Delta T_c{}^{o}K = 0.316\ g_v, \qquad g_v\ W/cm^{-3}$$
$$\Delta T_c{}^{o}K = 0.89\ g_A, \qquad g_A\ W/cm^{-2}$$

where the generation rates are calculated per unit volume and per unit area taking into account the WG22 narrow dimension. For typical d.c. currents of less than 50μA this temperature rise was very small, being less than $1^{o}K$.

3.5.3. Carrier Concentration Variations

The temperature increase may affect the carrier concentration by two main mechanisms, ionisation of impurities and the movement of the conduction band edge. The former is not important above $300^{o}K$ since in the material supplied all impurities were ionised below this temperature, however at $77^{o}K$ there was some freeze out, so that this mechanism must be accounted for there. 9% in 2.4×10^{15} slice, 4½% in 7.2×10^{14} slice, broadly agreeing with data in Blood et al (20).

Movement of the band edge would affect the population by changes in the intrinsic concentration as follows:

$$N_i = \left(N_c N_v \exp - \frac{E_g}{KT}\right)^{1/2}$$

From the condition of charge neutrality and the intrinsic relation:

$$n_e + N_A = n_h + N_D, \quad n_e n_h = N_i^2$$

and considering an n-type material with $N_A = 0$, we find that:

$$n_e = \frac{N_D}{2}\left\{1 + \sqrt{1 + \frac{4N_i^2}{N_D^2}}\right\}$$

substitution for N_i into this, and the relations for N_c and N_v,

$$N_c = 2\left(2\pi m_e^* kT/\hbar^2\right)^{3/2}, \qquad N_v = 2\left(2\pi m_h^* kT/\hbar^2\right)^{3/2}.$$

yields:

$$n_e = \frac{N_D}{2}\left[1 + \left\{1 + \frac{2}{N_d^2}\left(\frac{4\pi kT}{h^2}\right)^3 \left(m_e^* . m_h^*\right)^{3/2} \exp\left\{\frac{-1}{kT}\left(\mathcal{E}_{go} - \frac{\partial \mathcal{E}_g . T}{\partial T}\right)\right\}\right\}^{1/2}\right] \tag{3.25}$$

If this value of n_e is calculated and compared to N_D there are two regions of interest to us. If $n_e \simeq N_D$ then the material is said to be saturated and the only carriers are electrons as far as our cases are concerned. Should $n_e > N_D$ then the material is behaving partially intrinsically and both types of carrier contribute to the conductivity. In this case both the electron and hole properties must be included in calculation or investigation of the velocity-field characteristic.

A computer programme was written to evaluate the effects and the results indicated that the material would be saturated at temperatures less than 550°K. Even for the largest temperature rises the semiconductor does not behave intrinsically.

For an experiment at 77°K however the freeze out effect would mean the possibility of a parabolic distribution with +10% increase over the ambient concentration at the centre. This would increase the population by $^2/_3$ of 10% and would decrease the measured peak to valley ratio by approximately 10% according to the figures of Glover - see Fig. 3B.

3.6. EXPERIMENTAL APPARATUS

3.6.1. Description

This is shown in Figure 3F in block diagram form. The magnetron operates close to 35 GHz, it is driven by a modulator and is capable of producing 200 nS pulses at pulse repetition frequencies between 500 and 2000 per second. The output of the magnetron is fed via a four-port circulator, to protect the valve, to the main waveguide run. The output power is monitored via a 44 dB cross coupler feeding a thermistor and a power meter.

The sample holder is inserted in the main section, which is terminated in a high-power load. Two 40 dB directional couplers sample the power before and after the test section and form the basis for the bridge circuit. Here the powers are combined via the isolators and hybrid-tee junction to a crystal detector, the output of which is monitored via a sampling oscilloscope. The attenuator and phase shifter A are used to establish convenient zero data, the rotary vane attenuator and phase shifter B are used to measure the power absorbed by production of a null crystal output.

The first 40 dB directional coupler and the 12 dB coupler form the basis for comparison of incident and reflected powers in the main run. The switch S is used to consign power from either forward or reverse directions to the calibrated attenuator C. This is used to maintain a constant level on the second crystal detector, hence relative power levels being easily obtained without calibration of the crystal.

Both the detecting crystals and also the d.c. bias circuit, which will be described in Chapter 5, are monitored by a sampling oscilloscope (Tektronix 533 or 564).

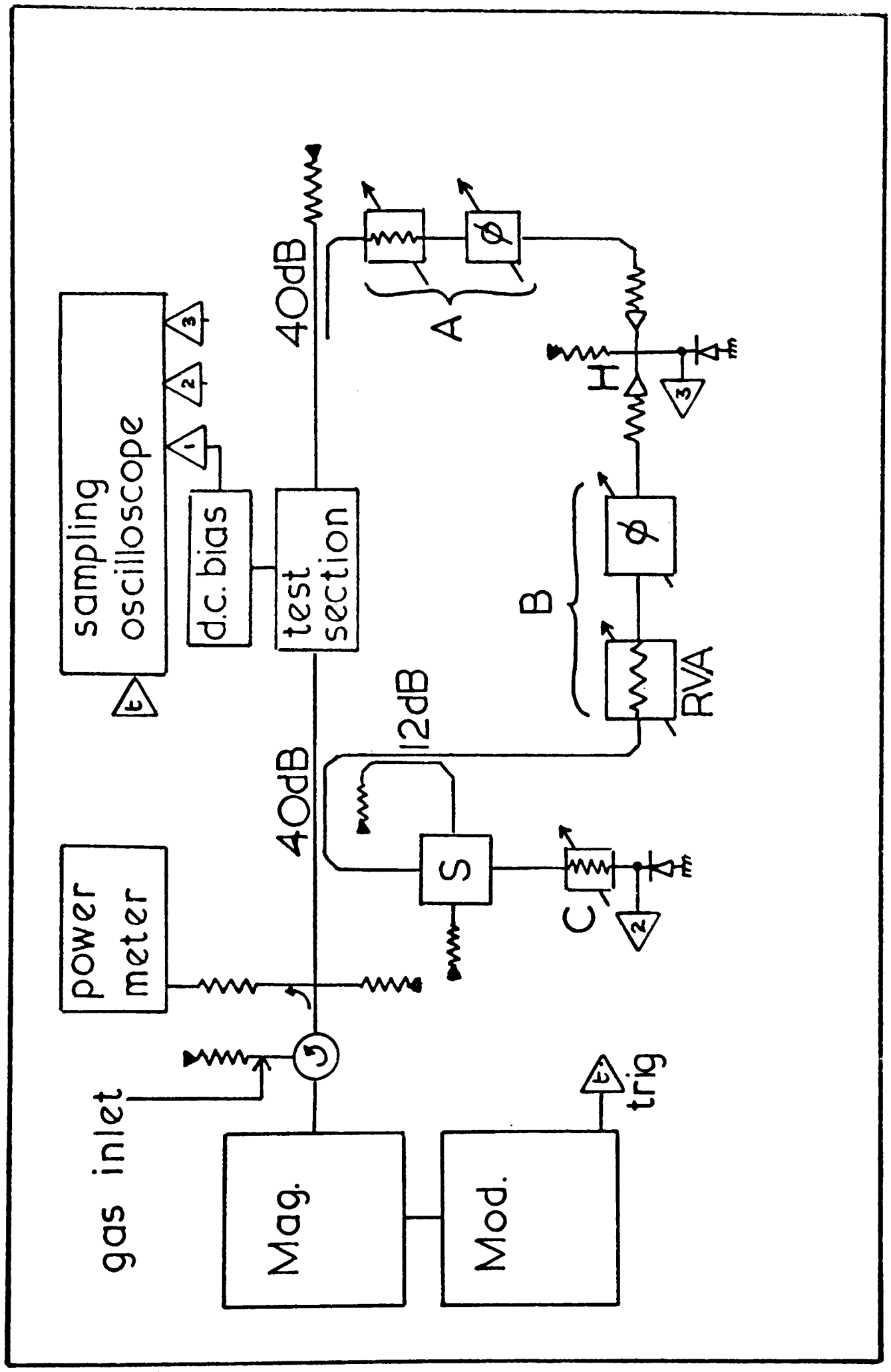

FIG. 3F

The experimental apparatus .

The main waveguide run may be pressurised via an inlet near the circulator. For very high powers sulphur hexafluoride was pumped into the guide up to two atmospheres pressure. It has improved dielectric breakdown characteristics compared to air (102) see Fig. 3G. For low temperature experiments helium was employed, but due to its poorer dielectric performance (103) compared to air, the power levels were limited.

3.6.2. Calibration

Various tests were made to establish the performance of the system. Errors in power monitoring, pulse shape and duty cycle, guide wavelength and frequency variations were measured.

The correlation between power monitored on the meter using the thermistor, and that calculated from pulse shape, duty cycle etc. were found to agree to $\pm$ 2%, the main error being rise time and fall time of pulses. Typical pulse shapes are shown in Fig. 3H, together with a null obtained showing the effect of chirp in the edges of the pulse.

The guide wavelength and frequency were measured for various power levels using a VSWR carriage and a cavity wavemeter. The results are shown in Figure 3J. There was a variation of wavelength with power amounting to $\pm$ 0.9% the salient values being:

	$P_{I(av)}$	λ_g	λ_o	F_{calc}	$F_{W/m}$
	2W	10.96 mm	8.66 mm	34.65 GHz	34.68 GHz
	10W	10.76 mm	8.50 mm	35.30 GHz	35.30 GHz
mean		10.83 mm	8.59 mm	34.90 GHz	34.85 GHz

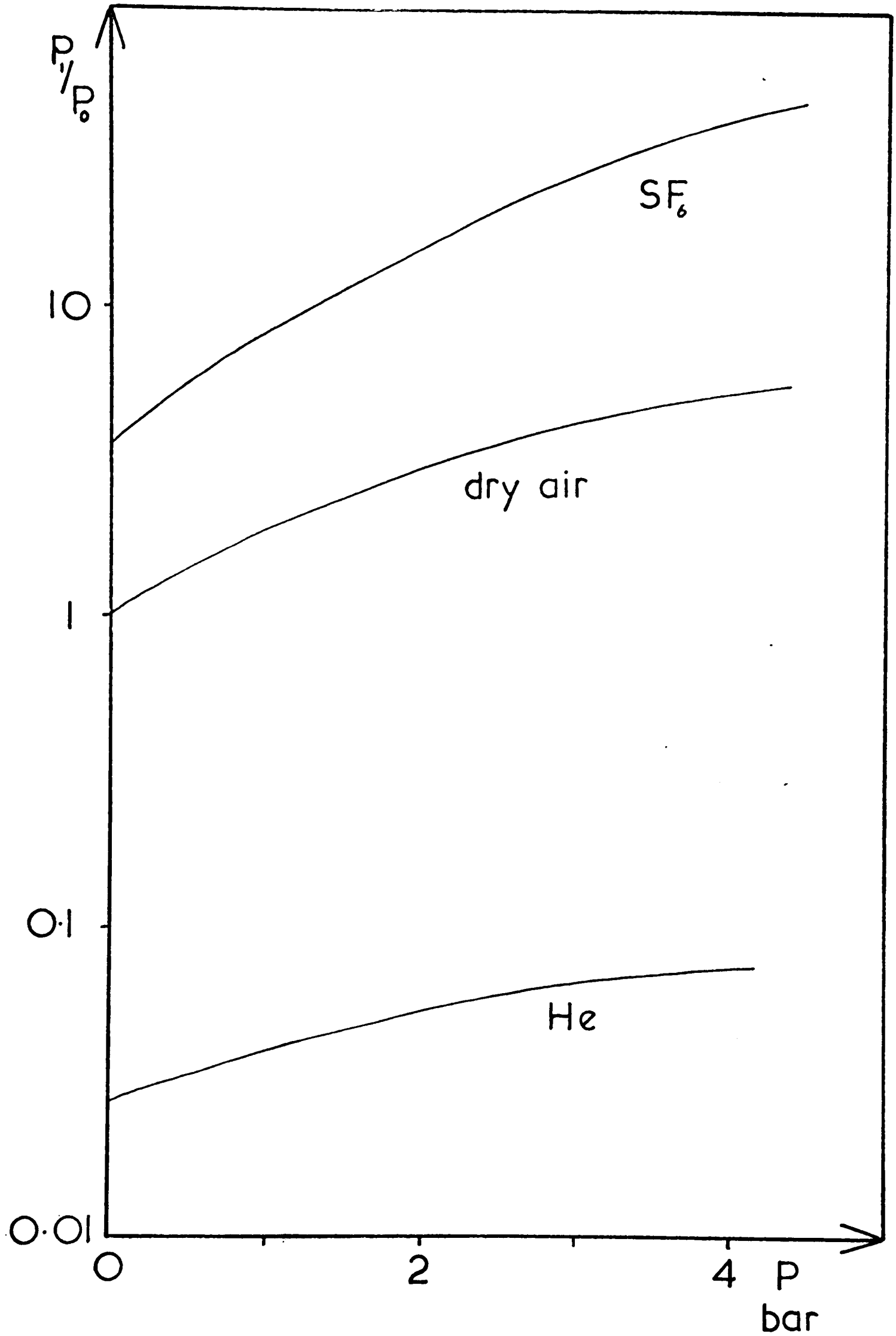

FIG. 3G

Gas breakdown fields.

relative to air at 1 bar.

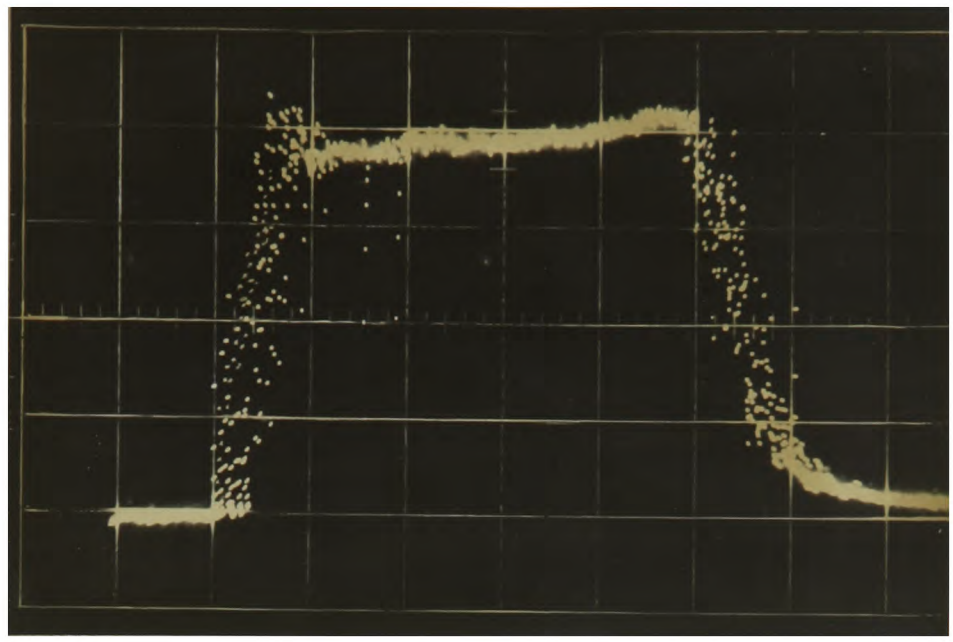

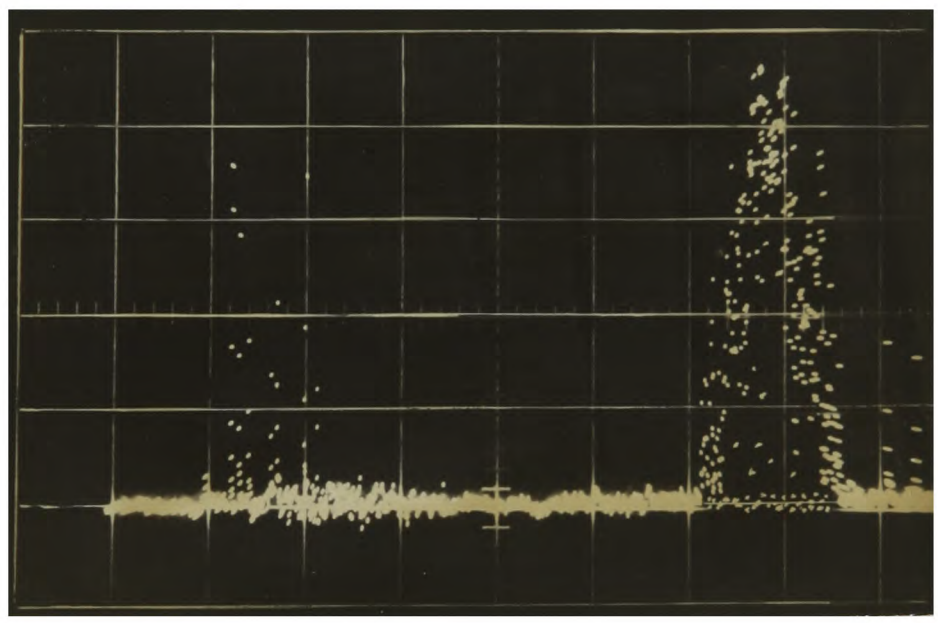

horiz: time - 50nS/cm.

vert: xtal 2. r.f. mon. - 10mV/cm (W_i 24kW)

xtal 3. null - 2mV/cm

FIG. 3H

Magnetron performance -

(i). r.f. pulse shape. (ii). chirp effects on null.

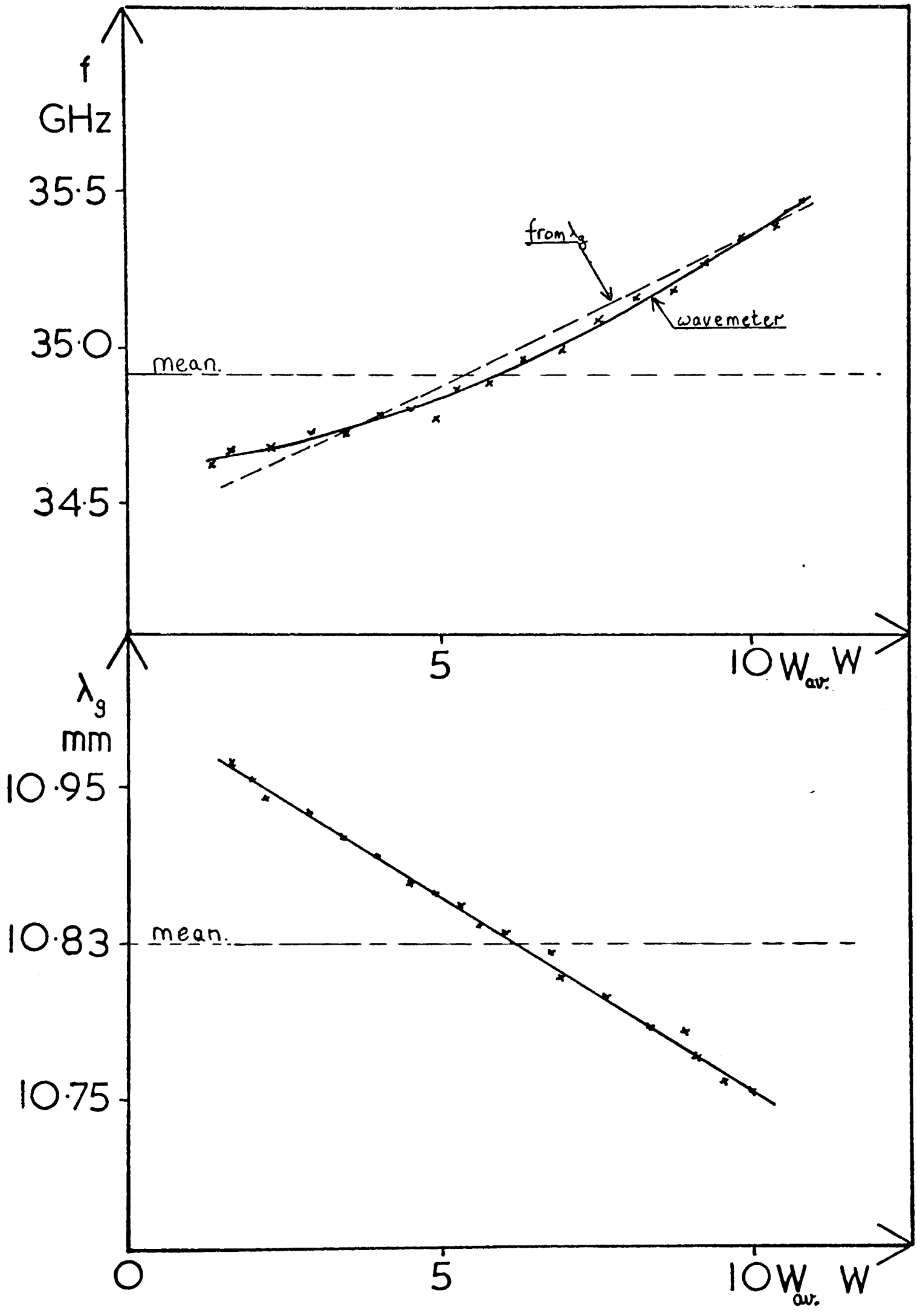

FIG. 3J

Magnetron performance -

(i). frequency (ii). guide wavelength.

The correlation between calculated and measured frequency was better than $\pm$ 0.4%.

Knight (104) tested the harmonic generation of this magnetron and found the harmonic powers to be as shown below. I checked that the measurable harmonic power of the first and above was less than -60 dB approximately.

n	harmonic power dB
2	-58
3	-77
4	-86
5	-89
6	$>$ -97

The assumptions concerning harmonic content are clearly justified $h_2 \ll 1$, being $10^{-5.8}$ and $h_n = 0 \quad n \geqslant 3$ is obeyed since $h_n \leqslant 10^{-7.7} \quad n \geqslant 3$. The output is monochromatic as far as the experiment is concerned.

3.6.3. Estimation of Accuracy

For the experiment described in § 3.2 the results required for analysis are measurements of the d.c. conductivity and power absorbtion of the post. The former will be described in § 5 and the latter outlined here.

The average power monitored on the power meter is multiplied by the duty cycle, calculated from pulse shape, length and repetition frequency, to obtain the pulse power. This can be checked against relative readings using the calibrated attenuator (2) and the crystal detector. Measurements of forward and reverse fractions of power are calculated from this as well. The transmitted power can be monitored and compared to the incident power at the post using the rotary vane attenuator and hence the absorbed fraction calculated.

The error in calculating the incident power derives from errors

in reading the meters and scales and combining these should be 2% or less, as long as the correlation between power meter readings and pulse power monitor is good over the experimental range. The transmitted fraction may be estimated to approximately 4% due to the datum fluctuation over the frequency range inherent in the variation of power during the experiment. Efforts to allow for this effect may improve the accuracy of the calculation by approximately 2%.

Hence for mid power measurements with neither reflected, nor absorbed fractions of the power less than 10% of the incident level the calculation of absorbed power can be made to within 5% accuracy.

Chapter four.

Computer simulation and analysis.

4.1. EXPERIMENTAL SIMULATION

4.1.1. Programme Description

The equations derived in Section 3.2.1. leading to

$$\bar{\sigma}(E_o) = \frac{2}{\pi}\int_0^{\pi/2} J'(E_o \sin\phi).\, d\phi \qquad (3.8)$$

were derived with certain assumptions. These were checked using the computer (ICL1906A) to examine an 'ideal' velocity-field characteristic as follows:

$$v(E) = \mu_o E. \qquad E \leqslant E_T$$

$$v(E) = \left(1-\frac{1}{r}\right)\mu_o E_T . \exp-\left(a_e(E-E_T)\right) + \frac{1}{r}\cdot \mu_o E_T \qquad E \geqslant E_T$$

$$E_T = 10 kV.cm^{-1}\ ,\ \mu_o = 3.10^3\ cm^2.V^{-1}.s^{-1}\ ,\ r = 2{\cdot}5\ ,\ a_e = 5{\cdot}6\,10^{-5}\ cm.V^{-1}$$

This gives a peak velocity of 3×10^7 cms^{-1} at 10 $kV.cm^{-1}$ and a valley velocity of 1.2×10^7 cms^{-1} at high fields, the negative differential mobility is -1000 $cm^2.V^{-1}.s^{-1}$ just after threshold. This compared well to the data published when the simulation was made in 1972; the particular differences being no velocity sublinearity below threshold and a singularity at threshold where the first derivative is infinite. The doping level of the 'ideal' sample was taken as $10^{15}.cm^{-3}$ giving:

$$\sigma_o = 0.48\ \mho\, cm^{-1} \qquad \rho_o = 2.2\ \ \Omega cm$$

assumed uniform within the samples. These values obey the of space-charge control criteria and the affects of non-obeyance are ignored in the results.

Calculations were performed to investigate the accuracy of the Taylor's series approximation and the numerical neglect of higher terms. The effect of d.c. and harmonic terms was programmed. The calculations were continued to include the numerical significance of the terms in the approximation of eq. (3.10).

4.1.2. Results

The current as an instantaneous function of time is shown at Fig. 4A for typical field quantities. The effect of the threshold field is clear, producing a reduction in current flow although the voltage is increased, and the d.c. bias current produces a perturbation from the zero d.c. condition.

The integral of this curve was performed numerically using a 401-step Simpson Rule and compared with the value from the Taylor series:

$$\bar{J}(E_0 E_1 h_2) = \frac{1}{2\pi}\int_0^{2\pi} J\,d\phi + \frac{E_1}{2\pi}\int_0^{2\pi} J'\,d\phi + \frac{h_2 E_0}{2\pi}\int_0^{2\pi} J'\sin 2\phi\,d\phi +$$
$$+ \frac{E_1^2}{4\pi}\int_0^{2\pi} J''\,d\phi + \frac{h_2 E_1 E_0}{2\pi}\int_0^{2\pi} J''\sin 2\phi\,d\phi + \frac{h_2^2 E_1^2}{4\pi}\int_0^{2\pi} J''\sin^2 2\phi\,d\phi .$$

which we may write as

$$\bar{J} = J_1 + J_2 + J_3 + J_4 + J_5 + J_6$$

These results are shown in Fig. 4C, and the typical $\bar{J}/J_0$ in Fig. 4B. The error is less than 1% providing the d.c. to r.f. ratio is 10^{-3} or less. This is perfectly feasible. The harmonic term was 10^{-6}, comparing with the experimental value. The effect of inserting a 1% harmonic ($h_2 = 10^{-2}$) is to increase the error by at least an order of magnitude for a given d.c. to r.f. ratio.

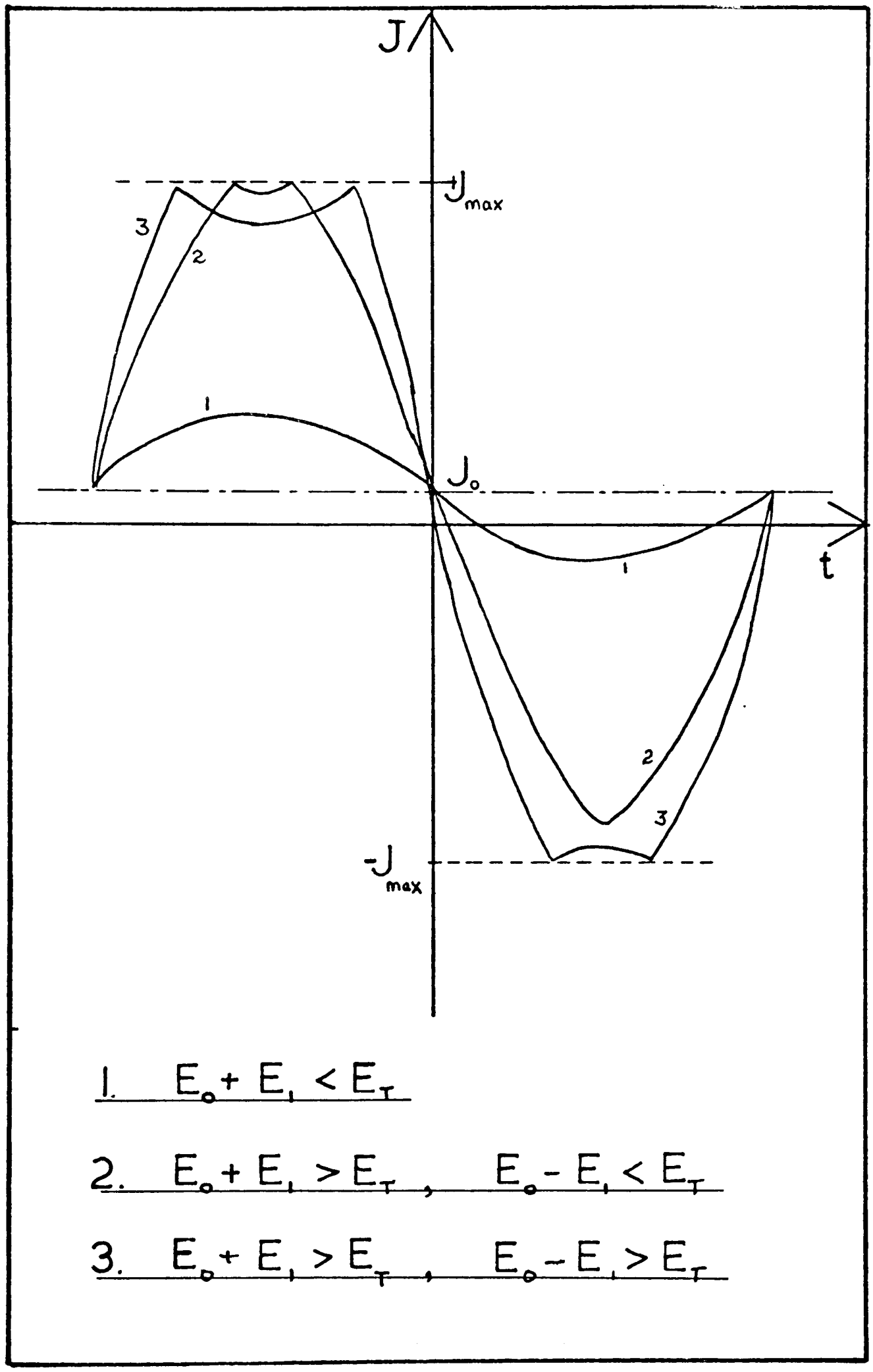

FIG. 4A

Instantaneous current –

typical computer results.

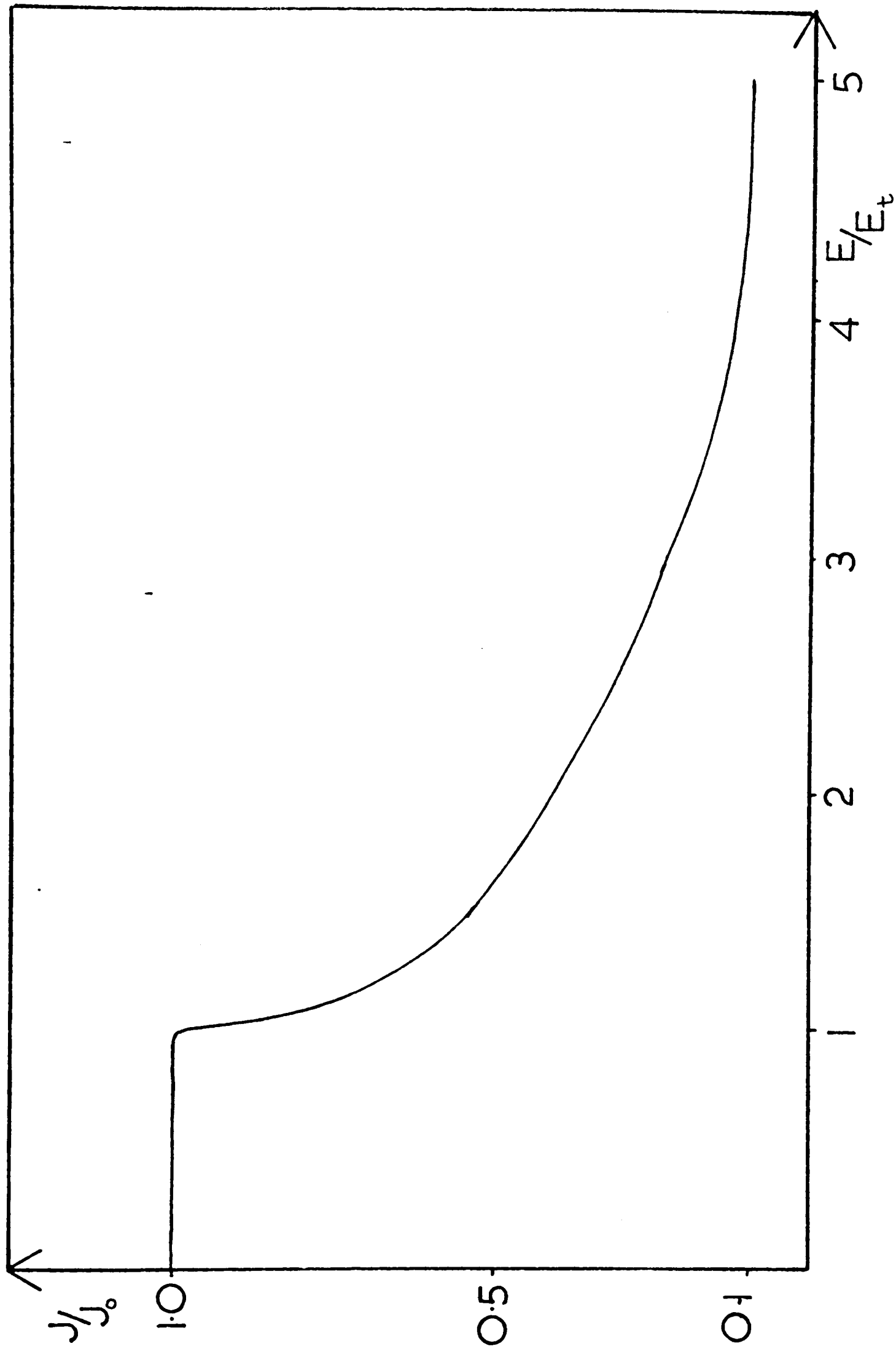

FIG. 4B

Average current –

typical computer results.

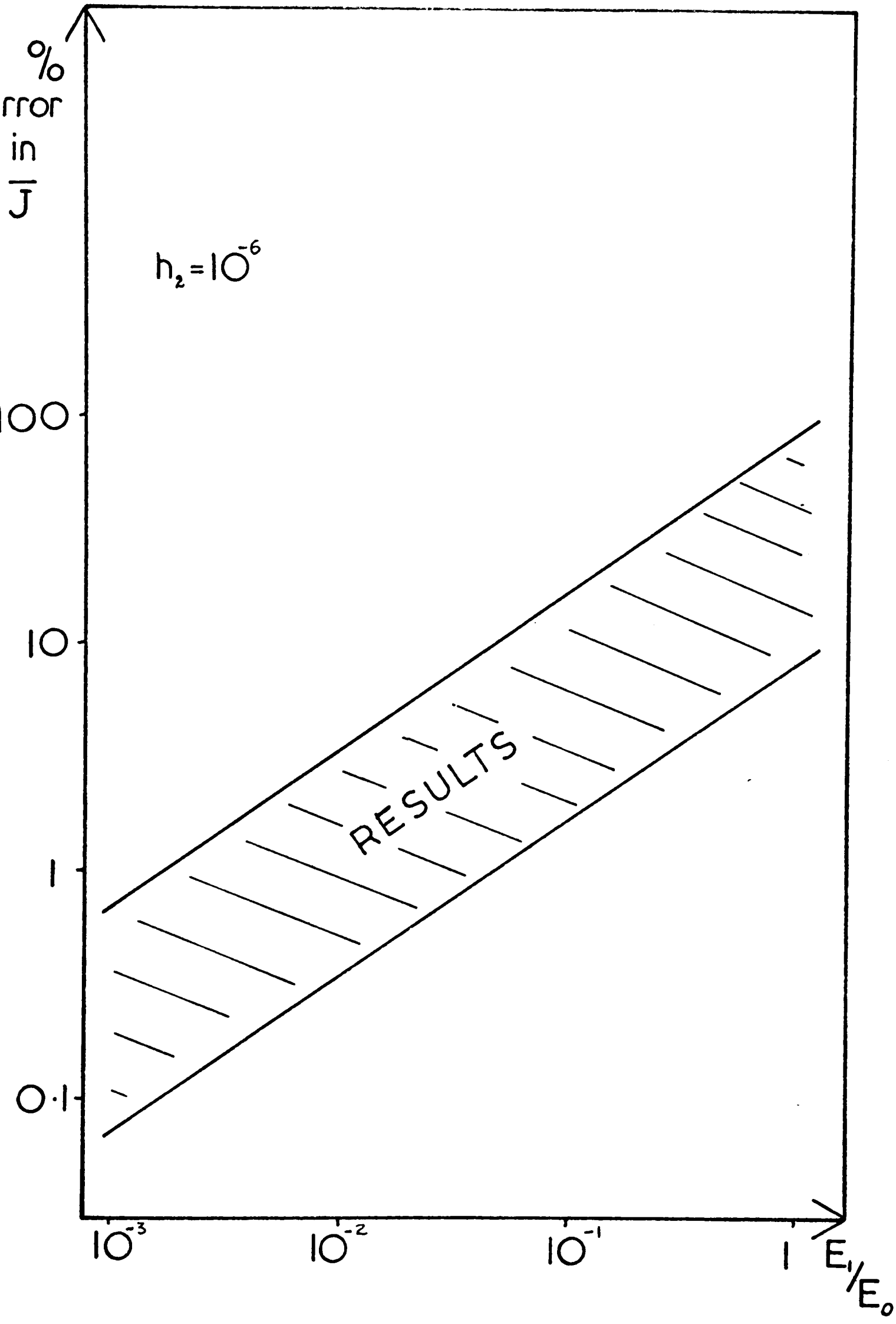

FIG. 4C

Taylor series expansion –

error vs. d.c. and r.f. field values.

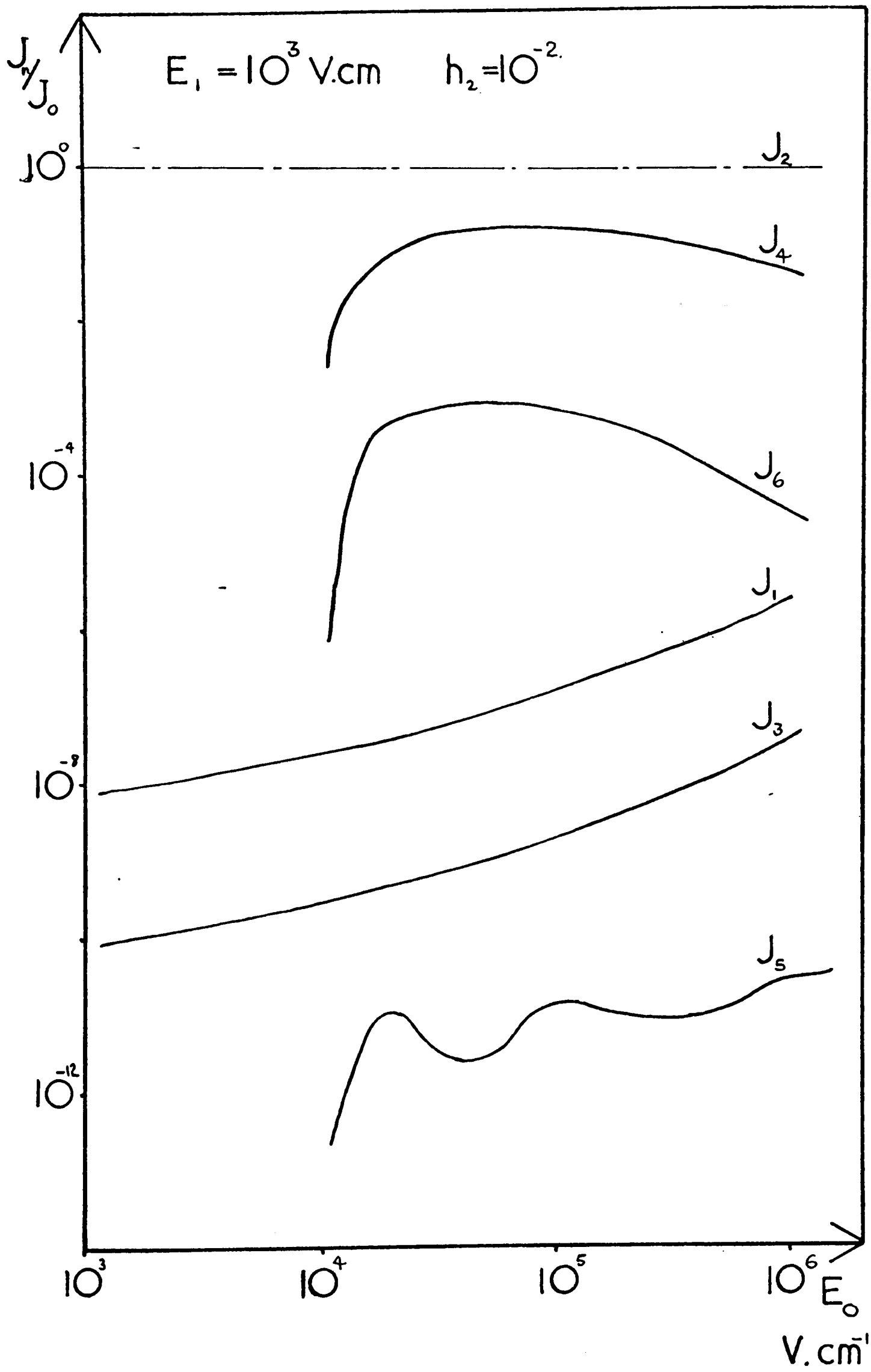

FIG. 4D

Taylor series expansion -

relative magnitude of terms.

The comparison of the magnitudes of the terms in the Taylor series approximation is shown in Fig. 4D, there the second (and largest) term is used as a basis and the others expressed as fractions of it.

The calculation was performed for a high value of $E_1 (10^3$ V/cm) and a large harmonic (1%). The only salient terms (apart from J_2) are J_4 and J_6, which may contribute up to 10% and 1% respectively . However with a smaller harmonic term $h_2 = 10^{-6}$, J_6 drops by 8 orders and may be neglected. The d.c. to r.f. ratio is high for $E_o \leqslant 10^5$ V.cm^{-1} compared to our criterion of 10^{-3}, if this is obeyed then the fraction J_4/J_2 goes down to 1% at its maximum, which compares to our previous criterion.

The calculation was continued to check the numerial approximation in (3.10) which is justified.

The data $\bar{J}/J_o$ was used to provide an input for the programmes written to analyse the experimental data.

4.2. EXPERIMENTAL ANALYSIS

4.2.1. Programme Description

The equation (3.11) requires solution by an iterative technique:

$$\frac{dW_a(E_o)}{dE_o} = \frac{W_a(E_o)}{E_o} + \frac{1}{2} V.E_o \bar{\sigma}(E_o) \qquad (3.11)$$

with the initial condition

$$W_a(E_o)_{E_o \to o} = \frac{1}{2} V \sigma_o E_o^2$$

The equation integrates via

$$\frac{E_o\, dW_a(E_o) - W_a(E_o)\, dE_o}{E_o^2} = \frac{1}{2}\, V.\bar{\sigma}(E_o).\, dE_o$$

and:

$$\frac{d}{dE_o}\left(\frac{W_a(E_o)}{E_o}\right) = \frac{1}{2}\, V.\bar{\sigma}(E_o).\, dE_o$$

to:

$$\frac{W_a(E_o)}{E_o} = \frac{V}{2}\int_o^{E_o} \bar{\sigma}(E_o).\, dE_o$$

We have measured W_a and $\bar{\sigma}$ so we specify a scheme such that

$$\left(\frac{W_a}{E_o}\right)^{i+1} = \frac{V}{2}\int_o^{E_o} \bar{\sigma}\left[E_o.\left(\frac{W_a}{E_o}\right)^{i}\right].\, dE_o$$

where i, i+1 are degrees of iteration, writing $y = \frac{W_a}{E_o}$, and $x = E_o$

we have:

$$y^{i+1} = \frac{V}{2}\int_o^{x} \bar{\sigma}(x.y^i)\, dx \qquad (4.1)$$

with a halting criterion, refer to Appendix 6.

$$|y^{i+1} - y^i| < \text{error}$$

This enables us to calculate $W_a(E_o)$ or $E_o(W_a)$ and hence transform $\bar{\sigma}(E_o)$ or $\bar{\sigma}(w_a)$.

Then integration of the solution to the equation for $\bar{\sigma}$ was performed:

$$J(E_o) = \int_o^{\pi/2} \bar{\sigma}(E_o \sin\phi).\, E_o \sin\phi.\, d\phi. \qquad (3.9)$$

This being performed by a 401 step Simpson rule. The system of programmes starting with v(E) to produce J(t) and hence $\bar{J}/J_o$, and W_a gave data to input to these programmes required for experimental analysis, thus providing a test of their accuracy.

4.2.2. Results from Theoretical Curves

Typical results for the recovery of the velocity-field characteristic are shown at Fig. 4E . Using good and sufficient data for the range chosen the recovery was good save that the singularity at threshold causes overshoot, which is inherited throughout the portion above threshold. Should the data be bad then errors show as in the second curve in 4E; $\pm$ 10% errors being inserted where shown. If the range is too large for the available data, there is a sharp increase of velocity above where the last data point fits.

The experimental analysis programmes could work to approximately 1% accuracy with ease without demanding enormous quantities of data. The solution of Schlömilch's equation and the Tschebychev approximation gave velocity field characteristics within 1% of each other using this 'ideal' data. The space-charge criterion was programmed as in eq. (3.22) after the Tschebychev coefficients had been rearranged to the power series, this was found to be satisfactorily obeyed for the ideal case.

4.2.3. Space-Charge Suppression Calculations

As mentioned previously, the simple 'no growth' criterion was checked for the 'ideal' case and found to be satisfactory. However the condition for no growth over many cycles was checked for both

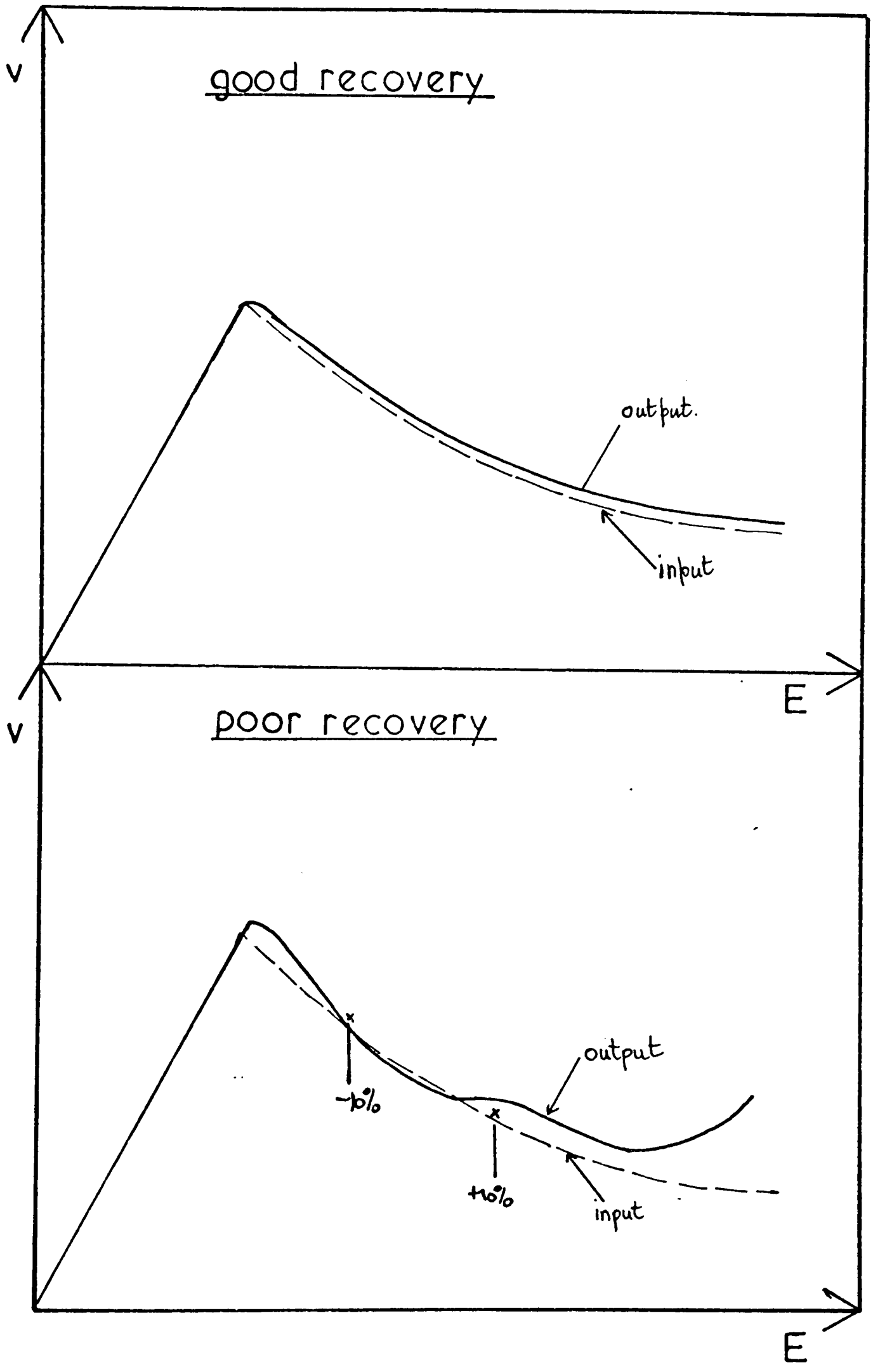

FIG. 4E

v(E) characteristic

typical computer data recovery.

gallium arsenide and indium phosphide. The former was included since it was intended to check the experimental system with this known material.

The equation derived for space-charge suppression was:

$$\frac{\phi_o}{\pi/2 - \phi_o} > \frac{|\bar{\mu}_N|}{|\bar{\mu}_P|} \qquad (3.24)$$

where $\bar{\mu}_N$ and $\bar{\mu}_P$ were the average negative and positive mobilities, and ϕ_o is $\sin^{-1}(E_T/E_{MAX})$, i.e. the instant at which threshold is reached, described as an angle.

For gallium arsenide μ_P = 7000 cm^2/vs, $|\mu_N|$ = 2000 cm^2/vs maximum, and the threshold-field is approximately 4 kV/cm. Taking a typical r.f. field of 20 kV/cm maximum the calculation in (3.24) yields

$$\frac{\phi_o}{\pi/2 - \phi_o} = 0.147 \qquad \frac{|\bar{\mu}_N|}{|\bar{\mu}_P|} = 0.4$$

which clearly contravenes the inequality, but if average mobilities are used, then $|\bar{\mu}_N| \simeq 800$ $|\bar{\mu}_P| \simeq 6{,}300$ $cm^2 v^{-1} s^{-1}$.

hence $$\frac{|\bar{\mu}_N|}{|\bar{\mu}_P|} = 0.127$$

this satisfies the inequality being, in any case, the more realistic approach.

Using the 'ideal' curve for indium phosphide calculation of ϕ_o and $|\bar{\mu}_N|$ were made from this for various values of E_o. The result is shown in Figure 4F, where the curves $\phi_o/\pi/2-\phi_o$ and $|\bar{\mu}_N|/|\bar{\mu}_P|$ are compared.

From this it is apparent that for fields less than 50 kV/cm the sample spends sufficient time in the subthreshold, positive mobility part of the characteristic to allow space-charge formation to decay away without any serious growth effect. However for fields in excess of 50 kV/cm this is not so and space charge growth may take place,

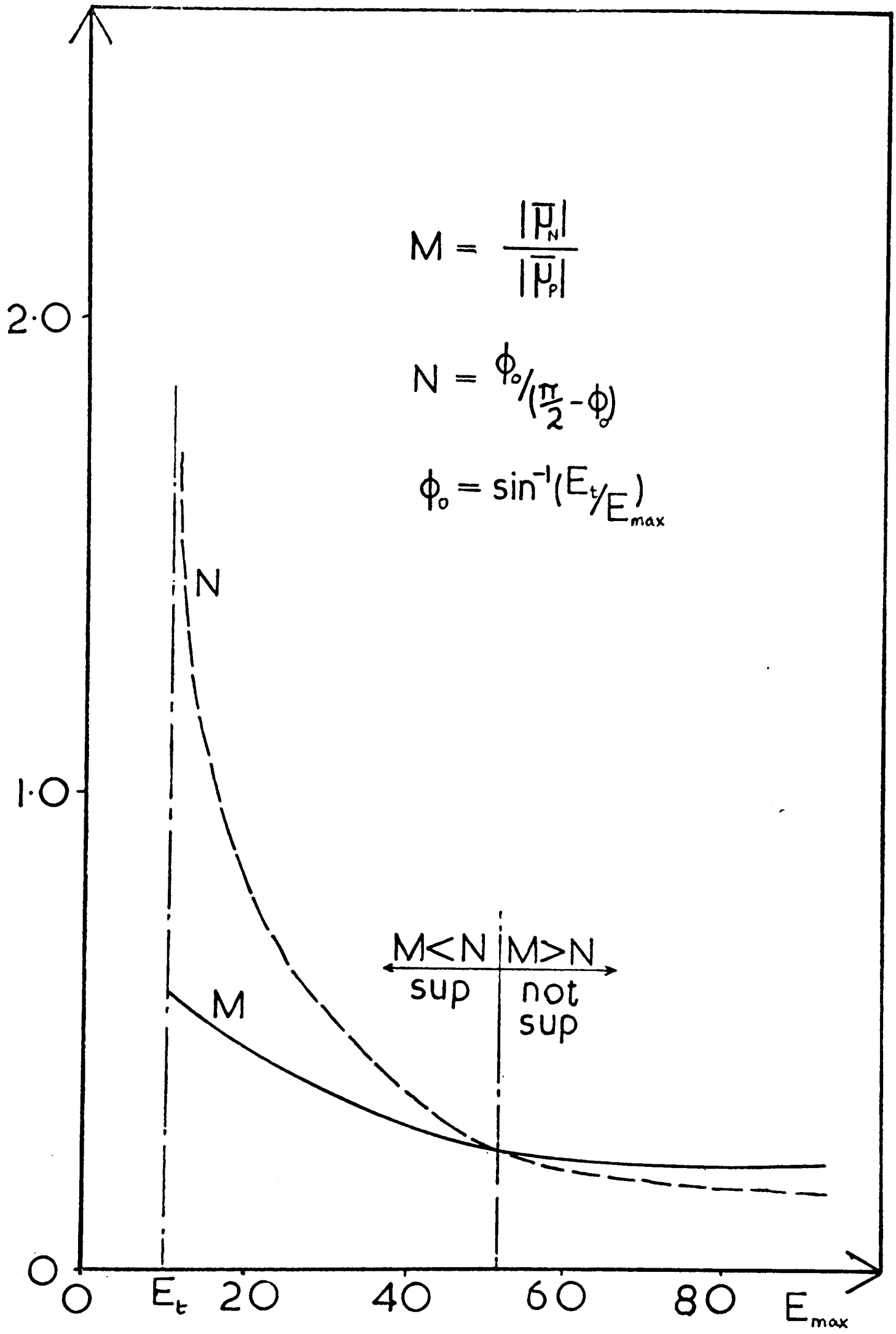

FIG. 4F

Indium phosphide –

theoretical space-charge suppression criterion.

hence distorting the results.

At 77°K the mobility of indium phosphide is a factor of ten larger than at 300°K at low fields, however after calculation based on the experimental, and predicted, results the criterion is almost identical to that at room temperature, and fields in excess of 50 kV/cm should be avoided.

4.3. MICROWAVE INTERACTION WITH SEMICONDUCTOR POSTS

4.3.1. Theory for Uniform Posts

This has been examined by Marcuvitz (92) who used a variational technique (see Appendix 4), to calculate the equivalent network impedances for a solid, isotropic, dielectric post, mounted inductively in the waveguide, the arrangement and equivalent circuit is shown in Fig. 4G. The expressions he derives are for a circular post, but using the functional relation between the diameter of the circular post (d_o) and the dimensions of a rectangular post (d_1,d_2) stated by Marcuvitz in his calculations (Fig. 4H) in the cases of conducting inductive posts and the experimental evidence of Holmes et al (93) regarding the equivalence of square and circular posts we may obtain reliable estimates of the properties of rectangular posts.

Marcuvitz uses a T-equivalent circuit and derives expressions for the network elements as follows:

$$\frac{2Z_a+Z_b}{Z_g} = \frac{-ja}{\lambda_g}\left\{\frac{2}{\hat{\epsilon}_r-1}\left(\frac{\lambda_o}{\pi d_o}\right)^2 - S_o - \frac{(\hat{\epsilon}_r-3)}{4(\hat{\epsilon}_r-1)}\right\} \quad (4.2.)$$

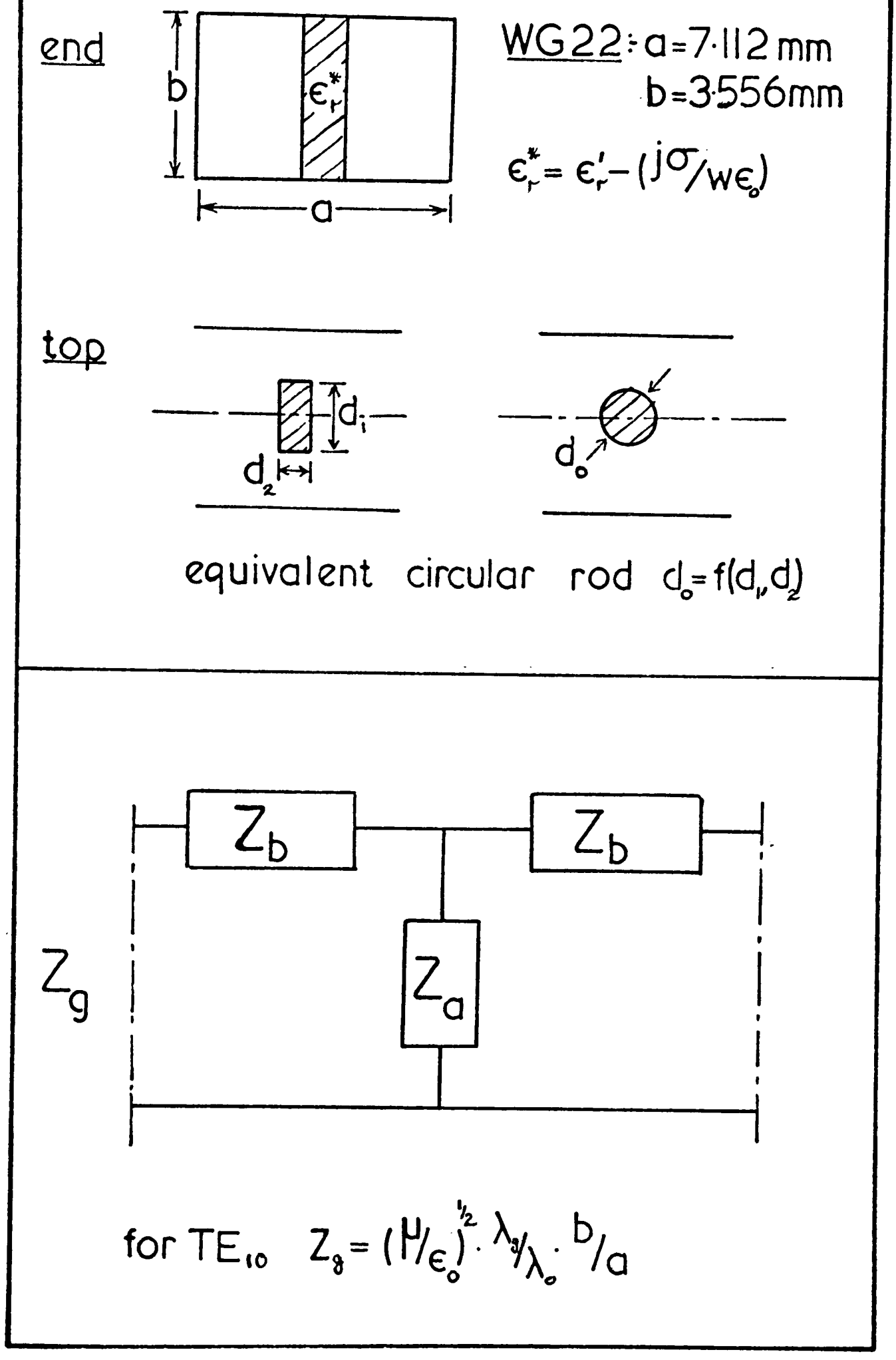

FIG. 4G

Dielectric post in waveguide-

(i). physical (ii) equivalent network.

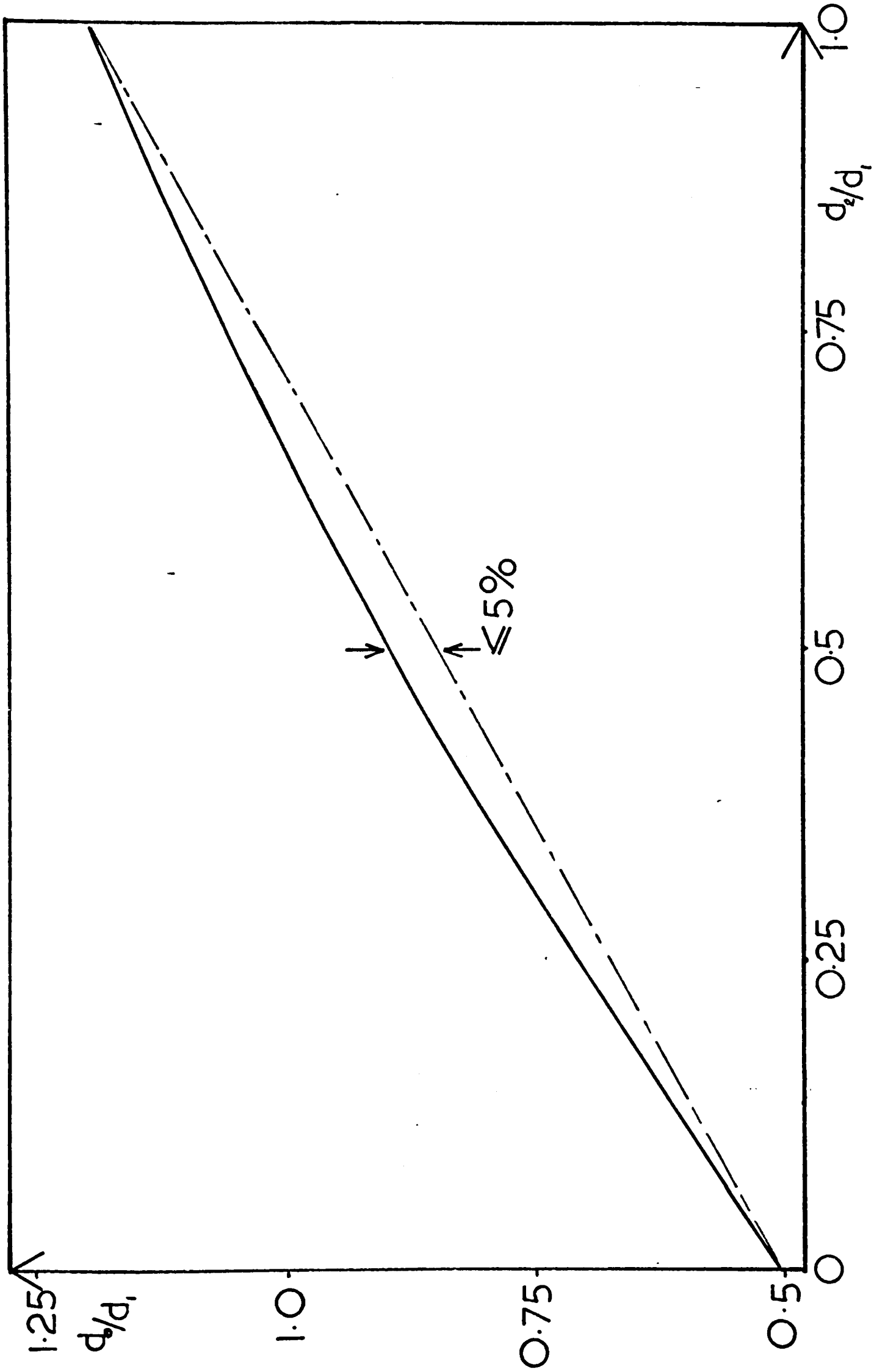

FIG. 4H

Inductive obstacles -

equivalent circular and rectangular dims.

$$\frac{Zb}{Zg} = \frac{j a}{8\lambda_g}\left(\frac{\pi d_o}{\lambda_o}\right)^2\left(\frac{\pi d_o}{a}\right)^2(\hat{\epsilon}_r - 1)\left\{1 + \left(\frac{\hat{\epsilon}_r - 2}{6}\right)\left(\frac{\pi d_o}{\lambda_o}\right)^2\right\} \qquad (4.3)$$

where $$\hat{\epsilon}_r = \epsilon_r - \frac{j\sigma}{\omega \epsilon_o}$$

and $$S_o = \ln\left(\frac{4a}{\pi d_o}\right) - 2 + 2\sum_{n=2}^{\infty} \frac{n - \left(n^2 - (2a/\lambda_o)^2\right)^{1/2}}{n\left(n^2 - (2a/\lambda_o)^2\right)^{1/2}}$$

These are applicable to better than 5% for a centrally mounted, dielectric post of circular diameter d_o, within the range $2a \geqslant \lambda_g \geqslant 2a/3$. This criterion is satisfied in the case under consideration since:

$$a = 7.112 \text{ mm}, \quad \lambda_g = 8.565 \text{ mm}$$

The effect of non-central positioning introduces multiplicative factors in the expressions (4.2) and (4.3) as follows:

$$\left(\frac{2Z_a + Z_b}{Z_g}\right)' = \operatorname{cosec}^2\frac{\pi x}{a}\cdot\left(\frac{2Z_a + Z_b}{Z_g}\right) \qquad (4.2a)$$

$$\left(\frac{Z_b}{Z_g}\right)' = \sin^2\frac{\pi x}{a}\left(\frac{Z_b}{Z_g}\right) \qquad (4.3a)$$

$$S_o' = \ln\left(\sin\frac{\pi x}{a}\frac{4_a}{\pi d}\right) - 2\sin^2\frac{\pi x}{a} + 2\sum_{n=2}^{\infty}\sin\frac{n\pi x}{a}\cdot f(n, a, \lambda_o)$$

where superscript **1** is the non-central value.

The numerical effect of this error in central positioning was calculated; for an error of 0.05a off centre the changes were

Z_a by +2.5%, Z_b by -2.5%

this, in our case, would be for an error in position of 0.356 mm, a value unlikely to be exceeded. Marcuvitz also places a restriction on dielectric constant for these expressions, 5% accuracy being maintained for

$$\sqrt{\epsilon_r} < 4$$

Since $\epsilon_r = 12.35$, this is satisfied.

The values of Za and Zb may be used to analyse the behaviour of the network from a scattering matrix approach as follows: (Ref. Appendix 5)

$$\begin{pmatrix} E_R \\ E_T \end{pmatrix} = \begin{pmatrix} S_{11} & S_{12} \\ S_{21} & S_{22} \end{pmatrix} \begin{pmatrix} E_I \\ 0 \end{pmatrix}$$

where E_I E_R and E_T are the incidents reflected and transmitted fields associated with the mode under consideration, which is fundamental rectangular TE_{10}. The Z matrix is written:

$$\begin{pmatrix} V_1 \\ V_2 \end{pmatrix} = \begin{pmatrix} Z_{11} & Z_{12} \\ Z_{21} & Z_{22} \end{pmatrix} \begin{pmatrix} i_1 \\ i_2 \end{pmatrix}$$

and from this definition, in this case we have

$$Z_{11} = Z_{22} = Za + Zb$$

$$Z_{12} = Z_{21} = Za$$

Using the relation between (S) and (Z) (appendix 5) we find:

$$S_{11} = S_{22} = \frac{(Z_{11}-Zg)(Z_{11}+Zg) - Z_{12}^2}{\Delta Z}$$

$$S_{21} = S_{12} = \frac{2Z_{12}Zg}{\Delta Z}$$

$$\Delta Z = (Z_{11}+Zg)^2 - Z_{12}^2$$

Solving this we find:

$$\frac{E_T}{E_I} = \frac{2Z\acute{a}'}{Z\acute{b}(2Z\acute{a}+Z\acute{b}') + 2(Z\acute{a}+Z\acute{b}') + 1}$$

$$\frac{E_R}{E_I} = \frac{Z\acute{b}(2Z\acute{a}+Z\acute{b}) - 1}{Z\acute{b}(2Z\acute{a}+Z\acute{b}) + 2(Z\acute{a}+Z\acute{b}) + 1}$$

The prime indicating normalisation to Zg. The power transmission and reflection coefficients γ_ω and Γ_ω are defined by:

$$\gamma_\omega = \left|\frac{E_T}{E_I}\right|^2 \qquad \Gamma_\omega = \left|\frac{E_R}{E_I}\right|^2$$

Hence these may be discovered via the latter two equations. The absorbed power may then be calculated via the expression:

$$W_a = W_I\left[1 - (\Gamma_\omega + \gamma_\omega)\right].$$

A programme was written to follow this analysis from the basic dimensions and data, via the network impedance values to the transmission and reflection coefficients and the absorbed power fraction. The term S_o is an oscillating series and some 10^5 terms were summed to obtain an accuracy of better than $\leqslant$ (0.1%), this being necessary to preserve the overall accuracy within the computer programme.

4.3.2. Results for Uniform Posts

Typical curves for the absorbed power fraction for various posts are shown in Fig. 4J. Post widths between 0.4 and 1.2 mm are used (note that the latter contravenes the maximum width criterion by 10%) and the general trends are clearly visible. As the conductivity increases from very small values, the absorbtion increases up to a maximum value of $\simeq$ 3dB. For conductivities higher than this then the post width dictates the secondary features due to resonant effects.

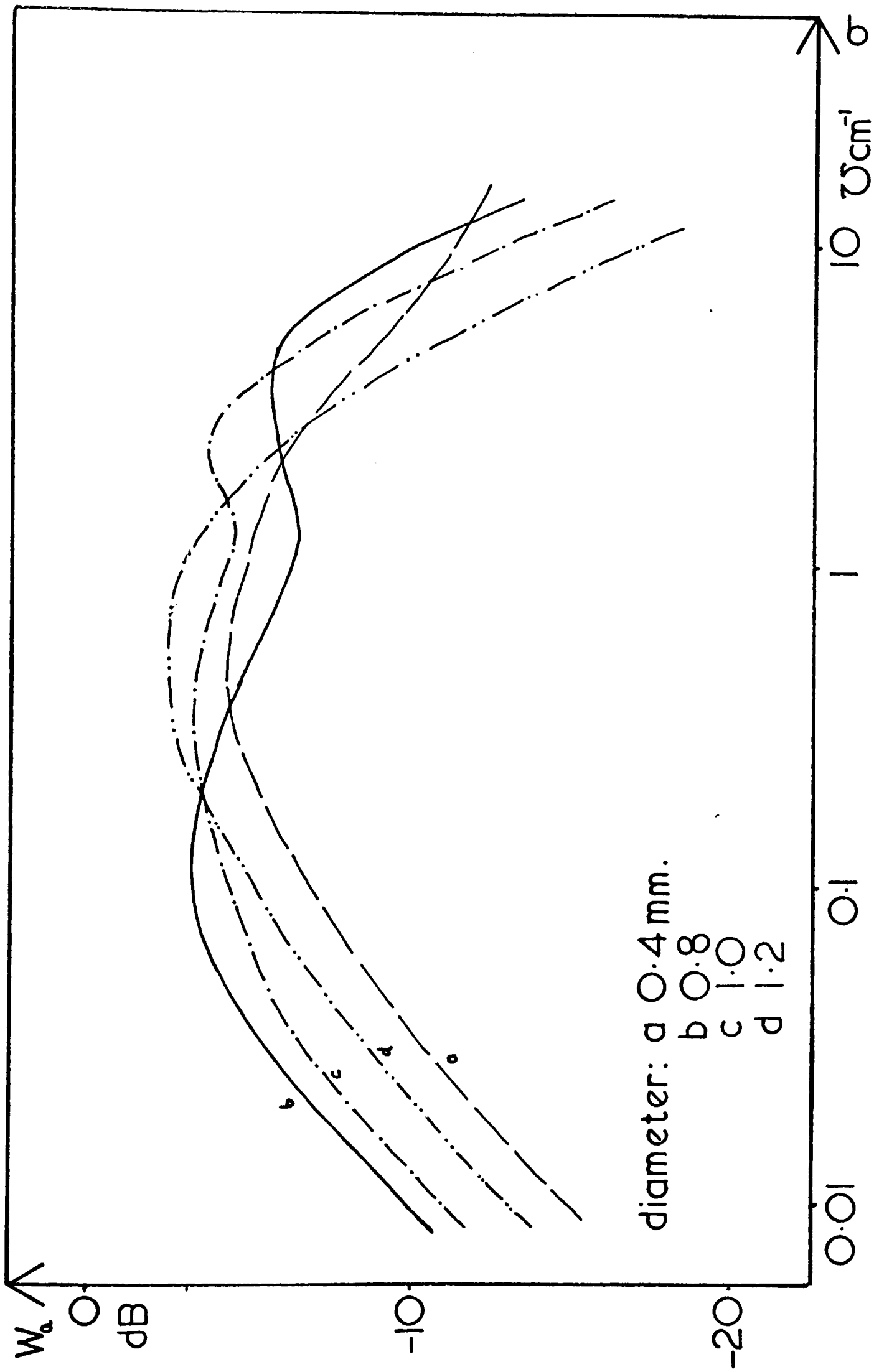

FIG. 4J

Inductive obstacle in WG22 at 35GHz.

power absorbtion vs. diameter and conductivity.

Curves for transmission and reflection coefficients for posts of 0.6 and 1.0 mm diameter are shown in Fig. 4K. The minima are due to resonant effects. These are calculated by Marcuvitz as follows for resonant effects in Za and Zb as follows:

$$\text{for Zb resonances} - \quad |\hat{\epsilon}_r| \simeq \left(3\lambda_g/4d_o\right)^2$$

$$\text{for Za resonances} - \quad |\hat{\epsilon}_r| \simeq \left(5\lambda_g/4d_o\right)^2 \qquad (4.4)$$

Substituting values for 0.6 mm and 1.0 mm width posts we find that the conductivity values corresponding to these resonances are:

	Za res.	Zb res.	
d_o = 0.6 mm	6.4	2.08	σ values
d_o = 1.0 mm	2.1	0.78	$\sigma\, cm^{-1}$

From the curves of Fig. 4K the shunt resonances (Z_a) are visible from the behaviour of the reflection coefficients, but the series resonances (Zb) are masked, presumably due to the relative magnitudes of the real and imaginary parts of the network impedances.

These general calculations outline the effects involved and suggest trends in behaviour, they are based on the exact solution involving all higher order modes excited around the obstacle. Acket et al (105) considered a simpler case where the sample impedance is much greater than the waveguide impedance. In order to describe the electric field at the sample boundary they combine:

$$Zg = \frac{b}{a}\sqrt{\frac{\mu_o \epsilon_o}{1-(\lambda_o/2a)^2}}$$

and

$$W = \frac{(E_1 b)^2}{4 Z_g}$$

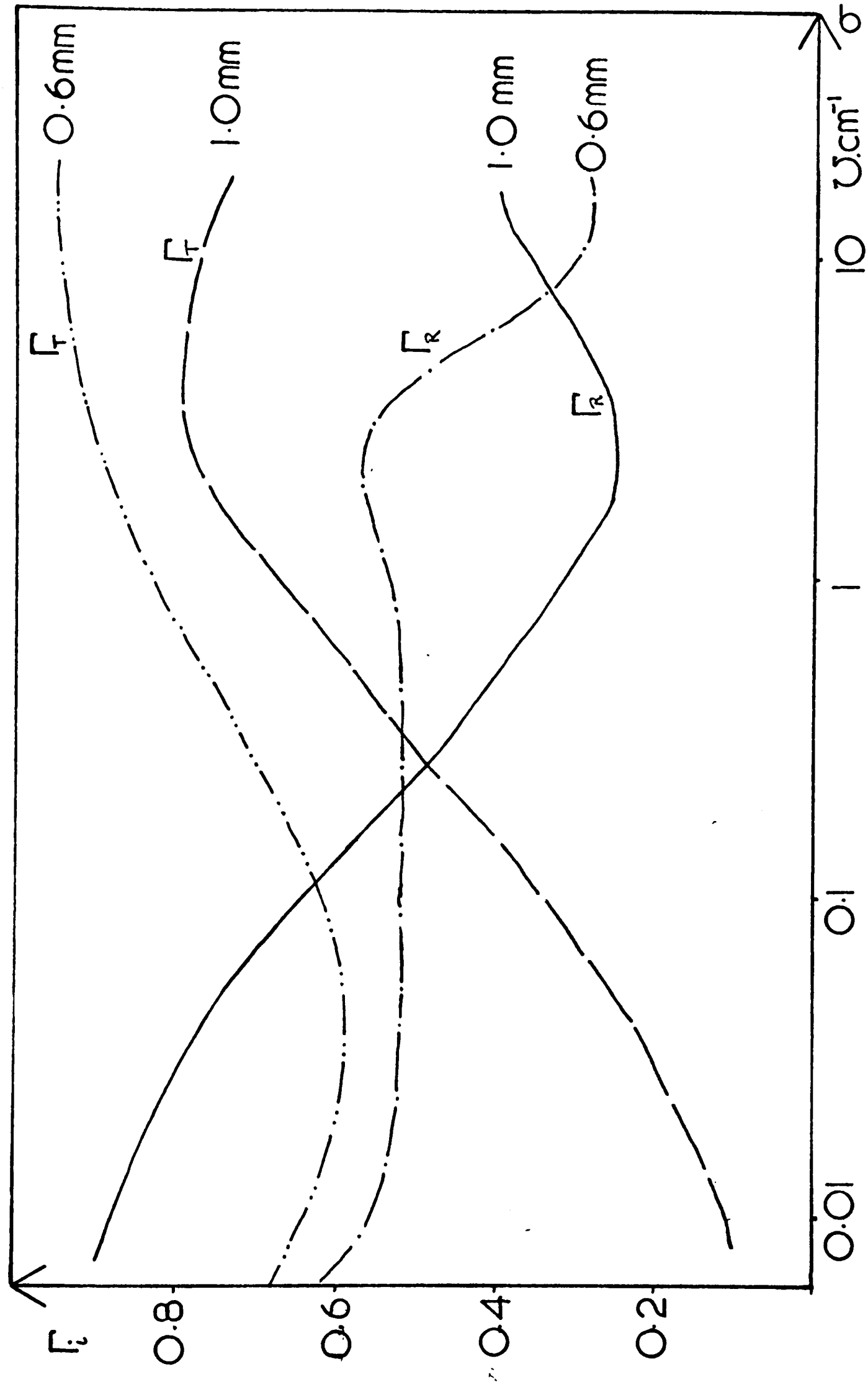

FIG. 4K

Inductive obstacle in WG22 at 35GHz.

transmission- and reflection-coefficients.

Thus, obtaining the maximum field, at the waveguide centre. They comment that when the waveguide and semiconductor post impedances are comparable then cut-off modes are excited around the obstacle and the complexity increases, this is the case previously examined following the analysis of Marcuvitz. Given the simpler case they relate the absorption data in the low-field limit, where J(E) is linear via:

$$E_1 = \frac{1}{b}\sqrt{R_{so} W_a}$$

where R_{SO} is the sample resistance at low-fields. They then proceed using the integral:

$$W_a = \frac{V}{2\pi}\int_0^{2\pi} J(E_1\cos\phi).E_1\cos\phi \; d\phi.$$

This approach they deem sufficient in microwave measurements of attenuation where the impedance criterion is obeyed,

Other workers have considered related problems and different geometries, these will be briefly outlined.

4.3.3. Theory for Composite Posts

The geometry of this situation is shown in Figure 4L, the data for both substrate and epitaxial layer properties being compared there.

For thin filaments of semiconductor mounted transversely in the centre of the waveguide Champlin (106,107) states the criteria for a first approximation to the TE_{10} fields as:

$$d \ll 2a/\pi \qquad (4.5)$$

and

$$d|\hat{\epsilon}_r - 1| \ll \left(\frac{\pi}{a}\right)\left(\frac{2}{\omega^2\mu_o\epsilon_o}\right)$$

then the fields in the semiconductor slab are

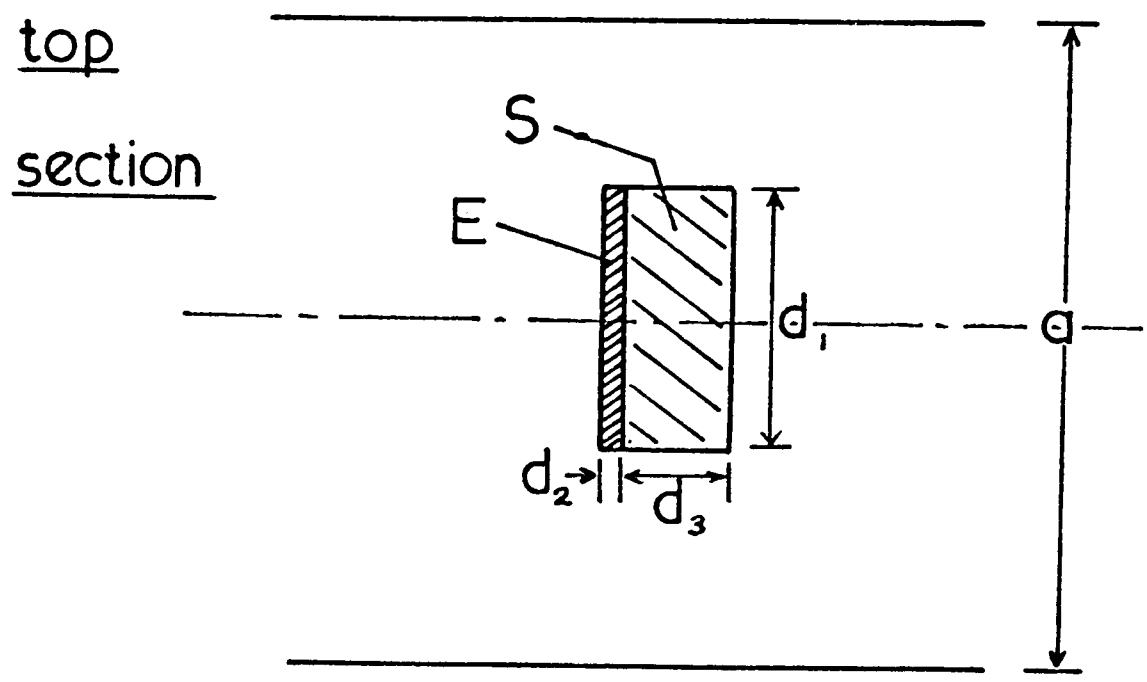

Epitaxial layer –

$5\mu < d_2 < 25\mu$

$0{\cdot}1 < \sigma < 1{\cdot}5\ \Omega.cm$

$5 < \epsilon_r'' < 75$

Substrate –

$0{\cdot}2 < d_3 < 0{\cdot}3\,mm \quad 0{\cdot}5 < d_1 < 1{\cdot}0\,mm$

$\sigma \simeq 10^{-4}\ \Omega.cm$

$\epsilon_r'' = 0{\cdot}005 \quad \epsilon_r' = 12{\cdot}35$

FIG. 4L

Epitaxial layer on s.i. substrate in waveguide – physical.

$$E_{s/c} = E_{wg}$$

$$H_{s/c} = \left(\frac{\gamma_{s/c}}{\gamma_{wg}}\right) H_{wg}$$

where $\gamma_{s/c} = \alpha_{s/c} + j\beta_{s/c}$.

$\gamma_{wg} = j\beta_{wg}$.

Champlin states that the condition (4.5) may be more severe than necessary and considering further orders obtains the criterion (107)

$$d|\hat{\epsilon}_r - 1|\left(\frac{a}{2\pi}\right)\omega^2\epsilon_o\mu_o \ll \pi. \qquad (4.6)$$

For indium phosphide in WG22 at 35 GHz this reduces to:

$$d|\hat{\epsilon}_r - 1| \ll 5.5, \quad (d \text{ in mms})$$

for a 1 Ωcm sample this places a thickness restriction of:

$$d \ll 0.11 \text{ mms}$$

viz. - a very thin sample

For anything but an infinitely long sample there will be reflections from both ends and a standing wave set up along the length of the sample, M.W. Gunn (108) comments on this that if the sample is longer than several wavelengths the evanescent modes excited by its presence will decay and if it is a high attenuation material then the reflection will be absorbed and little standing wave effect experienced. Both these workers considered samples such that the field was uniform within the sample, however this may not be so, especially if samples of widths as used in the experiments are considered. Andersen et al (109) report calculations of the field distributions in circular rods, centrally mounted in rectangular waveguide. Their approach is to consider three regions of the problem, the "input" and "output"

regions at distances greater than a/2 from the plane of the centre of the semiconductor post, in which the fields are expanded as a series of TE_{mO} modes (m = 1,3,5 ...) and the region of the "discontinuity" which is a square of side a, including the post. In this the fields are expanded as a series of cylindrical waves. By applying bounday condition at the walls and discontinuity surface, and point-matching at $Z = \pm a/2$, the junction between "discontinuity" region and input and output regions a solution may be obtained.

For semiconductors with positive conductance a typical result is shown in Fig. 4M. Those with negative conductance exhibited resonance phenomena associated with emission rather than absorbtion. Typical curves are shown at 4M. Writing the electric field in the dielectric as:

$$E_y = \sum_n C_n . J_n(\gamma_p, r) . \cos(n\theta) \qquad (4.7)$$

where: r, θ, y are co-ordinates (cylindrical polar)

γ_p is the complex propagation coefficient in the rod

$$\gamma_p = \omega\sqrt{\mu_o \epsilon_o \epsilon_p} = \omega\sqrt{\epsilon_p}$$

J_n and C_n are the Bessel function of complex argument of order n, and the complex expansion coefficient (n = 0, 1, 2...)

Curve (2) corresponds to a resonance where:

$$|C_o| \gg 1, \quad |C_o| \gg |C_n| \qquad n = 1,2....$$

a 'symmetric' case, whereas curve (3) corresponds to a 'dipole' resonance where

$$|C_1| \gg 1, \quad |C_1| \gg |C_n| \qquad n = 0,2,3....$$

The 'dipole' resonance condition is given approximately by:

$$J_o\left(Re\left(\gamma_p r_p\right)\right) = 0 \qquad (4.8)$$

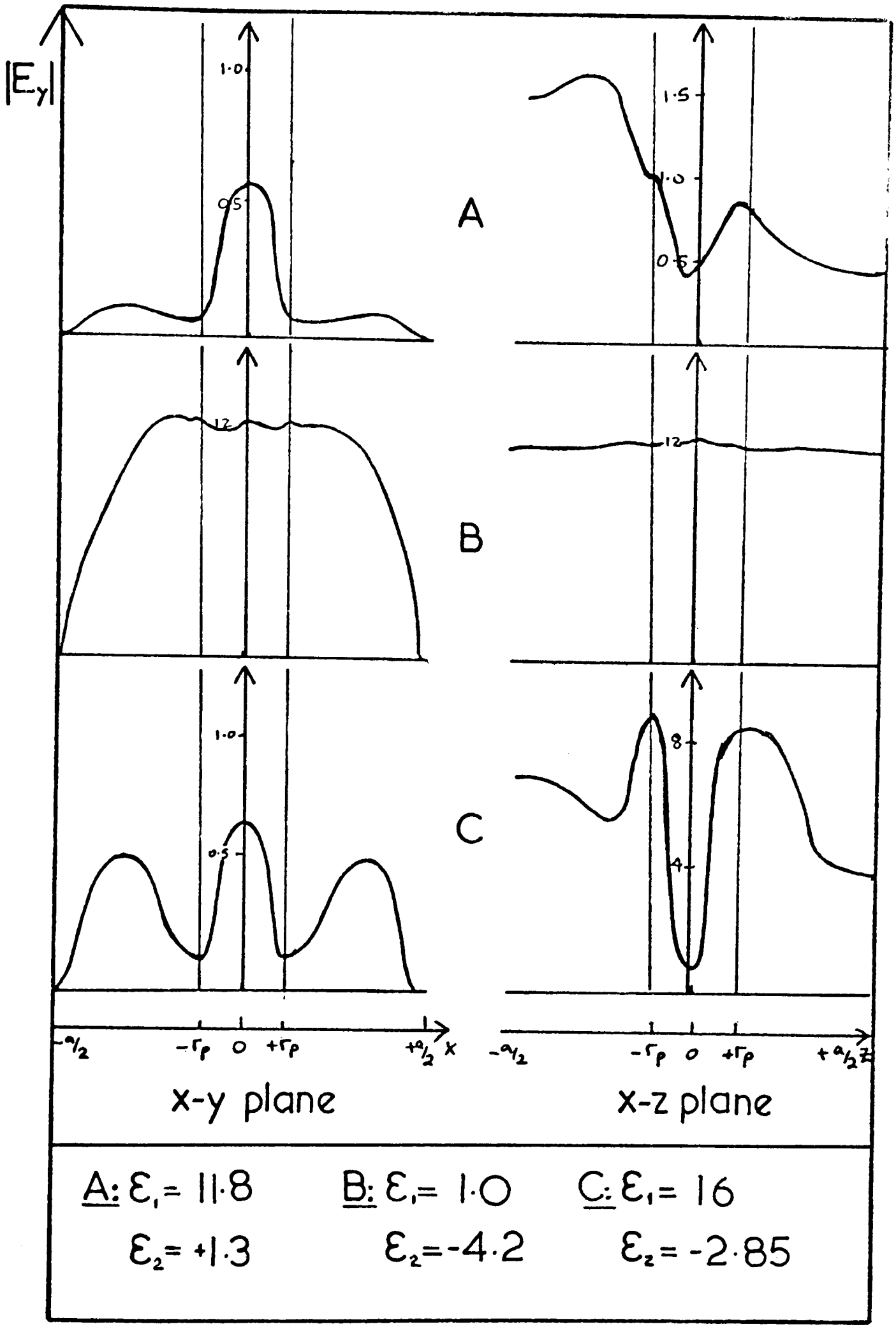

FIG. 4M

Electric-field in semiconductor rods (109)

$r_p/a = 0.1125$, $f/f_c = 1.661$ in all cases.

Curve (1) corresponds to n type Si of 40 Ωcm (0.025 $\mho$cm^{-1}) in WG22 at 35 GHz, the radius of the rod being 0.8 mm.

Curve (2) corresponds to an imaginary material with resistivity -12 Ωcm (0.083 $\mho$cm^{-1}).

Curve (3) corresponds to GaAs with resistivity 17.5Ωcm, and (conductivity 0.057 $\mho$cm^{-1}) similar dimensions to (1).

Following from equation (4.8) we may calculate the conductivities at which a post will exhibit a 'dipole' resonance - this being of interest since the field in the sample is non uniform, varying by factors of up to 80 over the sample cross section.

For posts of indium phosphide, having dimensions 0.6 mm and 1 mm diameter we find:

	d_o = 0.6 mm	d_o = 1.0 mm
σ values		
($\mho$cm^{-1})	0.04	-
for	0.53	0.135
resonance	1.46	0.44
	2.95	0.92
	4.9	1.6

These are different from those calculated after Marcuvitz's theory using the expressions for σ in eq. (4.4). Hence we may see that different workers have taken different types of approaches, but only verified some of the results by experiment. No general theory exists since the family of problems is quite complex.

A two-layer post is more difficult to analyse. The effect of the substrate may be to make the field in the epilayer more or less uniform than if it did not exist. Hence no calculations are presented here. The method of calculating the field in the epitaxial layer is confined to the derivation from the power absorbed by it, rather than by external effects such as transmission or reflection, which could be used to measure the properties of bulk, positive conductivity semiconductors rather more directly.

There is a possible margin of error in that the field across the sample section may be sufficiently non-uniform so as to only bias part of the section beyond breakdown. This would have the effect of "smoothing" the velocity field characteristic; rather than giving clear maxima and minima where they might exist.

In fact a general discussion of errors in measurement of semiconductor properties via transmission or reflection bridges was made by Datta et al (110), who comment on the accuracy of commercially available standards reducing the potential accuracy of the microwave methods, especially where measurements of effective mass have been required. They extended their work and reported in 1974 (111) an improvement using quarter wave transformers mounted in front of samples in the reflection bridge. These reports bear particularly on full WG section sized samples of semiconductor, not the inductive posts.

Chapter five.

Calibration using gallium arsenide.

5.1. EXPERIMENTAL TECHNIQUES

5.1.1. D.C. Bias Arrangements

The circuit for d.c. bias and monitoring of the current flowing in the samples is shown in Fig. 5A. The power is provided by a battery so as to eliminate hum and noise interference from d.c. supplies run from the mains. The polarity may be reversed and the exact voltage determined by a switch and potentiometer. The whole circuit is contained within a die-cast box to minimise stray pickup and screened coaxial leads were used for connection to the monitoring circuits and the device.

Typical monitored outputs are shown in Fig. 5B, showing clearly the conductivity change during the microwave pulse, for both polarities; and the detected r.f. on a damaged sample, improperly earthed.

Considering the equivalent circuit, also shown in Fig. 5A, we have three resistive elements in series. R_S the sample resistance, which is a function of field, R_D the resistance of the detecting circuit and R_X the remaining elements, being leads, contact resistance and that portion of the sample not exposed to microwave power. The equation relating the detected voltage and the other quantities is:

$$V_d = \frac{V_o}{R_S + R_X + R_D}$$

Assuming V_o to be constant and writing R_T for $R_X + R_D$, this being the total circuit resistance other than the part of the sample affected by microwave power, then let us write V_1 for the detected voltage in the absence of microwaves and V_2 for the detected voltage during the microwave pulse, similarly R_1 and R_2, then we have

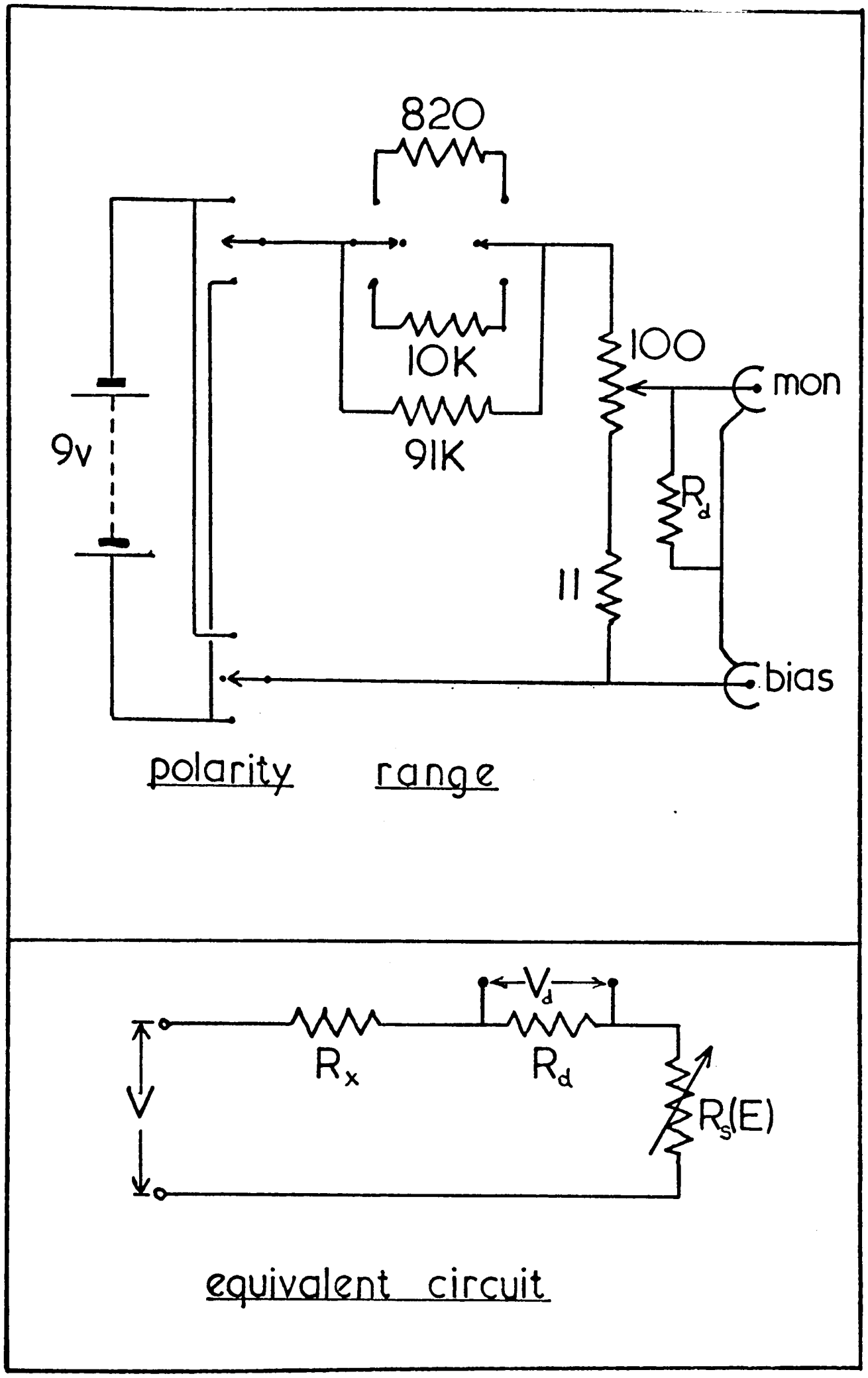

FIG. 5A

Experimental apparatus –

d.c. biassing arrangement.

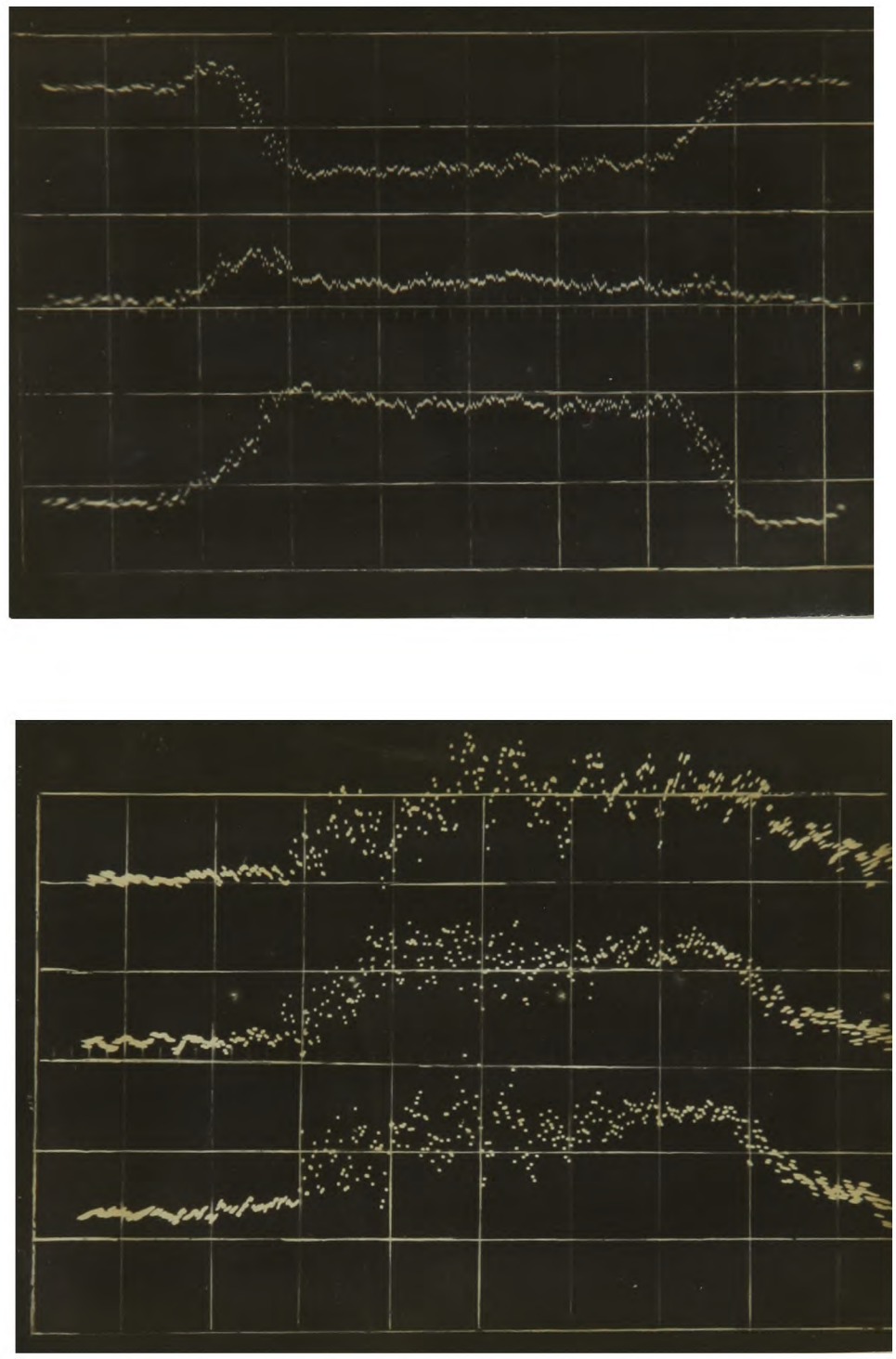

horiz: time - 50 nS/cm.

vert: d.c.mon 20 μA/cm R_D=1kΩ

2 μA/cm R_D=1kΩ

FIG. 5B

observation of 'microwave conductivity' - typical results.

$$\frac{V_2}{V_1} = \frac{R_1 + R_T}{R_2 + R_T}$$

this, after manipulation, yields:

$$\frac{R_1}{R_2} = \frac{V_2}{V_1}\left\{1 + \left(1 - \frac{V_2}{V_1}\right)\left(\frac{R_T}{R_1}\right)\right\}^{-1}$$

or, writing the conductivities, $\bar{\sigma}$ the average, and σ_o the low-field or static value

$$\frac{\bar{\sigma}}{\sigma_o} = \frac{R_1}{R_2}$$

after manipulation we find that:

$$\frac{\bar{\sigma}}{\sigma_o} = \frac{V_2}{V_1}\left\{1 + \left(1 - \frac{V_2}{V_1}\right)\left(\frac{R_T}{R_o}\right)\right\}^{-1} \qquad (5.1)$$

Ideally the resistance of all elements, other than the sample would be extremely small, such that:

$$\frac{R_T}{R_0} \ll 1$$

then:

$$\frac{\bar{\sigma}}{\sigma_o} \simeq \frac{V_2}{V_1}$$

However in the experiments this is difficult to attain for many reasons. Owing to limitations of applied d.c. field, for reasons of avoidance of undue sample heating, static d.c. field levels and feasibility of supply of large currents from other than secondary batteries, it was simplest to keep the d.c. current fairly small. This necessitated large detecting resistors, or very sensitive sampling oscilloscopes. To avoid undue noise interference a compromise was

reached between these various criteria. The sample dimensions are such that the contact separation is generous enough to avoid any part of the contacts projecting into the waveguide. This entails some portion of the sample will be unaffected by the r.f. fields - and hence contributing extra series resistance, in addition to the contact resistance.

The sample currents were mostly of the order of 20-40 μA and the detector resistor generally 1KΩ . The ratio R_T/R_0 was in the range 0.5 to 2.0, which gives the expression for the conductivity ratio, from equation (5.1) as follows:

$$\frac{\Delta V}{3-2\Delta V} \leqslant \frac{\bar{\sigma}}{\sigma_o} \leqslant \frac{2\Delta V}{3-\Delta V} \qquad (5.2)$$

where $\Delta V = V_2/V_1$.

Taking a value of $R_T/R_0 = 1$ then for large ΔV ($\simeq 1$), $\bar{\sigma}/\sigma_o$ is approximately equal to ΔV, but for small ΔV ($\simeq 0$), $\bar{\sigma}/\sigma_o$ tends to $\Delta V/2$. The accuracy of determination of $\bar{\sigma}/\sigma_o$ was to better than $\pm$ 5% giving an overall accuracy of the experimental ($\bar{\sigma}$, W_a) data pairs in the range $[\pm 8,10\%]$. Stray capacitance in the system contributed to the finite rise-times of the detected pulses, but these were not sufficiently large as to impair the accuracy of the experiment.

5.1.2. Sample Preparation Technique

The gallium arsenide was supplied by the Plessey Company Limited in the form of epitaxial wafers on semi-insulating substrates. These were first cleaved using a diamond scribe to produce parallel sided samples, whose dimensions satisfied the foregoing criteria. The process for contacting was now arranged as follows.

The sample was cleaned in trichloroethylene followed by deionised water. An etch was prepared using the following constituents (112).

100 ml H_2O deionised

5 ml NH_4OH 0.880 solution

20 ml H_2O_2 20 vol. solution

The etch rate was 2 μ /min and the etch was renewed every minute. Control of the layer thickness was therefore quite simple. The sample was washed in deionised water after etching and dried. Small sections of tin were cut from a 99.999% ingot using a scalpul retained for this purpose only. These were cleaned in trichloroethylene and dried.

The slice was placed in a small furnace and the beads of tin placed in the positions contacts were required. Forming gas ($9N_2:1H_2$) was passed through the furnace to remove all air and act as an inert atmosphere. The temperature was raised to 240°C when the tin melted, shown by the little beads balling up on the sample surface. The temperature was then increased to within the range 300-350°C and maintained there for 30 seconds. During this period the balls of tin collapsed and alloyed into the layer. The heater was then switched off and the whole arrangement allowed to cool, with no special profile control, whilst the inert forming gas atmosphere was maintained. The sample was then removed and the contacts filed flat.

The electrical characteristics were then measured using a curve tracer. The voltage-current characteristic was measured for both polarities up to the range, ten to twenty volts, depending on the sample resistance. Non-linearities were noted and the resistance calculated from the characteristic. The mechanism dimensions were then measured using a travelling microscope (to a accuracy of 0.01 mm). The surfaces and edges were checked for damage and the data from these measurements together with the manufacturers data used to calculate the resistance, which was compared to the electrical measurements using the curve tracer.

Selection of samples is limited to those with little damage, a good linear voltage-current characteristic in both directions and the best agreement between experimental and theoretical sample resistances (±10%). The samples are exposed to high power microwave pulses and the characteristics rechecked, any failures or remarkably changed characteristics are discarded. This system of manufacture produces about 70% useful samples from the initial batch cleaved from a layer.

5.1.3. Sample Holder

This is illustrated in Fig. 5C. It was designed to be of use at liquid nitrogen temperatures and hence was built to be accommodated within a brass pressure vessel and with all leads taken out of sealed tubes. The method of sealing is to trap an indium shim between the vessel and its lid. The samples were mounted on the removable section, transversely using silver conducting paint. Care was taken not to spill this into the waveguide, or onto the layer. The joint between the fixed and removable waveguide was also treated with conducting paint.

The sample was mounted in hollows cut out of the waveguide flange, this ensured central positioning. The coaxial connector screwed into the flange to provide the d.c. connection had a small copper strip soldered to its end, and the whole was potted in araldite epoxy resin; this avoided problems of insulation and mounting for each sample. The rear of the sample was insulated from the other flange by using strips of sellotape.

A washer was inserted between the flanges to join the waveguide walls, avoiding a discontinuity. This was shaped to allow the sample mounting points to be accessible, and could be secured with conducting paint.

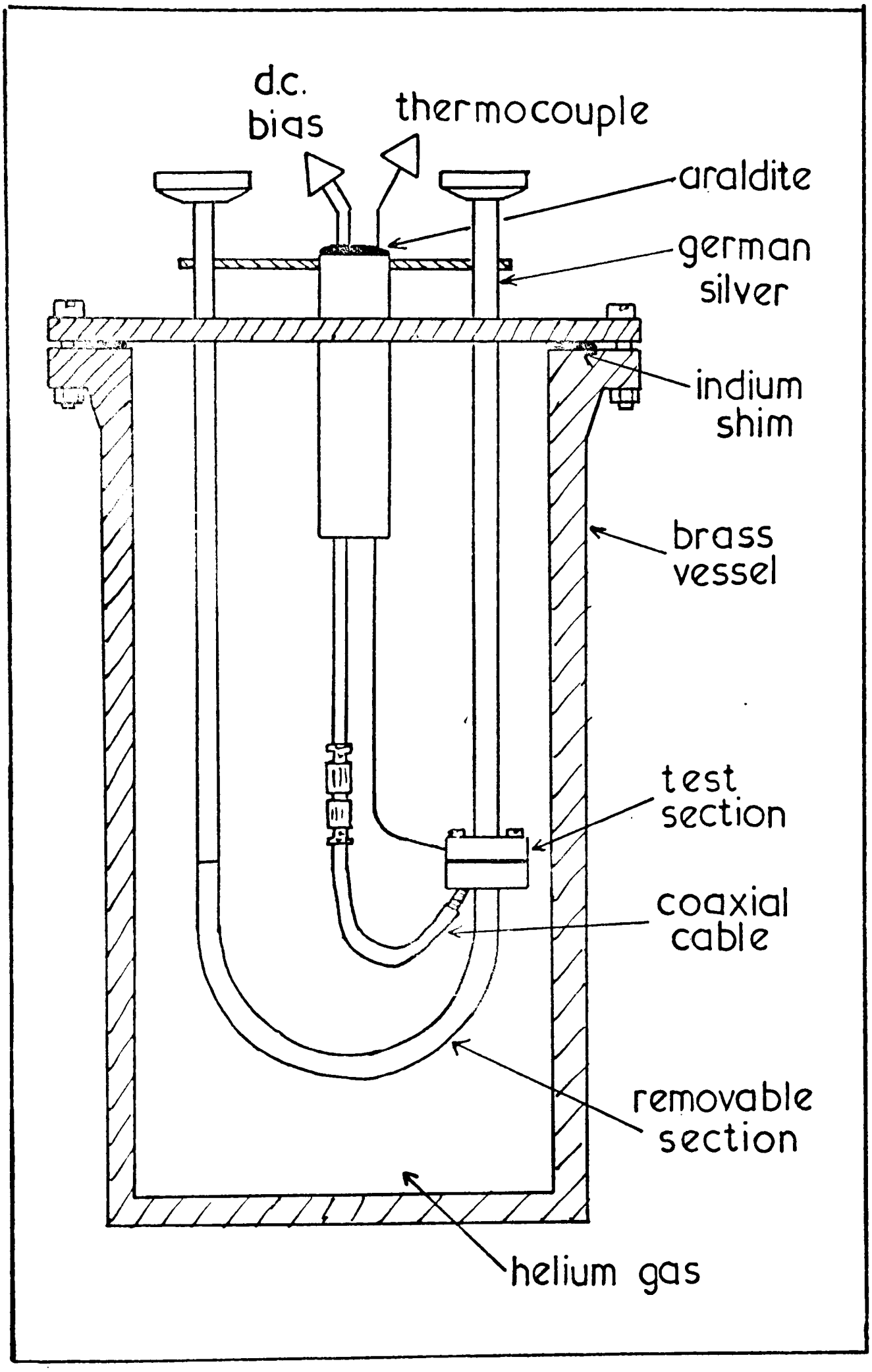

FIG. 5C

Sample holder.

(i). general view.

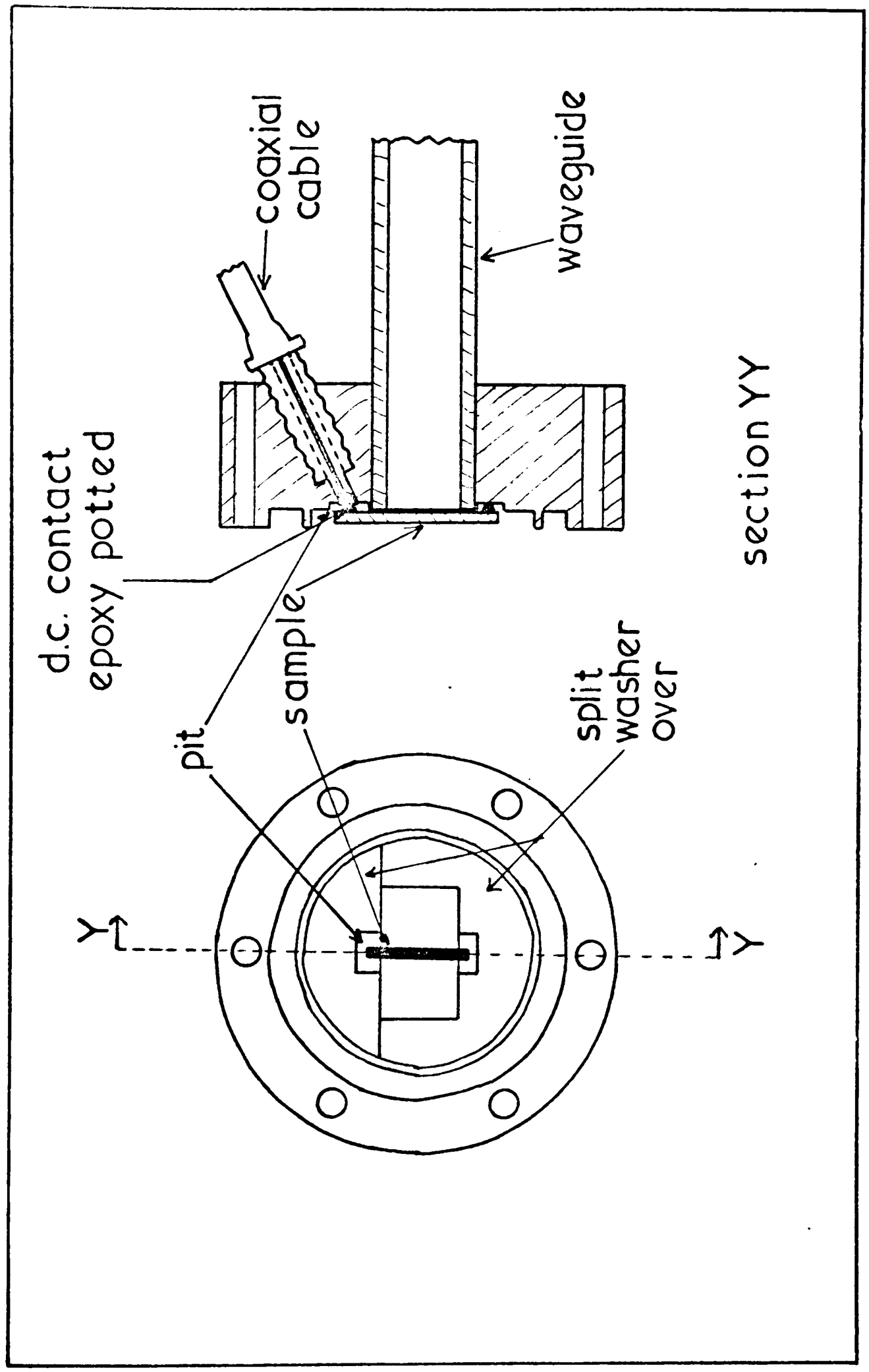

FIG. 5C

Sample holder

(ii) test section detail.

Data of performance with no sample in the holder were collected before and after an experimental run, these established the transmission and reflection characteristics of the sample holder alone and allowed the data of the power monitoring circuit and the rotary-vane attenuator to be set. Typical performance was with return loss of 19 dB, equivalent to 1.23% reflected power, and a VSWR of 1.23. The sample was then inserted and the contact resistance checked using the curve tracer to examine the linearity an addition to the d.c. resistance. D.C. bias was then applied and the experiment proceeded. The results gathered were analysed via the computer programmes described in Section 4.2.

5.2. EXPERIMENTAL RESULTS

5.2.1. Typical Experimental Data

Considering a sample GA11 as typical the data for this were as follows:

Overall size: $d_1 = 0.98$ mm, $d_2 = 0.20$ mm

Following Marcuvitz figures: $d_2/d_1 = 0.204$, $d_o/d_1 = 0.676$

$\therefore\ d_o = 0.662$ mm

Total sample volume = $0.716\ mm^3$

Epitaxial layer: 11.5μ thick of $n_e = 1.5 10^{15}\ cm^{-3}$ $\mu_o = 7000\ cm^2\ V^{-1}\ S^{-1}$

Conductivity: $\sigma_o = 1.68\ \mho cm^{-1}$

Theoretical resistance: $R_{TH} = 2.48\ k\Omega$

Measured resistance: $R_o = 2.71\ k\Omega$ $R_o/R_{TH} = 1.09$

d.c. bias current $\simeq 20\mu A$

Maximum power absorbed 8.1 kW (pulse)

Temperature rises: maximum at centre $\Delta T_c = +41^{\circ}K$ above ambient.

The value of $\bar{\sigma}/\sigma_o$ is shown at Figure 5D, demonstrating clearly the form of characteristic predicted theoretically. Figure 5E shows the fr: ctions of r.f. power reflected, transmitted and absorbed as a function of incident power. The calculations of the expected absorbtion level (by Marcuvitz's theory see section 4.3.) gave W_a = 6.09 dB for this sample whereas the actual absorbtion was higher in the experiment at 5 dB. The theory indicates increasing absorbtion for decreasing conductivity for this post dimension whereas the experimental results show a maximum absorbtion at 2.5 kW incident power, falling steadily above this value. These differences are due to the two component structure of the sample and the effect of the substrate on the fields in the epitaxial layer.

5.2.2. Computed Results

Using the experimental results shown in Figure 5D for $\bar{\sigma}\ (W_a)$ the computer was programmed to produce a $\bar{\sigma}(E_o)$ data set, shown at 5F. This may be analysed using the solution to Schlömilch's equation (3.9), directly or via the Tschebychev polynomial approximation to produce a velocity field characteristic. The results of both analyses are shown in Fig. 5G, together with velocity-field curves for two other samples GA8 and GA15. The data for the three samples is:

	n_o (cm^{-3})	μ_o ($cm^2V^{-1}S^{-1}$)	σ_o ($V\ cm^{-1}$)	$d_e(\mu)$
GA8	3×10^{14}	7,480	0.36	22
GA11	1.5×10^{15}	7,000	1.68	11.5
GA15	6.9×10^{14}	6,600	0.73	11

and the salient points from the velocity-field characteristics are as follows:

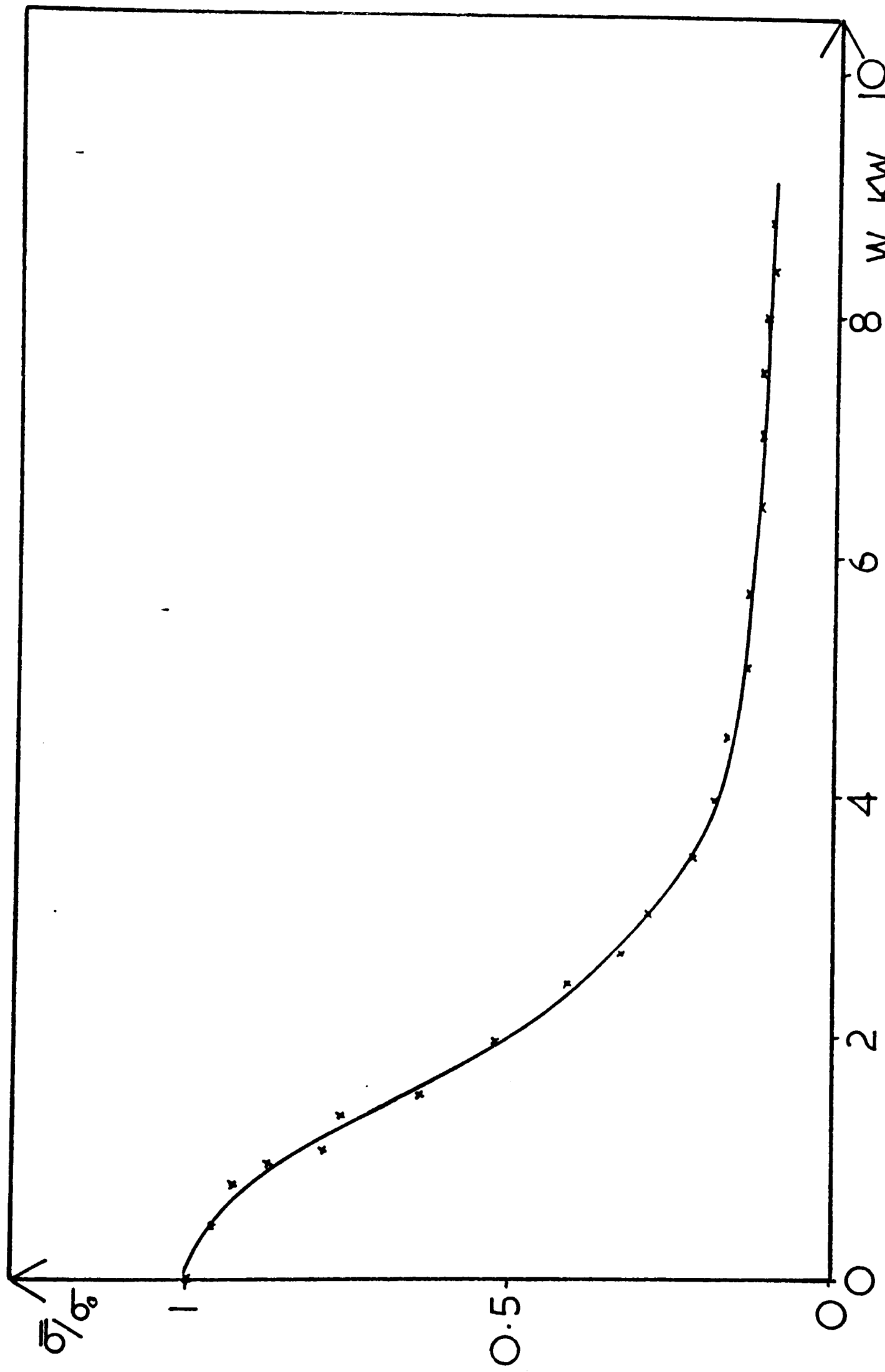

FIG. 5D

Sample GA11 -

average conductivity vs. incident power.

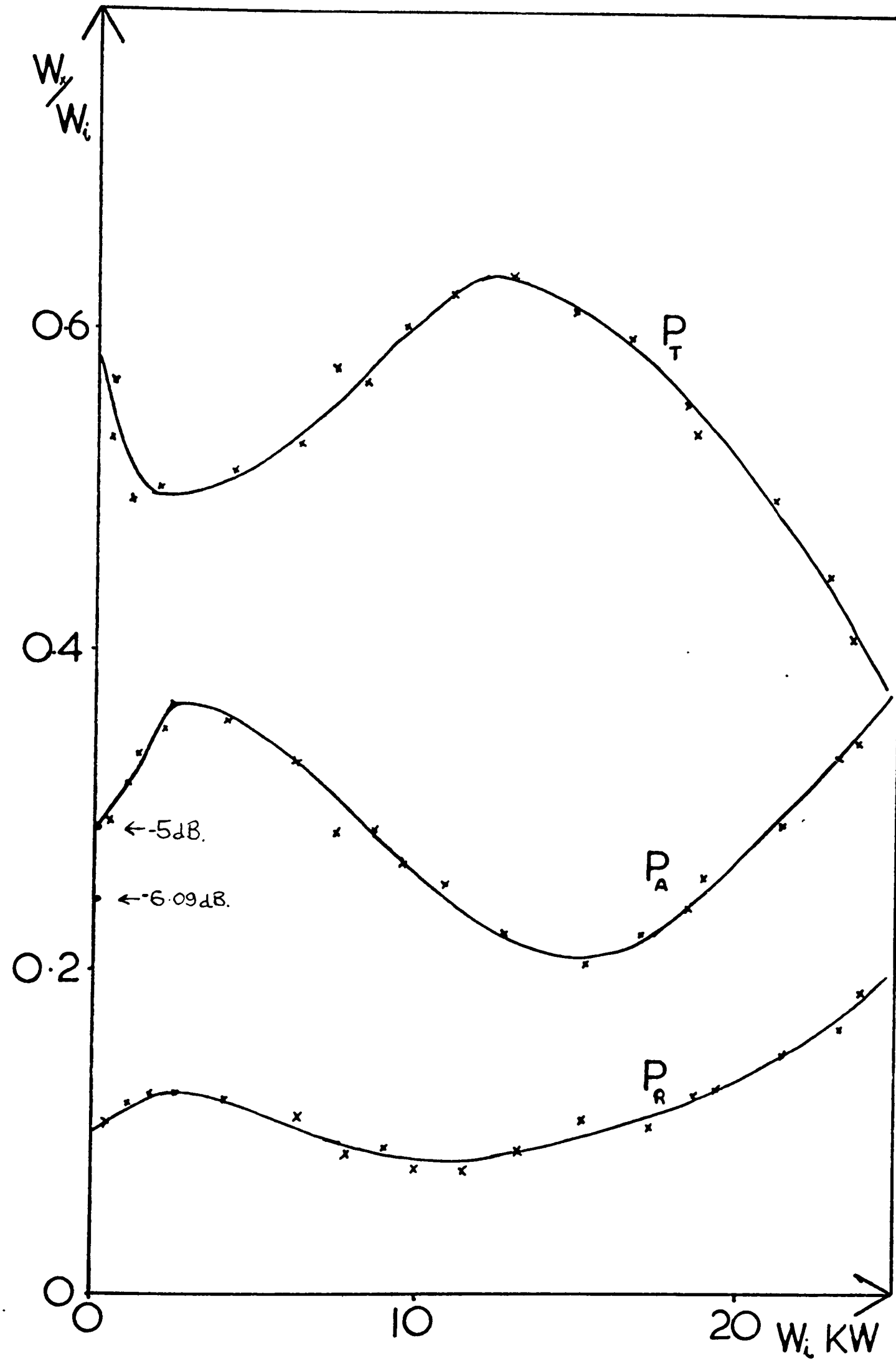

FIG. 5E

Sample GA11–

Power balance vs. incident power.

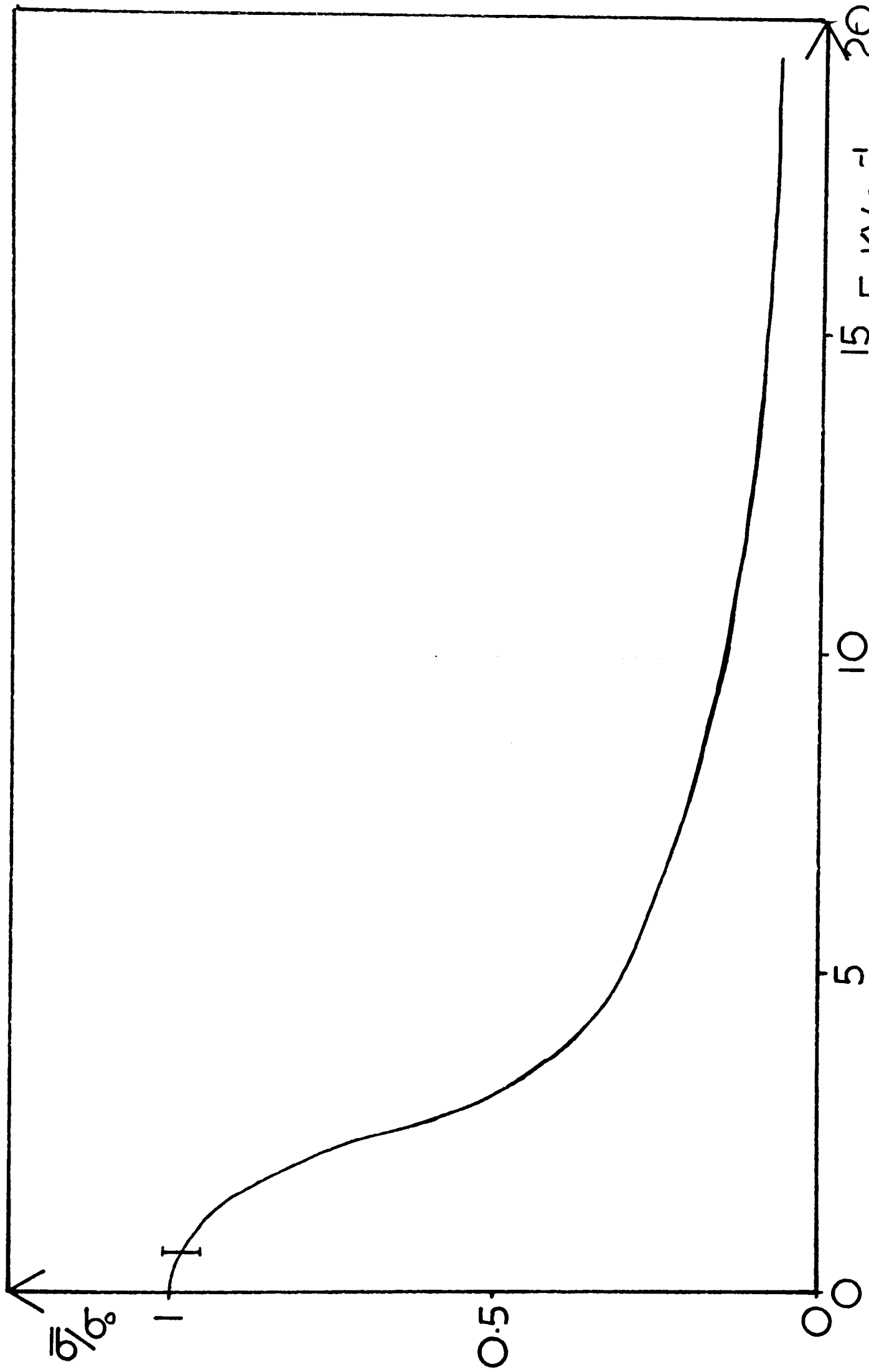

FIG. 5F

Sample GA11-

computed conductivity vs. field.

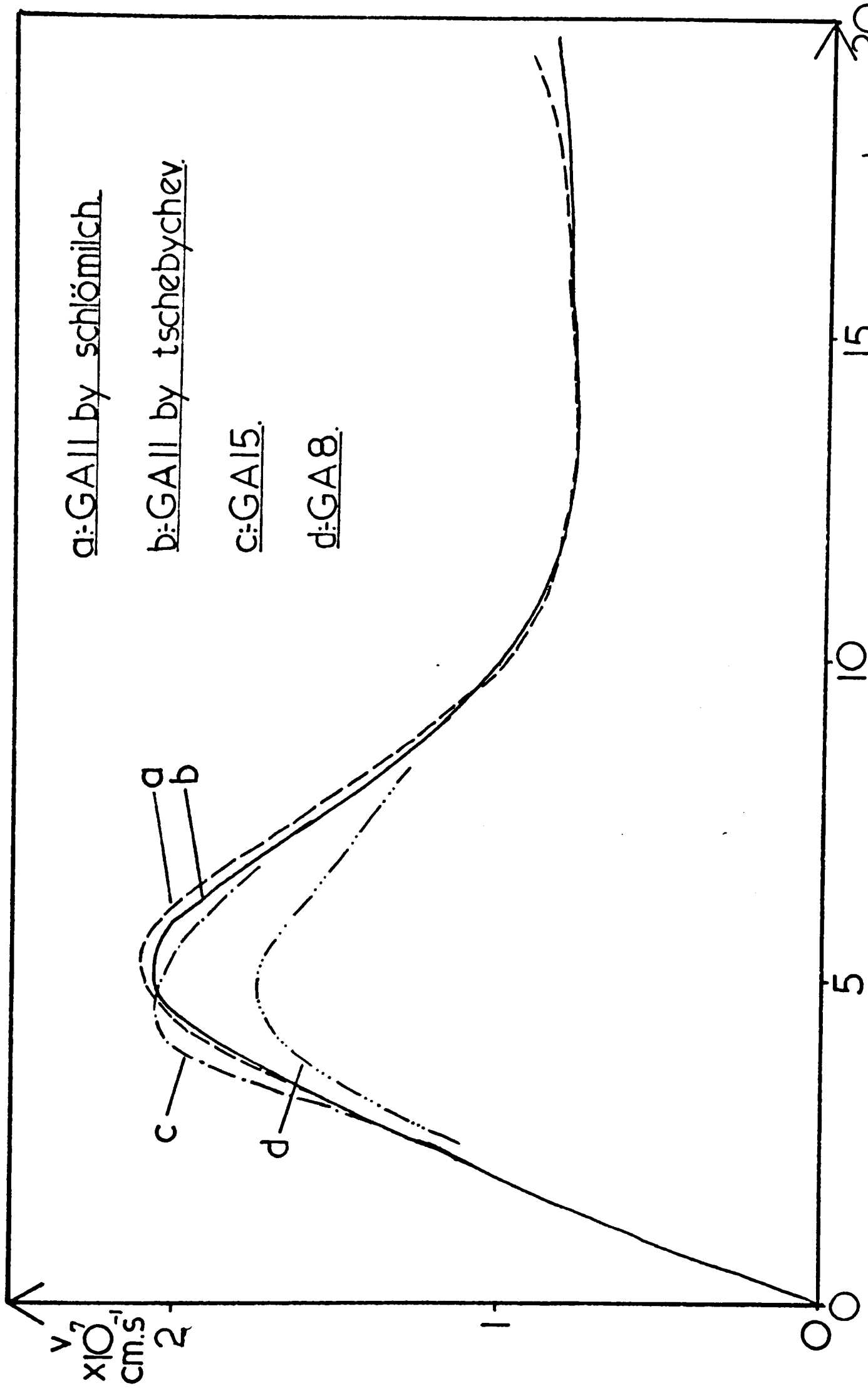

FIG. 5G

Gallium arsenide – v(E) characteristic

computed results at 300°K.

	V_p	E_T	V_v	μ_N	r
GA8	1.80	4.9	0.9	-1100	2.0
GA11	2.10	5.0	0.8	-2900	2.6
GA15	2.15	4.5	0.9	-2500	2.36
	$x10^7 cms^{-1}$	$kVcm^{-1}$	$x10^7 cms^{-1}$	$cm^2V^{-1}S^{-1}$	

Another sample was cut from the 0.73 Ωcm^{-1} layer and was thinned to a 5μ epilayer. This (GA12) gave results differing from GA11 by less than $\pm$ 3%, within the limits of experimental error.

Comparison of the three layers yields two possible effects. The negative mobility and peak-to-valley ratio decreased in GA8 with the lowest doping density - this may be the effect of inhomogeneity, a reduction in r from 2.6 to 2.0 is -23%, which according to Fig. 3B would arise from doping fluctuations such that $n_{min}/\bar{n}_\ell = 0.85$. However, the manufacturers indicate that the doping density fluctuations should be less than $\pm$ 5% giving $n_{min}/\bar{n}_\ell$ a value of 0.90. The peak velocity decreases as mobility (low field) increases. This contradicts the idea of a constant threshold field, which would give higher peak velocities for higher mobilities. These results indicate considerable sub-linearity in the subthreshold characteristics.

All layers were run with centre of sample temperatures less than 50°K above ambient.

5.2.3. Comparison with published Data

The results of Bostock (99), Fay et al (75), 'TLam et al (85) and Braslau et al (91) yield some points for comparison. Bostock used the same equipment, yet for a 0.13 Ωcm^{-1} sample he obtained much lower peak velocity and threshold field than other workers (1.5×10^7 cms^{-1} at 3.0 $kV.cm^{-1}$). This could be due to inhomogeneous doping, but the

threshold field is very low.

With regard to the negative mobility, Braslau et al (91) comment that this decreases with decreasing conductivity, this may also be due to doping fluctuations - as Glover (95) pointed out.

Braslau and Hauge also point out that the threshold field increases for increasing low-field mobility, which is in line with measurements made by'T.Lam et al (85). These are almost in line with the trend in section 5.2.2. of decreasing peak velocity for increasing low-field mobility. All the results are listed in Table 5H and referral to that will demonstrate, in general, higher peak velocities are measured for higher conductivity material, the particular exception being that of the very low conductivity material of Fay et al (75).

The experimental results agree well with published data, ex cept that the measured threshold field is approximately 20% higher than that generally accepted. This may be a substrate induced effect, increased absorbtion of r.f. power would overestimate the threshold field. The peak velocity data agrees closely with published data indicating any such simple overestimate of threshold field based on increased power absorbtion is not affecting this by the same proportion. An alternative explanation is that it is due to a relaxation effect, as suggested by Glover (86).

Comparison with now generally accepted data gives

	V_p	E_T	V_v	μ_n	r
data (113)	2.2×10^7	4.0	1.0×10^7	-2800	2.2
this work	2.1×10^7	4.9	0.9×10^7	-2200	2.3
	cms^{-1}	$kV.cm^{-1}$	cms^{-1}	$cm^2.V^{-1}S^{-1}$	-

A good agreement considering experiment error of some possible 15%.

FIG. 5H

Gallium arsenide - experimental results.

ref	low-field resistivity Ωcm.	conductivity $\mho$cm^{-1}	doping cm^{-3}	low-field mobility cm^{2}V^{-1}s^{-1}	peak-velocity cm s^{-1}	threshold-field KV cm^{-1}
75	5 10^2 - 10^3	.002 - .001	2.0 10^{12}	6250	2.0 10^7	4.0
91	20	0.05	4.5 10^{13}	7000	2.0 10^7	4.5
99	7.7	0.13	1.1 10^{14}	7000	1.5 10^7	3.0
91	7.1	0.14	1.2 10^{14}	7000	1.8 10^7	4.5
this	2.8	0.36	3.0 10^{14}	7480	1.8 10^7	4.9
91	1.5	0.66	5.2 10^{14}	8000	1.8 10^7	4.0
91	1.5	0.66	5.5 10^{14}	7500	2.2 10^7	4.0
this	1.4	0.73	6.9 10^{14}	6600	2.1 10^7	5.0
85	1.1	0.91	6.6 10^{14}	8640	2.2 10^7	4.0
this	0.6	1.68	1.5 10^{15}	7000	2.15 10^7	4.5

Chapter six.

Experimental results for indium phosphide.

6.1. EXPERIMENTAL DETAILS

6.1.1. Sample Preparation Procedure

This procedure was, in outline, similar to that adopted for the gallium arsenide samples. The material used in these experiments was supplied by the Allen Clark Research Centre of the Plessey Company Limited. The material was n-type epitaxial layers deposited on semi-insulating substrates. The active layer was silicon doped, this being 'residual' impurity doping rather than by specifically introduced impurities. The semi-insulating substrates were highly compensated with chromium, having a free carrier density of 10^{12}-10^{13} $cm.^{-3}$, and a low field mobility of approximately 200 $cm^2 . V^{-1} . S^{-1}$. The resistivity was in the range $3\ 10^3$-$3\ 10^4 \Omega cm$, significantly less than the corresponding semi-insulating gallium arsenide substrates, whose resistivity was some two orders greater. This may result in the substrates carrying a significant proportion of the d.c. bias current in the indium phosphide experiments; this possibly being enhanced should the contact material diffuse far enough through the active layer so as to make a direct n^+ contact. This effect may be enhanced by thermal or field induced means of compensation reduction. The carrier density profile (114) near the layers junction showed the transition from n to s.i. to be within one micron wide, the carrier density changing by some four orders of magnitude within this width.

The slices of material were cleaved using a diamond scriber and cut up into blanks prior to etching. Cleaning in trichloroethylene, methanol and deionised water was followed by a bromine-methanol etch. This removed surface damage and oxide layers and adjusted the active layer to the required thickness for the experiment. This etch was

used in two formulations, 4% v/v for fast removal, 5-6μ/minute (115) as compared to a slower rate of removal available from a 1% v/v solution giving 0.5μ/minute removed. The latter was used for accurate thinning, the former for removal of the epitaxial layer completely. The rates agree with the results of Becker (116) for these concentrations and crystal orientation. The etched surface of the epitaxial layer was covered with many tiny etch pits, although appearing highly polished to the naked eye.

After etching, the blanks were rinsed in methanol and placed in the small furnace for the tin-bead contacting process, which was similar in most respects to the treatment of the gallium arsenide samples. The particular variation was the employment of hydrochloric acid through which the forming gas was bubbled to provide hydrogen chloride whilst the tin was melting and wetting the indium phosphide epi-layer surface. The hydrogen chloride was turned off when the tin beads had collapsed onto the sample surface, forming gas only being circulated after then, during the alloying and cooling phases. Alloying times of 20 to 120 seconds were used, but no significant or correlatable variations in contact resistance were observed. This agreed with the results of Becker's (116) work on tin bead contacts on indium phosphide. He found an increase of contact resistance for longer alloying times (120 minutes) of between twice at 230°C and nine times short duration results at 330°C. I used alloying temperatures in the range 240-300°C. Good ohmic linear contacts could be reliably deposited using this method, especially onto the highest conductivity layers.

The samples were examined physically and electrically as for the gallium arsenide experiments, the success rate being around 55%,

slightly lower due to the difficulty of contacting the low conductivity layers reliably.

The experimental procedure followed was similar to that used in the examination of the gallium arsenide save that in order to achieve measurements above the threshold field considerably higher microwave powers were employed. This was due to the larger threshold field value - some three times the gallium arsenide value. Pressurisation of the main waveguide run with sulphur hexafluoride was necessary in order to prevent dielectric breakdown of the air at atmospheric pressure. The chances of this were also increased since non-unity VSWR obstacles placed in the waveguide caused considerable increases in electric field.

The samples were exposed to the highest power microwave radiation before experimental results were taken. This 'burn-in' test was used to eliminate samples which would be damaged by such exposure and render an experimental run useless. The d.c. characteristics were always checked before and after experimental runs to eliminate similar problems, a large change in resistance usually indicating radio-frequency damage, Some very slightly damaged samples yielded good results - however others yielded obvious inconsistencies.

Both contacts were of necessity as linear as possible, should either or both have been rectifying then the non-linearity would have resulted in detection of the incident microwave signal. This was observed in the absence of a d.c. bias as a pulse on the oscilloscope, and could be taken account of. Excess use of silver paint to form conducting bonds when mounting the samples also gave rise to this effect, care was taken to minimise it.

6.1.2. Sample Uniformity Examination

An experiment was set up to estimate the uniformity of the samples, since this may have indicated some reasons for low peak to valley

ratios (r) or particularly severe r.f. damage. It also measured the r.f. damage.

The arrangement and equipment is shown in Fig. 6A. A small jig was constructed from perspex having a 2 mm channel to accommodate the samples such that the contacts stood just proud of the top face of the perspex. The contacts were borne down upon by thin copper strips, fixed under bolts with tags for external connections. The jig was screwed to the base of a travelling microscope equipped with a micro-manipulator frame wired up with a probe. The probe had a needle of tip diameter approximately 15μ, which could be controlled in three dimensions with a resolution of 0.01 mm.

A pulse generator was employed in order that a high voltage be applied to the samples; this being pulsed at a low duty cycle (.01%) to avoid sample heating. Typically 400-500V signals were used at 1 KHz prf of width 100 nS. Typical power dissipation in a 2 kΩ sample was of the order of 12.5 mW; thus causing no appreciable heating.

Two measurements were made to assess the sample uniformity. The first to measure the current as a function of voltage, the second measuring voltage as a function of the distance along the sample. The first was to check any changes of sample resistance with bias, either due to the contacts or the material. The contacts had been examined by direct bias with dc up to about fifteen volts; this was a part of the initial electrical examination after alloying the contacts. This higher voltage check permitted examination up to fields of approximately 1.0 to 1.5 kV/cm, still well below threshold. No sub-linearity was detected in any of the samples within the experimental accuracy of $\pm$ 5%.

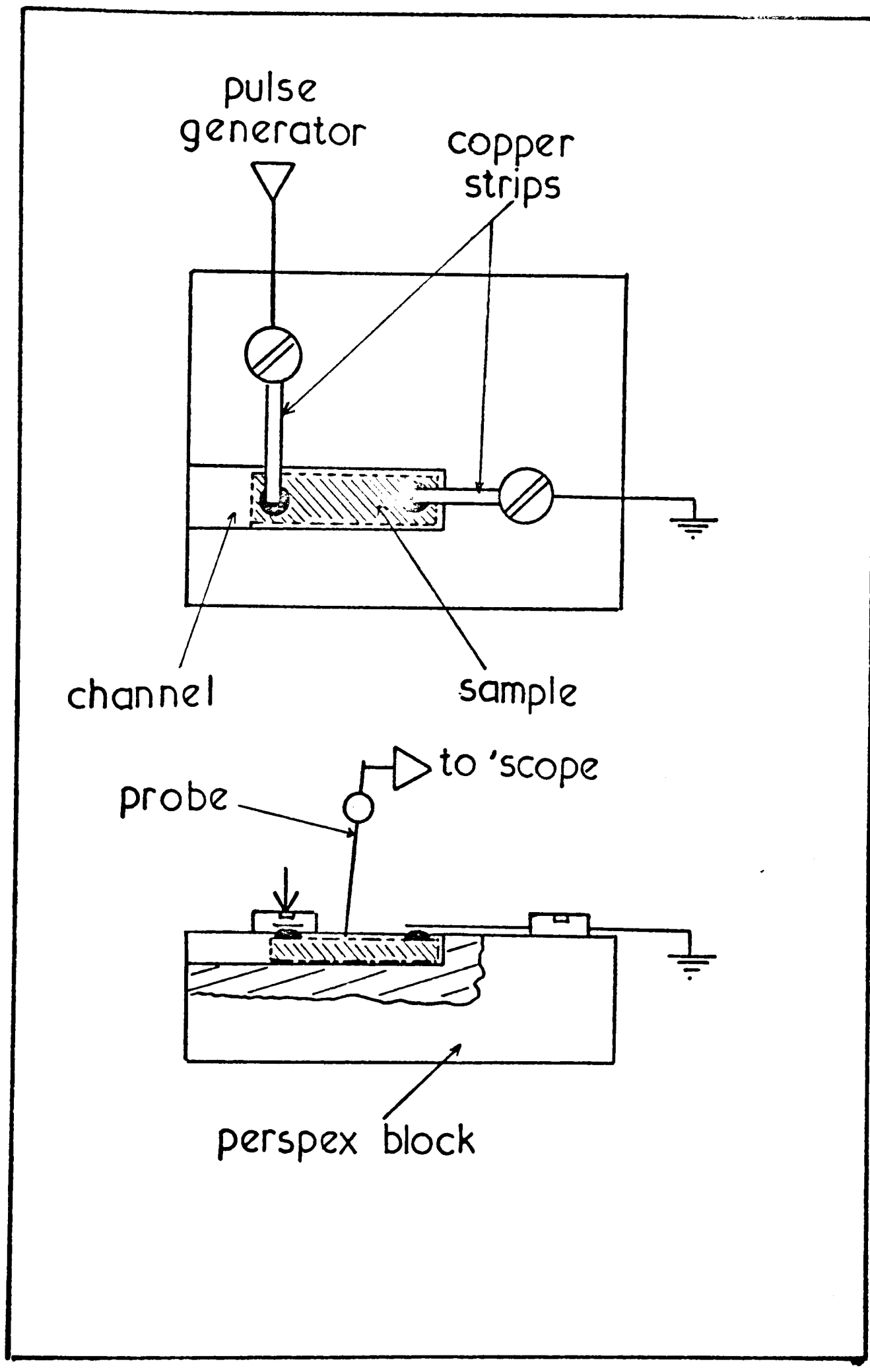

FIG. 6A

Sample uniformity investigation

experimental apparatus.

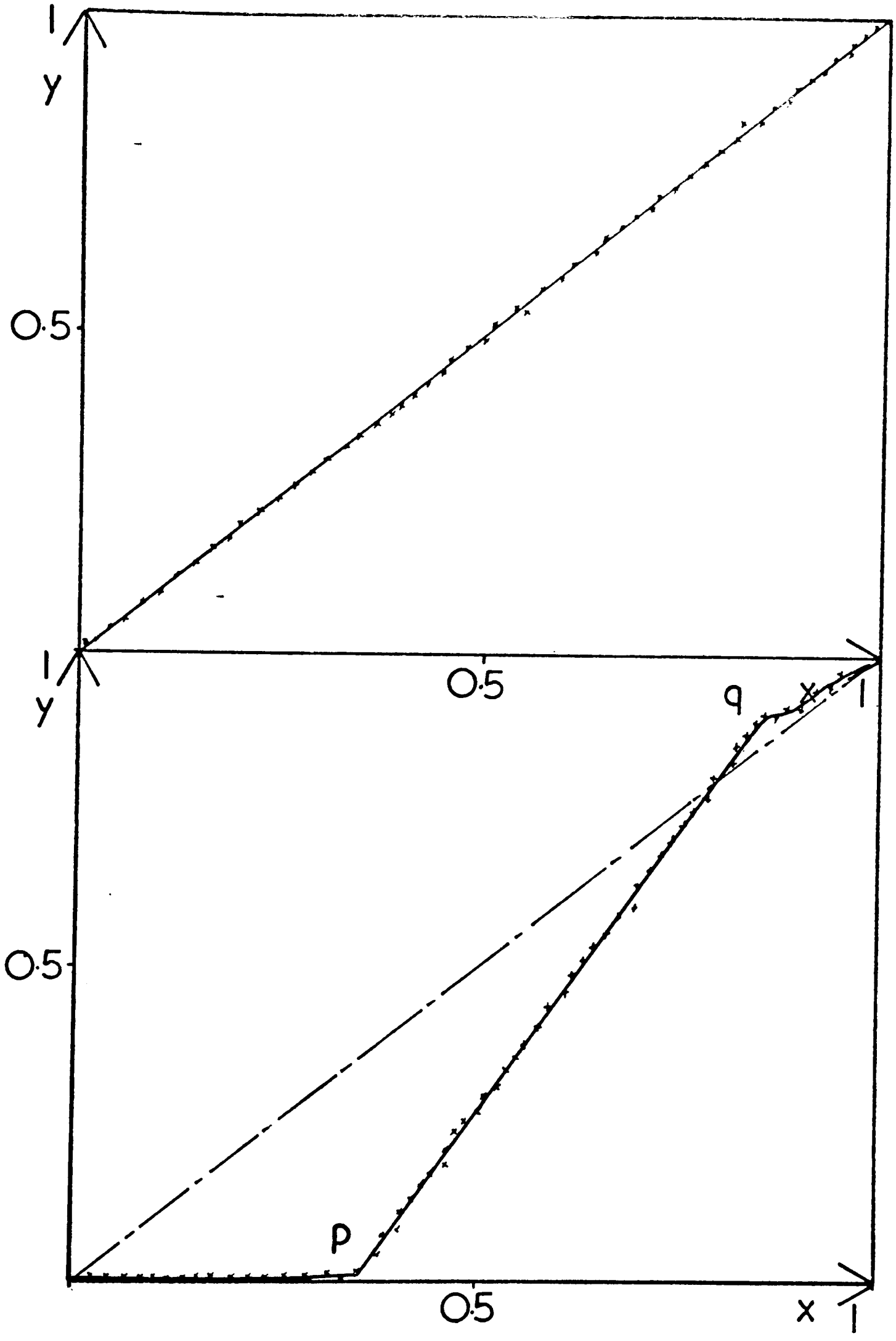

FIG. 6B

Sample uniformity, typical results

(i). sample IP16. (ii) sample IP7.

The second experiment obtained information relating the voltage at a function of position alone the sample. This was done by moving the point-contact probe along the sample and taking readings of the voltage at every 0.1 mm. This gave a resolution typically of 2% of the length, the accuracy was ± 2%. The curve of the voltage gradient was plotted and any departure from linearity could be attributed to four causes. Doping density fluctuation, layer thickness fluctuation, near contact effects, sample width variation. The latter two were not significant in the experiment since the alloying times were short and temperatures low, hence contact material had not diffused far enough for an effect to be measured, samples with non-parallel sides were difficult to make on account of the cleavage properties of the material, and only samples free of edge damage were used to avoid artificially induced high field regions. The manufactuerers guaranteed the layer thicknesses to better than 5% for these samples, also doping density fluctuations should have been less than 5%.

Typical plots for two samples are shown in normalised form at Fig. 6B. The upper graph shows a typical result from a satisfactory sample, the points all being within 5% of the linear slope which bears out the manufacturers data. The lower graph shows the plot from a damaged sample, damaged by the initial of 'burn-in' test. The graph shows the effect of presumed contact material migration in the region $x = 0$ to $x = 0.4$ (labelled p), two distinct regions of voltage gradients is near zero. There is also a discontinuity in gradient at $x = 0.85$ (labelled q), two distinct regions of voltage gradients being visible. Either the layer is thicker near q, or the carrier concentration is enhanced. Visual examination of this sample showed the surface between $x = 0$ and $x = 0.4$ to be crazed and covered by a network of dull fine cracks. The surface between $x = 0.4$ and $x = 1.0$ was smooth and mirror like.

All samples were checked after experimental runs had been performed

to investigate any possible correlation between damage and experimental behaviour. However very few samples surviving the initial r.f. burn-in test were damaged by the experimental work and no correlations could be made.

6.1.3. Considerations at Liquid Nitrogen Temperatures

Certain refinements were necessary in order to perform the experiment around 77°K. The sample in the holder was inserted into the brass pressure vessel as shown in Fig. 5C and this was sealed by catching an indium shin between the flanges. The vessel and wave-guide were pressurised with helium to prevent frosting at the liquid nitrogen temperatures. Helium however, has an inferior dielectric breakdown characteristic compared to air (see Fig. 3G) and as a consequence the experiment had to be terminated at lower powers than could be employed at room temperature. The use of sulphur hexa-fluoride was precluded at 77°K since it liquifies at 207°K.

After the vessel had been immersed in the dewar of liquid nitrogen it cooled fairly quickly (20 minutes) and once cooled little boil-off of coolant was experienced, this economy was assisted by a loose cover placed over the dewar after cool-down. The temperature was monitored via an iron/constantan thermocouple.

The low-field carrier mobility increases during the cool down to 77°K, where it was approximately ten times the room temperature value. Thus the resistance of the sample changes during cool down. This was monitored on an oscilloscope and used as a guide to the stability of the temperature when cooled. Typical mobility and resistance changes were:

Sample	Mobility μ_e cm^2/vs		Sample resistance R = KΩ	
	300°K	77°K	300°K	77°K
	Plessey Co. data		Experimental data	
IP20	4280	41,800	2.98	0.304
IP22	4450	47,000	8.72	0.825

This change in mobility resulted in adjustments being required to the data extraction relations between $\bar{\sigma}/\sigma_o$ and v/v_o (eq. (5.1)) and also a reconsideration of the space charge control criteria. Calculations of the ϱf product for the data above yield:

	ϱ_{300}	ϱ_{77}	ϱf_{300}	ϱf_{77}
IP20	0.61	0.069	21	2.4
IP22	1.94	0.197	68	6.9
	Ω.cm.		Ω.cm. GHz.	

Hence the criterion of eq. (3.2) that the ϱf product must be greater than 20 Ω cm GHz was contravened at this lower temperature. However the mobility decreased quickly with increasing field and calculations of the space-charge suppression criterion, eq. (3.22), in the computer programme for evaluation of the data via the Tschebychev polynomial approximation indicated that this was obeyed. In addition the criteria of eq. (3.24):

$$\frac{\bar{\mu}_N}{\bar{\mu}_P} < \frac{\phi_o}{\pi - \phi_o}, \qquad \phi_o = \arcsin \frac{E_T}{E_{max}} \qquad (3.24)$$

was satisfied for the fields used in the experiment.

Carrier freeze-out was less than 10% in all cases, typical figures being:

	$n_{300°K}$	$n_{77°K}$	$\Delta n/n_{300}$
IP20	$2.4\ 10^{15}$	$2.18\ 10^{15}$	-9.2%
IP22	$7.2\ 10^{14}$	$6.9\ 10^{14}$	-4.2%
	cm.$^{-3}$	cm.$^{-3}$	

These were also taken account of in the calculation of resistance and the velocity-field characteristic.

6.2. EXPERIMENTAL RESULTS

6.2.1. General Observations

The experimental data were compared for the different samples and cross-checked to eliminate errors as far as possible. One particular check was to evaluate the electric-field values in the guide at the plane of the sample via various approaches.

Considering the unperturbed, matched $TE_{10\square}$ mode we have for the maximum field at the centre of the broad wall

$$E_o = {}^1/b \sqrt{2 Z_g W_o}$$

$$Z_g = \frac{b}{a} \cdot \frac{\lambda_g}{\lambda_o} \cdot \left(\frac{\mu_o}{\epsilon_o}\right)^{1/2} \qquad \text{for } TE_{10\square} \text{ modes}$$

Knowledge of the various constants enabled this field to be calculated. Measurements of the incident and reflected powers enabled calculation of the VSWR of the obstacle which then led to the maximum and minimum fields in the guide as follows:

$$\left(\Gamma_V\right)^2 = \frac{W_R}{W_I} = \left(\frac{S-1}{S+1}\right)^2$$

$$E_{min} = \frac{E_o \cdot 2}{1+S}$$

$$E_{max} = \frac{E_o \cdot 2S}{1+S}$$

These field values were compared with the field in the sample computed via the programme analysing the data. For all samples it was found that:

$$E_{min} < E_{sample} < E_{max}$$

and also for the majority

$$E_{sample} = \gamma E_{max} \qquad (6.1)$$

with: $0.6 < \gamma < 0.8$

the factor γ increasing smoothly between the limits as the incident power was increased. No direct evidence was available, but these calculations served to suggest that these fields were consistent and no large resonant variations reported by Anderson et al (109) existed in the sample/waveguide interface, further borne out by the actual results obtained of the velocity-field characteristic.

Considering the ideal calculations where the waveguide is assumed lossless and the impedance is considered to be pure real; the sample appears to be at neither a VSWR maximum or minimum and therefore not a real impedance. It appears in general to present a complex network impedance along the lines of the analysis of Marcurvitz (92), and the power absorbtion data is examined and compared below.

6.2.2. Power Absorbtion

The absorbtion characteristics of two particular layers were examined. The first of these was the highest-resistivity layer available, for which the following data was available (at 300°K)

$$n_e = 1.4\ 10^{14}\ cm.^{-3} \qquad \mu_o = 3590\ cm^2.\ v^{-1}.\ s^{-1} \qquad \sigma = 0.08\ \mho\ cm^{-1}$$

Three samples were successfully contacted, albeit with high resistance contacts, data on these were:

Sample	Active layer dims mms	Sample cross sec. mms	R_{Theory} kΩ	R_1 kΩ	R_2 kΩ
IP5	4.39 x 0.94 x 0.009	0.94 x 0.35	89.2	100	167
IP8	4.08 x 1.00 x 0.005	1.00 x 0.35	102	160	140
IP12	5.48 x 0.40 x 0.003	0.40 x 0.35	570	810	1130*

*partially rectifying

The absorbtion as a function of incident power was measured for each of the three and also for the substrates IP5S and IP8S, the active layers having been etched off. The results of these measurements are shown at Fig. 6C.

The total absorbtion decreases as the epilayer thickness decreases, although the curves are not all similar, IP8 being far smoother than the other two. The absorbtion of the substrates is of the same order, but far more constant.

Using the theory of Marcuvitz (92) the diameters of the equivalent circular posts to the epilayers and the total posts are as follows together with the absorptions.

	Epitaxial layer		Total post cross section	
	d_{oe}	W_{ae}	d_{ot}	W_{at}
IP5	0.47	0.281	0.701	0.415
IP8	0.50	0.286	0.778	0.442
IP12	0.20	0.041	0.46	0.278
	mms		mms	

d_o = diameter of equivalent counterpart W_a = power absorbed

sub_e = epilayer sub_t = total(epilayer and substrate)

Clearly the figures for the total dimensions of the posts fit the zero field results more clearly, although IP8 exhibits much less absorbtion than the sample theory predicts, being nearest to the calculation based on the epitaxial layer alone. The substrate's theoretical absorbtion derived via the analysis of Marcuvitz is in the range -28 to

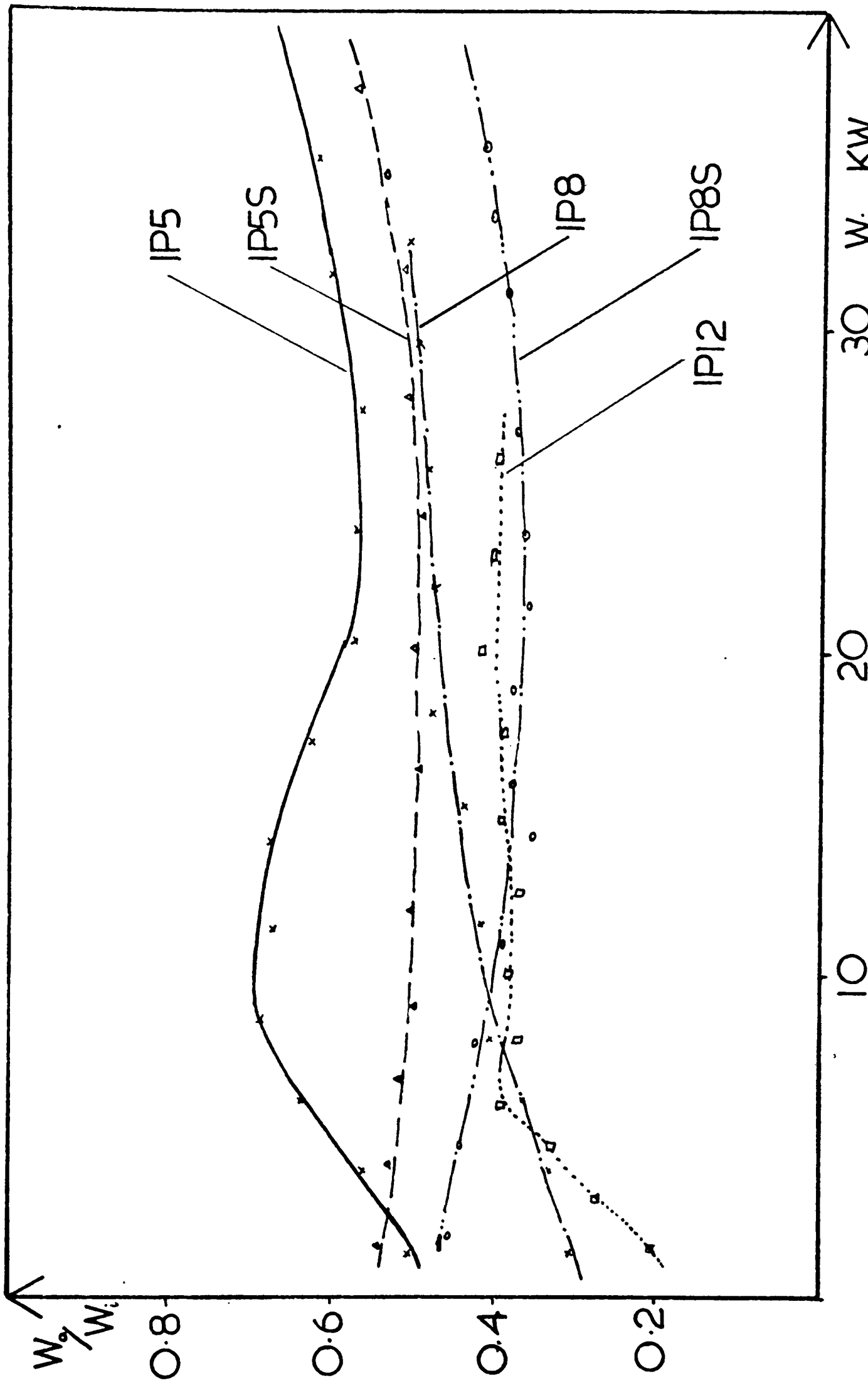

FIG. 6C

$\sigma = 0{\cdot}08\,\mho$cm layer and substrates-absorbed vs. incident power.

-30 dB, clearly contravened. The post width is wide compared to the theory of Champlin et al (106,107) and the fields distorted, perhaps because of resonant effects as suggested by Majborn (109), or the effect of having heavily compensated material in the guide with some 10^{16} carriers present rather than the 10^{13} free carriers. Indeed the absorbtion is typical of material having a resistivity in the range 0.10 - 0.16 $\mho cm^{-1}$; with a mobility of 200 $cm^2 . V^{-1} . s^{-1}$ this would give a carrier concentration of $3\text{-}5 \times 10^{15}$ cm^{-3}, near the true total density of all carriers.

The average temperature rises during these experiments were some +60 to +70°C over ambient due to the high absorbtion.

The layer had such poor contact properties that reliable d.c. conductance measurements were impossible; the only approach to the velocity-field characteristic would be via the measurement of bulk material, not epitaxial.

This problem was investigated further using a higher doping-density layer onto which good ohmic contacts were deposited. Data for this were:

$$n_e = 7.5\ 10^{14}\ cm^{-3} \quad \mu_o = 4{,}740\ cm^2\ v^{-1}\ s^{-1} \quad \sigma_o = 0.571\ \mho cm^{-1}$$

One sample was used to keep dimensions similar and it was progressively etched such that epitaxial layer thicknesses of 18.5, 15, 10 and 5 microns were examined. The substrate was also measured alone, with both back and front facing the generator to discover any surface finish effects. The results of these measurements are shown at Fig. 6D. The theoretical absorbtion by a post of σ_o = 0.571 $\mho cms^{-1}$ and dimensions of the total post was 38% (Marcuvitz (92)).

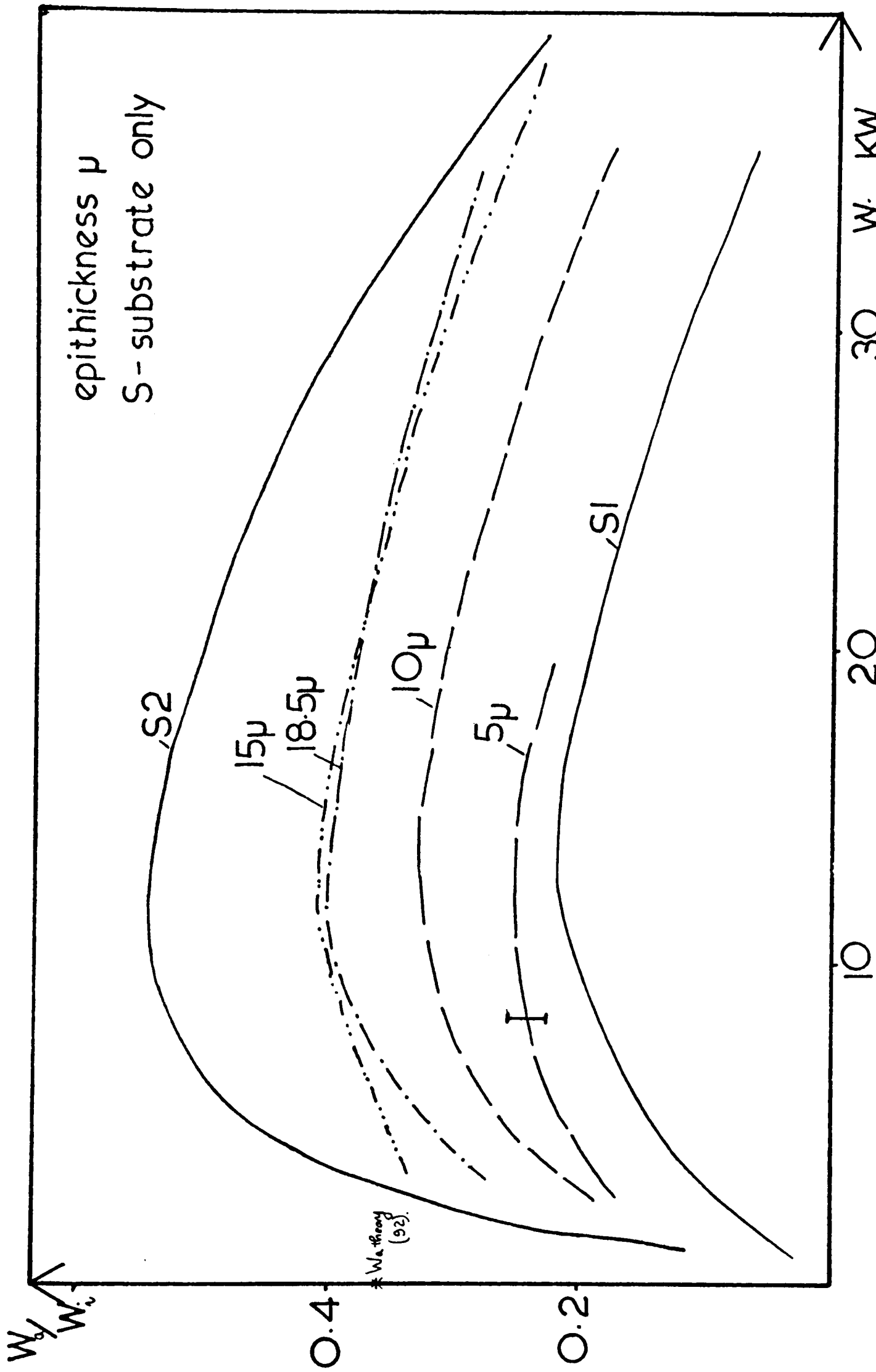

FIG. 6D

Sample IP16 ($\sigma = 0.57\ \Omega cm$)

absorbed vs. incident power

The results show a gradation of absorbtion proportional to the epilayer thickness, up to a critical thickness above which there was no increase. Here also the maximum agrees closely with Marcuvitz's theoretical prediction. The surface finish may have an effect, the substrate back was extremely rough by comparison with the front etched surface after removal of the epitaxial material. Analysis of the velocity-field characteristic from these results is described in Section 6.2.4.

The skin depth of the material is not significant here since, following the expression

$$\delta = (\pi f \mu \sigma)^{-\frac{1}{2}} \qquad \delta = 0.38 \text{ mm}$$

and for the maximum epitaxial layer thickness:

$$\frac{t_{epi}}{\delta} = \frac{18.5\ 10^{-6}}{3.8\ 10^{-4}} \simeq .05 \text{ of a skin depth}$$

6.2.3. Velocity-Field Characteristic from Power Absorbtion Data

It is now apparent from the foregoing that the simple one component, homogeneous post approach is inadequate due to perturbation of the fields by the substrates. One attempt was made to calculate data for a velocity-field characteristic from absorbtion data; which in this particular case agreed well with Marcuvitz (92) at low fields and behaved as predicted. This was a high conductivity layer with data:

$$n_e = 2.5\ 10^{15}\ cm^{-3}, \quad \mu_o = 4{,}200\ cm^2\ v^{-1}\ s^{-1}, \quad \sigma_o = 1.67\ \mho.cm^{-1}$$

$$W_{a\ theory} = -5.15 \text{ dB} \qquad W_{a\ exp} = -5.21 \text{ dB}$$

The conductivity was derived from the absorbed power data and the velocity-field characteristic calculated accordingly. The maximum absorbtion was -3.05 dB, yielding a conductivity of 0.18 at the minimum value. Hence ($\bar{\sigma}/\sigma_o = 0.109$). The velocity-field characteristic is shown in Fig. 6E. Data from this is compared with measurements of Hamilton (117) on the same slice material.

	V_p	E_T	v_v	$-\mu_n$	r
	cms^{-1}	kV/cm	cms^{-1}	$cm^2.v^{-1}\ s^{-1}$	-
IP10	$2\ 10^7$	6.5	$1.1\ 10^7$	-1600 ± 100	1.9
DKH (117)	$(1.7\ 10^7$ $-2.0)$	7.0	-	-	

The average sample temperature was $+40^{\circ}K$ over ambient.

The peak velocities differ but the threshold fields are in fair agreement, although both data are quite low compared to other measurements (see Ch. 2).

The errors in this approach are mainly concerned with the measurement of the power absorbed, and the effects on this power by the sample substrate, field perturbations etc. If the absorbed power was either measured too high (or affected by the sample such that it was higher than the simple homogeneous case) then $\bar{\sigma}(W_a)$ would have been underestimated since W_a rises for smaller $\bar{\sigma}$ for these particular sample dimensions. Pairing $\bar{\sigma}$ and W_a in the calculation for $\bar{\sigma}(E)$ would yield larger values of E for particular σ values. In V(E) the threshold field would be overestimated, and the peak-to-valley ratio (r) would also be overestimated. The negative mobility may well (fortuitously) remain accurate. Following the calculations through for W_a too small yields $\bar{\sigma}$ values too large and produces lower E_T, lower μ_n and lower r.

Considering the curve in Fig. 6E the threshold field is quite low, but agreeing with Hamilton (117), possibly suggesting under-

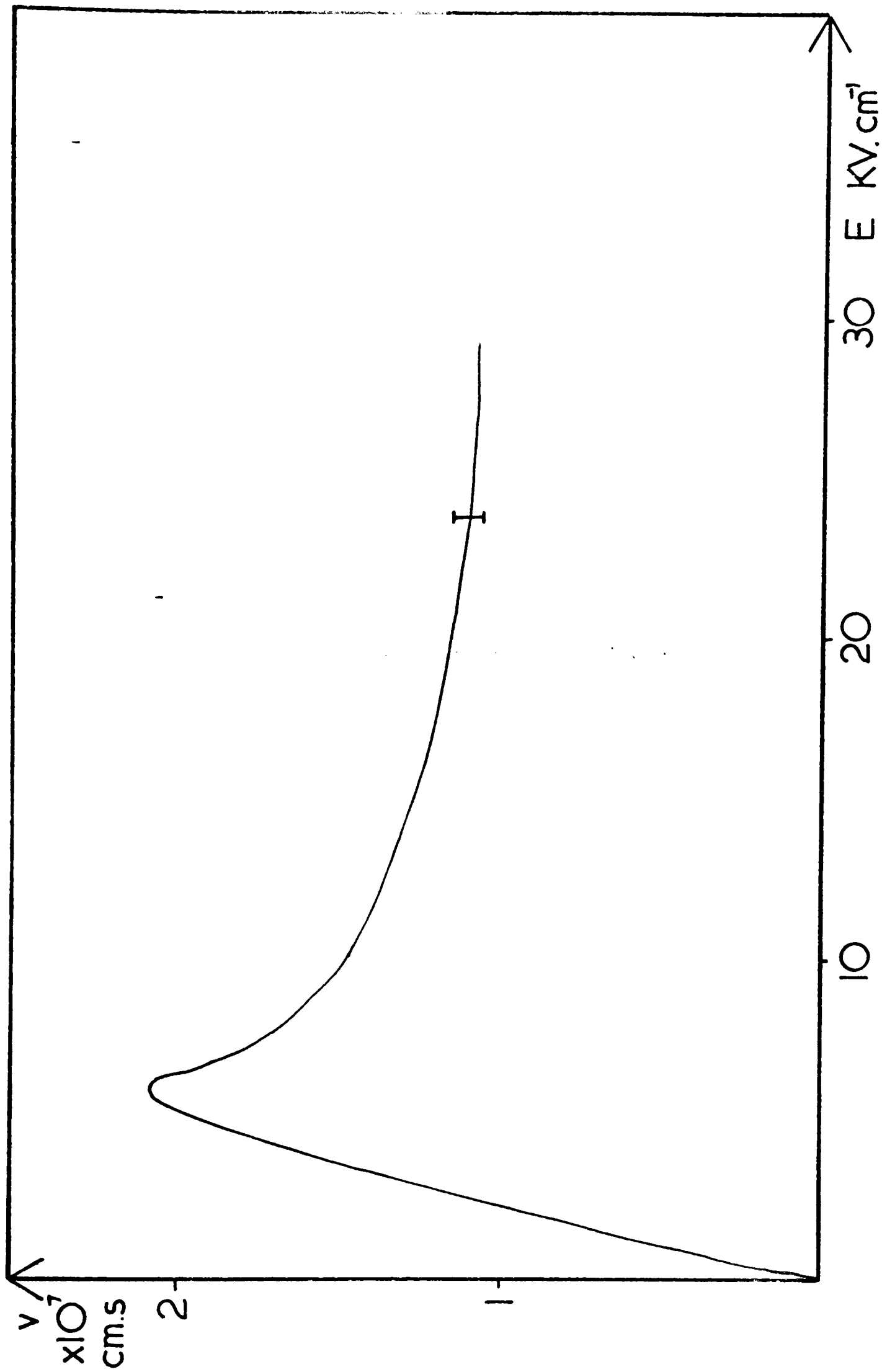

FIG: 6E

Sample IP10 - v(E) characteristic calculated using absorbtion data.

estimation of the absorbed power, also suggested by the low values of the peak velocity and peak-to-valley ratio. The negative mobility is however reasonable compared to other results. This is then a reasonable estimate of the general form of the characteristic although doubtful in overall numerical accuracy.

6.2.4. Variation of Epilayer Thickness

The results of IP16 for power absorbtion of various epitaxial layer thicknesses were extended by d.c. conductivity measurements. The velocity field characteristic was calculated for each condition. Two other samples were also measured being both from another layer and of different epitaxial layer thicknesses. Data for these were:

Sample	n_o cms^{-3}	μ_o $cm^2\ v^{-1}\ s^{-1}$	σ_o $\mho cm^{-1}$	Epilayer thicknesses μ
IP16	$7.5\ 10^{14}$	4470	0.57	5,10,15,18.5
IP11 IP14 }	$1.5\ 10^{15}$	4600	1.10	{ 12 6

The results are shown in Fig. 6F. The salient data are summarised below:

Sample		E_T $kV\ cm^{-1}$	V_p $x10^7\ cms^{-1}$	$-\mu_n(max)$ $cm^2\ v^{-1}\ s^{-1}$
IP16	5μ	15.5	3.25	-1000
	10μ	12.0	2.92	-1000
	15μ	10.0	2.84	-1100
	18.5μ	10.1	2.84	-1100
IP14	6μ	11.5	3.08	-1250
IP11	12μ	9.5	2.32	-600

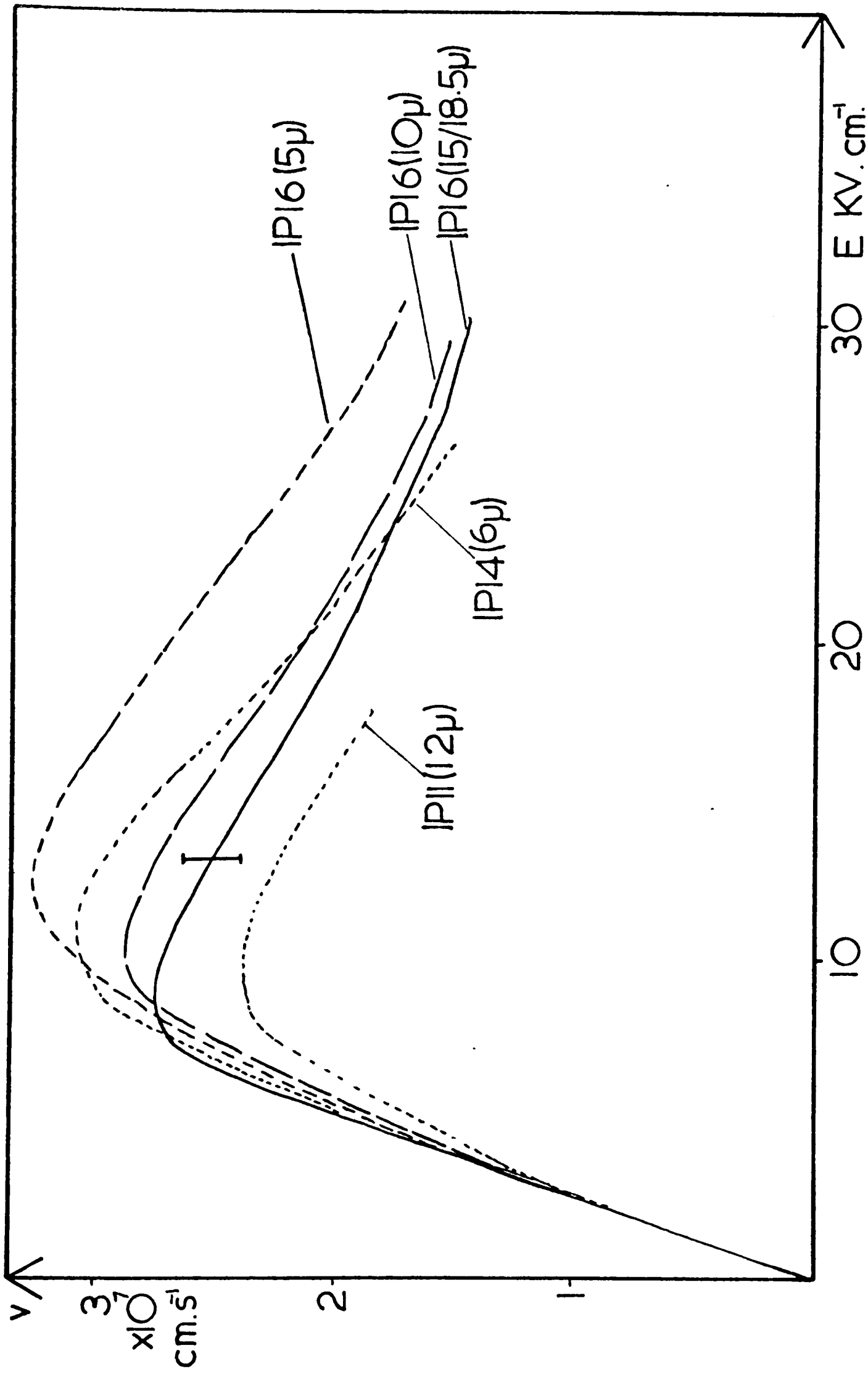

FIG. 6F

Variation of calculated v(E) curve with epitaxial layer thickness.

The samples IP11 and 14 show similar gradations except that there is a large change in the negative mobility; inexplicable, since doping profile variation and contact damage can both be excluded by the results of the post-experiment potential-probing test. The sample IP16 produced a more meaningful set of results since they all derived from the same sample. The gradation of calculated peak-velocity and threshold field values is clear; also the constant value of negative mobility.

Calculations of the fractions of power absorbed by the substrate and epitaxial layer were attempted from the experimental results, using the velocity-field characteristic as a correlating datum; no correlation was achieved using this approach. Using a simple ohmic heating approach, assuming constant and equal rf fields in both epilayer and substrate, then the ratio of powers absorbed by substrate and epilayer is:

$$\frac{W_{aS}}{W_{aE}} = \frac{\sigma_s V_s}{\sigma_\epsilon V_\epsilon}$$

(W_a = power absorbed, σ = conductivity V = volume)

using typical sample data as follows:

$$\sigma_S \simeq 10^{-4} \qquad \sigma_e \simeq 10^{0} \qquad V_S \simeq 1\ mm^3 \qquad V_e \simeq 3\ 10^{-2}\ mm^3$$

This ratio is of the order 1:300. Comparison of the results derived via Marcuvitż's analysis yields a similar ratio (1:300 = 24 dB).

Another possibility is that a space-charge build up was taking place and its rate of growth was controlled by the epilayer thickness - as in the analysis of Kino and Robson (118) concerning oscillation criteria for thin film layers. They derive a criterion for oscillation $n_d \geqslant 1.6\ 10^{11}\ cm^{-2}$ in a 'sandwich structure' where the thin layer is surrounded by insulating material of the same dielectric constant.

In the case of IP16 the doping density was n = 7.5 10^{14} cm^{-3} (σ_o = 0.571 $\mho cm^{-1}$). The n_d values were:-

d_e, μ	n_d, cm^{-2}
5	3.75 10^{11}
10	7.5 10^{11}
15	1.13 10^{12}
18.5	1.39 10^{12}

If this 'space-charge reduction' of the thinner layers was effective during these experiments then its effect would be most marked in the 5μ layer, which gave the highest values of peak velocity and threshold field in the experimental velocity field characteristic. Conversely space-charge instabilities produced the reduction in experimental values in the characteristic which would be in agreement with the experimental results of Glover (86) at 9.5 GHz. This thickness effect does not correlate with results of V(E) fig 6H from a number of layers but space-charge growth rates would strongly affect the measured absorbtion, and hence the characteristic, since the fields in the sample would not be constant across the sample area, which was assumed in the analysis. The effect was not observed in the gallium arsenide samples GA11 and GA12, as described in Section 5.2.3. The sample temperature rises were as follows:

	IP11	IP14	IP16
ΔT_c	36°K	37°K	52-68°K
ΔT_{av}	24°K	25°K	35-45°K

these being small enough to have no significant effect on the results.

6.2.5. Variation of carrier density

Measurements on a number of layers were made to investigate the variation of the velocity-field characteristic for different carrier densities. The data for the samples is shown at table 6G and the velocity-field characteristics at Fig. 6H. Data for sample IP16 thickest layer (18.5μ) and sample IP10 are shown for completeness.

The salient points on the characteristics are as follows:

Sample	N_o $cm.^{-3}$	V_p $x10^7$ cms^{-1}	E_T $kV.cm^{-1}$	μ_{nmax} $cm^2.v^{-1}s^{-1}$
IP21	$7.2\ 10^{14}$	2.63	10.7	-1200
IP22	$7.2\ 10^{14}$	2.57	10.5	-1150
IP16	$7.5\ 10^{14}$	2.84	10.0	-1100
IP17	$1.25\ 10^{15}$	3.08	11.0	-1350
IP18	$1.25\ 10^{15}$	2.95	10.8	-1350
IP11	$1.5\ 10^{15}$	2.30	9.5	-600
IP19	$2.4\ 10^{15}$	2.35	9.6	-1350
IP20	$2.4\ 10^{15}$	2.30	9.5	-1400
IP10	$2.5\ 10^{15}$	2.08	6.5	-1600

The gradations in the results are best described as follows: for the higher carrier densities the threshold field diminishes and hence the peak-velocity also diminishes. The peak-to-valley ratio should increase for the higher carrier densities since the negative mobility increases as the carrier density increases. The only seeming disagreement with these trends is IP11, although no obvious reason exists, all the tests were consistent with other samples.

Comparisons of the low-field mobilities and the maximum negative mobilities for these samples yield the following figures:

no.	layer thickness μ.	doping density cm^{-3}	mobility $cm^2 v^{-1} s^{-1}$	conductivity $\sigma\ cm^{-1}$	equiv diam mm.
IP5	9	$1.4\ 10^{14}$	3590	0.08	0.701
IP21	9	$7.2\ 10^{14}$	4450	0.515	0.682
IP22	9	$7.2\ 10^{14}$	4450	0.515	0.762
IP16	18.5	$7.5\ 10^{14}$	4740	0.571	0.678
IP17	15	1.2510^{15}	4680	0.935	0.706
IP18	15	1.2510^{15}	4680	0.935	0.652
IP11	12	$1.5\ 10^{15}$	4600	1.10	0.961
IP14	6	$1.5\ 10^{15}$	4600	1.10	0.588
IP19	13.5	$2.4\ 10^{15}$	4280	1.64	0.817
IP20	13.5	$2.4\ 10^{15}$	4280	1.64	0.614
IP10	8	$2.5\ 10^{15}$	4200	1.67	0.810

FIG. 6G

Indium phosphide samples – data

FIG. 6H

Indium phosphide - v(E) characteristic experimental results. 300°K.

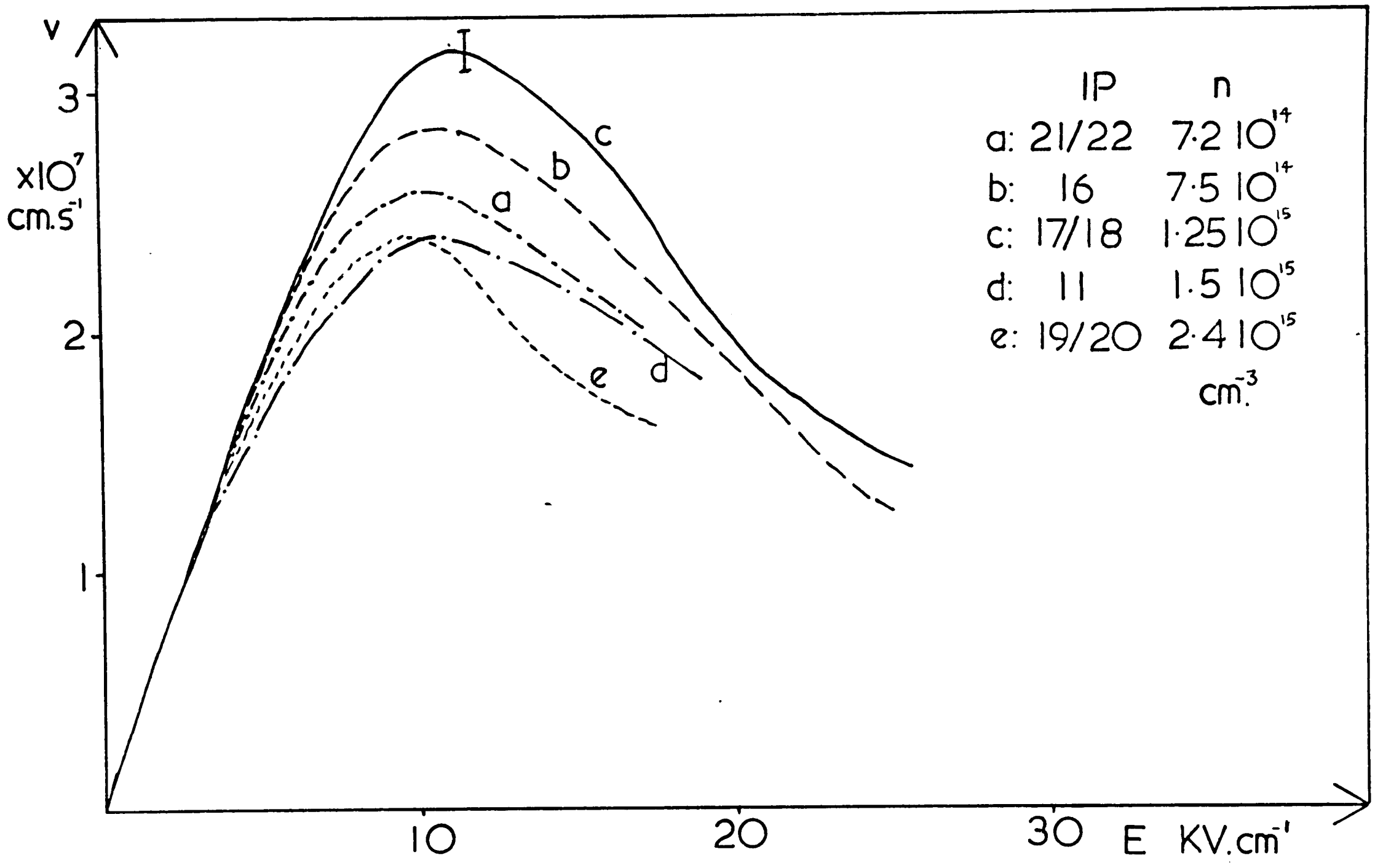

Sample	μ_o $cm^2\ v^{-1}\ s^{-1}$	$\mu_{n\,max}$ $cm^2\ v^{-1}\ s^{-1}$	$\lvert\mu_{n\,max}/\mu_o\rvert$
IP21	4450	-1200	.260
IP22	4450	-1150	.250
IP16	4740	-1100	.232
IP17	4680	-1350	.288
IP18	4680	-1350	.288
IP11	4600	-600	.130
IP19	4280	-1350	.318
IP20	4280	-1400	.327
IP10	4200	-1600	.381

Hence it appears (save IP11) that the ratio $|\mu_n/\mu_o|$ increases as the low field mobility decreases; i.e. the negative mobility is not particularly affected by low field mobility, although the higher carrier densities yield higher negative mobilities.

The samples were run with maximum average temperatures +30 to +45°K above ambient.

6.2.6. Velocity-Field Characteristic at 110°K

Two layers were investigated, two samples from each being examined. The velocity-field characteristics are shown at Fig. 6J, and the salient data, together with 300°K data, is shown below:

FIG. 6J

Indium phosphide - v(E) characteristic experimental results 110°K

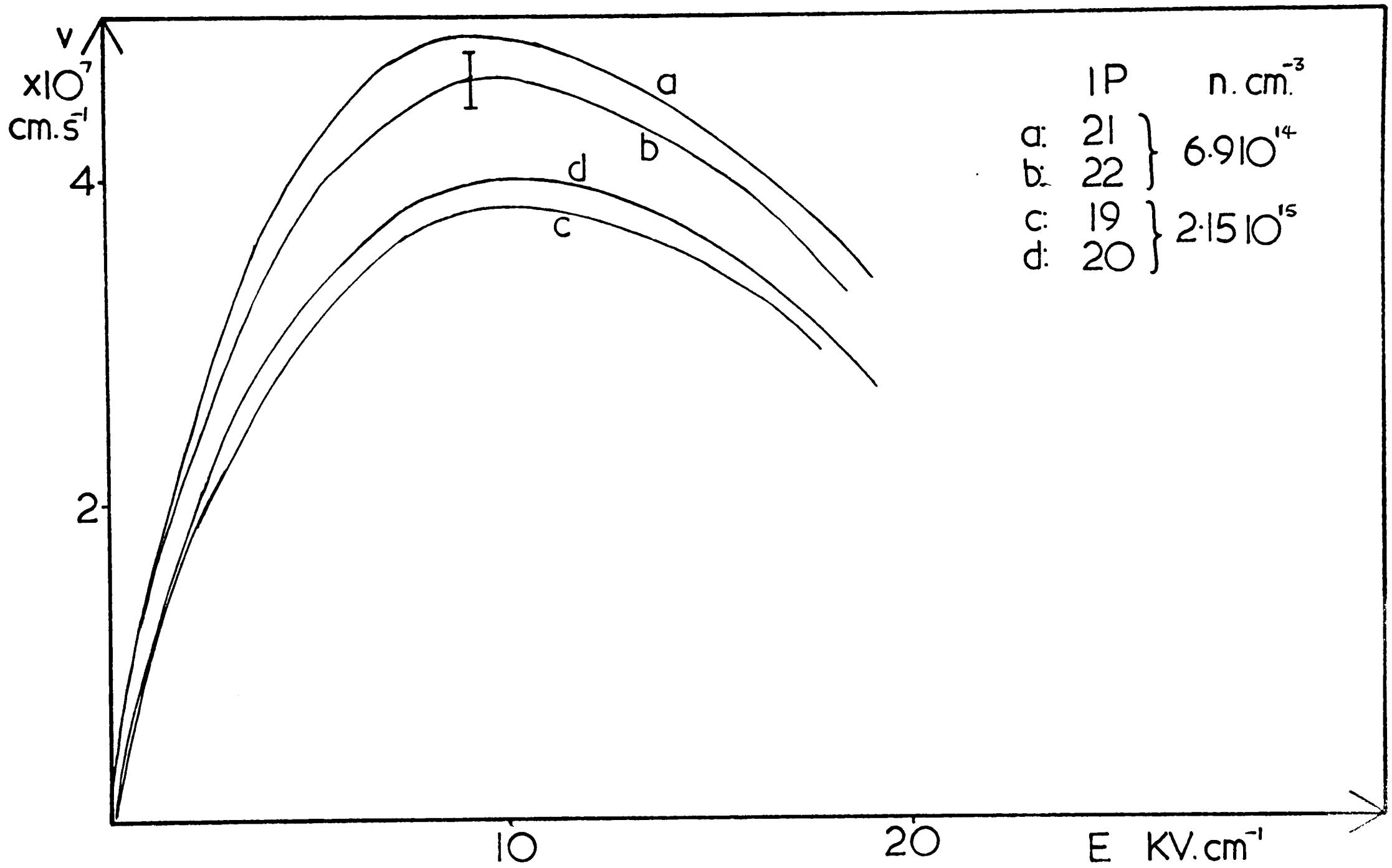

Sample		N_o cm^{-3}	V_p $x10^7$ cms^{-1}	E_T $kV.cm^{-1}$	$\mu_{n_{max}}$ $cm^2.v^{-1}.s^{-1}$
IP19		2.18×10^{15}	3.86	8.9	-1450
IP20		2.18×10^{15}	4.02	9.3	-1450
IP19/20	300°K	2.4×10^{15}	2.33	9.55	-1300
IP21		6.9×10^{14}	4.96	9.5	-1700
IP22		6.9×10^{14}	4.70	9.0	-1750
IP21/22	300°K	7.2×10^{14}	2.60	10.6	-1175

No obvious consistency is observed from different samples from the same layer, but the higher carrier density layer exhibited a slightly lower threshold field and considerably lower peak velocity as at 300°K. The mobilities however behave in the opposite fashion at 77°K compared to 300°K.

The sample temperatures were in the range +30 to +45°K above ambient (77°K) average. Assuming parabolic distributions of temperature the actual temperatures at the centre of the samples were

	T_c °K
IP19	97
IP20	107
IP21	99
IP22	100

(6.24)

6.3. DISCUSSION OF EXPERIMENTAL RESULTS

6.3.1. Reconsideration of Assumptions

The assumptions presented in Section 3.2. during the development of the experimental analysis are now reviewed in the light of the experimental results. These concerning material dimensions and static field gradients were justified and the results indicate no need for their recalculation. The relative magnitudes of the d.c., r.f. and r.f. harmonic terms obeyed the criteria set out previously in the work. The mathematical approximations in the analysis appeared consistent and the Taylor expansion, iterative and numerical integration techniques produced no large errors or apparently anomalous results from the experimental data.

Doping inhomogeneity and epilayer thickness were stated to be within $\pm$ 5% by the manufacturers. The major sources of error, therefore are space-charge growth and inertial effects associated with energy relaxation.

Energy relaxation effects would tend to overestimate the peak velocity and threshold field, whilst space-charge growth would tend to underestimate it, due to decreased power absorbtion. The energy relaxation time was estimated by Glover (68) from his experiments to be 0.177 pS and hence the product of this and frequency is

$$(\omega\tau_e)^2 = 0.14$$

which, although less than unity, is not considerably less than unity. This should produce an error of some +16% (68) in the peak velocity and peak-to-valley ratio, also a smaller, but of similar order, error in the threshold field.

Space charge growth effects may be involved, especially since the variation of power absorbtion with epitaxial layer thickness is so marked. However the 'nd' products for these layers were in the range $6.5\ 10^{11}$ and $3.2\ 10^{12}\ cm^{-2}$, considerably larger than the limiting value $1.6\ 10^{11}\ cm^{-2}$ calculated by Kino and Robson (118). The specimen IP16 etched from 18.5 μ to 5 μ changed the nd product from $1.39\ 10^{12}$ to $0.37\ 10^{12}$ still above the critical value, which should be smaller since the samples have air on one side rather than insulating semiconductor on both sides as in Kino and Robson's case. Hence there should be no space charge suppression in thin specimens.

No modification of the experimental results will be made since the relaxation errors are of the same order as the experimental error, and any errors due to space-charge growth should be small, considering the space-charge suppression criteria were obeyed, both the sample resistivity value and the computed expressions during the data analysis.

The experimental error is assessed at 15%, 5% in measurement of microwave data values, 5% in measurement of d.c. conductivity values and 5% for material uniformity. The results are shown at table 6K and summarised at Fig. 6L. The standard deviation of peak velocity (10%) and threshold field (6%) agree well with the predicted experimental accuracy.

6.3.2. Comparison with Published Data

The experimental velocity-field characteristic may be compared with both theoretical estimates and experimental results of other workers, the latter by both microwave heating methods and domain analysis. Of the theoretical estimates (refer fig. 2K) the best

		n_o	σ_o	$v_p \times 10^7$	E_t	$-\mu_n$
300 K	IP21/22	$7.2\ 10^{14}$	0.515	2.6	10.6	-1175
	IP16	$7.5\ 10^{14}$	0.571	2.8	10.0	-1100
	IP17/18	$1.25 10^{15}$	0.935	3.0	10.9	-1350
	IP11	$1.5\ 10^{15}$	1.10	2.3	9.5	- 600
	IP19/20	$2.4\ 10^{15}$	1.64	2.33	9.55	-1300
	*IP10	$2.5\ 10^{15}$	1.67	2.08	6.0	-1600
average (excl*)				2.63	10.2	-1190
				±0.27	± 0.59	± 190
st.dev.%				10.3%	6.0%	16%
110 K	IP21/22	$6.9\ 10^{14}$	5.08	4.83	9.25	-1700
	IP19/20	$2.18 10^{15}$	14.5	3.93	9.1	-1450
average				4.38	9.18	-1575
				±0.52	±0.26	± 160
st.dev.%				12%	3.0%	10%
$\frac{X(110\ K)}{X(300\ K)}$				1.66	0.91	1.33

$v_p \times 10^7$ cms^{-1}
E_T KVcm^{-1}
$-\mu_n$ cm^{2}v^{-1}s^{-1}

FIG. 6K

Indium phosphide - v(E) characteristic

salient experimental data.

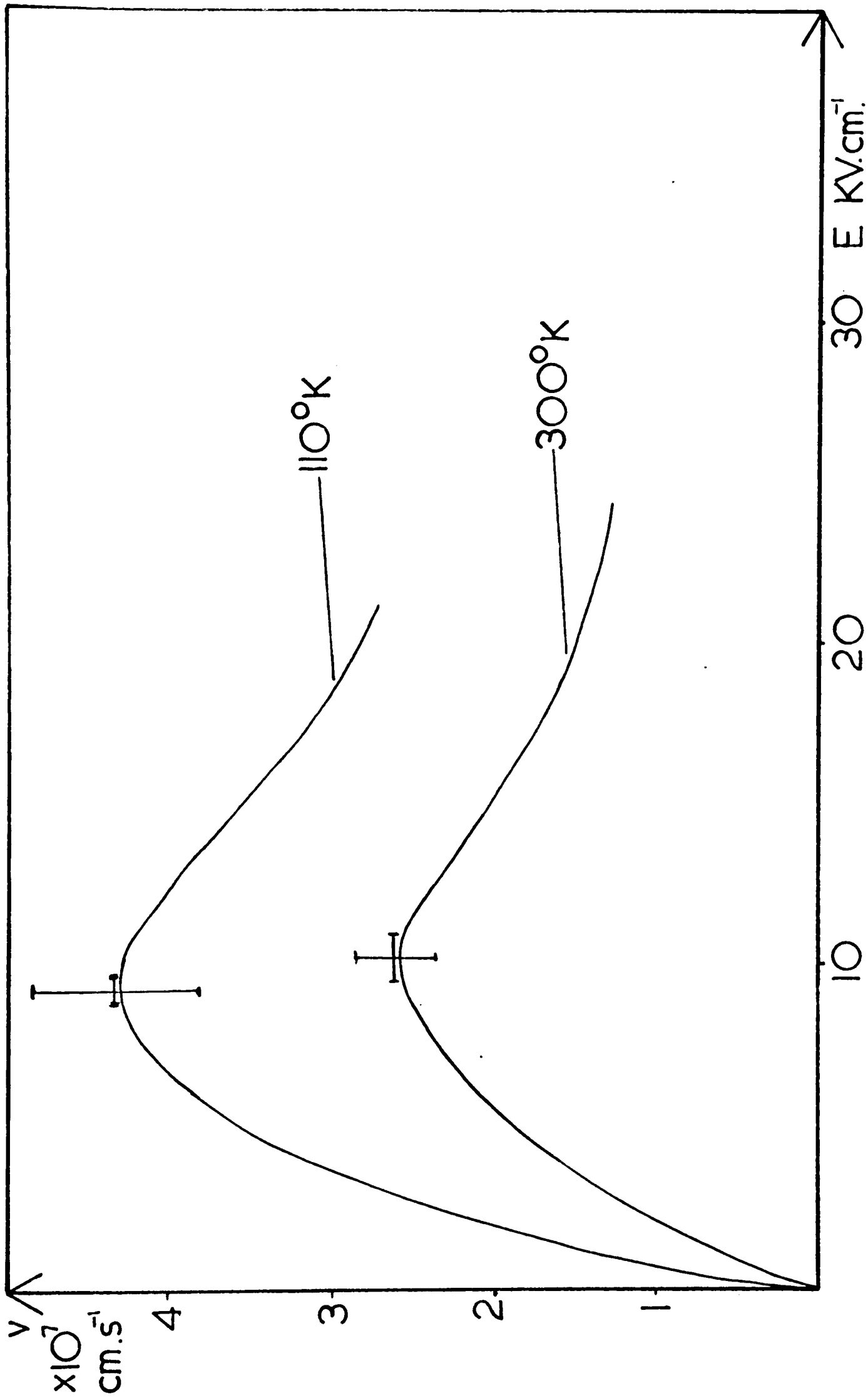

FIG. 6L

Indium phosphide - v(E) characteristic

experimental curves:- (i).110°K. (ii).300°K.

agreement is found with the three-level calculation of Hammar et al (57) and the two level calculations of Fawcett et al (60); the threshold field being lower than both these except that use of the screened pseudopotential method by Fawcett et al (61) produced better agreement as to the threshold field. These theoretical results are summarised as follows.

	V_p	E_t	
This work	2.63 ± .27	10.2 ± .59	
Fawcett et al (60,61)	2.45 - 2.5	10 - 11	(2 level)
Hammar et al (57)	2.5	11	(3 level)
Hilsum et al (58)	2.1 - 2.3	7 - 8	(3 level)
	$\times 10^7$ cms^{-1}	kV cm^{-1}	

This comparison points to an agreement with the system with $\Xi_{\Gamma L}$ = 3×10^8 eV cm^{-1} (61) in agreement with the work of Fawcett, whereas James (65) has suggested that

$$4.1\ 10^8 \leqslant \Xi_{\Gamma L} \leqslant 1.5\ 10^9 \text{ eV cm}^{-1}$$

perhaps the lower bound is indicated from these results.

Of the available experimental data (refer Fig. 3A) the results of this work agree well with the results of Glover (86) and Nielsen (88), although producing a lower threshold field than measured by all the microwave users. Agreement with dipole-domain measurements (80,81) is poor. A summary of the results is as follows.

	V_p	E_t	μ_n	Material used
This work	2.63 ± .27	10.2 ± .29	-1190 ± 190	Ep/S.I.
Glover (86)	2.7	11	-700	Ep/n^+
Nielsen (88)	2.5	11	-1000	Bulk
'T.Lam (85)	2.8	12	-1000	Ep/S.I.
Prew (80,81)	2.7	7	-2000	Bulk

Some variation with material quality is to be expected, also the users above have used three different types of material; bulk, epitaxial on n^+ and epitaxial on semi-insulating.

The microwave measurements predict higher threshold fields and peak velocities than domain measurements, the results of this work tending to fall in between the two extremes, but inclined towards the higher values. The trend of decreasing threshold field and increasing negative mobility with increasing material conductivity is not borne out by these other workers measurements. Majerfield et al (90) point out that use of the Hall mobility rather than the drift mobility may lead to overestimation of the peak velocity, which they measure by d.c. means as $2.5\ 10^7$ cms^{-1}, in close agreement with the results of this work. The threshold field they measured was in the range 10.5 - 11.5 kV cm^{-1}, slightly higher than the result of this work. However the agreement between various workers results is now quite reasonable especially considering Majerfield's sub-threshold measurements, Fawcett's theoretical calculations and the microwave experiments of Glover, Nielsen and this work. They suggest values for the characteristic as follows:

V_p = $2.5\ 10^7$ cms^{-1}

E_t = 10–11 kV cm^{-1}

μ_n = -1000 to -1200 cm^2 v^{-1} s^{-1}

These curves are plotted for comparison at Fig. 6M.

With regard to temperature effects on the velocity-field characteristic, there are two other results available for comparison at 100°K, one theoretical by James (10) and one experimental by Parkes et al (119), working on device performance data. Curves for 300°K and 100°K

FIG. 6M

Indium phosphide – v(E) characteristic

comparion of results.

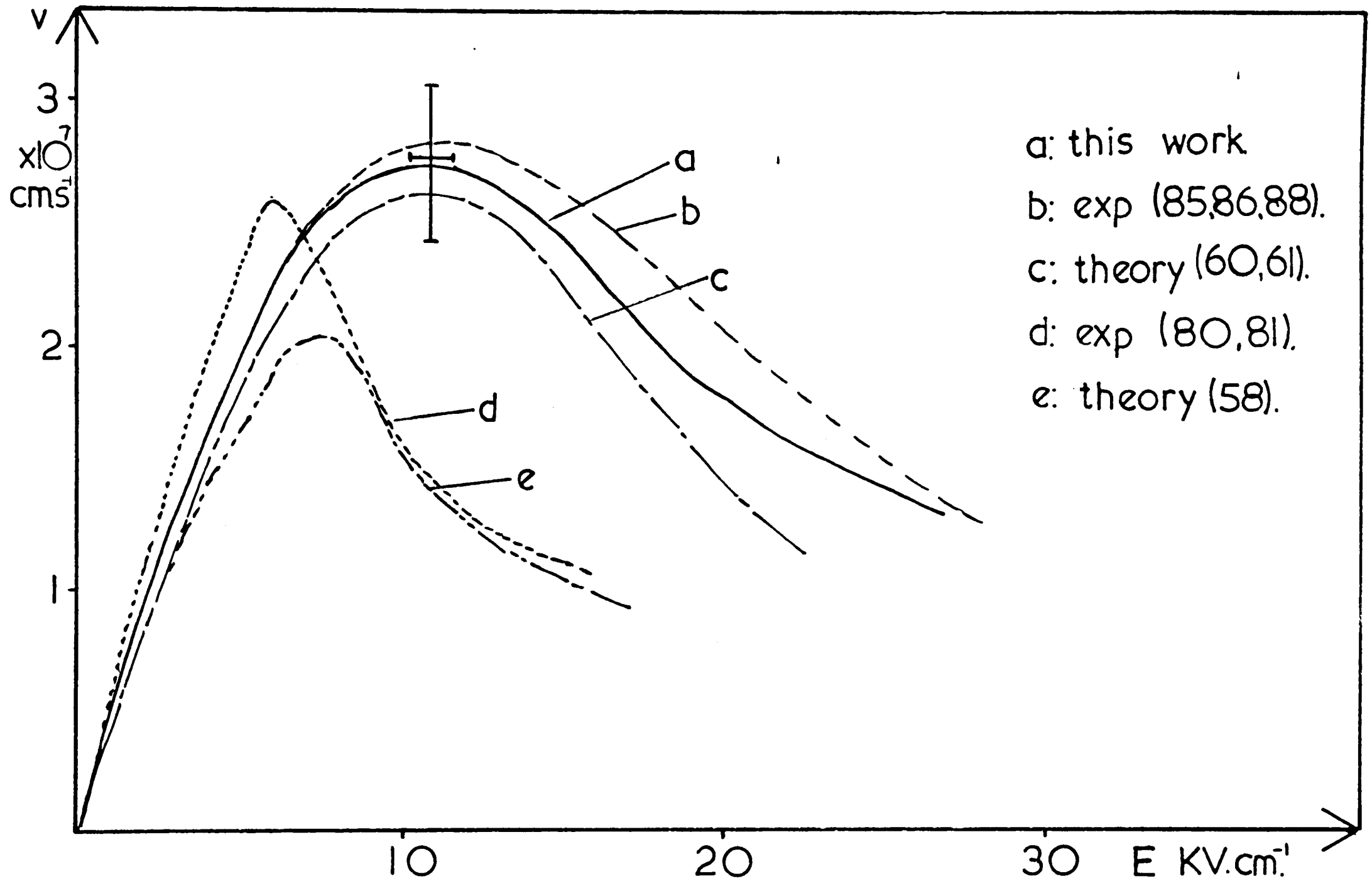

are shown at fig. 6N and data below.

	Threshold field kV.cm^{-1}			Peak velocity x10^{7} cms^{-1}		
	100°K	300°K	x(100)/x(300)	100°K	300°K	x(100)/x(300)
this work	9.18	10.2	-9%	4.38	2.63	+66%
James et al (10)	10	11	-9%	3.6	3.0	+12%
Parkes et al (119)	7	8	-8.8%	+12%	datum	+12%

Insofar as percentage changes in properties are concerned good agreement is found for threshold field variations between 300°K and 100°K. For the peak velocity however this work predicts far larger changes by cooling from 300°K to 100°K than other work. Should space-charge rearrangment have taken place then a lower velocity would have been measured. The ρf criteria are violated, but computed space-charge control criteria during the experimental analysis were not violated. The lower velocity measured for the higher conductivity layer (IP19/20) at 100°K may well have been due to some space-charge rearrangement. This does not explain the different between these results and those of Parkes et al (119).

The low-field mobility variations are, excluding the 1.4×10^{14} cm^{-3} layer (IP5,8) within a narrow range at both temperatures:

300°K $\quad 4200 \leqslant \mu_o \leqslant 4740$ cm^2. v^{-1}. s^{-1}. a variation of 13%

100°K $\quad 41{,}800 \leqslant \mu_o \leqslant 47{,}000$ cm^2. v^{-1}. s^{-1} a variation of 12%

This should have no direct effect on the general form of the characteristic, indeed as table (6.2.5) shows the negative mobility tends to show higher values for higher doping density, which itself tends to have lower mobility, contrary to the general observations summarised by Hilsum (29).

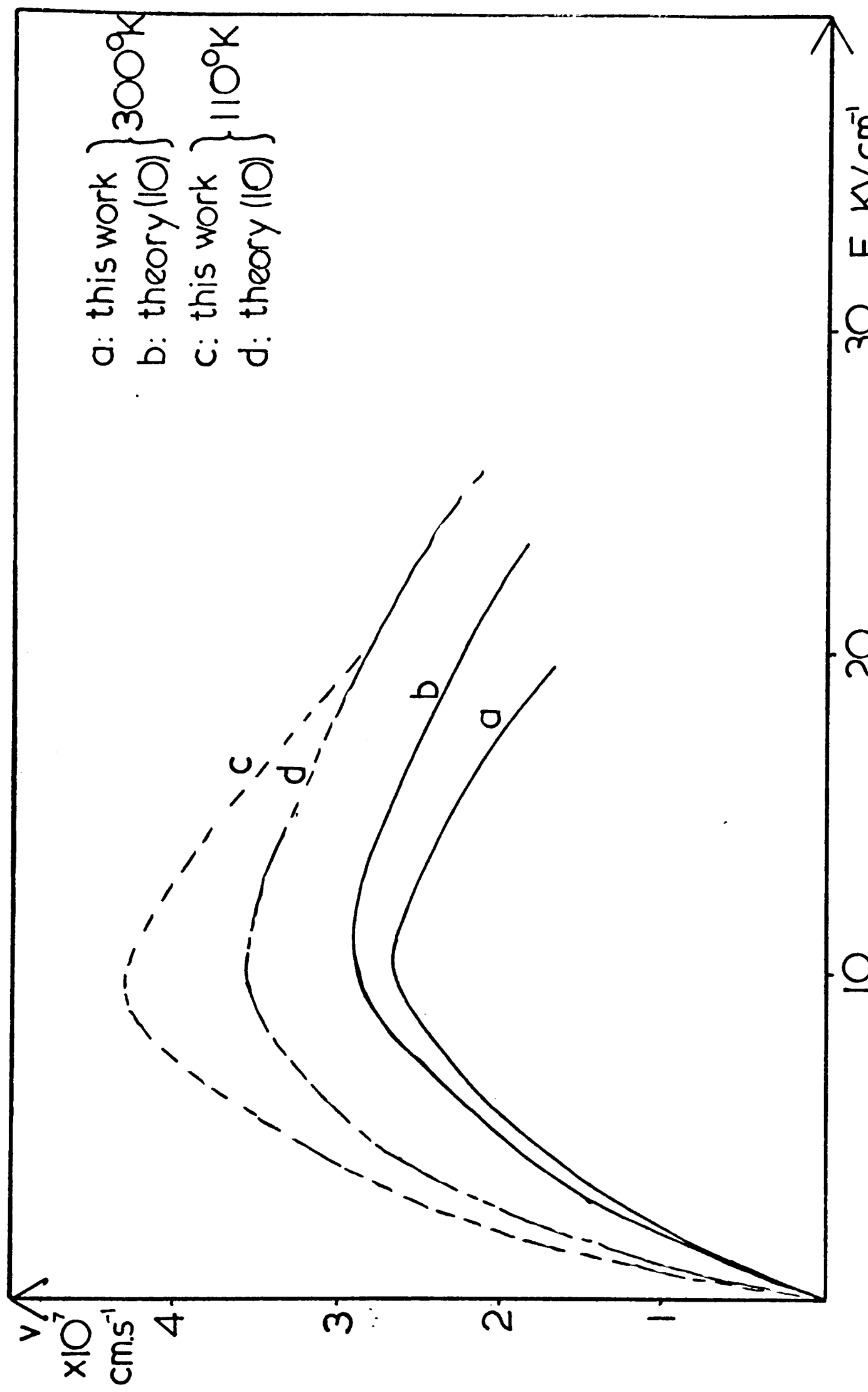

FIG. 6N

Indium phosphide - v(E) characteristic comparison of results.

No measurements extended to sufficiently high fields for the valley velocity to be measured reliably; this was due to dielectric breakdown within the waveguide section. Following the trends of other work it is to be expected that:

$$0.9 \leqslant v_v \leqslant 1.1 \times 10^7 \text{ cms}^{-1}$$

giving a peak-to-valley ratio:

$$2.15 \leqslant r \leqslant 3.2$$

with a median value of around 2.63. Hamilton (117) measured lower velocities than that suggested above, down to 0.7×10^7 cms^{-1} from observations of domains. This would give a high value for the peak-to-valley ratio r = 3.76. Insofar as prediction of a positive or zero saturated slope of the velocity-field characteristic above a minimum valley velocity at higher fields was possible, this would be more likely derived from domain measurements. No information was available from the microwave heating experiments of this work.

The disparities between various determinations of the velocity-field characteristic have been suggested to be partly due to a trapping phenomenon after workers (120,121) examining low-frequency current oscillations in high-resistance indium phosphide at low temperatures. They, following some theory of Ridley (122,123) have extended the ideas of preferential trapping of electrons transferred to the upper valley in the velocity-field characteristic measurements. Calculations of the characteristic for various relative capture rates lead to reductions in peak velocity and threshold field for high ratios of trapping probabilities. The traps in question were copper impurities in the indium phosphide. Teszner et al (124) comment that the drift-velocity is not significantly affected by such traps in epitaxial material for Gunn diodes, but that the domain dynamics are. Following this theory experiments studying domain dynamics may be more susceptible to errors due to the trapping phenomenon than microwave heating experiments performed on epitaxial material.

6.3.3. Comparisons with Equilibrium Parameters

A comparison of the carrier velocities measured and induced thermally in the valleys and at the Brillouin-zone edge was as follows. Reference to equation (2.9) yields data which shows ratios of drift-velocity to thermal-velocity as follows:

Temperature	Valley	vd/vth	(vd at threshold i.e = v_{peak})
300°K	Γ	0.68	
	L,X	1.5	
110°K	Γ	1.29	
	L,X	2.8	

In all cases the velocity corresponding to an electron energy at the zone-edge is at least ten times greater than any of the others. Thus we see that the electrons occupy only a small part of the Brillouin zone. The ratio of drift to thermal velocity is a measure of the carrier heating above the lattice temperature.

The peak velocity of 2.63×10^7 cms^{-1} at 300°K corresponds to a thermally induced velocity of an electron, if free ($m^* = m_o$) at 1100°K for upper valley electron ($m^* = 0.4\, m_o$) at 470°K, and if a lower valley electron ($m^* = 0.078\, m_o$) at 120°K. This heating effect is enhanced at the lower temperature.

6.3.4. Theoretical Device Efficiency

It is useful to consider the properties of a device manufactured from material having characteristics as measured by the foregoing experiments. For simplicity, the device is presumed to operate in an LSA mode (125), this giving the highest efficiency of the various modes (cf. § 3.5.2.). The fields in the diode device are shown schematically in Fig. 6P. There are two distinct regimes in the operation, one where the mobility of the carriers is positive, the other where it is negative or zero. The times spent in each are

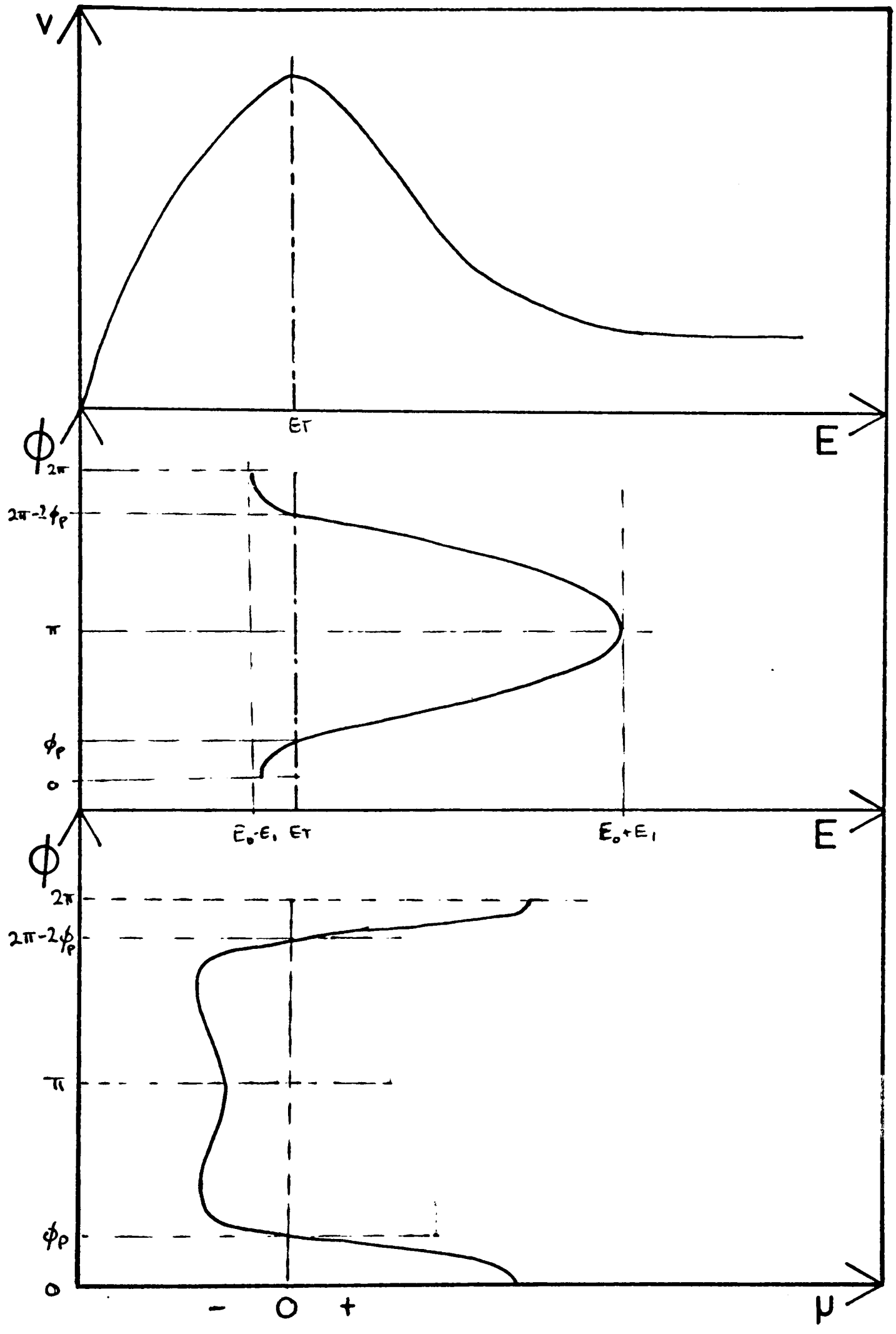

FIG. 6P

L.S.A. mode – biassing and waveforms

(i). voltage. (ii). electric-field. (iii). mobility.

represented by the angles such that

$$\phi_P + \phi_N = \pi$$

and from the equation for the field:

$$E = E_o - E_1 \cos\phi \quad , \quad \phi = \omega t.$$

when $E = E_T$, $\phi = \phi_P$

hence $$\phi_P = \arccos \frac{E_o - E_T}{E_1}$$

The positive mobility regime will be consumptive of power from the r.f. field, whereas the negative or zero mobility regime will result in power being dissipated to the r.f. field. Consequently it enables an efficiency to be specified such that:

$$\eta = -W_{rf}/W_{dc}$$

where η is the conversion efficiency, W_{rf} and W_{dc} are the net power consumptions by the device in the rf and dc fields respectively.

There is a space-charge-control criterion associated with the LSA mode, in comparison to the domain modes where build up into a domain is required. This is similar to that expressed as equation (3.23).

$$\exp\left(\frac{-t_p}{\tau_{dp}}\right)\left(\frac{-t_n}{\tau_{dn}}\right) < 1 \qquad (3.23)$$

as a criterion based on dielectric relaxation times (τ_{di}). Considering this we obtain:

$$\frac{\phi_P}{\phi_n} > \frac{\bar{\mu}_N}{\bar{\mu}_P}$$

where ϕ_P and ϕ_n are the times spent in positive and negative mobility regimes and $\bar{\mu}_P, \bar{\mu}_N$ are the average mobilities in those regimes. The equation may be rewritten:

$$\frac{\phi_p}{\pi - \phi_p} > \frac{\bar{\mu}_n}{\bar{\mu}_p}$$

Graphs of these functions are shown in Fig. 6Q and the resulting restriction on E_1 is shown as a function (E_1/E_0) plotted against E_0 in Fig. 6R. Fields greater than the limiting value of E_1 must be employed for a particular case so as to ensure sufficient time is spent in the positive mobility regime (ϕ_p) so as to ensure decay of any accumulation of space-charge. The employment of smaller fields will result in space-charge build up and as a consequence domain formation and operation in a mode other than LSA.

The power absorbed by a single carrier from the d.c. field applied to the device will be:

$$W_{dc} = \frac{qE_o}{2\pi} \int_{-\pi}^{+\pi} v \, d\phi.$$

and from the rf. field:

$$W_{rf} = \frac{qE_1}{2\pi} \int_{-\pi}^{+\pi} v \cos\phi \, d\phi.$$

These equations assume no space-charge perturbation, diffusion or relaxation, viz:

$$v(t) = v(E(t))$$

The efficiency (η) as before, is the fraction of dc power converted to rf

$$\eta = -W_{rf}/W_{dc}$$

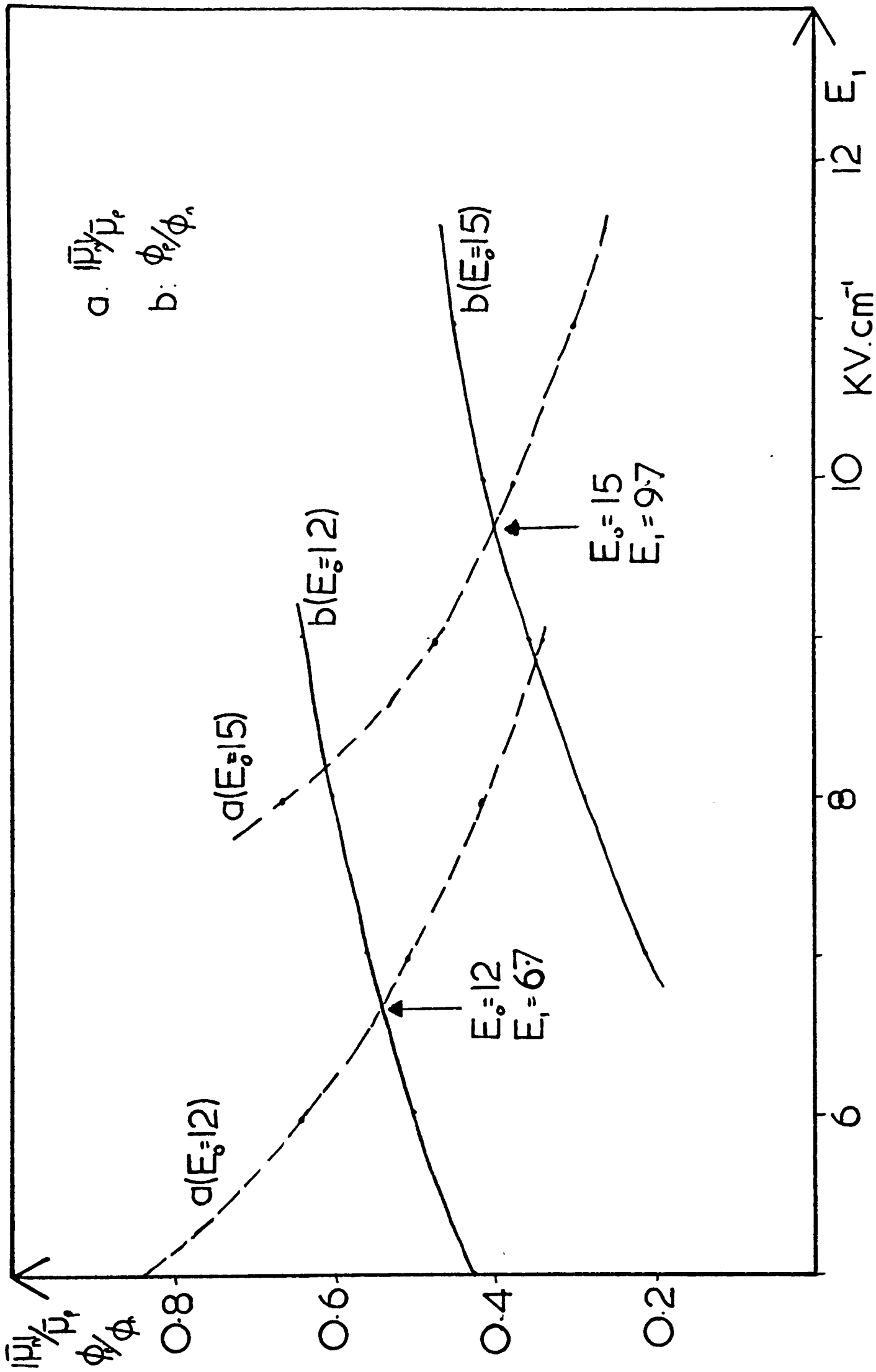

FIG. 6Q

L.S.A. mode –

space-charge control parameters.

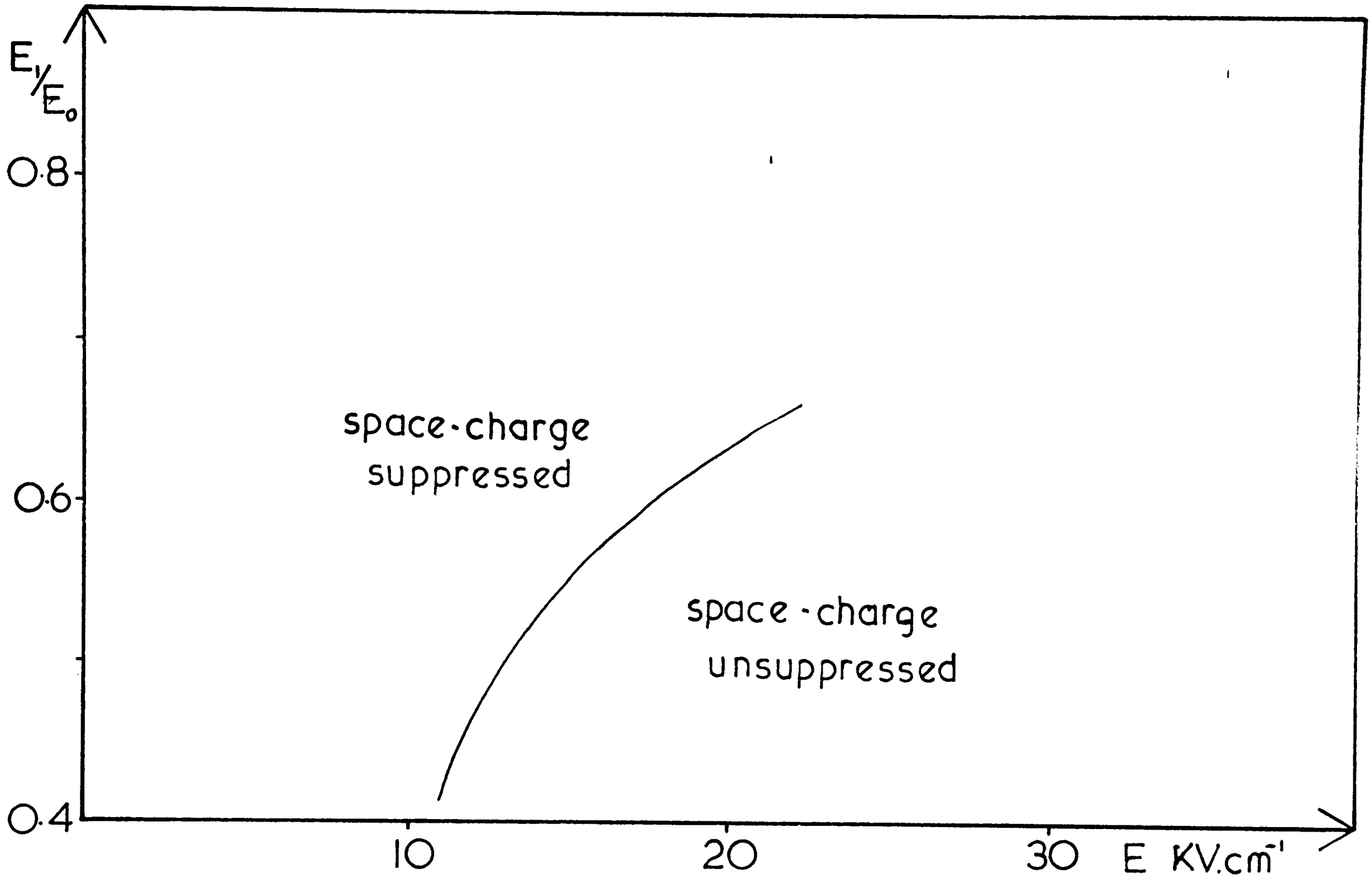

FIG. 6R

L.S.A. mode — space-charge field restrictions.

Normalising the equations to the notional threshold values,

$$E = E_t(a_o - a_1\cos\phi) \qquad E_o = a_o E_t, \quad E_1 = a_1 E_t$$

$$W_t = qE_tV_t$$

and from (6.43)

$$\frac{dv}{d\phi} = \frac{dv}{dE} E_t a_1 \sin\phi$$

$$\frac{dv}{d\phi} = \mu E_t a_1 \sin\phi.$$

rewriting the expression for rf and total power

$$\frac{W_{rf}}{W_t} = -\frac{1}{2\pi}\int_{-\pi}^{+\pi} \frac{v(\phi)}{v_t} a_1 \cos\phi \, d\phi.$$

integrating by parts, using the foregoing relations,

$$\frac{W_{rf}}{W_t} = \frac{a_1^2}{2\pi}\int_{-\pi}^{+\pi} \frac{\mu(\phi)}{\mu_o} \cdot \sin^2\phi \, d\phi. \qquad (6.2)$$

Similarly for the expression for the dc power as a fraction of the total:

$$\frac{W_{dc}}{W_t} = \frac{a_o v_\pi}{v_t} - \frac{a_o a_1}{2\pi}\int_{-\pi}^{+\pi} \frac{\mu(\phi)}{\mu_o} \cdot \phi . \sin\phi . d\phi \qquad (6.3)$$

The expression for efficiency then becomes:

$$\eta = \frac{\frac{a_1^2}{2\pi\mu_o}\int_{-\pi}^{+\pi} \mu(\phi)\sin^2\phi \, d\phi}{\frac{a_o v_\pi}{v_t} - \frac{a_o a_1}{2\pi\mu_o}\int_{-\pi}^{+\pi} \mu(\phi)\,\phi . \sin\phi . d\phi.} \qquad (6.4)$$

This was calculated using the velocity-field characteristic data obtained from the 300°K experiments. The results are plotted in Fig. 6S, the efficiency curves being shown for various values of dc field E_o, plotted against rf swing $\pm E_1$. The efficiency increases

up to a maximum dc field of 20 kV/cm, calculation was not extended beyond these due to non-availability of data. The form of the curves agrees with those obtained by Copeland (125). Taking account of the space-charge control requirement and its restriction on the rf swing E_1 for a particular E_o the highest efficiency obtainable for various values of E_o, conducive with values of E_1 giving space-charge control, are plotted in Fig. 6T.

They are compared there with the theoretical square-wave efficiencies calculated using the data derived from the experimental velocity field characteristic and the limitations imposed on fields to obtain the sinusoidal efficiencies of Fig. 6T; the calculation was based on those of Fig. 2J.

$$\eta = \frac{(r-1)}{(r+1)} \cdot \frac{(v_2/v_1 - 1)}{(v_2/v_1 + 1)} \qquad (6.5)$$

Comparison of these figures shows that the square-wave efficiency is three to four times that for simple sinusoids. The sinusoidal efficiency is also restricted above an operating point of (17 $\pm$ 12 kV/cm) due to space charge control effects (17 kV/cm = 1.95 E_T).

The above calculation for squarewaves assumes that the output is all useful, if not then the non-required harmonics will degrade the figures slightly up to $8/\pi^2$ for fundamental only. The effect of reducing the time spent in the negative mobility region and attaining a 'switching' type characteristic is seen to be important. This may be realised by a high value of the ratio between the circuit impedance and the diode negative resistance according to Fawcett at al (126), not necessarily a high Q circuit; they also suggest care in choice of $n(T)$ and $\mu(T)$ profiles in devices by improved heat sinking. Harmonic tuning may also be employed to achieve good space-charge control, indeed Kino et al (127) consider this a method of improving the performance efficiency of the domain modes of operation of Gunn devices.

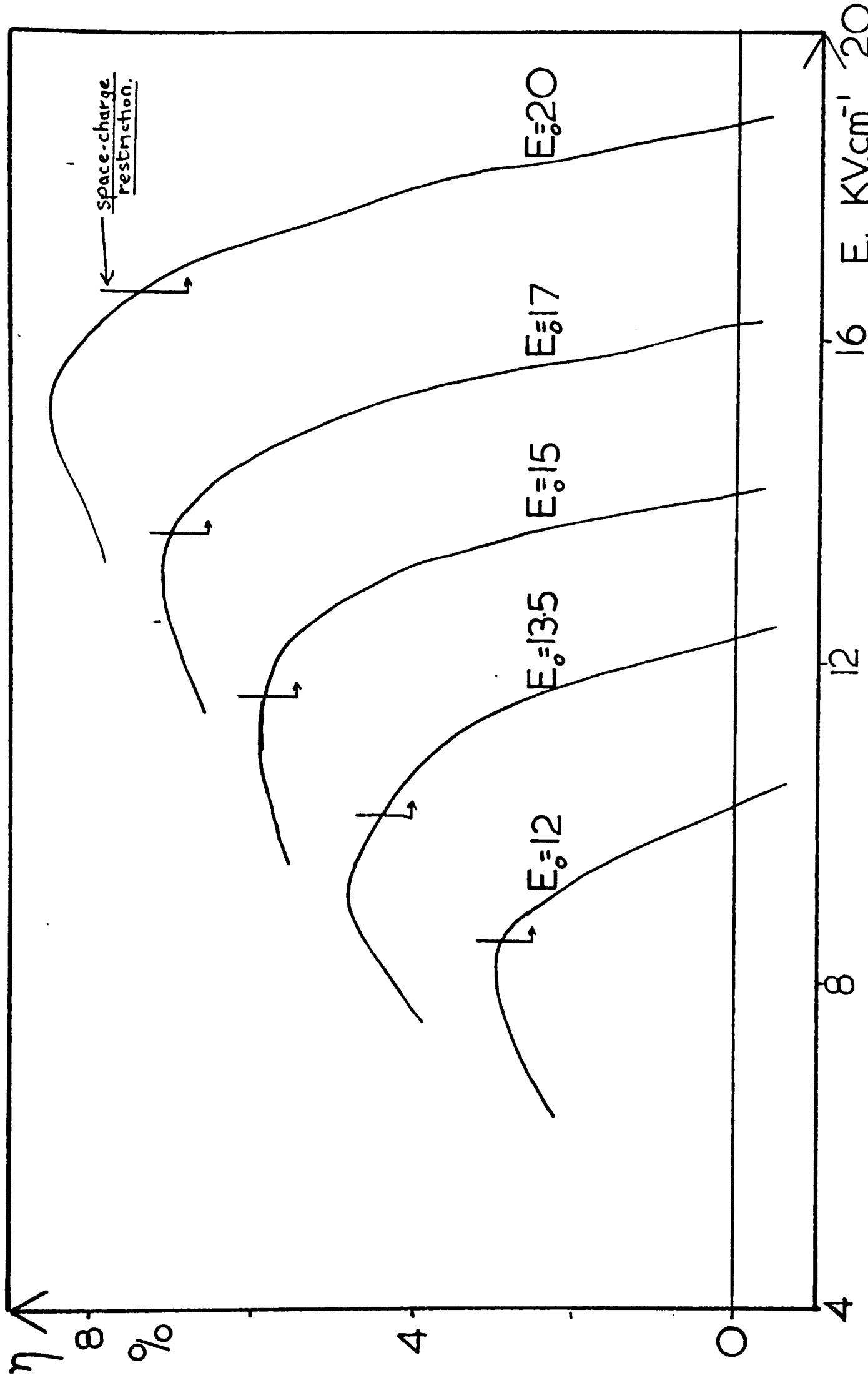

FIG. 6S

L.S.A. mode -

theoretical device - sinusoidal efficiency.

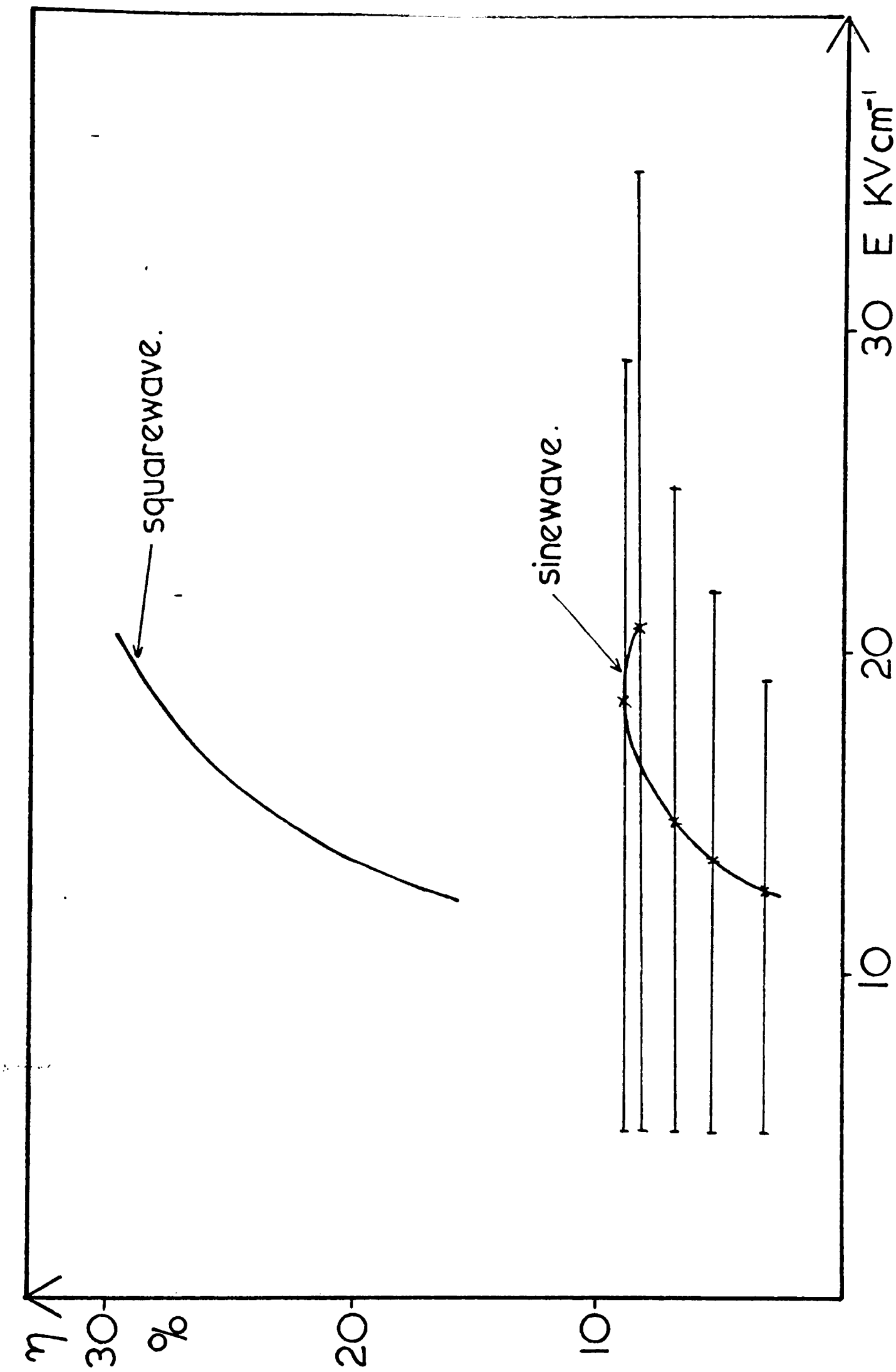

FIG. 6T

L.S.A. mode -

electric field swings and efficiencies.

FIG. 6U

LSA mode - squarewave efficiencies.

d.c. field E_0	r.f. field E_1	field ratio E_0+E_1 / E_0-E_1	effective peak-valley r	efficiency $\eta_0\%$	sinusoid efficiency $\eta_s\%$
12	7	3.8	1.79	16.5	2.7
13.5	8.5	4.4	1.99	20.9	4.4
15	10	5.0	2.09	23.6	5.9
17	12	5.8	2.15	25.8	7.0
20	15	7.0	2.20	28.0	6.9

The data obtained at 100°K was also investigated with a view to examining operating conditions at that temperature. Operation at the optimum fields for 300°K was prohibited by space-charge control cirterion being transgressed viz.

$$E_o = 17, \quad E_1 = \pm 12, \quad \phi_p/\phi_n = 0.305, \quad \bar{\mu}_n/\bar{\mu}_p = 0.750$$

however scaling via a_o and a_1 to the new threshold field (8 kV cm^{-1}) gave a permissible space-charge control arrangement, but a very reduced efficiency of only 0.2%. The space-charge control parameters are much more sensitive to the field-changes at this temperature compared to 300°K; this being due to the much higher positive mobility as the field decreases toward zero.

Shifting the operating point from $a_o = 1.67$, $a_1 = 1.33$ to $a_o = 1.67$, $a_1 = 1.25$ (this corresponding to a reduction in rf field swing from $\pm$ 10.6 to $\pm$ 10.0 KV cm^{-1}) just retains space-charge control and improves the efficiency to 6.1%. The overall order of the efficiency is not altered much by a temperature reduction from 300°K to 100°K due primarily to the shape of the velocity-field characteristic. Were the increase in peak velocity to improve the negative mobility, or the effective peak-to-valley ratio at a particular operating point then improvements in efficiency would be considerable.

Parkes et al (119) report significant variation in efficiency over a temperature range with higher temperatures causing a reduction in efficiency. They also report an improved high-frequency efficiency with the operating frequency band increasing as the temperature is lowered. The device efficiency will be strongly influenced by the effective velocity-field characteristic of the device at the particular operating temperature, apart from other environmental factors such as cavity design, coupling of loads etc.

Bosch et al (69) in their computer simulations find the highest efficiencies at lower bias fields roughly in agreement with these

results in the range:

$$2.5\ E_T < E_B < 3.0\ E_T$$

I have not attempted to investigate the upper-frequency limit since this required statistical knowledge of electron populations and relaxation time effects. This limit is assessed variously by workers as between 60 and 90 GHz. There arises a point of definition concerning space-charge quenching; whether it should be complete in every cycle or not built up over a number of cycles, these giving different criteria in analysis. Rees et al (128,129,130,131) in their device calculations find electronic relaxation times very significant in short samples with low carrier densities. This lower carrier density giving lower conductivity, higher dielectric relaxation time hence layers take longer to form and disperse, also less thermalisation effect. They describe an 'accelerated transit mode' and conclude an upper limit to 'true LSA' of 10-20 GHz,, whereas other modes continue to produce useful efficiencies at frequencies considerably higher than this, indeed they forecast (131) 10% at 40 GHz.

Chapter seven.

Conclusions and comment.

7.1. CONCLUSIONS

The aim of this work was to extend the available data on the velocity-field characteristic of electrons in indium phosphide, from this it may have been possible to predict more concerning the electronic structure and behaviour of devices manufactured from the material.

The characteristic was measured in epitaxial material at 300°K up to an electric field of 25 kV cm^{-1}. The threshold field was in the range 9.6 - 10.8 $kV.cm^{-1}$ the peak velocity in the range 2.35 - 2.90×10^7 cms^{-1} and the negative differential mobility value just above threshold from -1000 to -1380 $cm^2 . v^{-1} . s^{-1}$. These ranges expressing the deviations of the results, which were within the experimental error; assessed at 15%, 10% being of the experiment and 5% due to the variations in material properties. The results are from many measurements taken on material of mobility between 3590 and 4740 $cm^2 . v^{-1} . s^{-1}$ and doping densities in the range $7.2\ 10^{14}$, $2.4\ 10^{15}$ cm^{-3}. Variations in the characteristic were observed from layer to layer and accurate measurement is strongly dependent on material quality, which may be one reason for the considerable variations in the experimental results of other workers, apart from their use of bulk, epitaxial on n^+ or epitaxial on semi-insulating material.

At 100°K the measured threshold field had diminished by 9% (8.92 - 9.44 $kV.cm^{-1}$), the peak velocity increased by 65% (3.86 - 4.90×10^7 cms^{-1}), and the negative mobility increased by 33% (1415 - 1735 $cm^2 . v^{-1} . s^{-1}$). No information was gathered directly on the valley velocity or the behaviour of the curve at very high fields; but using other workers data the peak-to-valley ratio was predicted to be in the range $2.15 < r < 3.2$.

The perturbing factors in the experiment having most significant effects on the results were specimen uniformity, temperature, diffusion, space-charge and energy relaxation effects. The sample uniformity was measured to better than 5% by the suppliers of the material. Relative thickness of epilayer and substrate were found to affect the results to some degree. Temperature effects were minimised by the use of low duty-cycle pulsedrf radiation. Diffusion was neglected, space-charge effects accounted for during the experimental analysis and energy relaxation, if important, comparing estimates of other workers, was within the experimental error, so no account was made of it in the results.

Device efficiency was estimated for notional devices operating in sinusoidal or squarewave LSA modes. The maximum sinewave efficiency was calculated to be 7% and that for squarewaves some fourtimes as great. No account was taken of frequency limitations in the analysis. The effects of space-charge control criteria on the efficiency were clearly demonstrated. The velocity-field characteristics form also being quite a sensitive curve in the calculations, especially at 100°K. Indeed contrary to expectations of improved efficiency owing to higher peak-to-valley ratio, the efficiencies were lower, mainly due to space-charge control parameters restricting the operating conditions.

The possibility of effective-mass anisotropy (65) was not investigated with the samples available as they were all of identical orientations, certainly changes in mounting techniques would have been necessary, or possibly better - the manufacture of different orientations in similarly shaped samples might be more reliable.

7.2. COMMENT

There are three main avenues of investigation of relevance to the microwave solid-state material and device work. These are improvements in experimental methods and techniques, improvements in material quality and materials themselves and also more insight and data on device analysis.

Experimental methods and techniques could include better estimates of, or improved investigation into, the effects of doping and carrier density effects, the diffusion constant and relaxation phenomena. Knowledge of more data on these important parameters would improve the accuracy of determinations of fundamental properties such as the velocity-field characteristic. The microwave method of investigation, as used in this work, is limited by effects of space-charge, relaxation and high-field problems. It must be used in conjunction with pulsed current-voltage plotting below threshold and domain investigations above threshold; if possible a time-of-flight technique (77,132) would be useful for comparison. All of these applied to identical material samples, preferably cut from the same slice, would give a better overall picture of the fundamental property and the individual experimental capabilities.

Improvement in material quality would be derived from better manufacturing methods and manufacturing tolerances. New materials to be considered and investigated in the search for higher power, higher frequency, higher efficiency, lower noise devices might include the ternary systems. Indium arsenide phosphide and indium gallium arsenide; indeed Fawcett (133) et al mention the former system in their analysis of optimum materials for microwave semiconductor application. The exhaustive analysis of a ternary system would involve considerable toil, especially in growth and accurate determination of composition. It may be found that different compositions yield

optimum power, efficiency, frequency and noise performances. This conflict may result in trade-off in devices for different applications. Insofar as a completely new material is concerned it must have a distinct increase in transit velocity or peak-to-valley ratio to achieve a significant performance gain.

Examination of devices is vital to the development programme of a newer material, this includes work on new design methods now being reported (134) and investigation into device design, particularly reported in the case of contacts on Gunn oscillators (42-47) and amplifiers (135-137). Work on microstrip circuits and waveguide cavity design is also an essential part of this development, harmonic tuning has been outlined (see 6.3.3.) and this may offer some advantages over the simpler commercially available designs in the hunt for higher efficiencies.

Data from these alternative avenues of work may be examined in two distinct ways, one, experimental work could lead to better device design and manufacture and two, analysis of the device and environment could lead to improved understanding of fundamental properties and hence guide experimenters to design experiments to measure these properties.

Two possible examples for analysis are the suggested effective mass anisotropy reported by James (65) and the trapping phenomena reported by Teszner et al (124).

Both of these could be examined by direct experimental approaches on material grown in different orientations or doped with particular impurities; and by device manufacture using these specially grown slices, and the results compared to gain more insight into the processes. Certainly there is considerable scope for experimental work on indium phosphide, as also technological improvements, before any other materials are studied exhaustively.

7.3. Normalisation of results to drift mobility.

The experimental values of the velocity-field characteristic described in this work were normalised in calculation using the values of Hall mobility available from the manufacturers data. Majerfield et al (90) pointed out that this basis for normalisation of results may partly explain the significant scatter in peak-velocity values, being 2.4 - 3.0 x 10^7 cm.s^{-1}. It may be more meaningful to normalise all results to the low-field value of the drift mobility. The difference in values of the two mobilities is expressed in the Hall scattering factor:

$$r_h = \frac{\mu_H}{\mu_D} \qquad (2.6)$$

The values of this constant at the two temperatures of interest for the epitaxial type material used in the experiments are (142):

110°K $r_h = 1.08$

330°K $r_h = 1.17$

Using these, the experimental results were recalculated simply by proportion, since the mobility value occurs only once in calculation of the velocity-field characteristic, in the final multiplicative relation between current/field and velocity/field curves after the Schlömilch inversion of the experimental results:

$$v(E) = \frac{J(E)}{n\,q_e} \qquad \text{or} \qquad v(E) = J(E)\,\frac{\mu_o}{\sigma_o}$$

The results are plotted at fig 7A, together with those of Fawcett et al (140) by calculation and Majerfield et al (141) by subthreshold probing experiments. The salient data from these results are as follows:

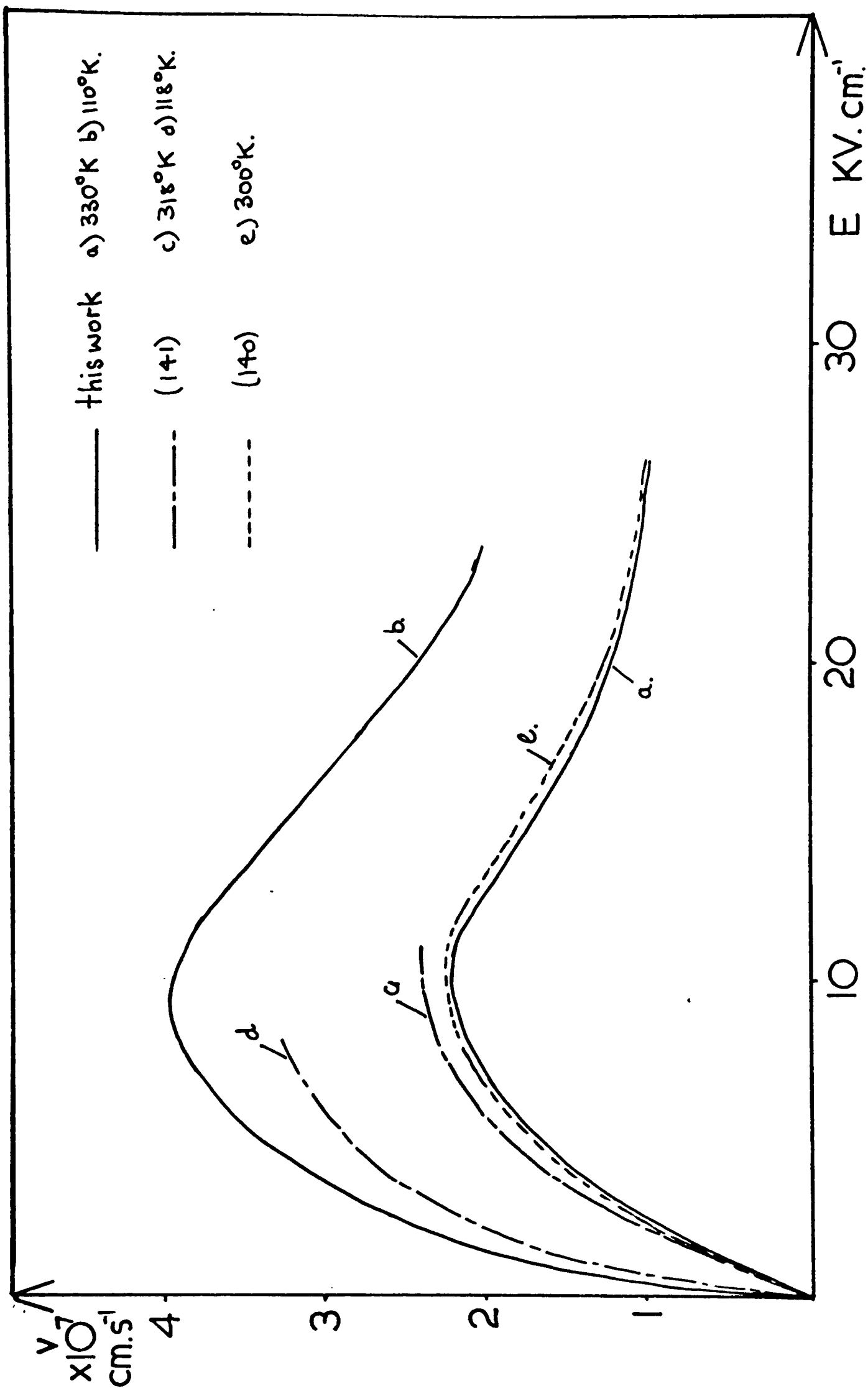

FIG. 7A

v(E) normalised to low-field drift mobility.

comparison of results.

	v_p	E_t	$-\mu_n$	T
this work	2.25 ±.23	10.2 ± .6	-1020 ±160	330
(140)	2.3	10.1	-1000	300
(141)	2.45	11.4	-	318
this work	4.05 ±.48	9.18 ±.26	-1460±145	110
(141)	3.3	8.0	-	118
	$x10^7$ cm.s^{-1}	KV.cm^{-1}	cm^{2}V^{-1}s^{-1}	°K

The results around 330°K agree reasonably well, no evidence of significent perturbation of the results by non-linear effects being evident. This is not so at 110°K; there being a 15% difference in threshold-field values and a 22% difference in the peak-velocity values obtained by the different experimental techniques. This disparity may be due to the effects of relaxation phenomena, which would affect the microwave experiment, not the subthreshold measurements. Ashida et al (143) found increased relaxation effects at lower temperatures in their work on gallium arsenide; not merely the carrier energy relaxation time increasing, but also the intervalley scattering time increasing at lower temperatures. These relaxation effects cause overshoot of the velocity-field characteristic calculated from data derived by microwave heating experiments, the overshoot being more marked in peak-velocity values than in threshold-field values (96). This is the most probable effect causing the apparant disagreement between the results of the different experiments at 110°K.

VELOCITY/FIELD CHARACTERISTIC OF *n*-TYPE INDIUM PHOSPHIDE AT 110 AND 330 K

Indexing terms: Electrical conductivity of solid semiconductors and insulators, III–V semiconductors, Indium compounds, High-field effects

The technique of microwave conductivity measurement was employed to investigate the velocity/field characteristic of epitaxially grown indium phosphide. Cooling the material from 330 to 110 K produced a 10% decrease in threshold field and a 70% increase in peak velocity. Measurements of variation of power absorption with epitaxial layer thickness are also reported.

A high-power microwave technique, similar to that employed by Glover,[1] has been used in the determination of the velocity/field characteristic of *n*-type indium phosphide, both at 330 and 110 K. Samples of the compound were fabricated from epitaxial material on semi-insulating substrates.* These had carrier concentrations in the range $7{\cdot}2\times10^{14}$–$2{\cdot}5\times10^{15}\,cm^{-3}$. Samples approximately 0·8 mm wide and 6 mm long were cleft from these chips and alloyed tin dot contacts placed on the epilayer at both ends. These samples were mounted inductively in rectangular fullheight waveguide (WG22).

The experimental microwave system was similar to that used by Bostock and Walsh[2] in their work on gallium arsenide, and was calibrated by this material. 35 GHz radiation was used to avoid space-charge instabilities, and a low duty cycle ($\leqslant 0{\cdot}05$ %) was employed to avoid undue heating. The temperature rise was calculated to be less than 45 deg K at the centre of the sample and generally less than half this value during the 200 ns pulse. The magnetron used was capable of producing up to 40 kW. To avoid dielectric breakdown, the waveguide was filled with sulphur hexafluoride at two atmospheres absolute pressure. This could not be used at liquid-nitrogen temperatures, and the experiment was terminated at lower powers, about 25 kW compared with 40 kW at room temperature. The carrier freezeout was stated to be less than 10%[3] down to 77 K, the increase in mobility being approximately tenfold at this temperature. Calculations of space-charge growth criteria indicated no instabilities at either temperature.

The experimentally measured data were in the form of absorbed power and average d.c. conductivity measured during the microwave pulses.[2] As the incident power was increased, there was a decrease in the transmitted and absorbed power fractions and a corresponding increase in reflected power. The data pairs were transformed by an iterative scheme on the computer† to obtain the function $\bar{\sigma}(E)$, the average conductivity as a function of the microwave electric field. This method obviates the necessity of calculation of the field in the waveguide using obstacle theory, e.g. Marcuvitz,[4] with its attendant assumptions regarding the fields at the semiconductor–air interfaces in the waveguide. The power absorbed by the semi-insulating substrates was small; consistent results were obtained with this fraction neglected.

The function $\bar{\sigma}(E)$ was inverted using the solution of Schlomilch's equation[5] to obtain the velocity/field characteristic $v(E)$. This was also performed on the computer, and space-charge control parameters were checked during this calculation. The experimental errors were assessed at ±10%, material uniformity at ±5%[3] yielding an error band of approximately ±15%. The standard deviation of the results compares well with this figure.

Measurements on a number of layers with carrier concentrations in the range $7{\cdot}2\times10^{+14}$–$2{\cdot}5\times10^{15}\,cm^{-3}$ led to variations in threshold field of 10·7 to 9·5 kV cm^{-1} and peak velocities 2·8 to $2{\cdot}3\times10^{7}$ cms^{-1}. The negative differential mobility was $-1190\pm190\,cm^2\,V^{-1}\,s^{-1}$, the lower-carrier-concentration slices tending to exhibit smaller mobilities. Comparison of the values between 110 and 330 K is shown in Table 1 and in the curves of Fig. 1.

Table 1

Temperature	Threshold field	Peak velocity	N.D. mobility
K	kV cm^{-1}	$\times10^7$ cms^{-1}	cm^2.V^{-1} s^{-1}
300	10·2±0·6	2·6±0·3	−1190±190
110	9·2±0·3	4·4±0·44	−1360±120

Table 2

Epilayer thickness	Threshold field	Peak velocity	N.D. mobility
μm	kV cm^{-1}	$\times10^7$ cms^{-1}	cm^2 V^{-1} s^{-1}
18·5	10·0	2·84	−1100
15	10·0	2·84	−1100
10	12·2	2·92	−1000
5	15·1	3·25	−1000

Power absorptions for a sample having various epitaxial layer thicknesses were measured at 330 K by successively etching the sample surface; velocity/field characteristics calculated gave salient data (Table 2).

These small changes would be accounted for partly by the relatively increased power absorption by the substrate for thinner epilayers; alternatively, dimension effects may govern this behaviour, although no correlation was obtained in calculation of *nd* products that would conform to the theory of Kino and Robson.[7]

The results shown in Fig. 1 fall into general agreement with both theoretical and experimental data so far reported; e.g. Fawcett and Herbert;[8] however, the negative differential mobility is appreciably higher than in some previous microwave measurements.[1] Temperature reduction to 110 K yields results agreeing with the results of Parkes and Taylor[9] on devices.

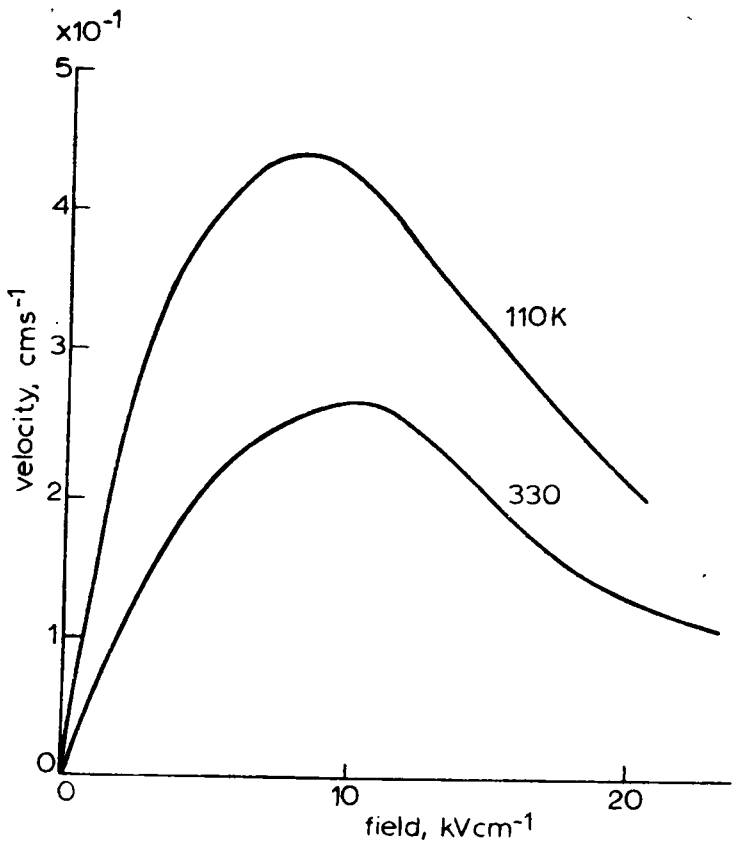

Fig. 1 *Velocity/field characteristic of indium phosphide*

Acknowledgments: This work was supported by the UK Science Research Council. Acknowledgments are made for useful discussions and practical help to the staff of the Department of Engineering Science, University of Oxford, and to G. Gibbons of the Allen Clark Research Centre.

R. L. TEBBENHAM
D. WALSH

Department of Engineering Science
Oxford University
Parks Road, Oxford OX1 3PX, England

27th January 1975

* Supplied by the Allen Clark Research Centre of The Plessey Co. Ltd.

† ICL1906A

References

1 GLOVER, G. H.: 'Microwave measurements of the velocity-field characteristic of *n*-type indium phosphide'
2 BOSTOCK, D. A., and WALSH, D.: 'Variation of the velocity/field curve of gallium arsenide in the range 40–180°C', *Electron. Lett.*, 1969, **5**, pp. 623–624
3 Data from the Allen Clark Research Centre, The Plessey Co. Ltd.
4 MARCUVITZ, N.: 'The waveguide handbook' (McGraw-Hill, 1951)
5 WHITTAKER, E. T., and WATSON, G. N.: 'A course of modern analysis' (CUP, 1945), p. 229 *et seq.*
6 GLOVER, G. H.: 'Studies of electron energy relaxation times in gallium arsenide and indium phosphide', *J. Appl. Phys.*, 1973, **44**, pp. 1295–1301
7 KINO, G. S., and ROBSON, P. N.: 'The effect of small transverse dimensions on the operation of Gunn deivces', *Proc. Inst. Elec. Electron. Eng.*, 1968, **56**, pp. 2056–2057
8 FAWCETT, W., and HERBERT, D. C.: 'High field transport in gallium arsenide and indium phosphide', *J. Phys. C.*, 1974, **7**, pp. 1641–1654
9 PARKES, E. P., and TAYLOR, B. C.: 'The effects of temperature on epitaxial indium phosphide transferred electron devices', *IEEE Trans.*, 1973, **ED–20**, pp. 852–855

References.

1. Most recently available data from many sources.

2. 'Microwave Journal' (Artech-Mass), and manufacturers' literature.

3. Ruttan, T.G., IEEE Trans. MTT-22 (2) 142 (1974).

4. Bachmann, K.J. and Buehler, E., J. Electrochem. Soc. 121 (6) 835 (1974).

5. Shurmer, H.V. 'Microwave semiconductor devices' 178 (Pitman-Lon-1971).

6. Roderick, E.H., J. Phys D (Appl. Phys) 3 (8) 1153 (1970).

7. Willardson, R.K. and Beer, A.C., 'Semiconductors and Semimetals' 2 118 (Academic Press-Lon-1966).

8. 'Diffusion Data' (Trans. Tech. Pub. - Germany) various issues.

9. Jones, H., 'The theory of the Brillouin zone and Electronic States in Crystals' 121 (New Holland Pub. Co. - Amsterdam - 1962).

10. James, L.W., Van Dyck, J.P., Haerman, F. and Chang, D.M., Phys; Rev. B1 (10) 3998 (1970).

11. Pitt, G.D., J. Phys. C (Solid State) 6 (9) 1586 (1973).

12. Donovan, B. and Angress, J.F. 'Lattice Vibrations' 103 (Chapman and Hall - Lon - 1970).

13. e.g. Magdelung, O., 'Physics of III-V Compounds' 22 (Wiley-NY-1964).

14. Smith, R.A., 'Semiconductors' 293 (CUP-1964).

15. Friedel, J., 'Dislocations' 206, 211, (Pergamon-Oxf-1964).

16. Kelley, A. and Groves, G.W., 'Crystallography and Crystal Defects' 218 (Longmans-Lon-1970).

17. Hartnagel, E.L. and Weiss, B.L., Solid State Electron. 17 (8) 799 (1974).

18. Erginsoy, C., Phys. Rev. 79 1013 (1950).

19. Conwell, E.M. and Weisskopf, Phys. Rev. 77 388 (1950).

20. Blood, P. and Orton, J.W., J. Phys.C. (Solid State) 7 (5) 893 (1974).

21. Alfrey, G.F. and Borcherds, P.H. J. Phys. C. (Solid State) 5 (15) L275 (1972).

22. Shockley, W. and Bardeen, J. Phys. Rev. 77 338 (1950).

23. Howarth, D.J. and Sondheimer, E.H., Proc. Roy. Soc. Lond. A219 53 (1953)

24. Ehrenreich, H., J. Phys. Chem. Solids, 2 (2) 131 (1957).

25. Ehrenreich, J., J. Phys. Chem. Solids 8(2) 130 (1959).

26. Hilsum, C. and Rose-Innes, A.C., 'Semiconducting III-V Compounds' 118 (Pergamon-Oxf-1961).

27. e.g. ibid. 122.

28. Ehrenreich, J., J. Phys. Chem. Solids 12(1) 97 (1959).

29. Hilsum, C., Electron. Lett. 10(13) 259 (1974).

30. Conwell, E.M . and Vassal, M.O. IEEE Trans. ED-13 (1) 22 (1966).

31. Hilsum, C. and Rees, H.D., Electron. Lett. 6 (9) 277 (1970).

32. Gunn, J.B., IBM J. Res. Develop. 8 (2) 141 (1964).

33. Butcher, P.N., Fawcett, W. and Hilsum, C., Brit. J. Appl. Phys. 17 841 (1966).

34. Kuru, I., Robson, P.N. and Kino, G.S., IEEE Trans. ED-15 (1) 21 (1968).

35. Conwell, E.M., IEEE Trans. ED-17 (4) 262 (1970).

36. Kao, K.C., Solid State Commun. 9 (10) 599 (1971).

37. Boers, P.M., Acket, G.A., Paxman, D.M. and Tree R.J., Electron. Lett. 7 (1) 1 (1971).

38. Hilsum, C., Mullin, J.B., Prew, B.A., Rees, H.D. and Straughan, B.W., Electron. Lett. 6 (10) 307 (1970).

39. Prew, B.A., Electron. Lett. 7 (19) 584 (1971).

40. Braddock, P.W. and Gray, K.W., Electron. Lett. 9 (2) 36 (1973).

41. Barkaran, S. and Robson, P.N., Electron. Lett. 8 (5) 137 (1972).

42. Colliver, D.J., Hilsum, C., Joyce, B.D., Morgan, J.R., Rees, H.D. and Knight, J.R., Electron. Lett. 6 (14) 436 (1970).

43. Colliver, D.J., Morgan, J.R. and Taylor, B.C., Electron. Lett. 7 (2) 50 (1971).

44. Gibbons, G. and White, P.M., Electron. Lett. 7 (7) 150 (1971).

45. Colliver, D.J., Gray, K.W. and Joyce, B.D., Electron. Lett. 8, (1) 11 (1972).

46. Colliver, D.J., Irving, L.D., Pattison, J.E. and Rees, H.D., Electron. Lett. 10 (11) 221 (1974).

47. Paxman, D.H. and Tree, R.J., Electron Lett. 7 (10) 240 (1971).

48. Zimmerl, O.F., Electron. Lett. 6 (23) 729 (1970).

49. Geraghty, S. and Gibbons, G., Electron. Lett. 6 (11) 584 (1970).

50. Carroll, J.E., Electron. Lett. 6 (13) 393 (1970).

51. e.g. Sze, S.M., 'Physics of Semiconductor Devices' 749 (Wiley-NY-1969).

52. e.g. Bulman, P.J., Hobson, G.S. and Taylor, B.C., 'Transferred electron devices' 144 (Academic Press-Lon-1972).

53. e.g. Ziman, F., 'Electrons and Phonons' 264 et seq (Clarendon Press-Oxf-1963).

54. Bløtekjaer, K., IEEE Trans. ED-17 (1) 38 (1970).

55. Herbert, D.C., J. Phys. C. (Solid State) 6 (18) 2788 (1973).

56. Heinle, W., Phys. Letters 35A (5) 365 (1971).

57. Hammar, C. and Vinter, B., Solid-state Commun. 11 (11) 751 (1972).

58. Hilsum, C., and Rees, H.D., Electron. Lett. 7 (15) 437 (1971).

59. Fawcett, W., Boardmann, A.D. and Swain, S., J. Phys. Chem. Solids, 31(9) 1963 (1970).

60. Fawcett, W. and Herbert, D.C., Electron Lett. 9 (14) 308 (1973).

61. Fawcett, W. and Herbert, D.C., J. Phys. C. (Solid State) 7 (9) 1641 (1974).

62. Bauhahn, P.T., Haddad, G.I., and Massari, N.A., Electron. Lett. 9 (19) 460 (1973).

63. Hillbrand, H.A., J. Phys. C. (Solid State) 5 (24) 3491 (1972).

64. Hillbrand, H.A., Electron. Lett. 7 (17) 495 (1971).

65. James, L.W., J. Appl. Phys. 44 (6) 2746 (1973).

66. Kane, E.O., J. Phys. Chem. Solids 1 (4) 249 (1957).

67. Herman, F., Kortum, R.L., Euglin, C.D., Van Dyck, J.P. and Stillman, S., "Methods of Computational Physics" 8 (Academic Press-NY-1968).

68. Glover, G.H., J. App. Phys. 44 (3) 1295 (1973).

69. Bosch, R. and Thim, H.W., IEEE Trans. ED-21 (1) 16 (1974).

70. Hammar, C. and Vinter, B., Electron. Lett. 9 (1) 10 (1973).

71. Marshak, A.H. and Assaf, D., Solid-State Electron. 16 (6) 675 (1973).

72. Hauge, P.S., IEEE Trans. ED-18 (6) Corresp. 390 (1971).

73. Carroll, J.E., 'Hot-electron microwave generators', 76 (E. Arnold-Lon-1970).

74. Ruch, J.G. and Kino, G.S., Appl. Phys. Lett. 10 (2) 40 (1967).

75. Fay, B. and Kino, G.S., Appl. Phys. Lett. 15 (8) 337 (1969).

76. Boers, P.M., Electron. Lett. 7 (20) 625 (1971).

77. Evans, A.G.R. and Robson, P.N., Solid State Electron. 17 (8) 805 (1974).

78. Boers, P.M., Phys. Lett. 34A (6) 329 (1971).

79. Bastida, E.M., Fabri, G., Svelto, V. and Vaghi, F., Appl. Phys. Lett. 18 (1) 28 (1971).

80. Prew, B.A., Electron, Lett. 8 (24) 598 (1972).

81. Prew, B.A., Solid State Electron 17 (7) 725 (1974).

82. Kaul, R., Grubin, H.L., Ladd, G.C. abd Berak, J.M., IEEE Trans. ED-19 (8) 988 (1972).

83. Boers, P.M., Electron. Lett. 9 (6) 134 (1973).

84. Prew, B.A., Electron. Lett. 9 (10) 236 (1973).

85. 'T.Lam, H. and Acket, G.A., Electron. Lett. 7 (24) 722 (1971).

86. Glover, G.H., Appl. Phys. Lett. 20 (6) 224 (1972).

87. Glover, G.H., J. Appl. Phys. 42 (10) 4025 (1971).

88. Nielsen, L.D., Phys. Lett. 38A (4) 221 (1972).

89. Hilsum, C. and Rees, H.D., Electron. Lett. 8 (15) 373 (1972).

90. Majerfield, A., Potter, K.E. and Robson, P.N., J. Appl. Phys. 45 (8) 3681 (1974).

91. Braslau, N., and Hauge, P.S., IEEE Trans. ED-17 (8) 616 (1970)

92. Marcuvitz, N., 'The Waveguide Handbook' 265 et seq (McGraw Hill-NY-1951).

93. Holmes, D.A., Feucht, D.L., and Jacobs, H., Solid-State Electron. 7 (4) 267 (1964).

94. e.g. Whittaker, E.T. and Watson, G.N., 'A course of modern analysis' 229 et seq (C.U.P.-1945).

95. Glover, G.H., Appl. Phys. Lett. 17 (11) 472 (1970).

96. ibid, 18 (7) 290 (1971).

97. Champlin, K.S. and Glover, G.H., J. Appl. Phys. 37 (6) 2355 (1966).

98. Tree, R.J., Josh, M.J. and Foxon, C.T., Solid-State Electron. 14 (6) 519 (1971).

99. Bostock, P.A. and Walsh, D., Electron Lett. 5 (24) 623 (1969).

100. Zucker, J., Fowler, V.J. and Conwell, E.M., J. Appl. Phys. 32 (12) 2606 (1961).

101. Carslaw, H.C. and Jaeger, J.C., 'Conduction of Heat in Solids' 82 et seq,108 et seq (Clarendon Press-Oxf-1959).

102. 'Microwave Handbook' ed. E. Saad 31 (Artech-Mass-1971).

103. Meek, J.M. and Craggs, J.D., 'Electrical breakdown of gases' 321 (Clarendon Press-Oxf-1953).

104. Knight, D.J., D. Phil. Thesis OUEL 191 (1965).

105. Acket, G.A. and DeGroot, J., IEEE Trans. ED-14 (9) 505 (1967).

106. Champlin, K.S. and Armstrong, D.B., Proc. IRE 50 (2) Corresp. 232 (1962).

107. Champlin, K.S., Proc. IEEE 52 (9) Corresp. 1061 (1964).

108. Gunn, M.W., Proc. IEEE 52 (2) Corresp. 185 (1964).

109. Anderson, J.B. and Majborn, B., IEEE Trans. MTT-16 (3) Corresp. 194 (1968).

110. Datta, A.N. and Nag., B.R., IEEE Trans. MTT-18 (3) 162 (1970).

111. Roy, P.K. and Datta, A.N., IEEE Trans. MTT-22 (2) 194 (1974).

112. Hamilton, D.K., private communication.

113. e.g. Bulman, P.J., Hobson, G.S. and Taylor, B.C., 'Transferred electron devices' 97 (Academic Press-Lon-1972).

114. Cardwell, M.J., and Peart, R.F., Electron. Lett. 9 (4) 88 (1973).

115. Hilsden, F.J., private communication.

116. Becker, R., Solid-State Electron. 16 (11) 1241 (1973).

117. Hamilton, D.K. private communication.

118. Kino, G.S. and Robson, P.N., Proc. IEEE Letters 56 2056 (1968).

119. Parkes, E.P. and Taylor, B.C., IEEE Trans. ED-20 (10) 852 (1973).

120. Tokumaru, Y. and Mikoshiba, N., Solid-State Commun. 10 (3) 261 (1972).

121. Tokumaru, Y. and Mikoshiba, N., Japan J. Appl. Phys. 12 (11) 1753 (1973).

122. Ridley, B.K., Brit. J. Appl. Phys. 17 (8) 595 (1966).

123. Ridley, B.K., Crisp, J.J. and Shishiyanu, F., J. Phys. C. (Solid-State) 5 (2) 187 (1972).

124. Teszner, J.L. and Boccon-Gibod, D., J. Appl. Phys. 44 (6) 2765 (1973).

125. Copeland, J.A., J. Appl. Phys. 38 (8) 3096 (1967).

126. Fawcett, W. and Taylor, B.C., IEEE Trans. ED-17 (10) 907 (1970).

127. Kino, G.S. and Kuru, I., IEEE Trans. ED-16 (9) 735 (1969).

128. Jones, D. and Rees, H.D., Electron Lett. 8 (14) 363 (1972).

129. ibid 8 (23) 566 (1972).

130. ibid 9 (5) 105 (1973).

131. ibid 10 (12) 234 (1974).

132. Ruch, J.G. and Kino, G.S., Phys. Rev., 174 (3) 921 (1968).

133. Fawcett, W., Hilsum, C. and Rees, H.D., Electron. Lett. 5 (14) 313 (1965).

134. Sechi, F.N. and Zieger, D., 'Microwave Journal' 16 (4) 47 (1973).

135. Thim, H.W., Electron. Lett. 7 (4) 106 (1971).

136. Sitch, J.E., Electron. Lett. 10 (6) 74 (1974).

137. Corlett, R.M., Griffeth, I., and Purcell, J.J., Electron Lett. 10 (15) 307 (1974).

138. e.g. Lanczos, C. 'Applied Analysis' 178, 245 (Pitman-Lon-1957).

139. e.g. ibid 396.

Appendices.

APPENDIX 1

THE SCHLOMILCH EQUATION (94)

If $f(x)$ is a function such that within the range $-\pi \leqslant x \leqslant +\pi$ $f'(x)$ is continuous then

$$f(x) = \frac{2}{\pi}\int_0^{\pi/2} \bar{\phi}(x\sin\theta)\,d\theta \qquad (A.1.1)$$

has a solution

$$\bar{\phi}(x) = f(0) + x\int_0^{\pi/2} f'(x\sin\theta)\,d\theta \qquad (A.1.2)$$

We have

$$\bar{\sigma}(E_0) = \frac{2}{\pi}\int_0^{\pi/2} J'(E_0\sin\phi)\,d\phi. \qquad (3.8)$$

multiplying by E_0 and noting that $J(0) = 0$.

$$E_0.\bar{\sigma}(E_0) = J(0) + \frac{2}{\pi}E_0\int_0^{\pi/2} J'(E_0\sin\phi)\,d\phi. \qquad (A.1.3)$$

Comparing this to (A1.2) and inverting to the form (A1.1)

$$J(E_0) = \frac{2}{\pi}\cdot\frac{\pi}{2}\cdot\int_0^{\pi/2} \bar{\sigma}(E_0\sin\phi).E_0\sin\phi.d\phi. \qquad (A1.4)$$

this being the form of eq. (3.9).

APPENDIX 2

TSCHEBYCHEV POLYNOMIAL APPROXIMATION (138)

If we write an approximation to a function $f(x)$ within the interval $[a,b]$ as a power series $p_n(x)$, of degree n, this will have an error corresponding to

$$e_n(x) = f(x) - p_n(x)$$

writing $p_n(x)$ explicitly

$$p_n(x) = a_o + a_1x + a_2x^2 + \ldots + a_nx^n$$

then: $e_n(x) = f(a_o, a_1 \ldots\ldots a_n)$

The best approximation is one such that $e_n(x)$ is minimum in the interval $[a,b]$. This is termed the oscillation property of the approximation to $f(x)$. Ideally for $(n+2)$ points x_i in $[a,b]$ the error attains a maximum value $\pm E_m$, hence

$$e_n(x_i) = f(x_i) - p_n(x_i) = (-1)^i E_m$$

A good approximation may be some other polynomial $q_n(x)$, which has $(n+2)$ alternate maxima and minima, but not all of the same magnitude viz:

$$e_1 \leqslant e_n \leqslant e_2$$

the method of construction of this is to choose $(n+1)$ points within $[a,b]$, and to formulate the polynomial

$$a_o + a_1x_i + a_2x_i^2 + \ldots\ldots + a_nx_i^n = f(x_i)$$

$$0 \leqslant i \leqslant n$$

which determines the coefficients a_r. The error vanishes at these $(n+1)$ points and the extrema a,b. Hence $(n+2)$ error values occur in between producing a particular set of errors. This is the general polynomial approach.

A Tschebychev polynomial of degreein $\cos\theta$ has the oscillation property such that for the range $[0,\pi]$ it has alternate maxima and minima at n+1 points.

Writing $X = \cos\theta$ we deduce the Tschebychev polynomial

$$T_n(x) = \cos(n \cos^{-1} x) \qquad -1 \leq x \leq +1$$

this is then a polynomial of degree n with alternate maxima and minima at (n+1) points

$$x_r = \cos r\pi/n \qquad 0 \leq r \leq n$$

Thus if k_n is the coefficient of x^n in $T_n(x)$ we may approximate the sample polynomial x^n by $p_{n-1}(x)$, so

$$p_{n-1}(x) = x^n - k^{-1}T_n(x)$$

which is the best approximation since

$$x^n - p_{n-1}(x) = k^{-1}T_n(x)$$

which has the required oscillation property with (n+1) maxima and minima, alternate and all equal.

If the approximation is economised such that

$$f(x) = \sum_{r=0}^{n} a_r x^r \qquad \text{n-finite}$$

this terminates the series, obtaining a polynomial and a remainder, dominated by the first neglected term if the series is rapidly convergent. This will have only two extremes and will be monotomic, thus the truncated series will not necessarily satisfy the mathematical criteria of a good approximation, although the numerical error may be small.

The error in the approximation as described by:

$$F(x) = \sum_{r=0}^{n} a_r T_r(x)$$

where $n < \infty$

is

$$E(x) < a_n T_n(x)$$

within the range $-1 \leqslant x \leqslant +1$

Whether this is of significance is calculable only by checking throughout all the range.

APPENDIX 3

GAUSS LEGENDRE QUADRATURE (139)

Consider a function f(x) in the range $\left[-1, +1\right]$, and n+1 values within this range

$$y_j = f(x_j) \qquad 0 \leqslant j \leqslant n$$

in general this will be insufficient to specify f(x). It would be possible to interpolate using a polynomial of degree (n-1) assuming y_j values at x_j points, but this would give no control between the points. Let us write

$$F_n(x) = (x-x_1)(x-x_2)(x-x_3) \text{ --- } (x-x_n)$$

and from this obtain polynomials $Q_j(x)$ by:

$$Q_j(x) = \frac{1}{F'n(x_j)} \cdot \frac{Fn(x)}{(x-x_j)} \qquad 0 \leqslant j \leqslant n$$

These have the property:

$$Q(x) \neq 0 \qquad x = x_j$$

$$Q_j(x) = 0 \qquad x = x_k$$

and

$$p_{n-1}(x) = y_1Q_1(x) + y_2Q_2(x) + \ldots\ldots + y_nQ_n(x)$$

which satisfies the criteria $y = y_j$ at $x = x_j$. This function is unique since no other function may possess this property. The area is defined by:

$$A = \int_{-1}^{+1} f(x)dx = \int_{-1}^{+1} p_{n-1}(x)dx$$

which leads to

$$A = \sum_{j=1}^{n} y_j \int_{-1}^{+1} Q_j(x)\cdot dx.$$

For any distribution x_j, $Q_j(x)$ is unique and the integral:

$$\int_{-1}^{+1} \Theta_j(x)\,dx$$ has a definite value independent of y.

An orthogonality condition is included such that

$$\int_{-1}^{+1} F_n(x) \cdot x^{\alpha} = 0 \qquad 0 \leqslant \alpha \leq n$$

$F_n(x)$ is identifiable with the Legendre polynomial of degree n, the zeroes of which gives the x_j ordinates. These and the weights w_j have been tabulated for reference in many books.

Hence the method is to decide how many points j to use, therefore deciding n. The values of w_j and x_j for the n ordinates are tabulated and then the computation can be done of:

$$y_j = f(x_j)$$

$$\bar{A} = \int_{-1}^{+1} f(x)dx = \sum_{j=1}^{n} w_j y_j$$

where $\bar{A}$ is the area required.

The error in this approximate integration can be estimated, with difficulty, from knowledge of the 2^{nth} derivative of f(x) at some point within the range $[-1, +1]$. It is:

$$\bar{\eta} = \frac{(n!)^2}{(2n)!^2} \quad \frac{2^{2n+1}}{2n+1} \quad f^{1(2n)}\ (\theta) \quad -1 \leqslant \theta \leqslant +1$$

Should the function f(x) possess a zero 2^{nth} derivative then the error is zero. An alternative approach uses knowledge of the first derivative of the function such that

$$\bar{\eta} = \frac{1}{2n+1} \left\{ f(1) + f(-1) - \bar{A} - \sum_{j=1}^{n} w_j f^1(x_j) \right\}$$

or expanded

$$\bar{\eta} = \frac{1}{2n+1} \left\{ (y_1 + y_n) - \sum_{j=1}^{n} w_j (y_j + y_j) \right\}$$

Calculation of this is required for each function $y = f(x)$ and each integral; no general form exists. In the case of 24 ordinates the error is given by

$$\bar{\eta} = 2.4\ 10^{-60}\ f^{12n}(\theta)$$

For the function in question $f^{12n}(\theta) \ll 1$ since the function is smooth. Hence the error is very small.

APPENDIX 4

SOLUTION OF WAVEGUIDE OBSTACLE IMPEDANCE (92)

Considering an obstacle in waveguide in which the fundamental TE_{10} mode is propagating. For that mode we have:

$$E_x = E_z = 0$$

$$E_y = \frac{-jE_o w \mu a}{\pi C} \cdot \sin \frac{\pi x}{a} \cdot \exp(-j\beta Z)$$

$$Hx = \frac{j\beta a}{\pi} \sin \frac{\pi x}{a} \exp(-j\beta Z)$$

$$Hy = 0$$

$$Hz = \cos \frac{\pi x}{a} \exp(-j\beta Z)$$

$$\beta = 2\pi \left\{ \frac{1}{\lambda_o^2} - \frac{1}{(2a)^2} \right\}^{1/2}$$

These data may be matched to the solution of the general propagation equations in the obstacle planes as required. Marcuvitz cites a method used by Schwingler as follows:

$$E_{oy} = E_{Iy} + j\gamma c\mu \int_{S'} J(x,'z') . G(x,z;x,'z') ds'$$

where γ = free space propagation coefficient

$J(x,'z')$ is the polarisation current density in the dielectric at $(x,'z')$

$G(x,z;x'z')$ is the field at (x,z) due to a unit current filament at $(x,'z')$. This satisfies the inhomogeneous wave equation:

$$\left(\nabla_{xz}^2 + \gamma^2\right) G(x,z;x';z') = -\delta(x-x') . \delta(z-z').$$

The fields deduced from the expression for E_{oy} matched to the first set of conditions are reducible to a network impedance via the matrix analysis:

$$\begin{pmatrix} v_1 \\ v_2 \end{pmatrix} = \begin{pmatrix} Z_{11} & Z_{12} \\ Z_{21} & Z_{22} \end{pmatrix} \begin{pmatrix} i_1 \\ i_2 \end{pmatrix}$$

which by symmetry gives

$$Z_{11} = Z_{22}$$

and reciprocity

$$Z_{12} = Z_{21}$$

A variational technique yields a solution E_s to make $(Z_{11} + Z_{12})$ stationary via:

$$\frac{-j2(Z_{11}+Z_{12})(\epsilon_r-1)k^2}{R_a} = \frac{\int_{s'} E_s^2(x,z)\,dS' - (\epsilon_r-1)\,\ell^2 \int_s \int_{s'} E_s(x,z)\; G(x,z;x',z')\,dS\,dS'}{\left[\int_s E_s\; E_{Ie}(x,z)\,.\,dS\right]^2}$$

E_{Ie} is the even component of the incident electric field.

APPENDIX 5

SCATTERING MATRIX ANALYSIS

For a two-port network it is convenient to have the network parameters defined in terms of forward and reflected waves. Referring to Fig. A5-A we consider the incident and reflected voltage waves at each port. These are normalised as follows

$$a_n = \frac{v_n^+}{\sqrt{Z_{on}}} \qquad b_n = \frac{v_n^-}{\sqrt{Z_{on}}}$$

The impedance Z_{on} is that impedance of the line or circuit connected to the port - not the input impedance or output impedance.

The scattering matrix is defined as

$$[B] = [S][A]$$

or

$$\begin{bmatrix} b_1 \\ b_2 \end{bmatrix} = \begin{bmatrix} S_{11} & S_{12} \\ S_{21} & S_{22} \end{bmatrix} \begin{bmatrix} a_1 \\ a_2 \end{bmatrix}$$

This may be extended to more complex networks of n ports and various relations concerning this matrix may be formed.

Reciprocal network, two port

$$S_{12} = S_{21}$$

Lossless network, two port

$$|S_{21}|^2 = 1 - |S_{11}|^2$$

Attenuation of a lossy network, defined as W_1/W_2

$$\frac{W_1}{W_2} = 1 - \frac{(S_{11})^2}{S_{21}^2}$$

and insertion loss

$$\frac{(a_1)^2}{(b_1)^2} = \frac{1}{(S_{21})^2}$$

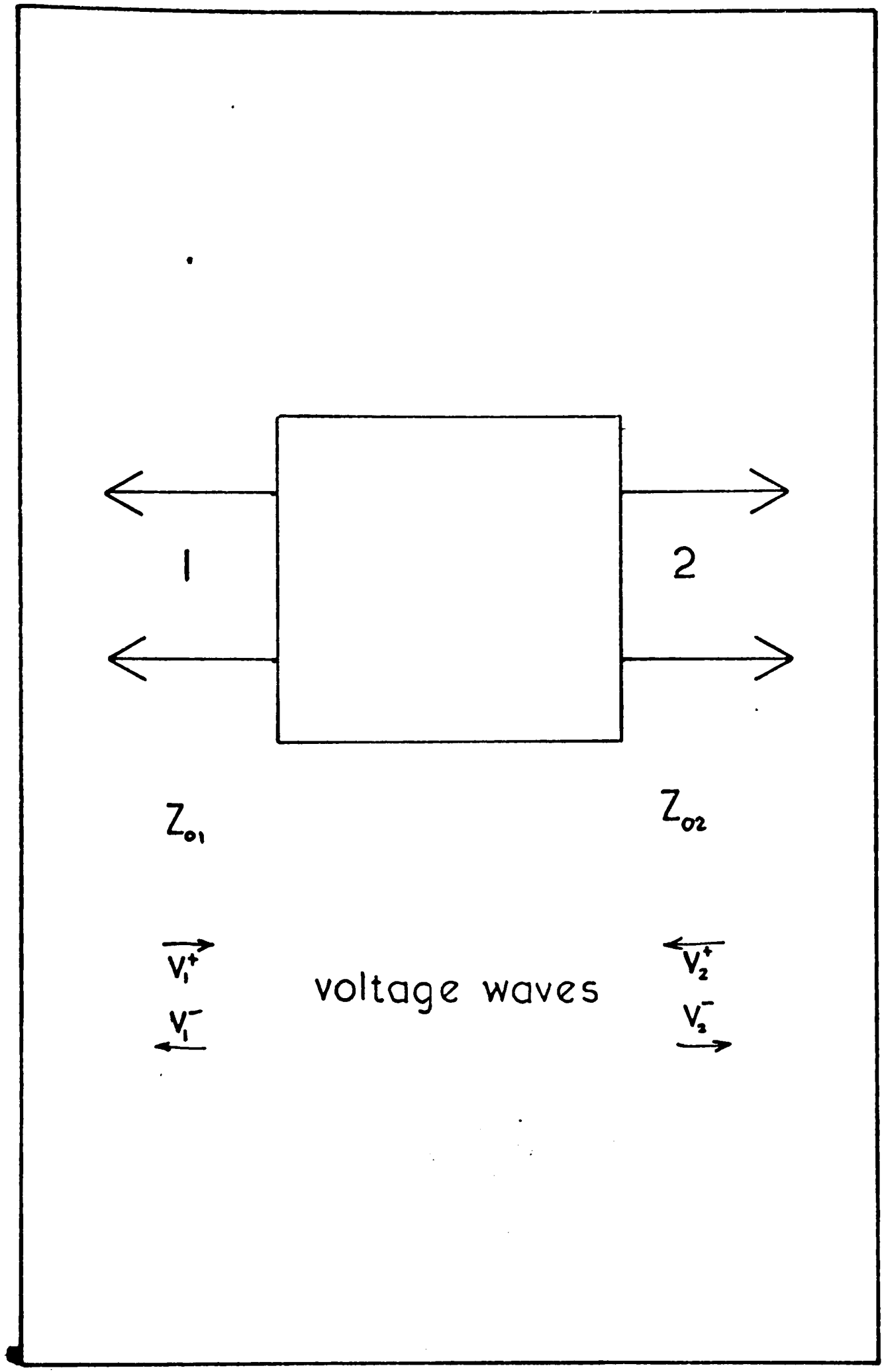

FIG. A5A

Two-port network

scattering matrix analysis - schematic.

These find considerable application in the analysis of complex multi-port networks by signal flowgraphs, and also in the characterisation of two port devices.

The equation connecting the impedance and scattering matrices is

$$(S) = ((Z) - Z_o(I))((Z) + Z_o(I))^{-1}$$

where

$$(Z) = \begin{pmatrix} Z_{11} & Z_{12} \\ Z_{21} & Z_{22} \end{pmatrix}, \qquad I = \begin{pmatrix} 1 & 0 \\ 0 & 1 \end{pmatrix}$$

and Z_o is the normalising impedance. Computation of this yields

$$\frac{1}{\Delta Z}\left\{\begin{array}{l}\left[(Z_{11}-Z_o)(Z_{22}+Z_o)-Z_{12}Z_{21}\right]\left[2\,Z_{12}Z_o\right]+ \\ \qquad \left[2\,Z_{21}Z_o\right]\left[(Z_{11}+Z_o)(Z_{22}-Z_o)-(Z_{12}Z_{21})\right]\end{array}\right\}$$

where $\Delta Z = \left[(Z_{11} + Z_o)(Z_{22} + Z_o) - Z_{12}\,Z_{21}\right]$

The symmetry of the problem in Ch. 4 yields the simplified reciprocal result.

APPENDIX 6

ITERATIVE SOLUTION OF THE POWER ABSORBTION/ELECTRIC FIELD EQUATION

The equation connecting the absorbed power and the electric-field was derived as :

$$\frac{dW_a(E_o)}{dE_o} = \frac{W_a(E_o)}{E_o} + \frac{V}{2} \cdot E_o \bar{\sigma}(E_o) \qquad (3.11)$$

which was integrable to:

$$\frac{W_a(E_o)}{E_o} = \frac{V}{2} \int_o^{E_o} \bar{\sigma}(E_o).\, dE_o$$

which we may write as:

$$\frac{W_a(E_o)}{E_o} = \frac{V}{2} \int_o^{E_o} \bar{\sigma}\left[E_o \cdot \frac{W_a(E_o)}{E_o}\right] dE_o \qquad (A6.1)$$

We have measured the function $\bar{\sigma}(W_a)$ experimentally and by using the iterative scheme outlined here we may calculate the field values to make eq. A6.1 consistent for corresponding values of $\bar{\sigma}$ and W_a. It will then be possible to deduce the function $\bar{\sigma}(E_o)$.

Let us write:

$$\frac{W_a}{E_o} = y \ , \quad E_o = x.$$

we may now write A6.1 as:

$$y = \frac{V}{2} \int_o^x \bar{\sigma}(x.y).\, dx. \qquad (A\ 6.2).$$

We select a set of equidistant points x_i such that the maximum valued x_n is equal to the largest value of electric field for which we wish to perform calculations, bearing in mind the maximum field we expect to be attained in any particular experimental run. For the first point x_1 we make a trial solution $(y_1)^1$ and we compute a second value following eq A6.2:

$$(y_1)^2 = \frac{V}{2} \int_0^{x_1} \bar{\sigma}(x_1, (y_1)') \, dx$$

the values of $\bar{\sigma}$ being extracted from the experimental data of $\bar{\sigma}(W_a)$. The value of $(y_1)^2$ is not necessarily equal to $(y_1)^1$ and since trial solutions $(y_i)^1$ were always selected to be smaller than the expected value then

$$(y_i)^{j+1} \geqslant (y_i)^j \qquad \text{(A6.3)}$$

where we are considering the (j+1)th and jth iterations of the ith value of y corresponding to the ith value of x. The newly calculated value of $(y_1)^2$ is then inserted into the integral in the RHS of eq A6.2 and after another iteration we obtain:

$$(y_1)^3 = \frac{V}{2}\int_0^{x_1} \bar{\sigma}\left(x_1, (y_1)^2\right) dx.$$

This process continues at the field value corresponding to x_1 until the value of the iterated variable y_1 converges such that:

$$\left|(y_1)^{n+1} - (y_1)^n\right| \leqslant \text{a truncation error.} \qquad \text{(A6.4)}$$

so that we now have a consistent set of values for the variables in the equation A6.2 at the point x_1:

$$y_1 = \frac{V}{2}\int_0^{x_1} \bar{\sigma}\,(x_1, y_1)\, dx.$$

where:

$$y_1 = (y_1)^n$$

which is the value defined by the condition A6.4. The iteration process is halted at point x_1 and moves one step along the field values to x_2. Here the iteration is started with a trial value of y_2 defined as:

$$(y_2)^1 = y_1 \qquad \text{(A6.5)}$$

this preserves the relation A6.3 by selection of a smaller than expected trial value for the variable y at the commencement of the iteration.

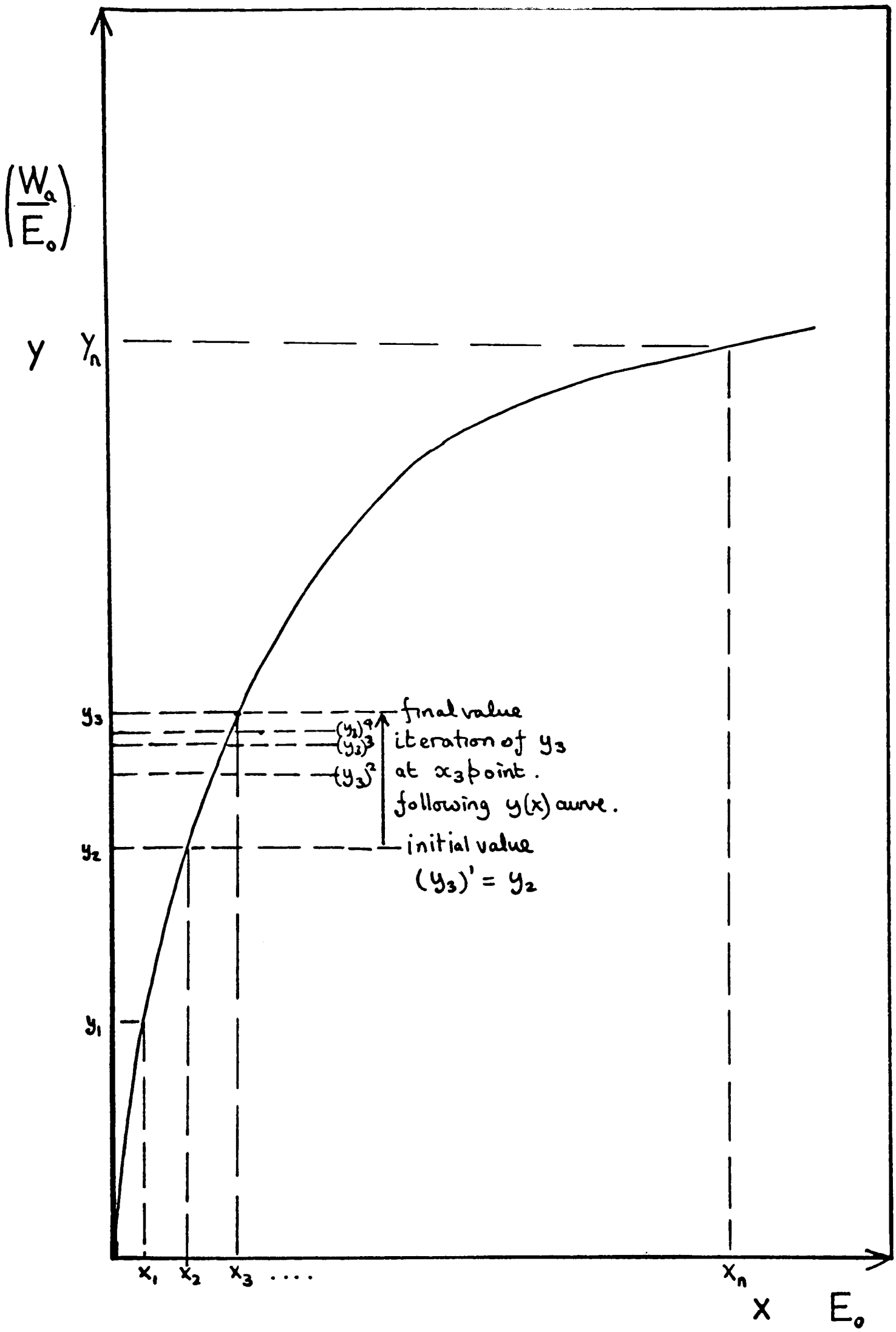

FIG. A6A

Iteration of power-absorbtion/electric-field equation.

The iteration proceeds using the equation A6.2 at the new point x_2 so that the value of the variable y converges to y_2 following the method outlined for the point x_1, y_1. The process is shown schematically at figure A6A.

The function y(x) is plotted step-by-step following the iteration of equation A6.2. for all the points x_i. Following our definitions between A6.1 and A6.2 we now have the function $W_a(E_o)$. We now compare on the computer the values of $W_a(E_o)$ and $\bar{\sigma}(W_a)$ and thereby calculate the function $\bar{\sigma}(E_o)$. This is the function we require to perform the Schlömilch inversion as described by equation 3.9.

The effect on the accuracy of this numerical iteration technique of the truncation error defined in A6.4 and of the step length between successive field values (x_n, x_{n+1}) was investigated during the testing of the analysis programmes described in section 4.2.2. to produce the results shown in fig 4E. The truncation error was specified to be 1 in 10^5 for most analysis; but 1 in 10^4 could be used for small field ranges when the number of iteration points x_n was not too great (in an effort to economise on computer time) this reducing the accuracy of the routine from better than 1% overall to about 5% overall.